



HAL
open science

Ceria supported single-site catalysts prepared by surface organometallic chemistry for the reduction of nitrogen oxides by ammonia (NH₃-SCR)

Cuirong Chen

► **To cite this version:**

Cuirong Chen. Ceria supported single-site catalysts prepared by surface organometallic chemistry for the reduction of nitrogen oxides by ammonia (NH₃-SCR). Catalysis. Université Claude Bernard - Lyon I, 2022. English. NNT : 2022LYO10132 . tel-04719170

HAL Id: tel-04719170

<https://theses.hal.science/tel-04719170v1>

Submitted on 3 Oct 2024

HAL is a multi-disciplinary open access archive for the deposit and dissemination of scientific research documents, whether they are published or not. The documents may come from teaching and research institutions in France or abroad, or from public or private research centers.

L'archive ouverte pluridisciplinaire **HAL**, est destinée au dépôt et à la diffusion de documents scientifiques de niveau recherche, publiés ou non, émanant des établissements d'enseignement et de recherche français ou étrangers, des laboratoires publics ou privés.



**THESE de DOCTORAT DE
L'UNIVERSITE CLAUDE BERNARD
LYON 1**

**Ecole Doctorale N°206
Chimie, Procédés, Environnement**

Discipline :
Chimie et applications

Soutenue publiquement le 29/11/2022, par :
Cuirong CHEN

**Ceria supported single-site catalysts prepared
by surface organometallic chemistry for the
reduction of nitrogen oxides by ammonia (NH₃-
SCR)**

Devant le jury composé de :

LIOTTA, Leonarda	Directrice de Recherche ISMN, CNR, Palerme	Rapporteuse
GAUVIN, Régis	Directeur de Recherche IRCP, CNRS, Paris	Rapporteur
GIROIR-FENDLER, Anne	Professeure IRCE-LYON, CNRS, Lyon	Présidente de jury
NGUYEN, Hai P.	Ingénieur Toyota Motor Europe, Zaventem	Examineur
KADDOURI, Akim	Professeur Université Lyon 1, Lyon	Directeur de thèse
TAOUFIK, Mostafa	Ingénieur de Recherche CP2M, CNRS, Lyon	Co-Directeur de thèse

Université Claude Bernard – LYON 1

Président de l'Université	M. Frédéric FLEURY
Président du Conseil Académique	M. Hamda BEN HADID
Vice-Président du Conseil d'Administration	M. Didier REVEL
Vice-Président du Conseil des Etudes et de la Vie Universitaire	M. Philippe CHEVALLIER
Vice-Président de la Commission de Recherche	M. Jean-François MORNEX
Directeur Général des Services	M. Damien VERHAEGHE

COMPOSANTES SANTE

Faculté de Médecine Lyon-Est – Claude Bernard	Doyen : M. Gilles RODE
Faculté de Médecine et Maïeutique Lyon Sud Charles. Mérieux	Doyenne : Mme Carole BURILLON
UFR d'Odontologie	Doyenne : Mme Dominique SEUX
Institut des Sciences Pharmaceutiques et Biologiques	Directrice : Mme Christine VINCIGUERRA
Institut des Sciences et Techniques de la Réadaptation	Directeur : M. Xavier PERROT
Département de Formation et Centre de Recherche en Biologie Humaine	Directrice : Mme Anne-Marie SCHOTT

COMPOSANTES & DEPARTEMENTS DE SCIENCES & TECHNOLOGIE

UFR Biosciences	Directrice : Mme Kathrin GIESELER
Département Génie Electrique et des Procédés (GEP)	Directrice : Mme Rosaria FERRIGNO
Département Informatique	Directeur : M. Behzad SHARIAT
Département Mécanique	Directeur : M. Marc BUFFAT
UFR - Faculté des Sciences	Directeur : M. Bruno ANDRIOLETTI
UFR (STAPS)	Directeur : M. Yannick VANPOULLE
Observatoire de Lyon	Directrice : Mme Isabelle DANIEL
Ecole Polytechnique Universitaire Lyon 1	Directeur : Emmanuel PERRIN
Ecole Supérieure de Chimie, Physique, Electronique (CPE Lyon)	Directeur : Gérard PIGNAULT
Institut Universitaire de Technologie de Lyon 1	Directeur : M. Christophe VITON
Institut de Science Financière et d'Assurances	Directeur : M. Nicolas LEBOISNE
ESPE	Directeur : M. Pierre CHAREYRON

There is a crack in everything, that's how the light gets in.

Acknowledgment

This thesis is carried out in the laboratory of 'Catalysis, Polymerisation, Processes and Materials' (CP2M -UMR 5128) hosted in Ecole Supérieure de chimie, physique électronique de Lyon. The first acknowledgements go to the director of the laboratory, Dr Timothy Mckenna, and the director of the school, Mr Gerard Pignault, for having hosted me in their establishment which has allowed me to conduct the research work related to this thesis.

This topic is initiated by a collaboration between CP2M and Toyota Motor Europe (TME), in the research of innovative NH₃-SCR catalysts prepared by surface organometallic chemistry.

Time flies so fast. I am grateful to everyone I have met in the past three years. It is your support that allows me to continue to complete this work. I would like to thank the China Scholarship Council (CSC). Thanks for giving me this opportunity to start my research in an international environment. Every achievement of mine is supported by this funding. Gratitude to my strongest country.

The person I want to thank the most is my supervisor, Mostafa TAOUFIK, for your three years of teaching. Surface organometallic chemistry was a very unfamiliar subject to me three years ago. It's thanks to your support and teaching through lively activities that I can now confidently say that I'm doing research in organometallic chemistry, which is a very complex chemistry discipline. I would also like to thank Kai Chung SZETO, especially for all your help since my first day in Lyon. Thank you for helping me understand and solve all the basic scientific problems I encountered in this subject, and thank you for teaching me to use all the reaction instruments and the experimental operations. In life, I appreciate you and your wife, Linger LOU, a lot for your meticulous care and support.

Also, I want to say thank you to my co-supervisor Akim KADDOURI. Heterogeneous catalysis requires a lot of effort to characterize. Thanks for your help in the characterization process. Additionally, I would like to thank you for all the administrative help during my Ph.D. in France, which made my research life easier.

Dr. Aimery DE MALLMANN, thank you for all the help that you provided in X-ray absorption and EPR experiments, as well as administrative supports. Many thanks to our administrative manager, Emmanuelle FOUILLHE and for the entire staff of CP2M. My deepest gratitude goes to the staff of engineers Dr. Nesrine OUSLATI, Dr. Anne BONHOMME, and Dr. Pascal BARGIELA. I appreciate a lot to the knowledge you offered as well as the help you have done on my sample in solid state NMR, Raman and XPS analysis.

The members of the jury (Leonarda Francesca LIOTTA, Anne GIROIR-FENDLER, Régis GAUVIN) are acknowledged for having accepted to evaluate this work. Particularly Dr Hai P. NGUYEN (TME), for having initiate this collaboration and for the fruitful discussions over the years.

To my dear lab mates, Paolo, Jessy, Isah, Nicola, Sara, Antony, Felipe, Yulan, and Ning, thank you for your help in the lab staff and your generous love for my life in France. To my Chinese friends I met in Lyon, Qilin XIN, Yanchun DING, Chenglong GE, Chunyan QIN, Xin HE, Haosheng LIANG, and Feng PAN. Thanks for our meeting, I will always remember the stories that happened in Lyon. Le souvenir, c'est la présence invisible.

The last one I would like to thank is myself. Thanks for your courage and persistence.

You are the best!

Abbreviations

Δ	Thermal treatment
δ	Chemical shift
$\delta(\text{A-B})$	Deformation frequencies of A-B bond
$\nu(\text{A-B})$	Stretching frequencies of A-B Bond
Å	Angstrom
BET	Brunauer, Emmett, Teller
<i>t</i> Bu	<i>tert</i> iobutyl group -C-(CH ₃) ₃
DRIFT	Diffuse Reflectance Infrared Fourier Transform
EXAFS	Extended X-Ray Absorption Fine Structure
XANES	X-ray absorption near edge structure
GC	Gas Chromatography
IR	InfraRed
NMR	Nuclear Magnetic Resonance
SOMC	Surface Organometallic Chemistry
GHSV	Gas Hourly Space Velocity
TEM	Transmission Electronic Microscopy
STEM	Scanning Transmission Electron Microscopy
EDX	Energy Dispersive X-Ray
HRTEM	High-resolution transmission electron microscopy
XPS	X-ray photoelectron spectroscopy
THF	Tetrahydrofuran
<i>t</i> BuOH	<i>tert</i> iobutanol
XRD	X-Ray diffraction
DFT	Density Functional Theory
EPR	Electron paramagnetic resonance
XAS	X-ray absorption spectroscopy
EXAFS	Extended X-ray absorption fine structure
ppm	part per million
nm	nanometre
cm ⁻¹	reciprocal centimetre
a.u.	atomic unit

Contents

CHAPTER I Description of Ceria based catalysts for NH₃-SCR	21
1. Structure and Properties of Ceria	22
1.1 Fundamental structure of Ceria	22
1.2 Common crystalline facets in Ceria	23
1.3 Intrinsic defects: oxygen vacancy	26
1.4 Extrinsic defects: doping defects.....	28
1.5 Redox pairs Ce ³⁺ /Ce ⁴⁺	30
1.6 Acid-base property	31
2. Applications of Ceria in catalysis.....	33
2.1 Photocatalytic reactions.....	33
2.1.1 Photocatalytic oxidation	34
2.1.2 Photocatalytic reduction	35
2.2 Selective oxidation	36
2.2.1 CO oxidation	36
2.2.2 N-H oxidation.....	38
2.3 Selective reduction	40
2.3.1 CO ₂ reduction	40
2.3.2 NH ₃ -SCR	41
3 Surface organometallic chemistry for the preparation of supported catalysts.....	50
3.1 Introduction of surface organometallic chemistry	50
3.2 Support materials for Surface Organometallic Chemistry	52
3.2.1 Silica as support.....	52
3.2.2 Alumina as support.....	54
3.3 Selected examples of SOMC on group V and VI transition metals	56
3.3.1 Surface Organometallic Chemistry of Group V	56
3.3.2 Surface Organometallic Chemistry of Group VI.....	58
4 Objective of the thesis	60
Reference.....	62
	11

CHAPTER II Surface Organometallic Chemistry of [W(\equivCtBu)(CH₂tBu)₃] on CeO₂₋₂₀₀ of the development of highly active NH₃-SCR catalysts	75
1 Introduction	76
2 Preparation and characterization of CeO ₂₋₂₀₀ support.....	79
2.1 Preparation of CeO ₂₋₂₀₀	79
2.2 Characterization of CeO ₂₋₂₀₀ by DRIFT spectroscopy.....	82
2.3 Characterization of OH groups in CeO ₂₋₂₀₀ by titration with Al(iBu) ₃	83
2.4 Characterization of CeO ₂₋₂₀₀ by solid state NMR.....	84
2.5 Characterization of CeO ₂₋₂₀₀ by X-ray photoelectron spectroscopy	85
3 Preparation and characterization of W(\equiv CtBu)(CH ₂ tBu) ₃ supported on CeO ₂₋₂₀₀	87
3.1 Preparation of [W(\equiv CtBu)(CH ₂ tBu) ₃]/CeO ₂₋₂₀₀ [W-a]	87
3.2 Characterization of [W-a] by Mass balance analysis.....	88
3.3 Characterization of [W-a] by DRIFT spectroscopy	88
3.4 Characterization of [W-a] by Nitrogen adsorption-desorption isotherm measurements	89
3.5 Characterization of [W-a] by solid state MAS NMR.....	90
3.6 Characterization of [W-a] by X-ray diffraction analysis.....	92
3.7 Characterization of [W-a] by X-ray photoelectron spectroscopy analysis and Electron paramagnetic resonance	93
3.8 Characterization of [W-a] by X-ray absorption spectroscopy.....	94
4 Preparation and characterization of W-oxo supported on CeO ₂	96
4.1 Preparation of W-oxo/CeO ₂ [W-b].....	96
4.2 Characterization of [W-b] by Elemental analysis and DRIFT spectroscopy	97
4.3 Characterization of [W-b] by Raman spectroscopy	100
4.4 Characterization of [W-b] by Nitrogen adsorption-desorption isotherm measurements	101
4.5 Characterization of [W-b] by HRTEM and STEM.....	102
4.6 Characterization of [W-b] by X-ray photoelectron spectroscopy	103
4.7 Characterization of [W-b] by X-ray absorption spectroscopy	103
5 Catalytic performance investigation.....	105
5.1 Catalytic performance in NO conversion and N ₂ Selectivity	105
5.2 Recycling and tolerance of H ₂ O of Ceria supported tungsten-oxo catalysts.....	107

5.3 Structure-reactivity relationship in NH ₃ -SCR	109
5.3.1 Catalytic performance	109
5.3.2 Surface acidity	111
5.3.3 Redox ability	112
6 Conclusion.....	114
Reference.....	116

CHAPTER III Novel vanadium supported on CeO₂ catalysts prepared by SOMC: Effect of precursors and vanadium loading on the activity for NH₃-SCR reaction..... 125

1 Introduction	126
2 Preparation and characterization of V-oxo supported on CeO ₂₋₂₀₀ using [V(=O)(OEt) ₃] ₂ as precursor	130
2.1 Preparation of [V(=O)(OEt) ₃] ₂ /CeO ₂₋₂₀₀ [V1-a]	130
2.2 Characterization of [V(=O)(OEt) ₃] ₂ /CeO ₂₋₂₀₀ [V1-a]	131
2.2.1 Characterization of [V1-a] by Elemental analysis	131
2.2.2 Characterization of [V1-a] by DRIFT spectroscopy	131
2.2.3 Characterization of [V1-a] by solid state NMR	132
2.2.4 Characterization of [V1-a] by Electron Paramagnetic Resonance	133
2.3 Preparation of V-oxo/CeO ₂ [V1-b] from [V(=O)(OEt) ₃] ₂ /CeO ₂₋₂₀₀ [V1-a]	134
2.4 Characterization of V-oxo/CeO ₂ [V1-b]	135
2.4.1 Characterization of [V1-b] by Elemental analysis and DRIFT spectroscopy	135
2.4.2 Characterization of [V1-b] by Raman spectroscopy	136
2.4.3 Characterization of [V1-b] by ⁵¹ V MAS solid state NMR	137
2.4.4 Characterization of [V1-b] by X-ray photoelectron spectroscopy	138
2.4.5 Characterization of [V1-b] by Electron paramagnetic resonance	139
2.4.6 Characterization of [V1-b] by X-ray absorption spectroscopy	140
3 Investigation of NH ₃ -SCR Catalytic performance	142
3.1 Catalytic performance of [V1-b] for NO conversion and N ₂ Selectivity	142
3.2 Effects of vanadium loading.....	142
3.2.1 Effects of vanadium loading on catalytic activity	143

3.2.2	Investigation of surface species by DRIFT spectroscopy.....	144
3.2.3	Investigation of surface species by ⁵¹ V MAS NMR.....	146
4	Preparation and characterization of V-oxo supported on CeO ₂₋₂₀₀ with precursor [V(CH ₂ SiMe ₃) ₄]	148
4.1	Preparation of [V(CH ₂ SiMe ₃) ₄]/CeO ₂₋₂₀₀ [V2-a].....	148
4.2	Characterization of [V(CH ₂ SiMe ₃) ₄]/CeO ₂₋₂₀₀ [V2-a].....	148
4.2.1	Characterization of [V2-a] by mass balance analyses.....	148
4.2.2	Characterization of [V2-a] by DRIFT spectroscopy.....	149
4.2.3	Characterization of [V2-a] by solid state NMR and EPR spectroscopies.....	150
4.2.4	Characterization of [V2-a] by X-ray photoelectron spectroscopy.....	151
4.2.5	Characterization of [V2-a] by X-ray absorption spectroscopy.....	152
4.3	Preparation of V-oxo/CeO ₂ [V2-b].....	153
4.4	Characterization of V-oxo/CeO ₂ [V2-b].....	153
4.4.1	Characterization of [V2-b] by Elemental analysis and DRIFT spectroscopy.....	153
4.4.2	Characterization of [V2-b] by Raman spectroscopy.....	155
4.4.3	Characterization of [V2-b] by ⁵¹ V MAS solid state NMR.....	155
4.4.4	Characterization of [V2-b] by X-ray photoelectron spectroscopy.....	156
4.4.5	Characterization of [V2-b] by X-ray absorption spectroscopy.....	157
5	Preparation and characterization of V-oxo supported on CeO ₂₋₂₀₀ with precursor [V(=O)(OtBu) ₃]	159
5.1	Preparation of [V(=O)(OtBu) ₃]/CeO ₂₋₂₀₀ [V3-a].....	159
5.2	Characterization of [V(=O)(OtBu) ₃]/CeO ₂₋₂₀₀ [V3-a].....	160
5.2.1	Characterization of [V3-a] by Elemental analysis and DRIFT spectroscopy.....	160
5.2.2	Characterization of [V3-a] by solid state NMR.....	161
5.3	Preparation of V-oxo/CeO ₂ [V3-b] from [V(=O)(OtBu) ₃]/CeO ₂₋₂₀₀ [V3-a].....	162
5.4	characterization of V-oxo/CeO ₂ [V3-b].....	162
5.4.1	Characterization of [V3-b] by DRIFT spectroscopy.....	162
5.4.2	Characterization of [V3-b] by Raman.....	163
5.4.3	Characterization of [V3-b] by ⁵¹ V MAS solid -state NMR.....	164
6	Effects of precursor for V-oxo/CeO ₂ on NH ₃ -SCR Catalytic performance.....	165
6.1	Catalytic performance in the NO conversion and N ₂ Selectivity.....	165

6.2 Structure-reactivity relationship in NH ₃ -SCR	166
7 Conclusion.....	167
Reference.....	169
CHAPTER IV Selective Catalytic Reduction of NO_x with NH₃ over niobium supported on CeO₂ prepared by Surface Organometallic Chemistry	175
1 Introduction	176
2 Preparation and characterization of Nb(OEt) ₅ /CeO ₂₋₂₀₀ [Nb-a].....	178
2.1 Preparation of [Nb(OEt) ₅] ₂ /CeO ₂₋₂₀₀ [Nb-a].....	178
2.2 Characterization of [Nb-a] by Elemental analysis	179
2.3 Characterization of [Nb-a] by DRIFT spectroscopy.....	180
2.4 Characterization of [Nb-a] by Nitrogen adsorption-desorption isotherm measurements.....	181
2.5 Characterization of [Nb-a] by solid state NMR	181
3 Preparation and characterization of Nb-oxo supported on CeO ₂	182
3.1 Preparation of Nb-oxo/CeO ₂ [Nb-b]	182
3.2 Characterization of [Nb-b] by Elemental analysis and DRIFT spectroscopy.....	182
3.3 Characterization of [Nb-b] by Time-of-flight secondary ion mass spectrometry.....	183
3.4 Characterization of [Nb-b] by X-ray photoelectron spectroscopy and EDX Mapping.....	184
3.5 Characterization of [Nb-b] by X-ray Adsorption spectroscopy	185
4 Catalytic performance investigation.....	187
4.1 Catalytic performance (NO conversion and N ₂ selectivity) of [Nb-b].....	187
4.2 Effect of Nb loading on catalytic performance over [xNb-b] (x=0.2 wt%, 0.5 wt%, 1.0 wt%, and 1.8 wt%)	188
5 Comparison of different group V and VI transition metals supported on Ceria	188
5.1 Structure of catalysts based on CeO ₂ supported metals (M=V, Nb, Mo, W).....	188
5.2 Comparison of the NH ₃ -SCR performance over Metal-oxo/CeO ₂ (Metal=W, Mo, Nb, V) catalysts	192
6 Conclusion.....	195
Reference.....	195
CHAPTER V Conclusion and perspectives	201
Experimental section.....	209

General introduction

The rapid development of the economy has increased energy demand. As the main original energy, fossil fuels are widely used in industrial production, vehicles, and ships, emitting a large amount of harmful pollutant NO_x (mainly including NO and NO₂). The NO_x treatment methods are mainly divided into pre-treatment, combustion treatment, and post-treatment. However, the pre-treatment mainly requires a pre-treatment of the fuels resulting in important costs. The combustion treatment always needs strict conditions in actual industrial production and automobile exhaust treatment. Post-treatment, especially selective catalytic reduction with NH₃ is one of the promising methods to remove NO_x, producing clean N₂ and H₂O to avoid secondary pollution. The commercial catalyst V₂O₅-WO₃/TiO₂ has already been widely used in industries. Nevertheless, the catalytic conversion efficiency, operation temperature window, thermal stability, and recycling ability may still be improved. Moreover, vanadium is fairly volatile under typical catalytic conditions, resulting in the emission of toxic vanadium species. Therefore, the choice and design of novel efficient NH₃-SCR catalysts are imminent.

Apart from TiO₂, CeO₂ has demonstrated to be a promising support material for NH₃-SCR, due to its superior oxygen storage, thermal stability, and acidity. Although ceria itself possesses activity under typical NH₃-SCR conditions, the low activity has been assigned to the lack of acidity. The most common strategy to increase activity is to introduce another element, first of all to increase the acidity and to create the necessary acid/redox pair, proposed as the active site for this reaction. The introduced element or elements can be situated either on the surface or in the bulk (mixed oxide), depending on the catalyst preparation techniques (aqueous impregnation, co-precipitation, sol-gel), the loading of the novel element and the pre-treatment conditions. These classical synthetic methods usually provide an uncontrolled and ambiguous mixture of surface species. Obviously, such materials are unsuitable for mechanistic studies, determination of the active site and eventually distinguishing the catalytic role of each element. Consequently, several reaction mechanisms have been proposed, but yet no general agreement is reached. Nevertheless, the proposed mechanisms, always involve acidic and redox sites. This leads to another problematic, which is the type of acidity participating in the reaction mechanism. Several reports claim that it is Lewis acidity, while others demonstrate that it is rather Bronsted acidity (particularly for zeolitic systems, but also for metal oxide systems). Recently, single-site catalysis attracts a lot of attention, as multiple publications propose that the active site over traditional metal-oxide

catalysts (olefin metathesis, oxidation, dehydrogenation/hydrogenation of hydrocarbons) is an isolated metal site with a controlled coordination sphere. Single-site catalysts generally exhibit a higher atom efficiency and are more suitable for active site probing and mechanistic studies. As all sites are supposedly accessible, the activity per metal is expected to increase. Surface organometallic chemistry (SOMC) is considered to be an efficient method for immobilizing single-site moieties on the surface of oxides, particularly via the protonolysis of specific organometallic complexes. It has paved the way for researching the nature of active sites, determination of elementary steps of catalytic reactions, discovery of new reactions and acts as a bridge between homogeneous and heterogeneous catalysis. The choice of the promoting element is important. In the literature, most of the transition state metals have been studied, giving indeed different catalytic performances. This work is focused on early transition state metals of groups V and VI, owning high oxophilicities and redox capabilities, they may generate acidity (both Lewis and Bronsted) and can lead selectively to isolated metal oxo species.

This work covers the preparation and characterization of ceria-based single-site catalysts for the reduction of nitrogen oxides by ammonia. SOMC approach is applied to obtain metal-oxo on the surface of ceria, which is regarded as the active site in the NH_3 -SCR reaction. Widely used additional metals for NH_3 -SCR reaction, from groups V and VI (W, Mo, V, Nb), are applied by designing suitable organometallic precursors, grafting them on a dehydroxylated ceria support, oxidizing the grafted species and applying further thermal treatments. The resulting materials are well-characterized and evaluated in a continuous flow reactor. Furthermore, the structure-activity relationship of the various surface species is investigated. This thesis is divided into 5 Chapters:

Chapter I is devoted to drawing up the knowledge of structure, properties, and applications in redox reactions of ceria-based heterogeneous catalysts. The state of the art in ceria-based catalysts for redox reaction and their structure-activity relationship is presented. In particular, the research status of ceria-based catalysts in NH_3 -SCR reaction is discussed. After the bibliographic study, we present our goals and strategies employed for this work.

Chapter II is devoted to the investigation of the surface of the ceria. The optimized temperature of calcination and dehydroxalation are determined by In-situ DRIFT and XRD. The number of active surface hydroxyls and the mobility of lattice oxygen in ceria structure

are studied. To synthesize the predicted active species W-oxo on the surface of ceria, a novel strategy is designed in that tungsten Schrock complex $[W(\equiv C\textit{t}Bu)(CH_2\textit{t}Bu)_3]$ is grafted onto ceria followed by oxidation under air. The grafting and oxidation process are disclosed based on structural characterization. The catalytic performances in NH_3 -SCR and structural stability are evaluated and compared to those of bulk ceria and WO_x/CeO_2 synthesized by the classical impregnation method.

Chapter III is dedicated to vanadium supported on ceria prepared by SOMC. Catalysts prepared from different vanadium precursors and with different vanadium loadings have been synthesized, characterized and tested in NH_3 -SCR reaction. In order to prepare isolated V-oxo/ CeO_2 catalysts, different precursors (the dimeric V^{5+} precursor $[V(=O)(OEt)_3]_2$, monomeric V^{4+} precursor $[V(CH_2SiMe_3)_4]$, and monomeric V^{5+} precursor $[V(=O)(O\textit{t}Bu)_3]$) are grafted on the dehydroxylated ceria, followed by the calcination at 500 °C. These materials have been structurally characterized and investigated for NH_3 -SCR reaction.

Chapter IV extends this strategy to obtain niobium-oxo supported on CeO_2 by grafting $[Nb(OEt)_5]_2$ on the support and calcining under air at 500 °C. The obtained materials have been characterized and the calcined sample has been submitted to NH_3 -SCR reaction. The catalytic activity of different metal oxo supported on ceria catalysts synthesized during this thesis has been compared, and the most promising system has been identified.

Finally, **Chapter V** brings a general conclusion and perspectives suggested for future researches.

CHAPTER I

Bibliography study

1. Structure and properties of ceria

Cerium, originating from rare-earth minerals Bastnasite, Monazite, and Loparite, is one of the most abundant elements, comparable in abundance to copper[1]. Cerium dioxide exhibits good thermostability even in harsh environments, such as temperatures up to 2000 K[2]. In addition, materials based on ceria have low toxicity and are compatible with many biological and inorganic materials[1][3]. Due to the reasons mentioned above, ceria has been employed in many applications over the past few decades. The exclusive properties are closely related to the unique crystal structure, oxygen vacancies, $\text{Ce}^{3+}/\text{Ce}^{4+}$ redox couple, and acid-base properties situated on different crystal planes.

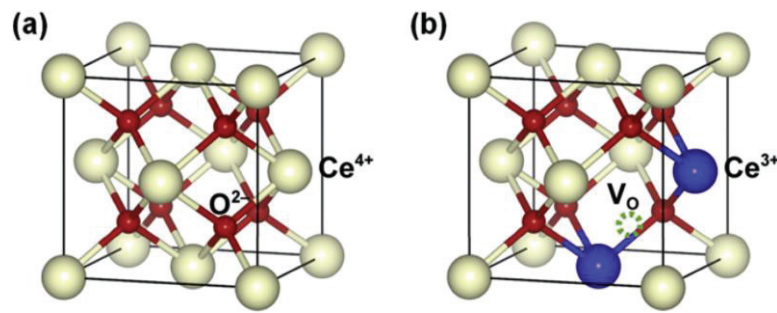
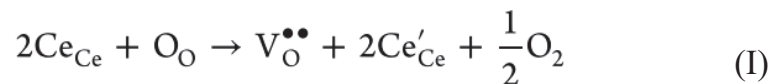


Fig. 1 Schematic illustration of the crystal structure of (a) ideal CeO_2 , and (b) CeO_2 in the presence of one oxygen vacancy accompanied by two generated Ce^{3+} species [4]

1.1 Fundamental structure of ceria

CeO_2 typically presents the form of the cubic fluorite crystal structure (cubic closest packed) described by the $\text{Fm}\bar{3}\text{m}$ space group. As shown in Fig. 1a, the Ce atoms constitute the closest packed layer, while O atoms are situated in the tetrahedral holes (100% filled)[4]. The electronic configuration of an isolated Ce atom is $[\text{Xe}] 4f^1 5d^1 6s^2$, which is mixed with a $4f \text{L}^{n-1}$ configuration due to the similar energies of 4f and orbitals of ligand valence level [5]. This makes a reversible charge transfer between $4f^1 5d^0 \text{Ce(III)}$ and $4f^0 5d^0 \text{Ce(IV)}$, which is a unique behavior among rare-earth metals[6]. Usually, non-stoichiometric CeO_{2-x} can be obtained as the following equation (I): oxygen is released followed by oxygen vacancy formation and leaving two electrons reducing Ce^{4+} to Ce^{3+} , as shown in Fig. 1b. Moreover, CeO_{2-x} has high oxygen mobility through the unoccupied octahedral hole, which is beneficial to heterogeneous catalysis reactions through the storage and release of oxygen.



1.2 Common crystalline facets in ceria

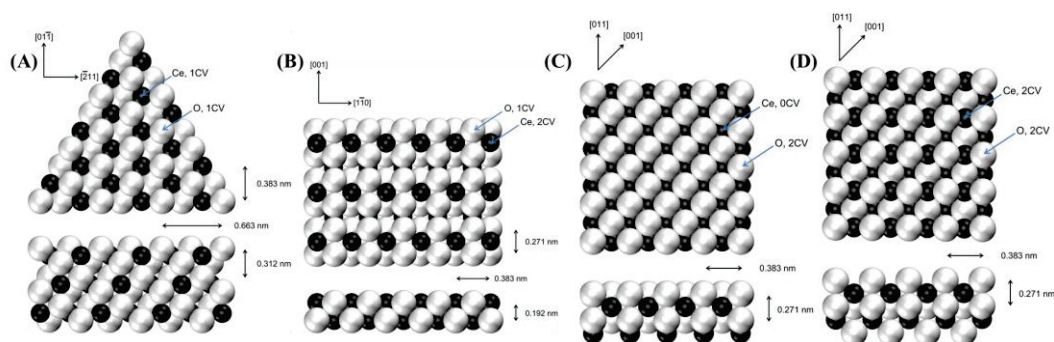


Fig. 2 Atomic configurations of different crystal planes (A) $\text{CeO}_2(111)$, (B) $\text{CeO}_2(110)$, and (C, D) $\text{CeO}_2(100)$ in unit cells. (Ce: black spheres; O: the white spheres). CV refers to the number of coordination vacancies around the Ce and O atoms[7]

Generally, three typical lattice planes ((111), (110), (100)) are most exposed on the surface of Ceria. Different crystalline planes exhibit varied atomic arrangements and compositions, which present different coordination environments of Ce^{4+} . Furthermore, these crystal facets may possess unique reactivity for catalytic reactions and provide various structure-activity correlations[8]. Characteristic parameters from DFT calculations of different crystal planes from the literature[9] are presented in Table 1.

Table 1 Characteristics of the low-index surfaces of $\text{CeO}_2(111)$ [9]

	111	110	100
Coordination Numbers	O (3), Ce (7)	O (3), Ce (6)	O (2), Ce (6)
Coordinative unsaturated sites	O (1), Ce (1)	O (1), Ce (2)	O (2), Ce (2)
Surface energy (eV) ^a	0.69 (0.68)	1.26 (1.01)	2.05 (1.41)
Oxygen vacancy formation energy (eV) ^b	2.60	1.99	2.27

^a Unrelaxed and (relaxed) values of surface energies.

^b Vacancy formation energy.

As shown in Fig. 2A, $\text{CeO}_2(111)$ is a Tasker Type 2 oxide surface[10] described by three layers, O–Ce–O, with charge neutrality. As for the coordination environment, O and Ce each have a single coordinately unsaturated site. When reduced, a single O anion is presumably removed, producing two Ce^{3+} . $\text{CeO}_2(110)$ is a Tasker Type 1 oxide surface with the same composition in each layer and presents charge neutrality (Fig. 2B). On the $\text{CeO}_2(110)$ surface, O exhibits one unsaturated coordination site, and Ce shows two unsaturated coordination sites. Atomic configurations of $\text{CeO}_2(100)$ in Fig. 2C is a Tasker Type 3 oxide surface with an O–Ce–O–Ce layered structure[10], which is unstable due to the presence of a surface dipole. To

eliminate the dipole moment, the model is corrected by removing half of the ions from one layer and moving them to the opposing face (Fig. 2D). Herman[11] used mass spectroscopy of recoiled ions (MSRI) to investigate the structure, and found atomic configurations being consistent with Fig. 2D. O and Ce on the surface of CeO₂ (100) each have two unsaturated coordination sites. When CeO₂(100) is treated with a reducing agent, O from the outer layer is removed, which increases the unsaturated sites on the surrounding Ce³⁺ cations.

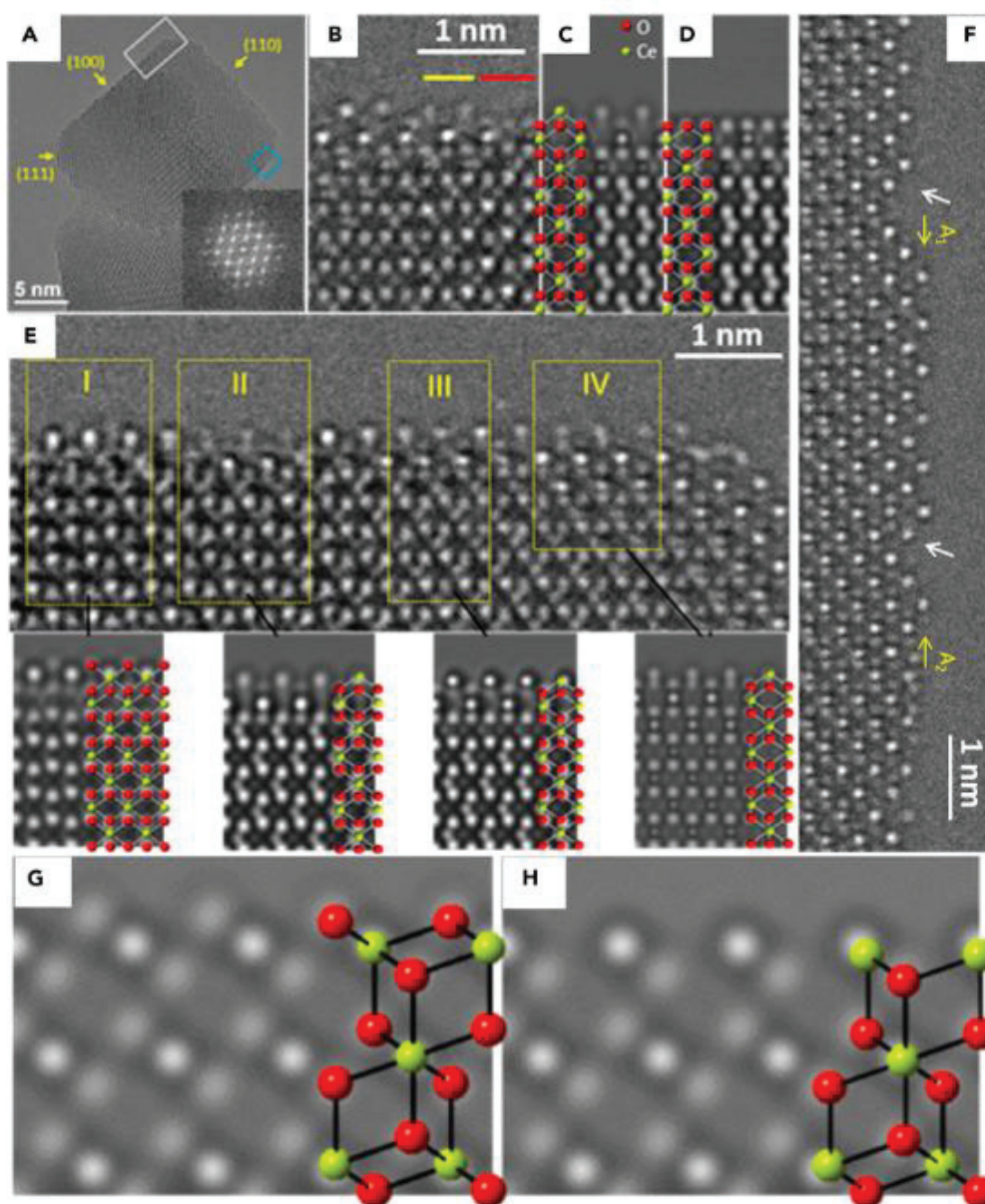


Fig. 3 (A) HRTEM image of a typical CeO₂ nanocube. (B) A magnified HRTEM image from the blue region in (A). (C, D) The comparisons between simulation and experimental HRTEM results. (E) HRTEM images and simulation results from magnified HRTEM image of the (100) surface (the white square in (A)). (F) An experimental HRTEM image of the CeO₂(110). (G, H) Details of HRTEM images and simulations of the CeO₂ (111) surface with O/Ce terminations[12]

Direct visualization of the surface atoms by a spectroscopic technique is crucial to correct the model from theoretical simulation. Marks and his co-workers[12] systematically investigated the atomic structures using the aberration-corrected HREM over CeO₂ nanocubes (Fig. 3A) synthesized by the hydrothermal method. Fig. 3C-E shows the HREM images of CeO₂(100) which is well-matched with the simulated model. A lot of oxygen vacancies are presented in CeO₂(110)(Fig. 3F), which is consistent with the lower oxygen vacancy energy for CeO₂(110) listed in Table 1. Compared to the simulated images, HREM experimental images in Fig. 3G, H confirm the termination with O on the surface of CeO₂(111). These images demonstrate that a hexagonal arrangement of anions and cations is present on CeO₂(111), and its spacing is consistent with bulk termination. Similar results have been observed by Gritschneider and his co-workers[13].

In a catalytic reaction, the adsorption of reactants on the CeO₂ surface and the surface redox properties vary with the different atomic arrangements and coordination environment. On the surface of CeO₂(111), reactants cannot easily form a bridged bonding with two Ce atoms because of the presence of O and the distance between two Ce atoms. However, it is possible to have a bridge bond between two adjacent Ce cations on the surface of CeO₂(100), resulting from more Ce exposure. Mullins *et al.*[14] have investigated the TPD process of oxidized CeO₂(111) and CeO₂(100) after adsorption of water at 180 K. They have found that hydroxyls are more stable on the oxidized CeO₂(100) than CeO₂(111) due to the different amounts of unsaturated coordinated sites. This is consistent with calculation results from Molinari *et al.*[15] showing that the dissociated state of water is most stable on CeO₂(100).

As mentioned in Table 1, oxygen vacancies formation energy varies with crystal facets. Wu and his co-workers[16] have synthesized ceria nanorod ((110) + (100)), nanocube ((100)), and nano-octahedra ((111)). They have found that intrinsic defects (see section 1.3) in all these different ceria are Frenkel-type oxygen defects, and the number of defects inside decreases from ceria nanorod ((110) + (100)) > nanocube ((100)) > nano-octahedra ((111)). Wang *et al.*[17] reported that positively charged gold is stabilized by an interaction with oxygen vacancy sites, which is dominant in Au/CeO₂ nanorods with a proportion of 71%, followed by Au/CeO₂ nanocube and Au/CeO₂ nano-octahedra.

1.3 Intrinsic defects: oxygen vacancy

Defects in the crystal structure are zones where regular crystal patterns are interrupted and form a disorder in a perfectly ordered system, increasing its entropy and impacting the reactivity of solid materials. Generally, defects in materials can be classified into intrinsic and extrinsic. The intrinsic defects in ceria crystals depend on the temperature and oxygen pressure in the environment. Different CeO_{2-x} composites can be formed in the absence of extrinsic dopants. When CeO_2 is near to nanoscale, a substantial concentration of punctual defects is beneficially formed at high temperatures on surfaces, under low oxygen partial pressures [6][7]. In addition, oxygen vacancies formation energies of intrinsic defects vary with exposed crystal planes, as mentioned before.

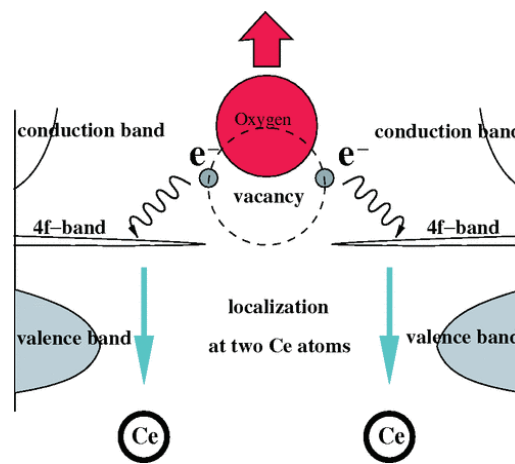


Fig. 4 Illustration of the formation process of oxygen vacancy[18]

As shown in Fig. 4, an oxygen atom moves away from its lattice position, creating a vacancy and leaving two electrons behind that can reduce cerium, related to the quantum effect of localization/delocalization of the 4f electron of cerium[18][19]. Moreover, the bulk oxygen would give a continuous supply to the surface due to the oxygen diffusion, which usually improves the ceria's reducibility. When the ceria-based materials are treated with an O-rich ambience, the oxygen vacancies will be readily healed, making these materials suited for oxygen storage buffering during the catalytic process[20]. Madier and his co-workers[21] observed that the total number of oxygen atoms exchanged at 600 °C is much larger than the calculated number of surface oxygens, suggesting the participation of bulk oxygen in the isotope oxygen exchange process on Ce-Zr mixed oxides (CeZrO_x), and confirming the oxygen mobility between surface and bulk.

Oxygen vacancy, a vital defect in the ceria structure, plays a pivotal role in controlling the storage and release of oxygen and serves as adsorption and activation site. High-resolution scanning tunneling microscopy (STM) offers the opportunity to visualize the oxygen vacancies directly. Esch and his co-workers[22] systematically studied the structure of such vacancy by STM on the surface and subsurface (Fig. 5). In combination with DFT calculations, they reported that the formation of oxygen vacancies makes electrons localized on Ce atoms (the formation of Ce^{3+}). The localized electrons turn this site more reactive, especially for electrophilic substances.

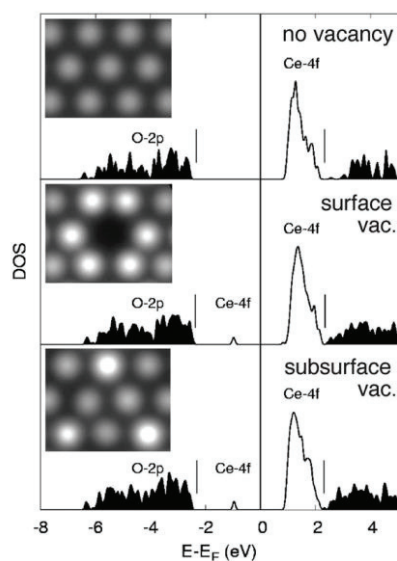


Fig. 5 STM images and calculated density of states (DOS) of $\text{CeO}_2(111)$ [22]

Furthermore, oxygen isotopic-exchange measurements with $^{18}\text{O}_2$ labeling and mass spectroscopic analysis shed light on more detailed investigations on the redox process and kinetic study of oxygen activation and diffusion on the surface and bulk during the reaction process. Holmgren *et al.*[23] reported that isotopic oxygen exchange on Pt/CeO_2 does not proceed via Pt but occurs directly on ceria, which is different from $\text{Pt/Al}_2\text{O}_3$ where the exchange strongly depends on the Pt content. Descorme and his co-worker[24] observed the presence of superoxide sites at room temperature by combining isotopic oxygen exchange with FTIR on $\text{Ce}_x\text{Zr}_{1-x}\text{O}_y$ during oxygen adsorption. Moreover, they proposed that binuclear oxygen species may be involved in oxygen mobility on ceria-based materials. Using laser Raman spectroscopy and isotopic exchange, Ozkan and his co-workers[25] had previously reported that adding Ca to Co/CeO_2 increased O-mobility and resulted in higher H_2 yields in ethanol steam reforming.

Oxygen vacancies may have a crucial role in several catalytic reactions. For instance, the NO-ceria interaction in NH₃-SCR reaction strongly depends on the surface oxidation state of ceria. Yang *et al.*[26] calculated the adsorption energy of NO on reduced and non-reduced CeO₂. They found that the adsorption energy of NO on reduced ceria is almost ten times higher than that on unreduced ceria. Zhang and his co-workers[27] got similar results from DFT+U calculations, and they further proposed that NO preferably adsorbs at the surface oxygen vacancy. Oxygen vacancies in ceria have been reported not only to adsorb reactants like NO but also to activate them. Nolan *et al.*[28] explained the N-N bond formed accompanied by the lengthening of the N-O bond when two NO molecules are adsorbed at neighboring vacancy sites. In addition, oxygen vacancies may also act as binding catalytically active species to ceria [22]. For example, Fu and his co-workers[29] demonstrated that the formation of well-dispersed non-metallic gold on the ceria surface related to the partial lattice filling of vacant Ce sites by Au^{δ+}, is responsible for the water-gas shift catalysts activity.

1.4 Extrinsic defects: doping defects

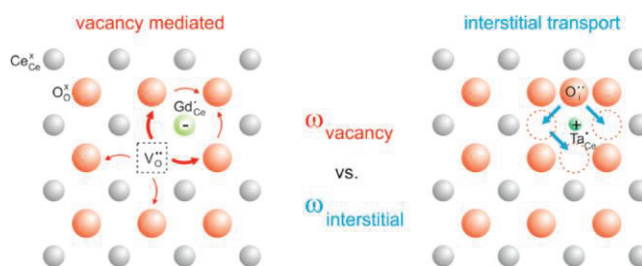


Fig. 6 Illustration of different extrinsic defects[30]

The extrinsic defects, originating from doping with a foreign element, in the ceria crystal structure are likely to occur on atoms that have a similar size as Ce but with a different oxidation state, or other tetravalent cations[31]. Such defects can be created by three different approaches: I) When low-valence metal ions are introduced, the missing positive charge is compensated by creating extrinsic oxygen vacancies. For instance, ceria-based materials doped with low-valence acceptor cations, Ca²⁺, Gd³⁺, and Sm³⁺ show a high ionic conductivity, resulting from more oxygen vacancies as charge carriers[30]. II) When high-valence metal ions are incorporated, the extra positive charge would be compensated by both Ce³⁺ and O interstitials[32]. Heinzmann and his co-workers[30] observed interstitial oxygen besides regular lattice oxygen in Ta-doped ceria by ¹⁷O NMR, which is absent in Gd-Doped (the difference is illustrated in Fig. 6). III) When CeO₂ is doped by other tetravalent cations,

host materials are easily reduced, which generally enhances oxygen storage capacity. Sossina M. Haile and his co-workers[33] found that ceria materials even with a low 5 mol% Zr substitution exhibited an extent of reduction compared with undoped ceria. They attributed this enhancement in the reducibility to the preferred presence in Zr-doped materials of a Zr configuration with a 7-fold (over 8-fold) coordination by oxygen, accompanied by the creation of oxygen vacancies.

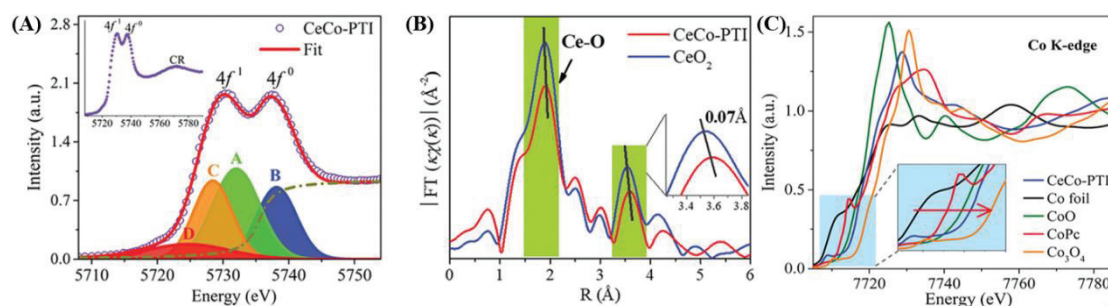


Fig. 7 (A) Normalized XANES spectra at Ce LIII-edge of CeCo-PTI. (B) Fourier-transformed EXAFS spectra of CeCo-PTI and CeO₂. (C) Normalized XANES spectra at Co K-edge of CeCo-PTI (references: Co foil, CoO, CoPe, and Co₃O₄) [34]

Defect-induced local distortions and short-range associates are non-periodic, and thus not easily detected by conventional X-ray powder diffraction. Recently, researchers developed several analytic methods which could provide further insights into defect-induced local distortions without relying on long-range periodic symmetry[31]. Thermo-gravimetric processes and conductivity measurements combined with defect chemical modeling and atomistic simulations provide more information about enthalpies and entropies of defect interactions[33]. By careful peak assignment, Raman spectroscopy may reveal local structural changes, reflecting the presence of defects[26]. X-ray absorption fine structure (XAS) spectroscopy techniques (EXAFS and XANES) shed light on probing the local bonding environment of metals in ceria and its derivatives, offering information on the coordination environments of defects and next-nearest neighbors in the atomic structure[31]. After performing X-ray absorption spectroscopy (XAS) measurements at the Co K-edge and Ce LIII-edge over CeCo-PTI (as shown in Fig. 7), Cheng and his co-workers[34] disclosed the coordination environment around Ce and Co species and found a longer shifted bond distance assigned to Ce-Co bonds formation from Ce LIII-edge EXAFS.

1.5 Redox pairs $\text{Ce}^{3+}/\text{Ce}^{4+}$

Ce^{3+} is obtained by the reduction of Ce^{4+} upon the formation of oxygen vacancy. DFT calculations have revealed that the surface truncation of corners, steps, and kinks are typically recognized as frequent locations where reduced Ce^{3+} are expected to exist[7]. Directly visualizing Ce^{3+} , like analyzing the shape and positions of ionization edges, can shed light on the distribution of valence state $\text{Ce}^{4+}/\text{Ce}^{3+}$. Sara and her co-workers [35] used EELS and electron tomography to investigate the distribution of Ce valences of CeO_2 nanostructures. Fig. 8 provides 3D visualizations of the octahedral and truncated octahedral of CeO_2 , the $\text{Ce}^{3+}/\text{Ce}^{4+}$ (red/green) distributed in these morphologies and its slice across. The homogeneous shell thickness of the $\text{CeO}_2(111)$ octahedral facets (Fig. 8a-c) suggests that Ce^{3+} is evenly distributed across the facets. Moreover, quantitative results on Ce^{3+} were deduced from this approach, showing that the Ce^{3+} concentration on the $\text{CeO}_2(111)$ is likely to be 20%-30%, while 54% of Ce^{3+} are present in the corners. They also reported the HAADF-STEM reconstructions of a truncated octahedral morphology, which exposed more $\text{CeO}_2(100)$ (Fig. 8d). Comparing the slices in Fig. 8c and 8f, surface facet $\text{CeO}_2(100)$ shows a higher degree of surface reduction than $\text{CeO}_2(111)$. In addition, Turner and his co-workers[36] reported that only Ce atoms in the top layer were reduced to Ce^{3+} , and the mixed $\text{Ce}^{4+}/\text{Ce}^{3+}$ layers emerged on the second and third atomic layers on the surface of $\text{CeO}_2(111)$.

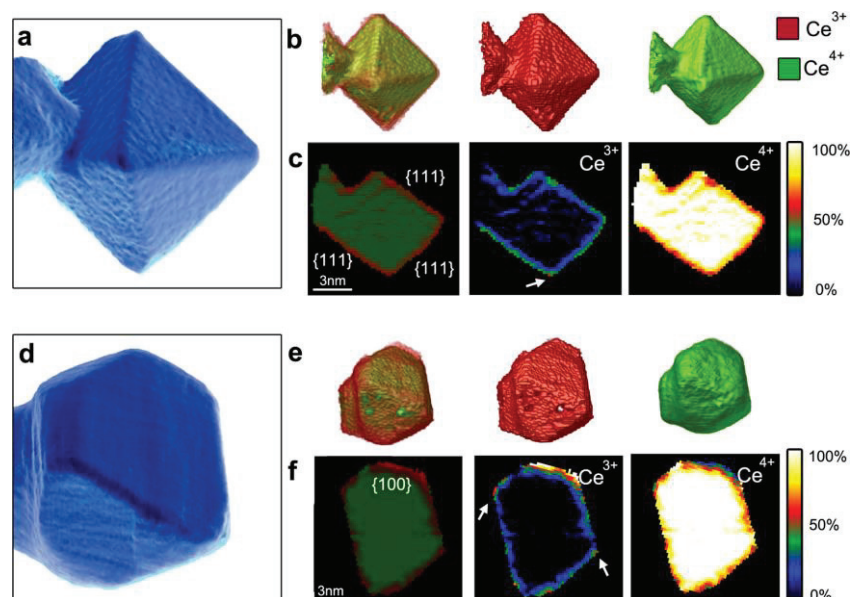


Fig. 8 STEM-EELS analysis of the $\text{Ce}^{4+}/\text{Ce}^{3+}$ distribution inside CeO_2 nanostructures. (a,d) HAADF-STEM reconstructions of a near-perfect and a truncated octahedral ceria particle. (b,e) Corresponding 3D visualizations of the nanoparticles showing the valency results for Ce^{3+} and Ce^{4+} from results of EELS. (c,f) Slices through quantitative distribution of Ce^{3+} and Ce^{4+} [35]

Heterogeneous catalytic reaction occurs on the active site which occasionally is the interface between the support and the immobilized element. Therefore, the $\text{Ce}^{3+}/\text{Ce}^{4+}$ redox pair present on the catalyst's surface could participate in the reaction cycle and shows great significance in the catalytic performance. Qin and his co-workers[37] developed an amorphous Fe_2O_3 -modified CeO_2 catalyst to synthesize imine from benzyl alcohol and aniline. As shown in Fig. 9, Fe_2O_3 plays a vital role as an initiator in the [O] transfer cycle of $\text{Ce}^{4+}/\text{Ce}^{3+}$ by the strong synergetic effect between $\text{Ce}^{4+}/\text{Ce}^{3+}$ and $\text{Fe}^{3+}/\text{Fe}^{2+}$ redox pairs, which is also responsible for the high catalytic activity. Liu and his co-workers[38] reported that reducing Ce^{4+} to Ce^{3+} and Ni^{2+} to Ni^0 appeared at 700 K under 100 mTorr CH_4 , while it is absent in the single constituent. Since ceria supply oxygen species through the partial dissociation of carbon dioxide ($\text{CO}_2 \rightarrow \text{CO} + \text{O}$), which inhibits coke formation, the catalyst has a high degree of stability.

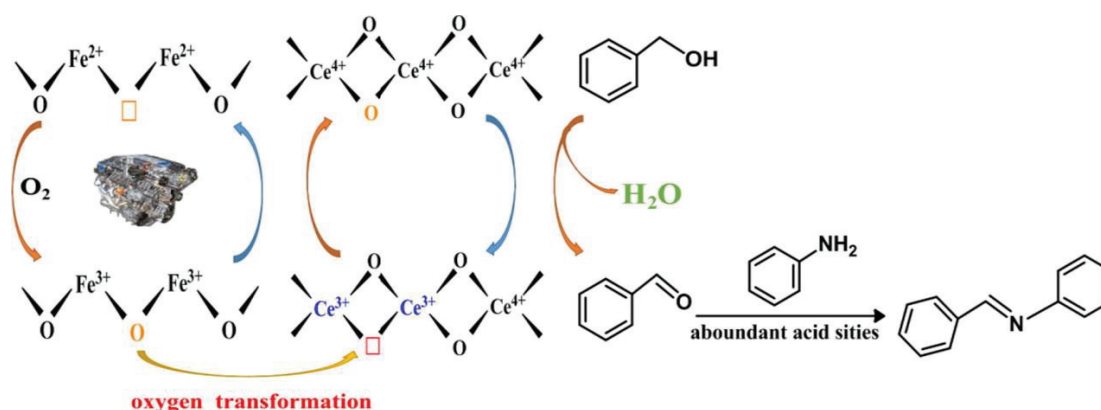


Fig. 9 Proposed reaction mechanism for CeO_2 catalyzed synthesis of imines from alcohols and amines[37]

1.6 Acid-base property

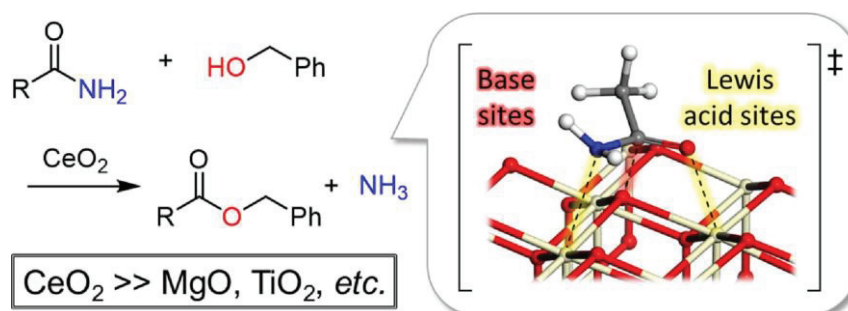


Fig. 10 Proposed reaction process and active sites for alcoholysis of amides on CeO_2 [39].

Metal oxide surface can be considered to constitute acid-base pair sites[14]. For pure ceria, cerium ions and oxygen vacancies are the Lewis acidity sites, while oxygen ions are the

source of basicity. Although the surface of metal oxide may be extensively protonated, it is widely accepted that CeO_2 lacks Brønsted-acid sites and exhibits weak Lewis acidity.[40] Lewis acidic sites show the importance of the adsorption of reactants. For example, Ce^{4+} , a Lewis acid center, is responsible for the adsorption of CO in oxidation reactions[41]. Different strategies have been demonstrated to introduce Brønsted-acid sites and adjust the ratio of Lewis acid sites by for instance controlled synthesis of ceria having a preferred facet on the surface[42], pretreatment with various acids[43][44], doping with transition state metals[45][46], and employment of mixed oxides[47][48]. For example, Nelson and his co-workers[49] adjust the ratio of different types of acidic sites by controlling the deposited phosphate amount.

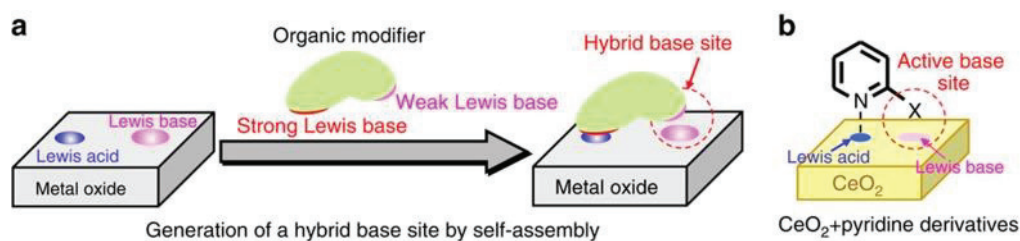


Fig. 11 (a) Strategy for the generation of heterogeneous/homogeneous hybrid catalyst self-assembly. (b) Self-assembled heterogeneous/homogeneous hybrid catalyst based on CeO_2 and pyridine derivatives[50]

Besides the acidity, the solid basic sites from the lattice oxygen may directly participate in the catalytic cycle for specific reactions. Takashi and his co-workers[39] observed that a nucleophilic attack by the lattice oxygen basic sites is the rate-determining step in the alcoholysis of amide. Additionally, the Lewis acid sites in ceria with the appropriate strength could speed up this process, producing higher activity with respect to MgO and TiO_2 (Fig. 10). Based on the unique acid-base property, self-assembled hybrid catalyst can be generated after adding a basic organic modifier[50]. The heterogeneous/homogeneous hybrid catalyst composed of CeO_2 and 2-cyanopyridine (Fig. 11) exhibits increased catalytic activity (reaction rate > 2,000-fold) for the hydromethoxylation of acrylonitrile compared to CeO_2 or 2-cyanopyridine alone. Wang and his co-workers[45] revealed that the interfacial $[\text{Ru}-\text{O}-\text{Ce}-\text{V}\ddot{\text{O}}]$ sites as Lewis acid–base pairs, including basic interfacial oxygen of $\text{Ru}-\text{O}-\text{Ce}$ linkage and the adjacent acid oxygen vacancy site, are the active sites for Ethylene Methoxycarbonylation.

2. Applications of ceria in catalysis

Ceria-based materials have found many applications due to the aforementioned properties. The essential features, such as high thermal stability, appropriate band gap value, oxygen storage capacity, redox and acid/base properties make such solids relevant within catalysis. Ceria-based materials are commonly used in selective oxidation reactions (CO oxidation, methane reforming, volatile organic compound decomposition, etc.). Selective reduction reactions are another significant application of CeO₂, like the reduction of NO_x, CO₂ reduction, and hydrogenation of alkynes. Moreover, the stable structural properties, adequate band gaps, and the presence of unique Ce³⁺/Ce⁴⁺ redox pairs make CeO₂ a promising material in photocatalytic applications. Reported examples are photocatalytic oxidations (such as alcohols, amines, and degradation of organic pollutions), photocatalytic reductions (CO₂, nitroaromatic compounds, and heavy metal ions), and other photocatalytic organic transformations (like photocatalytic Suzuki–Miyaura coupling reactions, and DNA photolyase). Besides, ceria-based materials have gained accelerated popularity in transforming nitriles and amides, thermochemical water splitting, organic synthesis using CO₂ as carbon feedstock, and the transformation of biomass and its derivatives. In this section, we focus on the roles of ceria-based catalysts in some redox reactions.

2.1 Photocatalytic reactions

Photocatalysis, excited by solar energy to generate photoelectrons and holes to achieve surface catalysis, is an environmentally friendly and sustainable technology that has received growing attention with respect to classical thermal catalysis[51]. CeO₂ is the typical indirect transition n-type semiconductor, with a special electronic configuration ([Xe] 4f¹ 5d¹ 6s²). Bulk CeO₂ has a broad band gap of nearly 3.2 eV, exhibiting a strong absorption at 350 nm resulting from a charge transition from O 2p to Ce 4f orbitals, but mainly absorbs UV light[52]. The unique redox pairs of Ce³⁺/Ce⁴⁺ are also beneficial to the charge transfer reactions. CeO₂ meets the criteria to become potential photocatalysts based on these unique electronic and photo-electronic properties. However, the photocatalytic activity of bulk CeO₂ is still limited by its low light utilization and bad separation efficiency of photoelectrons and holes. Therefore, researchers have conducted a variety of strategies to improve their photocatalytic activities, particularly in CO₂ fixation, and selective oxidation and reduction[40].

2.1.1 Photocatalytic oxidation

Ceria-based materials have been applied in the selective photocatalytic oxidation of alcohols, amines, and olefins into value-added chemicals[53][54][55]. Li and his co-workers[56] prepared a catalyst for the selective photocatalytic oxidation of benzyl alcohol to benzaldehyde with (Gold Core)@(Ceria Shell) nanostructures. As shown in Fig. 12, they found that photons excited from Au nanocrystal overcame the Schottky barrier on the interface and transferred to the conduction band of CeO₂ to generate Ce³⁺ species. In addition, adsorption of O₂ on the surface of the CeO₂ shell coordinated to Ce³⁺ species forms Ce-coordinated superoxide species (Ce(IV)-O-O•). This species accelerates the H-abstraction of -CH₂- group of benzyl alcohol and creates cerium hydroperoxide simultaneously, followed by abstracting a proton and forming benzaldehyde and H₂O₂. During this process, LSPR-induced Au core enhanced the light absorption, and Ce³⁺/Ce⁴⁺ redox pairs transferred the electrons from the inner layer of the CeO₂ shell to its outer layer, improving the separation efficiency and enhancing the catalytic activity.

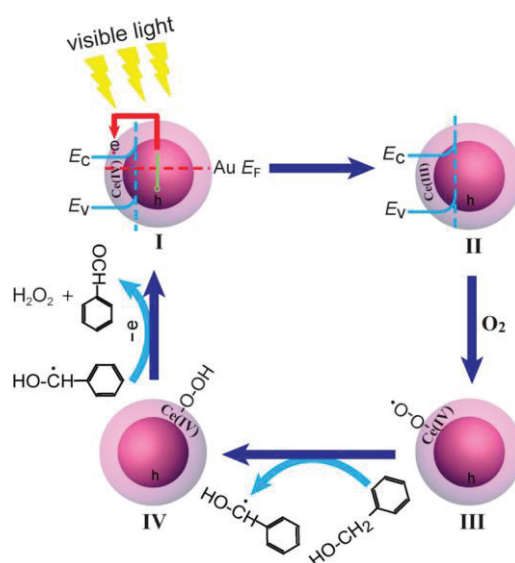


Fig. 12 Proposed mechanism for the selective oxidation of benzyl alcohol to benzaldehyde with O₂ over the (Au core)@(CeO₂ shell) nanostructure catalyst under visible light illumination by Li *et al.*[56]

Unlike the thermo-oxidative self-coupling of benzylamines to imines that requires external heat supply, the photo-oxidative pathway may occur at room temperature and is a more sustainable strategy[58]. Chai and his co-workers[57] reported a catalyst with CeO₂-rod/g-C₃N₄ heterojunction structure, which exhibited 3 times activity than that of pure CeO₂ or g-C₃N₄ in the photo-oxidative coupling of benzylamine under irradiation with a 300 W Xe arc

lamp at 308 K and with an air balloon. They explained the excellent activity of the prolonged photoinduced holes and superoxide radicals produced by the heterojunction structure (Fig. 13). In addition, the increased content of Ce^{3+} ions and oxygen vacancies were considered as the main factors.

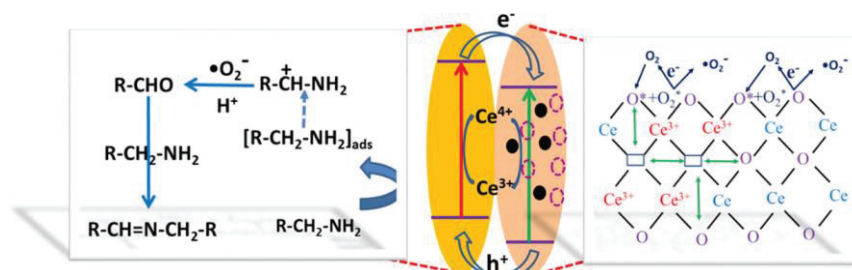


Fig. 13 Reaction mechanism of photo-oxidative coupling of benzylamines by the CeO_2 -rod/ $g-C_3N_4$ [57]

2.1.2 Photocatalytic reduction

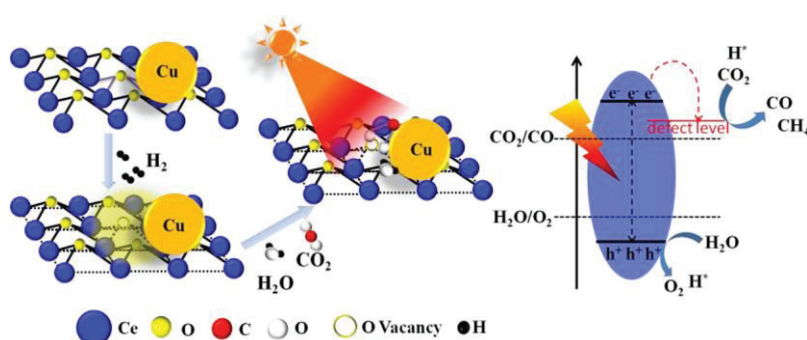


Fig. 14 Schematic illustration of the possible mechanism of CO_2 reduction over Cu/CeO_{2-x} [59]

Photocatalytic reduction of CO_2 with H_2O to CO and other hydrocarbons such as CH_4 , methanol, and $HCOOH$, is regarded as the cleanest and most promising solution to reduce the CO_2 concentration in the atmosphere[40]. Photogenerated electrons are produced by light excitation, and transfer to oxygen vacancies. CO_2 molecules adsorbed on this site can readily be reduced to CO . The holes on the VB of CeO_2 can oxidize H_2O to produce H_2 , which reacts with CO_2 to form CH_4 [40]. It is generally accepted that the introduction of oxygen vacancies modifies the intrinsic electronic properties and band gap of semiconductors by introducing a defect level (as shown in Fig. 14). Furthermore, the defect level could increase the absorption of visible light, improves the separation and transfer of photogenerated charge carriers, and consequently enhances the photocatalytic activity of semiconductors[60]. Wang *et al.*[59] generated and stabilized oxygen vacancies in CeO_{2-x} via the introduction of Cu in ceria,

enhancing CO₂ photocatalytic reduction activity with a CO yield of 8.25 μmol/g⁻¹ (26 times that of pure CeO_{2-x}) after 5 h of irradiation. Wang and his co-workers [61] reported that bidentate carbonate (CO₃²⁻) and bidentate bicarbonate (HCO₃⁻) are the major intermediates in CO₂ photoreduction. These species are likely to produce CO₂, which can be further reduced to CO and CH₄. In addition, the Ce³⁺ could increase the presence of these species by adjusting the CO₂ adsorption state.

2.2 Selective oxidation

2.2.1 CO oxidation

CO emission usually comes from the incomplete combustion of hydrocarbons. It is extremely toxic and can replace the oxygen attached to hemoglobin, restraining oxygen transport in the blood. Besides, CO promotes the harmful ozone O₃, another greenhouse gas in the atmosphere. Therefore, the oxidation of CO (2CO+O₂→2CO₂) is significant for automotive exhaust emission[62]. In the most recent generation of emission treatment catalysts, Pt and Pd-containing metal nanoparticles (NPs) are the most frequent additives to eliminate CO by oxidation. CeO₂ has an excellent oxygen storage capacity resulting from the unique redox pairs Ce³⁺/Ce⁴⁺ among the various metal oxides and is therefore suitable for oxidation reactions. Giulia *et al.*[63] reported that Pd supported on ceria rod (which exhibits CeO₂(111) facets) shows activity in CO oxidation at room temperature. In contrast, Pd supported by ceria cube (which exhibits CeO₂(100) facets) shows considerable activity at temperatures above 60 °C. Therefore, the activity of CO oxidation is related not only to the metal loading but also to the nature of the support.

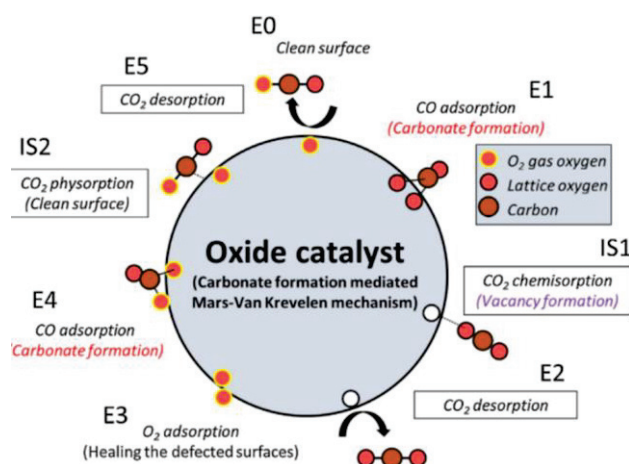


Fig. 15 Schematic illustration of the consecutive CO oxidation cycle on CeO₂(111) via MvK mechanism[19]

Mars-van-Krevelen is a convenient mechanism to explain the consecutive processes of CO oxidation on CeO₂-based materials[64]. As shown in Fig. 15, successive molecular adsorption and desorption reactions are included in all elementary steps. In the first oxidation process (E0-E2), intermediate carbonate (O-CO-O) is formed by CO adsorbed on the bridge site of lattice oxygen. It is transformed to adsorbed CO₂^{δ-}, followed by the desorption of CO₂ and leaving an oxygen vacancy site. In the second oxidation process (E3-E5), the oxygen vacancy site is filled with molecular O₂, and then the second CO molecular adsorbs onto this site to form second bridge-type carbonates. Similar to the first oxidation, carbonates in the second oxidation are transformed to CO₂^{δ-}. The catalyst is regenerated after the desorption of CO₂.

It is common to promote the oxidation ability of CeO₂-based catalysts with transition metals. Determining the maximum synergetic effect between the loaded metal and the support is significant for designing catalysts. Ha *et al.*[65] investigated the effect of the Au-CeO₂ interface on catalytic CO oxidation with two modeled Au/CeO₂(100) and Au/CeO₂(111). They found that the interaction of Au/CeO₂(111) is more able to reduce Ce⁴⁺ to Ce³⁺ and to easier produce oxygen vacancy, which is a crucial factor for the rate-limiting step in the CO oxidation process (formation of CO₂^{δ-} and desorption of CO₂). Liu *et al.*[66] found that the Ce-O bond was lengthened at the interface of Pd and CeO₂, which promotes the mobility and activity of surface O atoms and the transfer of electrons from Pd to the CeO₂ surface to form Ce³⁺. These electrons then move to adsorbed oxygen molecules to form active oxygen species. Furthermore, metal atom adsorption is affected by the redox ability of the supported oxides, and the effect of strong metal-support interaction (SMSI) is another essential factor for CO oxidation over metal-loaded CeO₂, which not only improves the resistance of metal atoms to sintering but also contributes to CO oxidation activity[67].

However, a system supported by noble metal would be deactivated due to a few impurities and high-temperature thermal treatment[68]. From an economic perspective, a catalyst based on non-noble metal or single-atom noble metal would like to be a more interesting alternative. For instance, Nie *et al.*[69] obtained an atomically dispersed Pt²⁺ on CeO₂ by steam treatment at 750 °C, which maintained the stability up to 800°C in oxidizing environments. Furthermore, they reported that active surface lattice oxygen near atomically dispersed Pt was earned by hydrothermal processes, significantly improving low-temperature CO oxidation. This material is the most active and stable CO oxidation catalyst when compared to other promising catalysts, such as CoCuCeOx and 0.5 % Pd/La-Al₂O₃. Yang *et al.*[68] developed a novel

inverse Cu(111)/CeO₂ catalyst, which shows a TOF 4-9 times higher than Pt(100), Pt(111), and Rh(111). Guo *et al.*[70] synthesized CuO/CeO₂-polyhedra with a higher content of active Cu⁺ species and more oxygen vacancies, which exhibited a broader operating temperature window (CO conversion > 99.0% in the 90-125 °C range) than promising commercial catalysts (Fig. 16).

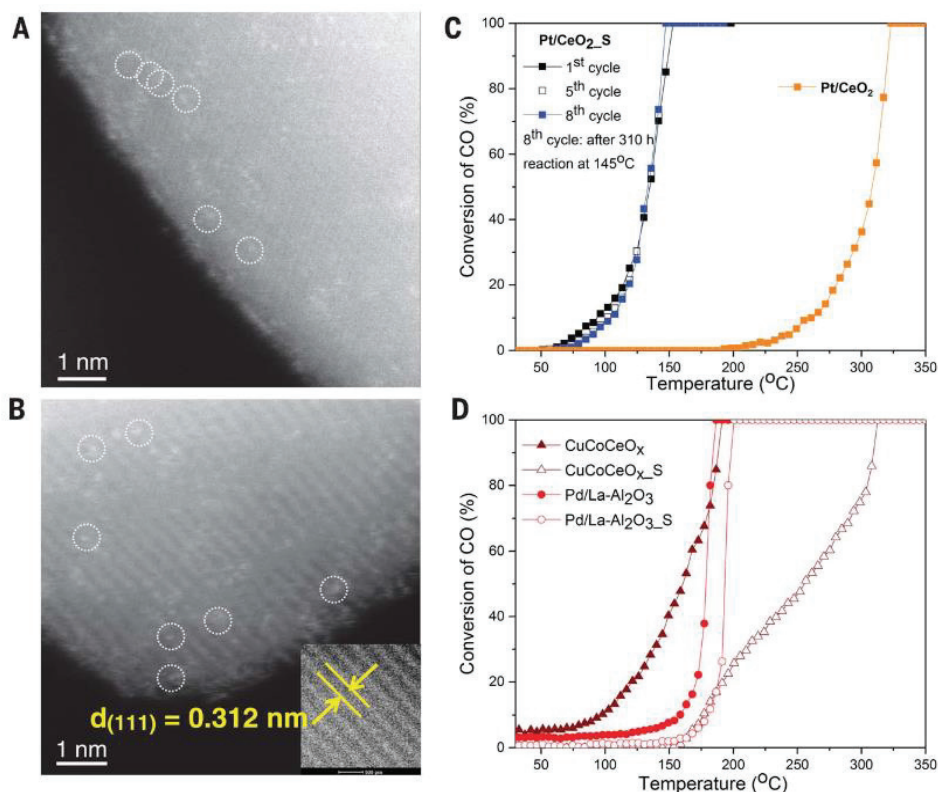


Fig. 16 STEM images of (A) Pt/CeO₂ and (B) Pt/CeO₂_S after 750 °C hydrothermal treatment. (C) CO conversion over Pt/CeO₂_S for several cycles and (D) comparison experiments with other different promising commercial catalysts [70]

2.2.2 N-H oxidation

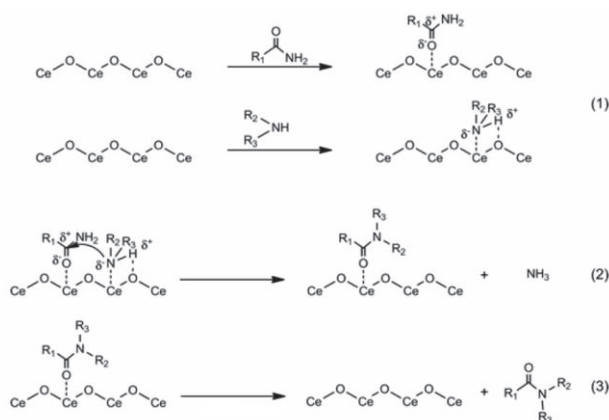


Fig. 17 Illustration of the reaction mechanism of transamidation reaction over ceria proposed by Tamura *et al.* [71]

Nitrogen-containing compounds hold a crucial role in pharmaceutical and agricultural products. A common strategy to access those compounds starting from an amine is synthesizing imine and other nitrogen-containing compounds by oxidative self-coupling. The weak Lewis-acid site and adjacent base sites of bulk CeO₂ could activate an amide and amine, which are promising candidates for transamidation and other reactions involving N-H oxidation, as shown in Fig. 17.[71] Metal-loaded ceria based material was also extensively studied for the N-H oxidation, such as Au/CeO₂-ZrO₂ for the oxidation of cyclic amines.[72]

Because of the challenge to identify N-containing intermediates and complex surface-active sites over the employment of mixed oxides, the mechanism of transamidation reaction is still under debate. Linda Al-Hmoud *et al.*[73] investigated the reaction pathway of oxidative self-coupling amines to imines over Cu/CeO₂. They reported the formation of imine intermediates PhCH=NH by dehydrogenation as the primary reaction, as shown in Fig. 18. Then, N-benzylidenebenzylamine is formed via direct coupling between imine intermediates and another benzylamine (pathway A), which is promoted by copper species. Another pathway, B, produces benzaldehyde enhanced by CeO₂ at a lower rate, while benzaldehyde spontaneously reacts with the second molecule (benzylamine). Putla *et al.*[74] reported that the interface between dispersed MnOx nanoparticles and the support, CeO₂ nanocubes, shows unusual lattice expansion and abundant oxygen vacancy defects, a critical factor of outstanding catalytic efficiency for the oxidation of benzylamine.

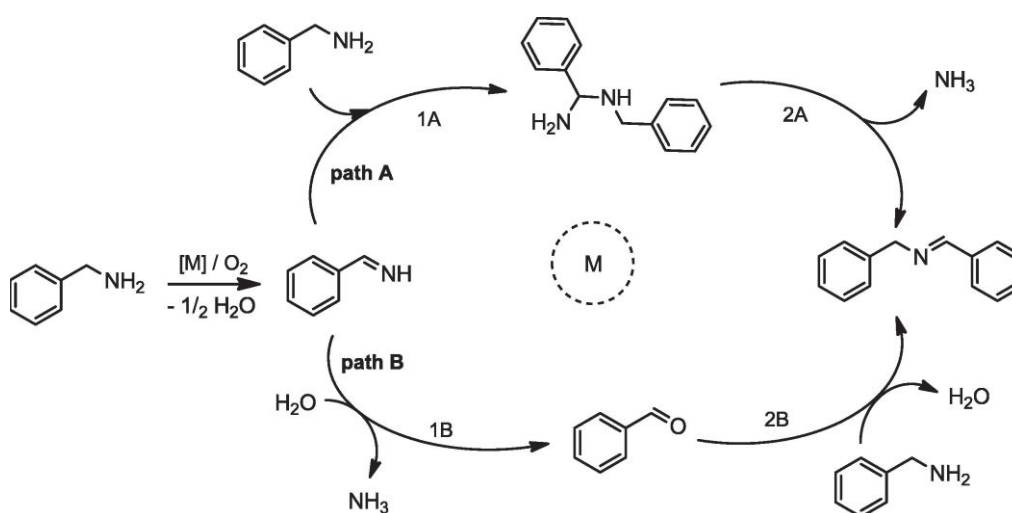


Fig. 18 Proposed reaction pathways for aerobic oxidation of benzylamine to benzylamine by Linda *et al.*[73]

2.3 Selective reduction

2.3.1 CO₂ reduction

For catalytic conversion of CO₂ into valuable chemicals, CO₂ reduction is the most important reaction that has to be mentioned because of the negative oxidation state of carbon in most organic compounds. Reverse water gas shift reaction (RWGS), methanol synthesis, and CO₂ methanation are common reactions to obtain valuable CO, CH₃OH, and CH₄. [75] Yang *et al.* [76] compared the support effect between Cu/CeO₂ and Cu/SiO₂ in RWGS. The Cu/CeO₂ was found to be four times more active than Cu/SiO₂ despite its similar Cu loading, particle size, and degree of Cu dispersion. The improved performance is attributed to the enhanced H-spillover at the abundant interfaces between CeOx and Cu nanoparticles, which facilitates the reduction of Cu and CeOx to Cu⁰ and Ce³⁺. The produced Cu⁰ and Ce³⁺ could rapidly dissociate the CO₂ to CO forming Cu⁺-CO intermediates.

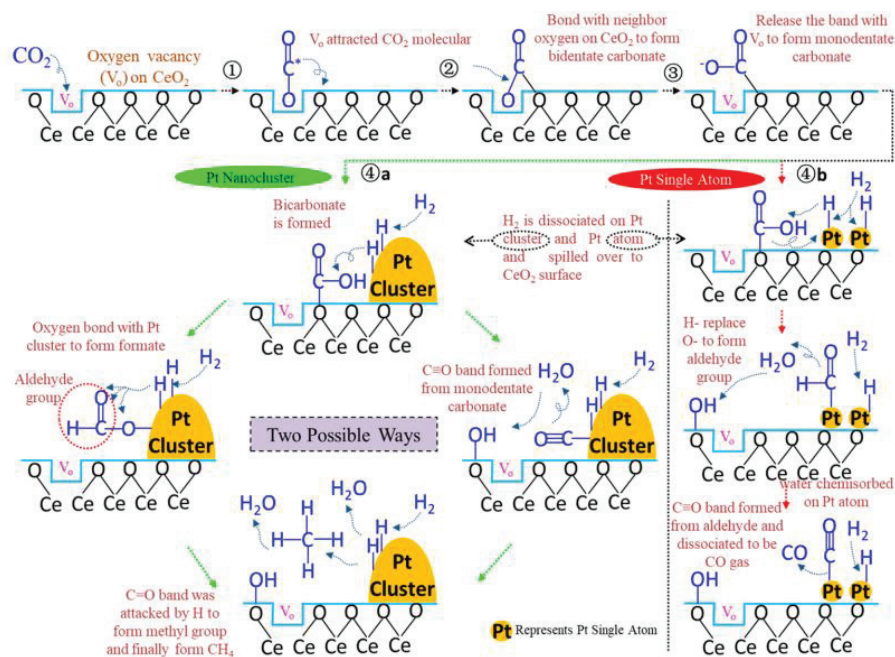


Fig. 19 Proposed reaction mechanism for CO₂ reduction on Pt/CeO₂. Illustration of reaction mechanism with 2 wt% Pt/CeO₂ (pathway 4a) and 0.05 wt% Pt/CeO₂ (pathway 4b) [77]

The formation of dispersed active species is beneficial in photocatalytic activity. Atomically dispersed single-atom catalysts can maximize the catalytic efficiency of various reactions while reducing the cost and quantity of catalysts. Wang and his co-workers [77] found that the single-atom catalyst Pt/CeO₂ (0.05wt% Pt/CeO₂) showed good thermal stability at 500 °C and a 7.2 times greater reaction rate than a nanocluster catalyst (2wt% Pt/CeO₂). After their

investigation, they attributed this excellent activity to different geometric Pt arrangements, which had an impact on the selectivity of CO and CH₄. Moreover, an isolated Pt atom weakly binds with CO, limiting further hydrogenation and blocking CO poisoning (Fig. 19).

2.3.2 NH₃-SCR

The dominating application of ceria within selective reduction involves deNO_x reactions. Nitrogen oxides, primarily comprising NO and NO₂, emitted from power stations, industries, and automobiles are regarded as the major source of atmospheric contaminations. Nowadays, governments worldwide have introduced strict legislation and policies for the emission of NO_x[78][79]. The efficient ways, such as exhaust gas recirculation, optimized fuel injection or using alternative tailormade fuels for superior combustion, are limited in widespread use[80]. Currently, selective catalytic reduction using NH₃ as a reduction agent has been commercially applied to both stationary and mobile applications[81][80].

Nowadays, the current commercial industrial catalyst for NH₃-SCR reaction is WO₃/V₂O₅/TiO₂, in which WO₃ is used as a promoter, V₂O₅ is the primary active component, and TiO₂ is used as the support. This catalytic system contains several issues: 1) V₂O₅ is toxic and volatile at high temperature; 2) a narrow operating temperature which limits the efficiency of DeNO_x; 3) selectivity and stability are poor at high temperatures[82]. The stoichiometric reactions of this process can be described as follows:



Ion-exchanged zeolite catalysts, especially Fe or Cu-exchanged zeolite, are other widely studied materials for NH₃-SCR reaction. Differently than for metal oxide catalysts, researchers attributed the reactivity of ion-exchanged zeolite catalysts to highly active isolated ion sites[83][84]. As shown in Fig. 20, it was proposed that NH₃ adsorbed on Cu²⁺ sites continually reacts with NO to form NH₂NO intermediates. Then Cu²⁺ was reduced to Cu⁺ while the intermediates decomposed. The Brønsted acid sites adsorbed NH₃ form NH₄⁺, playing a vital role in storing and supplying NH₃. NH₃ continuously reacts with NO₂⁻ to produce N₂ and H₂O, accompanied by the oxidation of Cu⁺ to Cu²⁺. Therefore, ion-exchanged zeolite catalysts show promising potential reactivity at low-temperatures due to the highly active NH₄⁺ formed by surface acidity and specially active isolated ion sites [82][85]. Park

and his co-workers[86] found that the isolated Cu^{2+} sites were transformed and redistributed. The structure of the ZSM-5 collapsed after hydrothermal aging ($T > 600\text{ }^\circ\text{C}$, 10 v% H_2O), leading to a significant decrease in NH_3 -SCR activity of Cu/ZSM-5 catalyst. Although ion-exchanged zeolites exhibit great catalytic activity, the stability of zeolites during high-temperature hydrothermal processes, SO_2 tolerance, and the effect of coking obstacles their practical applications due to the high temperatures produced from the engine combustion process and since the formation of water vapour is inevitable[87].

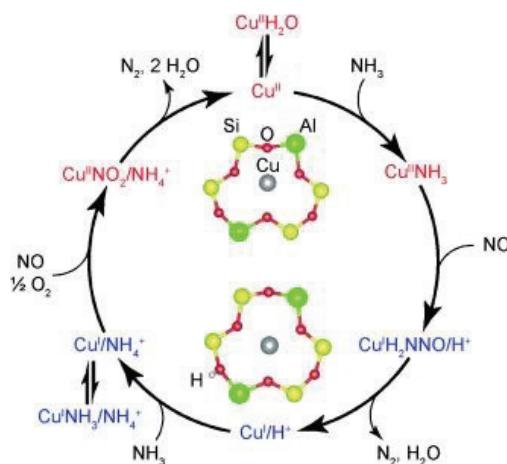


Fig. 20 Proposed SCR cycle over Cu-SSZ-13 at 473 K. Oxidized Cu (top) and reduced Cu (bottom) moieties in the redox cycle described by Paolucci *et al.*[83]

Like TiO_2 , with appropriate textural properties and favorable interaction with other components, ceria has been regarded as a promoter or support for NH_3 -SCR catalysts[88]. Gradually, researchers found that ceria can also work as an active component like V_2O_5 , which makes ceria one of the most promising candidates for the next generation of NH_3 -SCR catalysts [89]. NH_3 -SCR over a solid catalyst in the presence of excess oxygen is a complex interfacial chemical process. Essential elements, like various active sites, intermediates, and catalyst surface reconfiguration have to be investigated in order to understand how the ceria-based materials work in the NH_3 -SCR process[85][88]. Peng *et al.*[90] prepared WO_3/CeO_2 by coprecipitation of ammonium paratungstate and cerium nitrate, and used the in-situ DRIFT and in-situ Raman techniques in order to characterize the structure of surface species during the NH_3 -SCR reaction. Upon exposure of NH_3 at $200\text{ }^\circ\text{C}$, several new bands appeared at 1672, 1579, 1430, 1250 and 1174 cm^{-1} . Peaks at 1579 and 1174 cm^{-1} have previously been assigned to ammonia adsorbed on Lewis acidic site (originated from oxygen vacancies and unsaturated W^{n+}). Absorption at 1672 and 1430 cm^{-1} correspond to ammonia adsorbed on Brønsted acid

(localized on W-O-W or W=O from $Ce_2(WO_4)_3$). Moreover, from operando DRIFT studies, the intensity of pre-adsorbed NH_3 on Lewis acidic sites decreased faster than that of the Brønsted acid sites after introducing $NO + O_2$, suggesting that NO reacts preferably with ammonia sitting on a Lewis acidic site. Consequently, the authors proposed the E-R mechanism over CeO_2-WO_3 catalyst with two independent cycles, named redox cycle and acid cycle. In this proposal, Brønsted acid serves for adsorption of NH_3 in acid cycle, and the redox pairs Ce^{3+}/Ce^{4+} promote the activation of NH_3 and the following reaction with NO in the redox cycle, as shown in Fig. 21. However, the structure of different intermediates and the formation of N-N bond are not clearly explained.

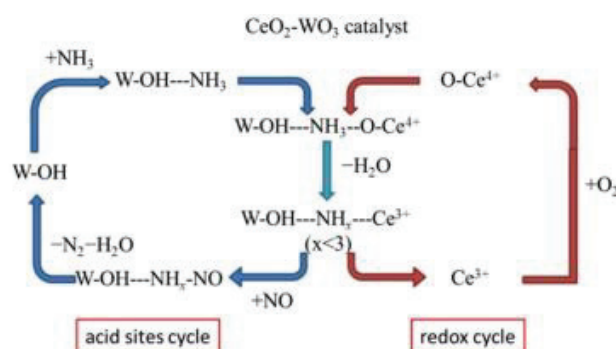


Fig. 21 Schematic proposed acid and redox cycles over the CeO_2-WO_3 catalyst[90]

The complete cycle in the NH_3 -SCR process needs multiple investigations taking into account the different active sites involved in the putative mechanism. Liu *et al.*[91] systematically studied the complete catalytic cycle of NH_3 -SCR mechanism over W-doped CeO_2 (Fig. 22), which consisted of four steps with different active centers: (i) Lewis acid site action, (ii) Brønsted acid site action, (iii) oxygen vacancy reaction, and (iv) catalyst regeneration. Similarly to other literature [92], they proposed that the catalytic activity attributed to the synergetic effects between acidity (both Lewis acid and Brønsted acid sites work for NH_3 adsorption) and redox ability (used for the activation of NH_3 , the H abstraction, and the reduction of NO). Moreover, they reported that oxygen vacancies produced by doping with W favorably tune the distribution of electrons in adsorbates and reacting molecules[93]. In the case of NH_3 -SCR reaction, localized Ce 4f electrons (around oxygen vacancy) may activate NO to produce NO^- that is then transferred to form $N_2O_2^{2-}$, which strengthens the N-N bond and promotes the formation of N_2 . As noted, there may be multiple mechanisms, various active sites, and different active intermediates in complex NH_3 -SCR reactions. Although the real mechanism is still under debate, the synergetic effects between acid sites and redox sites are essential in NH_3 -SCR reactions.

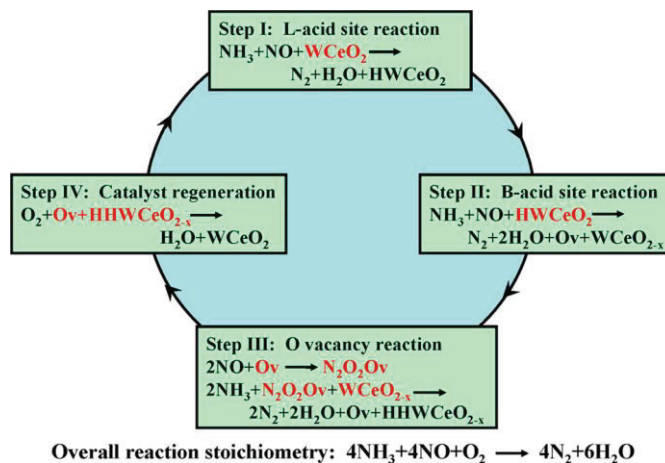


Fig. 22 Proposed catalytic cycle of NH_3 -SCR reaction over W-doped CeO_2 catalysts[91]

Bulk CeO_2 exhibits poor NH_3 -SCR activity. Hence, plentiful studies were conducted to improve the catalytic activity of ceria-based materials. Researchers generally introduce supplementary elements to alter the redox ability, surface acidity and morphology of the ceria support. The morphology of the catalysts, such as the exposed crystal plane and an enlarged surface area can influence the catalytic properties (as discussed in section 1.2). Hollow nanospheres of $\text{MnO}_x/\text{CeO}_2$ exhibited higher NO_x conversion than solid nanospheres. This difference is attributed to a higher surface area, better oxygen mobility, and abundant surface-active oxygen species[94].

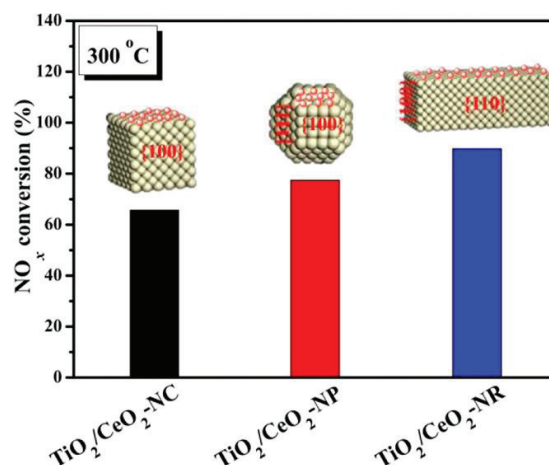


Fig. 23 NO conversion at 300 °C with different morphologies and exposed crystal-Plane of $\text{TiO}_2/\text{CeO}_2$ catalysts[95]

Cheng *et al.*[96] reported a Fe-Ce-Zr oxide with the three-dimensionally ordered microporous structure, which oxidized the soot below 400 °C and simultaneously removed NO in the 285–420 °C range due to the microporous structure and more oxygen vacancies from Fe substitution. As mentioned before, common morphologies of CeO_2 (NR nanorod, NC

nanocube, NP nanopolyhedra) exhibit various crystal planes with different oxygen vacancy formation energy. Yao *et al.*[95] found that TiO₂/CeO₂-NR exhibited a better NH₃-SCR activity than TiO₂/CeO₂-NC and TiO₂/CeO₂-NP (as shown in Fig. 23), since (110) exposed facets in nanorods possess lower formation energy of oxygen vacancies and exhibit the best reducibility and the strongest interaction between well-dispersed TiO₂ and CeO₂ nanorods.

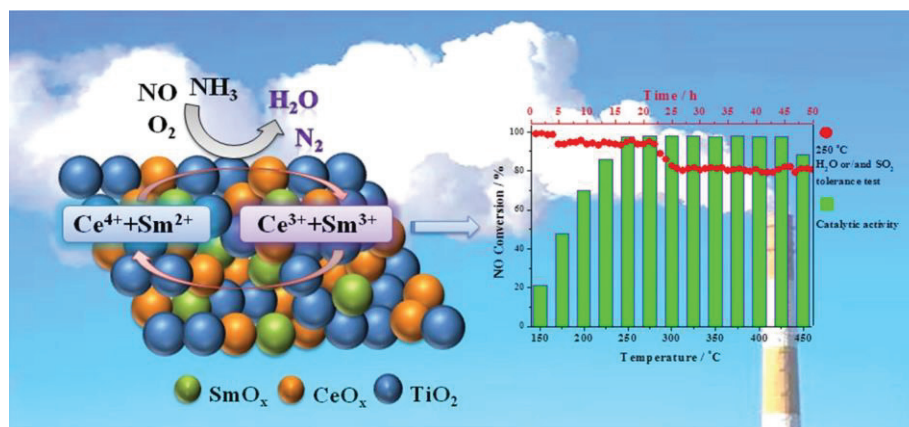


Fig. 24 Proposed mechanism and catalytic performances for NH₃-SCR reaction over Sm doped CeO_x/TiO₂[97]

The appropriate redox ability is essential for NH₃-SCR reaction. Promoting the oxidation of NO to NO₂, inducing the “Fast SCR” can result in higher overall SCR catalytic activity. For further improvement of the oxygen storage capacity of CeO₂, researchers developed several strategies to increase oxygen vacancies like doping or using another redox pair to facilitate the transfer between Ce³⁺ and Ce⁴⁺. Wei *et al.*[98] prepared Al³⁺ and Ta⁵⁺ doped CeO₂ for synergistic NH₃-SCR and the removal of chlorinated organics. Al-doped CeO₂ is believed to tailor the electronic structure of O 2p states and enhance the activities in the low-temperature region, whereas the authors claim that Ta provides more electrons to the coordinated oxygen atoms than Ce⁴⁺, resulting in the formation of more Lewis base sites and a decrease in the catalytic activity in the low-temperature region. Besides binary CeO₂-based materials, multivariate systems also exhibit excellent activity[99][100]. As shown in Fig. 24, The presence of redox cycles Sm²⁺ + Ce⁴⁺ ↔ Sm³⁺ + Ce³⁺ over Sm-doped CeO₂-TiO₂ suppress the electron transfer from SO₂ to Ce⁴⁺ and thereby enhance the resistance to SO₂. [97] Liu and his co-workers[101] reported that Cu-Ce-Ti ternary oxide possesses over 95% NO_x conversion obtained at 200 to 400 °C, and even at 150 °C it shows 73% NO_x conversion. They attributed this excellent activity to the presence of dual redox cycles (Cu²⁺ + Ce³⁺ ↔ Cu⁺ + Ce⁴⁺, Cu²⁺ + Ti³⁺ ↔ Cu⁺ + Ti⁴⁺) which decrease the energy required during the electron transfer between Cu, Ce and Ti active sites and promote the activation of NH₃ and NO.

Although the oxidation properties remain important for NH₃-SCR, over-oxidation of NH₃ needs to be avoided because it can decrease the likelihood of NH₃ interaction with NO. In addition, mechanisms for the formation of N₂O byproduct during NH₃-SCR reaction are still unclear, but it probably relates to redox properties such as NH₃ nonselective oxidation. In the E-R mechanism, ammonia is primarily adsorbed on Lewis acid sites on cerium atoms and the active surface oxygen speeds up the process by triggering successive H-abstractions on NH₃, resulting in the formation of NH₂ and NH species. Ma and his coworkers[102] proposed that N₂O is created after NH reacts with NO and O₂. In the L-H mechanism, N₂O is produced as a result of the reaction between NH₃ and surface nitrate.[103] Therefore, side reactions caused by excessive oxidation of NH₃ should be avoided, while keeping in mind that redox ability is essential to obtain high activity in the NH₃-SCR of NO.

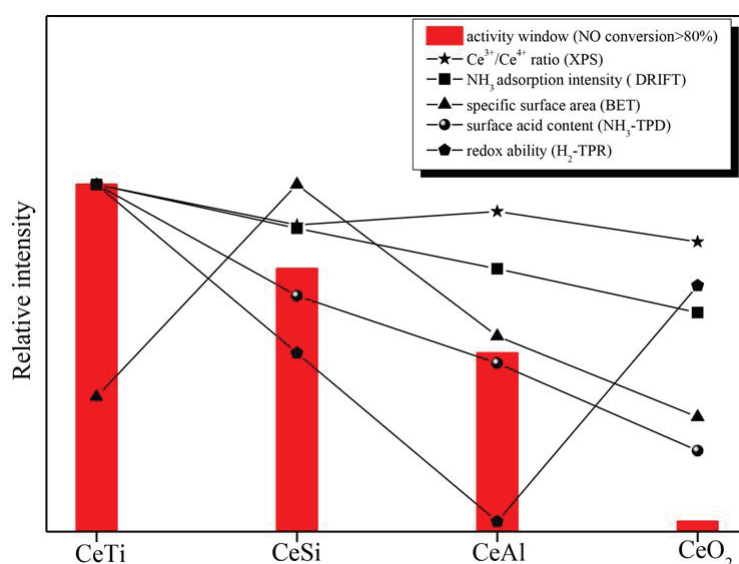


Fig. 25 Relationship between NH₃-SCR catalytic activity and physicochemical properties of CeM samples[107]

Apart from the redox properties, surface acidity is a second important parameter in NH₃-SCR reaction. Poor acidity used to lead to low NH₃-SCR activity, presumably due to low adsorption of NH₃ on the surface. Therefore, it is essential to develop strategies to enhance the surface acidity. Surface acidification and the introduction of foreign acidic sites are the common strategies that have been reported so far. Chang[104] *et al.* reported that CeO₂ prepared with sulfate forms Ce(SO₄)₂/CeOSO₄ which promotes the adsorption of NH₃ and reduces the partial oxidation to N₂O on Ce⁴⁺. H₃PO₄[42], HF [105], and HNO₃[106] modified CeO₂ are also reported. Zhang *et al.*[107] prepared a series of dual composites CeO₂-MOx (M=Ti, Si, and Al) and they found a catalytic activity that follows the order: CeTi > CeSi > CeAl > pure CeO₂, which is in agreement with the order of surface acidity (Fig. 25). Li *et*

al.[108] studied NO conversion activities of various metal oxides supported on CeO₂-ZrO₂ catalysts. The order of maximum activity of the different catalysts is the following: W (91%) > Mo (85%) > Mn (45%) > Cr (38%) > Fe (27%) > Co (8%). They attributed this phenomenon to the synergetic effects between acidity and redox ability. Although there is an agreement on the benefits of acidic sites for NH₃-SCR, attributed to a better adsorption capacity for NH₃, there is no clear evidence to point out whether the related acidic sites are of Lewis or Brønsted character. Several reports insist on the vital role of Lewis acidity in their catalytic system based on ceria[109][110]. Conversely, other works claim that the NH₃-SCR catalytic activity stems from the Brønsted acidity[111][112]. Noteworthy, Lewis acidic sites show higher thermal stability than Brønsted acid sites as shown by NH₃-TPD from in situ DRIFT [90][113].

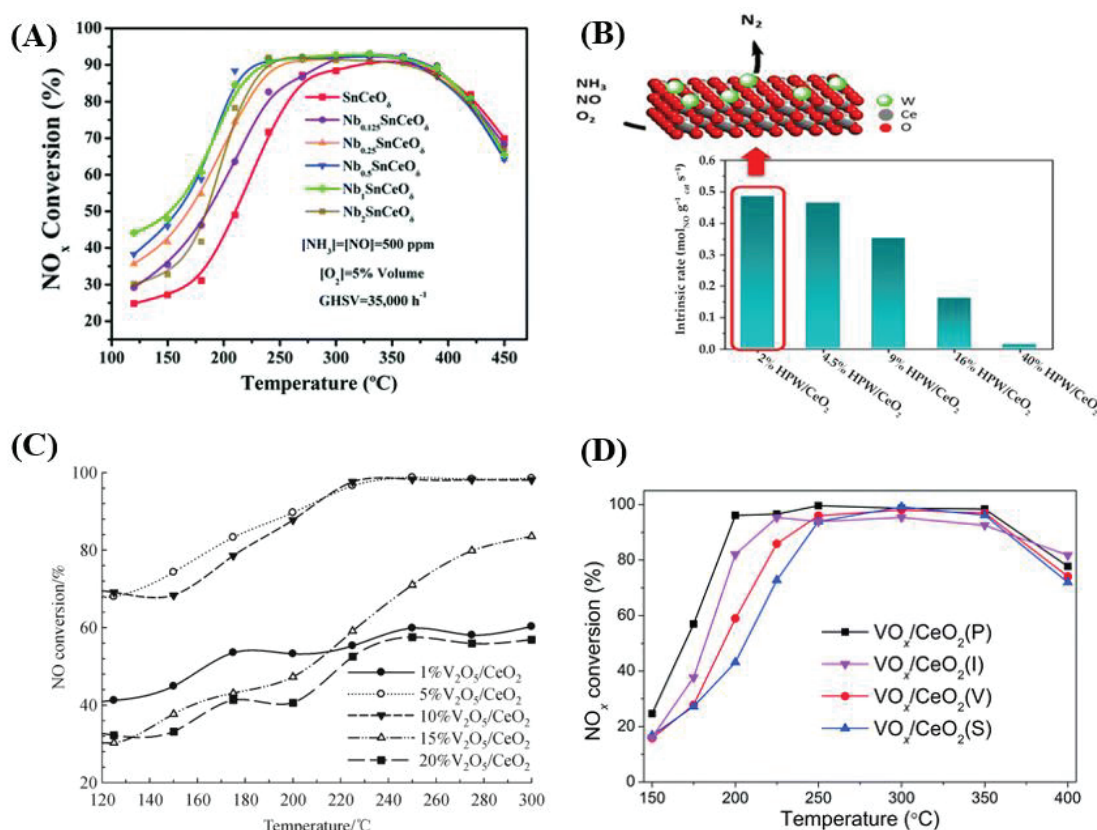


Fig. 26 (A) NO conversion for the Nb–Sn–Ce oxide catalysts with different Nb doping ratios[114]; (B) evaluation of NH₃-SCR activity over HPW/CeO₂[115]; (C) NO conversion obtained with V₂O₅/CeO₂ catalysts prepared with various V₂O₅ loadings and calcined at 400°C[116]; (D) NH₃-SCR activity over VO_x/CeO₂ catalysts prepared by different methods: P: precipitation, I: impregnation, V: rotary evaporation, S: sol-gel[117]

As mentioned above, the catalytic activity of ceria functionalized systems strongly depends on the synergetic effects between each component. At the same time, since acidity and redox properties are somewhat interconnected regarding the catalytic performance, a balance

between acid-base and redox ability must be considered to optimize the catalytic activity[88]. Therefore, an appropriate concentration of each component is significant. Yan and his coworkers[114] reported that Nb assists the production of oxygen vacancies that are used to trap active O₂ species and subsequently accelerate the catalytic cycle. They found that the low-temperature SCR activity (< 250 °C) is gradually enhanced as Nb concentration is increased (Nb/Ce = 0.125 to 0.5, as shown in Fig 26A), while supplementary niobium leads to a sharp decrease in SCR activity at high temperatures because of the formation of Nb₂O₅, which only barely converts NO_x in the operating temperature range (150-450 °C). The same phenomenon appears in the case of WO_x/CeO₂ system. El arrouji and her coworkers[115] reported that a low loading in tungsten (2 wt%) HPW/CeO₂ features the highest activity with a remarkable N₂ selectivity (99 %) at medium-high temperatures (300-515 °C) compared to that obtained with higher loadings (4.5 wt %- 40 wt%), as shown in Fig 26B. The explanation is attributed to the presence of substantial amounts of monomeric tungsten sites on the catalyst surface being most likely responsible for the reaction under these conditions. Concerning the well-established vanadium system, it is reported that the V_{0.75}Ce oxide catalyst displayed greater NH₃-SCR activity than the traditional V₂O₅-WO₃/TiO₂ catalyst[113].

Since V₂O₅ is volatile and toxic once emitted to the atmosphere, researchers devote to re-design the catalyst without the existence of crystalline V₂O₅ by using a low loading of vanadium[116]. To maintain the activity of VO_x/CeO₂, a good dispersion of vanadium on the support is necessary. Lian *et al.* [117] developed V₂O₅/CeO₂ catalysts with 3 wt% V loading from different synthetic methods: Rotary evaporation impregnation, homogeneous precipitation, incipient wetness impregnation, and sol-gel. They found that VO_x/CeO₂ prepared using homogeneous precipitation method demonstrated higher NH₃-SCR activity and higher SO₂ and H₂O resistance in comparison to other catalysts, resulting from a lower CeO₂ surface crystallinity on the surface and better dispersion of vanadium species (Fig. 26D). In summary, neat ceria contains the necessary components (acidity, redox properties) to carry out the NH₃-SCR reaction. However, the catalytic activity is limited by active site distribution, surface acidity, and redox ability. Therefore, diverse functionalization such as tailored facet exposure, surface modification and doping have been investigated with the aim to enhance the activity. However, it turns out that the necessary criteria are interconnected and need to be properly balanced for optimal performances. Moreover, there are still many controversies in

the study of the mechanism of NH₃-SCR: i) the role and necessity of Lewis or Brønsted acid sites; ii) the products NH_x from NH₃ activation; iii) the determination of the elementary steps between NH₃ (gaseous/activation moieties) and NO (gaseous/activation moieties) according to the L-H or E-R mechanism; iv) how do different active sites work synergistically in multivariate systems. These remaining issues are related to the complex nature of the NH₃-SCR reaction and the structure of published conventional catalysts which usually contain high metal loadings and different surface species. It is generally accepted that the active sites are coming from M=O, M-O-M' and M-OH moieties. Furthermore, a low loading but with highly-dispersed active sites leads to a more economical and active catalyst.

Table 2 Recent investigations for Low loading metal oxides supported on ceria.

Catalysts	Loading	Synthesis method	Reaction conditions	NO conversion	Literature
TiO ₂ -CeO ₂	Ti:Ce = 1:9	Hydrothermal	NO 500 ppm; NH ₃ 500 ppm; O ₂ 5% GHSV: 60000 ml/(g*h)	70% at 300 °C	[118]
Fe-Mn/ CeO ₂	5 wt% Mn 5 wt% Fe	Impregnation	NO 500 ppm; NH ₃ 500 ppm; O ₂ 11% GHSV: 36000 h ⁻¹	97 % at 200 °C	[119]
Mn/CeO ₂	5 wt% Mn	Impregnation	NO 500 ppm; NH ₃ 500 ppm; O ₂ 11% GHSV: 60000 h ⁻¹	T ₈₀ (175-250 °C)	[120]
Fe/CeO ₂ (Nitrite precursor)	6.5 wt% Fe	One-pot	NO 600 ppm; NH ₃ 600 ppm; O ₂ 5% GHSV: 60000 h ⁻¹	T ₈₀ (275-300 °C)	[121]
Fe/CeO ₂ (Sulfate precursor)	6.5 wt% Fe	One-pot	NO 500 ppm; NH ₃ 500 ppm; O ₂ 5% GHSV: 60000 h ⁻¹	T ₈₀ (250-450 °C)	[121]
Zr/CeO ₂	Zr:Ce = 1:9	Hydrothermal	NO 500 ppm; NH ₃ 500 ppm; O ₂ 5% GHSV: 60000 h ⁻¹	39 % at 200 °C	[122]
Al/CeO ₂	Al:Ce = 1:9	Hydrothermal	NO 500 ppm; NH ₃ 500 ppm; O ₂ 5% GHSV: 60000 h ⁻¹	30 % at 200 °C	[122]
Si/CeO ₂	Si:Ce = 1:9	Hydrothermal	NO 500 ppm; NH ₃ 500 ppm; O ₂ 5% GHSV: 60000 h ⁻¹	40 % at 200 °C	[122]
Co/CeO ₂	Co 10 wt%	Incipient wetness impregnation	NO 500 ppm; NH ₃ 500 ppm; O ₂ 10% 200 ml/min	70 % at 300 °C	[123]
V ₂ O ₅ - MnO ₂ /CeO ₂	5 wt% V ₂ O ₅ 5 wt% MnO ₂	Impregnation	NO 500 ppm; NH ₃ 500 ppm; O ₂ 5% GHSV: 160000 h ⁻¹	T ₈₀ (300-350 °C)	[124]
Nb/CeO ₂	20 wt% Nb	Impregnation	NO 500 ppm; NH ₃ 500 ppm; O ₂ 5% GHSV: 30000 h ⁻¹	T ₈₀ (175-450 °C)	[125]
WO _x /CeO ₂	2%-40%	Impregnation	NO 300 ppm; NH ₃ 360 ppm; O ₂ 12% GHSV: 60000 h ⁻¹	T ₈₀ (250-550 °C)	[115]
Mo _{0.1} CeSiO ₂	Mo:Ce = 0.1	Coprecipitation	NO 500 ppm; NH ₃ 500 ppm; O ₂ 5% GHSV: 90000 h ⁻¹	T ₈₀ (200-400 °C)	[126]

As shown in Table 2, W, Nb and V supported on ceria have been identified as promising candidates among several metal oxides supported on ceria, which is probably due to the following properties: i) presence of Lewis acid elements; ii) a Brønsted acidity brought to the support; iii) various oxidation states of the added metal; iv) presence of an oxophilic element resulting in a strong interaction with ceria. However, the classical reported synthesis

technologies that always result in a mixture of different surface species are unsuitable for further elucidation of the mechanism and the nature of the active sites. A primary issue to address is to synthesize catalysts containing uniquely one type of active site throughout the materials. An evident starting point is to focus on single atom with isolated species on the surface and determine the behavior of such species for NH_3 -SCR reaction.

3 Surface organometallic chemistry for the preparation of supported catalysts

Development of high-efficiency catalysts is a pursued objective within catalytic science. Supported metal oxides catalysts are widely used in industrial catalysis because of their robustness and easy preparation. Typically, in metal oxide or supported catalysts, only a fraction of the loaded metal is active, particularly for high metal loading materials[127][128]. As a result, more and more researchers attach their attention to single-atom catalysts, in which each metal atom acts as an active site. When metals are dispersed at atomic-scale sizes, several properties change, like an increased surface free energy, quantum size effects, unsaturated coordination environments, and stronger metal (metal oxides)-support interactions[129][130]. Generally, these changes result in different catalytic properties that used to be beneficial. Such systems, comprising a single atom supported on a surface, possess similar environments as in classical homogeneous catalysis, and are considered as a bridge connecting heterogeneous and homogeneous catalysis. In addition, since the surface species are isolated and uniform, single-atom catalysts are suitable for atomic scale understanding of heterogeneous catalytic reactions, with the help of characterization methods such as solid state NMR, EPR, XAS and HAADF-STEM[127].

3.1 Introduction of surface organometallic chemistry

Surface organometallic chemistry (SOMC), is an established "catalyst by design" approach to obtain heterogeneous catalysts. Generally, it generates well-defined surface organometallic fragments (SOMF) or surface coordination fragments (SCF) by grafting organometallic complexes on a surface oxide bearing one or more, ionic or covalent bonds to the support[130][131]. Fig. 27 illustrates the general synthesis and characterization methods used for surface organometallic complexes supported on metal oxides.

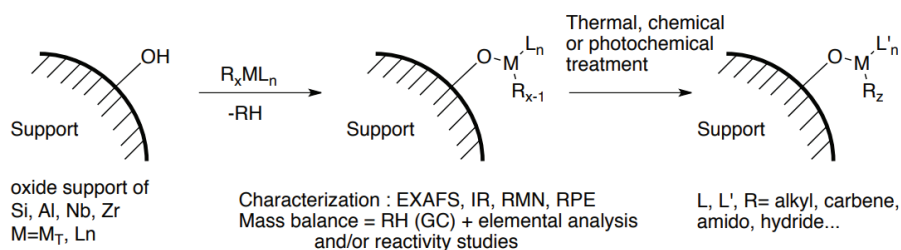


Fig. 27 Synthesis and characterization of organometallic complexes supported on metal oxides

Typically, SAC (single atom catalysis) usually focuses on precious metals[132], whereas SOMC is usually applied to early transition metals. Both approaches possess presumably isolated metal atoms on the surface, which gives the highest atom efficiency and helps researchers to clarify the elemental steps of the catalytic reaction. The isolated metal atoms on the surface of SOMC-prepared catalysts are pre-existed with spectator or reactive ligands such as halogen, N-heterocyclic carbene, amido, imido, alkyl, alkylidene, hydride, oxo, nitride, which may alter and tailor the catalytic activity [133]. Moreover, SOMC approach can also be used for the synthesis of single atom catalysts by removing all organic ligands with thermal treatments and non-oxidative procedures[134]. SOMC-prepared catalysts could be regarded as well-functionalized catalysts by introducing active moieties on the surface as single atom catalysts, which is a potential powerful approach in heterogeneous catalysis.

When the metal phase is constituted by isolated sites distributed on the support, the environment of the metal center and the surface of the support (all ligands around the metal, as well as the associated atoms) can be fully characterized by combining modern techniques: in-situ IR, UV, EPR, solid state NMR spectroscopy [135][136], DNP-SENS (dynamic nuclear polarization-surface enhanced NMR spectroscopy) and several X-ray absorption-based technique such as EXAFS (extended X-ray absorption fine structure) and XANES (X-ray absorption near edge structure) [137][138]. A sufficiently clear description of the materials at the atomic level is the basis for studying structure-activity relationships.

During the reaction process, the entire SOMF/SCF can act as the active site. Different catalytic reactions can be achieved through the combination of metals and specific ligands (predictive catalysts), as well as more in-depth study of the structure-activity relationship bearing the "presumed cycle" based on knowledge in molecular chemistry (organic, organometallic, coordination chemistry, biochemistry and so on). Similar to a classical approach in homogeneous catalysis, SOMC allows to design a heterogeneous catalyst for a given reaction

based on the proposed mechanism by varying the transition metal and the ligands. The resulting surface species is suitable for mechanistic investigations and can easily verify, reject or correct the initially proposed mechanism. Fig. 28 shows the flowchart describing the catalysis-by-design approach of SOMC to improve or discover catalytic reactions[131].

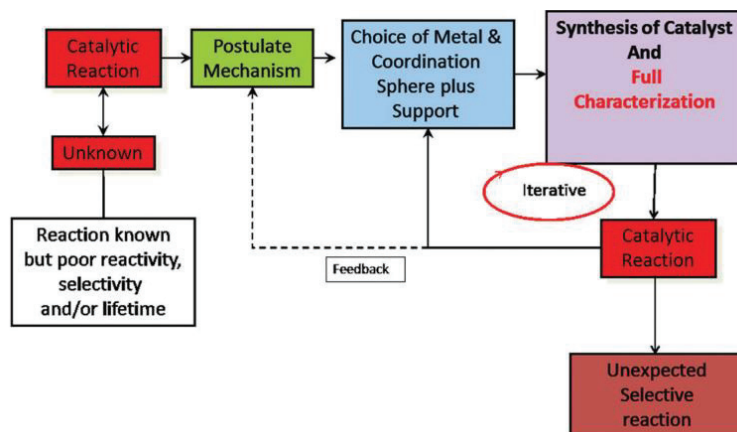


Fig. 28 Flowchart showing how the catalysis-by-design approach of SOMC can be applied to improve or discover catalytic reactions[131]

Surface organometallic chemistry has paved the way for novel catalytic reactions by combining the benefits of classical homogeneous and heterogeneous catalysis and has demonstrated the reliability for single-atom catalyst preparation. In the next sections, selected examples involving the preparation and application of supported catalysts synthesized by surface organometallic chemistry of Group V (V, Nb), VI (W) transition metals are presented.

3.2 Support materials for Surface Organometallic Chemistry

Our research team has been studying the grafting of multiple organometallic complexes on various supports[139] (amorphous inorganic oxides[140], zeolites[141], metal surfaces[142], MOF[143]). The most applied support materials in SOMC are silica and alumina.

3.2.1 Silica as support

Amorphous silica is the most exploited inorganic support in surface organometallic chemistry of transition metals, owing to its simple structure (non-paramagnetic, contains only one type of anchoring point, stable). Upon heat treatment under vacuum, silica material undergoes a dehydroxylation process involving condensation of adjacent silanol groups, giving isolated and bridged (in interaction through hydrogen bond) silanols. The concentration of different

silanol types can be altered depending on the temperature. Millot *et al.* [144] reported that sum of all silanols and bridged silanols decreased, while the isolated silanols increased as the dehydroxylated temperature increased. After extensive efforts in characterization (titration, IR, NMR, and theoretical methods), a widely accepted model accompanied by a certain amount of silanol groups is available for silica dehydroxylated at different temperatures.

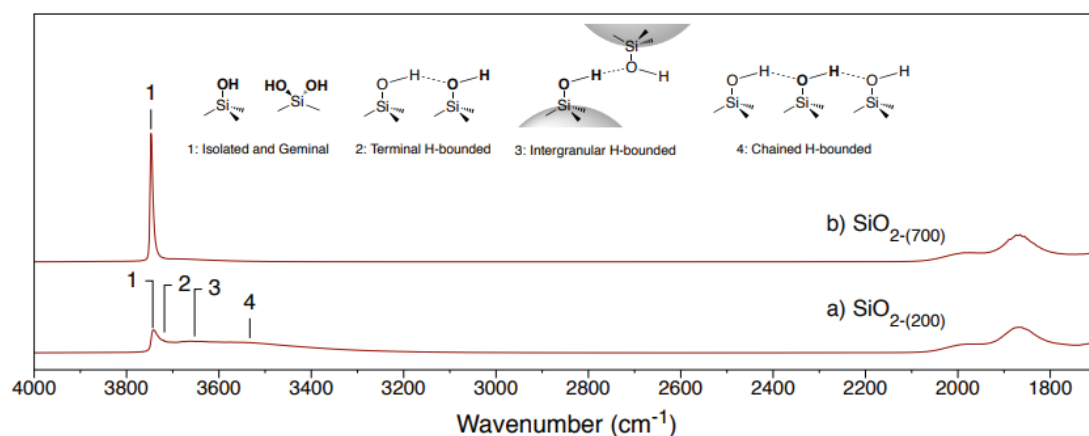


Fig. 29 DRIFT spectra of dehydroxylated silica at (a) 200 °C and (b) 700 °C (inset: corresponding surface structures illustrations)

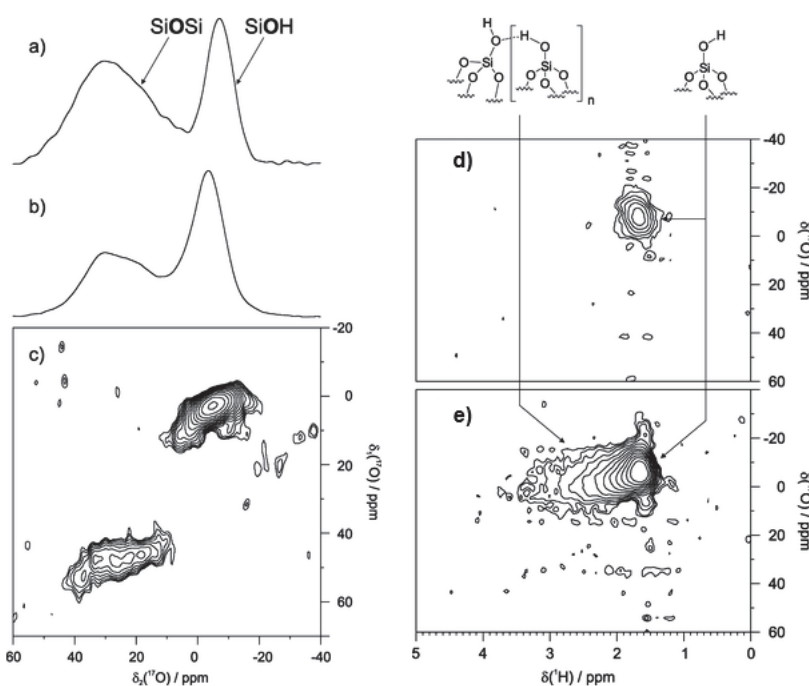


Fig. 30 ^{17}O MAS NMR spectra of (a) SiO_2^* -700; (b) SiO_2^* -200. (c) MQ MAS NMR spectrum of SiO_2^* -200. ^1H - ^{17}O J-HMQC MAS NMR spectra of (d) SiO_2^* -700; (e) SiO_2^* -200 (*: ^{17}O labelled)[145]

Two dehydroxylation temperatures (200 °C and 700 °C) have been frequently employed in SOMC. As shown in Fig. 29, both bridged and isolated silanols are present on the surface of a silica dehydroxylated at 200 °C (SiO₂₋₂₀₀), while only isolated silanols are observed in the case of SiO₂₋₇₀₀. These results are confirmed by ¹H-¹⁷O J-HMQC MAS NMR on a labeled silica (Fig. 30d and Fig. 30e) [145]. Looking at the simple ¹⁷O SSNMR of both silicas in Fig. 30a and Fig. 30b, the relative intensity of Si-O-Si is far higher for SiO₂₋₇₀₀, indicating that additional condensation has occurred.

3.2.2 Alumina as support

Alumina holds a vital role in adsorption and catalytic industries. However, the surface composition is far more complicated than silica, exhibiting multiple hydroxyls and acid sites. Mainly γ -Al₂O₃ is used as a support in SOMC due to the fairly high specific surface area and adequate density and distribution of hydroxyls on the surface that can be tuned by thermal activation.[146] DRIFT and NMR have been widely used to characterize Al₂O₃ hydroxyl groups, which have provided important insights into the alumina structure.[146-149] The essential features are summarized below.

Recently, Merle et al.[149] reported a systematic study Al₂O₃ as function of the dehydroxylation temperature (Fig. 31) by combining high field solid state NMR, DRIFT and DFT modelling. Multiple signals are present in the DRIFT spectrum (Fig. 31a) of Al₂O₃ with different thermal pretreatment, indicating the complexity of hydroxyls on the surface of Al₂O₃. Signals of hydroxyls in DRIFT spectra have been attributed to the terminal (μ^1), doubly (μ^2), and triply (μ^3) bridging hydroxyls. Besides, the surface OH density measured by chemical titration with Al_iBu₃ decrease from 3.0 to 1.1 OHnm⁻¹ with increasing annealing temperature (300-700 °C). The ¹H-¹H DQSQ MAS NMR spectrum and ¹H-²⁷Al D-HMQC MAS NMR spectrum in Fig. 31b and 31c provide more detailed information between different protons and the coordination geometry of the proximate Al centers. In addition, substitution of terminal hydroxyls through partial surface chlorination or reaction with CO₂ were conducted to confirm the detailed assignments. According to the relevant spectroscopies, the deduced hydroxyl structures are presented in Fig.31d. Site A, C and F are assigned to the terminal hydroxyls in different environments. The cross-correlation signals in A-B, C-D-E hydroxyls and auto-correlated signals F and G were also reflected by the intensity correction from ¹H-¹H DQSQ MAS NMR spectrum. Contrary to the traditional assignments of μ^3 -OH,[147] the

lowest-field minor signals (3-5 ppm) were assigned to H-bonding configuration due to the higher hydroxyl density, which is also mentioned in another research.[148]

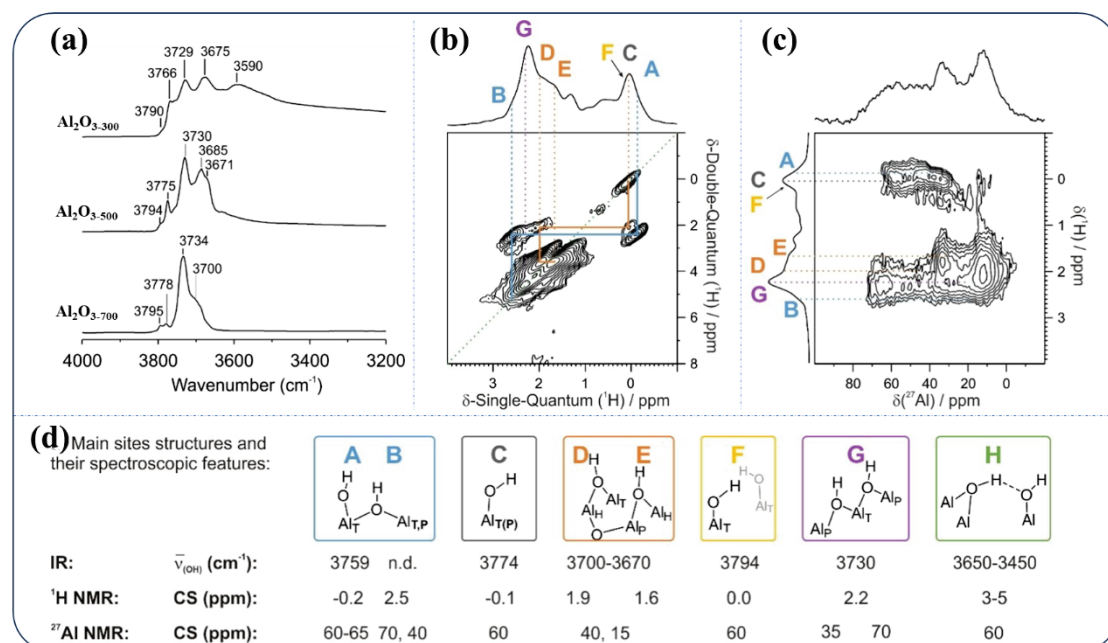


Fig. 31 (a) Infrared spectrum of Al₂O₃₋₃₀₀, Al₂O₃₋₅₀₀, Al₂O₃₋₇₀₀; (b) ¹H-¹H DQSQ MAS NMR spectrum and (c) ¹H-²⁷Al D-HMQC MAS NMR spectrum for Al₂O₃₋₇₀₀; (d) structures and spectroscopies features of deduced hydroxyls on the surface of for Al₂O₃₋₅₀₀ (Al_T: tetra-coordinated aluminum; Al_P: pentacoordinated aluminum; Al_H: hexacoordinated aluminum)[149]

Different theoretical models of alumina have been proposed[149, 150]. One of the earliest models with reactivity studies is represented by trihydrate γ -Al₂O₃ (Fig. 32a), with varying surface hydroxyls[150]. The adsorption strength of pyridine correlates with the force constant of the hydroxyl group, the one with the largest Lewis acidity (i.e., the one which leads to the most substantial pyridine adsorption) corresponding to the OH bonded to the tetrahedral Al (HO- μ^1 -Al_{IV}). In addition, different bridged OH possess different adsorption energy. By DFT calculations, Merle et al. proposed the different hydroxyl configurations on the surface of Al₂O₃₋₇₀₀ adsorbed with one water molecular. As shown in Fig 32b, they found the theoretical studies were in line with the specific sites proposed by spectroscopic features. Besides, several researches focused on the effect of the hydroxyl accessibility on reactivity and the relationship between OH group and Lewis acid sites in molecular-level.[151]

In summary, dehydroxylated γ -Al₂O₃ displays various aluminum hydroxyl, including terminal OH and bridged OH, with multiple structural possibilities (tetrahedral, pentahedral, and octahedral). This kind of complex surface offers different opportunities for the grafting of

organometallic species. It may also alter the properties of the grafted species originated by electronic effects or the presence of acid/base in proximity.[152]

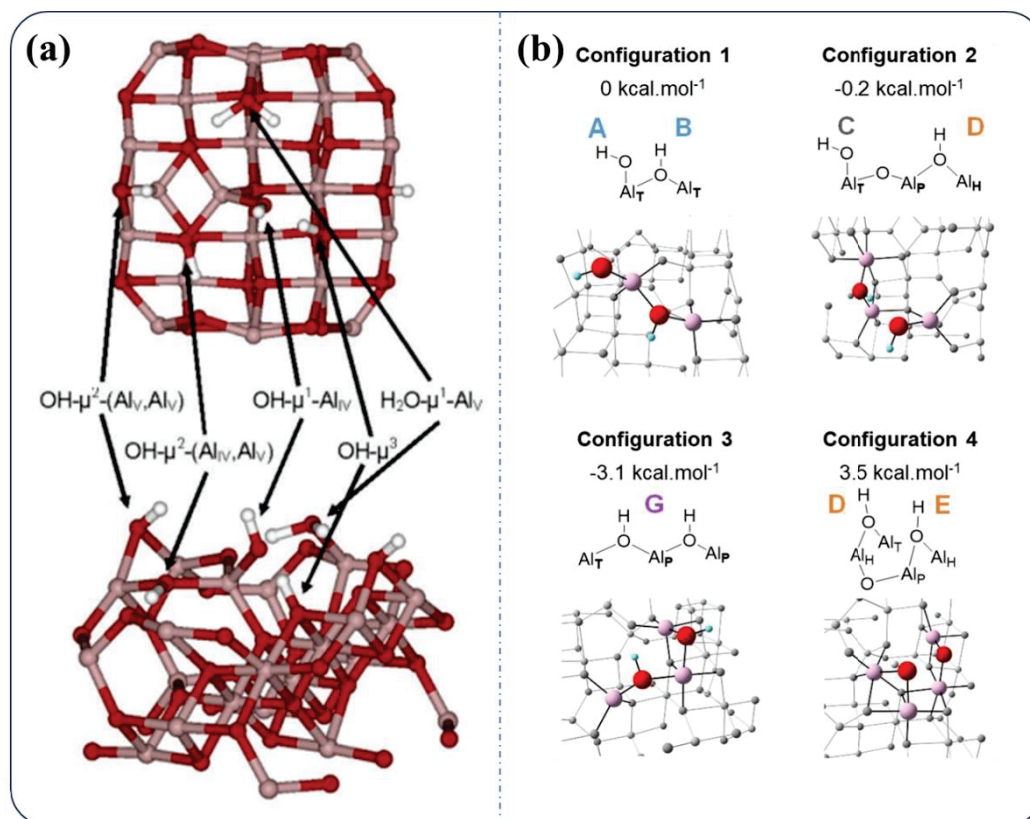


Fig. 32. (a) Trihydrated γ - Al_2O_3 model surface. (The coordination numbers are represented by the roman numbers in the index of Al).[150] (b) calculated OH configurations and their relative energies for surface of Al_2O_3 hydrated by one water molecular with OH density of 0.7 OHnm^{-1} [149].

3.3 Selected examples of SOMC on group V and VI transition metals

3.3.1 Surface Organometallic Chemistry of Group V

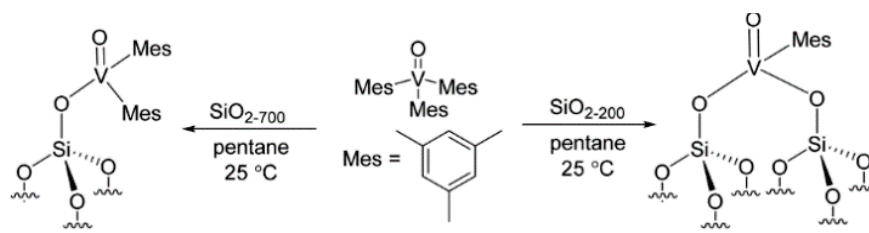


Fig. 33 Preparation of vanadium oxo catalysts by reaction between SiO_2-700 and SiO_2-200 with $[\text{V}(=\text{O})(\text{Mes})_3]$ [153]

Group V transition metals are known to be active in various catalytic reactions[154]. Highly functional but less expensive transition metals from Group V (vanadium) have found extensive applications as oxidation catalysts in the chemical, petroleum and environmental industries. For dehydrogenation reactions, classical vanadium-based catalysts contain a

mixture of different surface species, hindering the determination of the assignment of the role of each surface species. Szeto *et al.*[153] reported recently the first preparation of vanadium oxo catalysts for propane dehydrogenation (PDH) using SOMC through the grafting of $[V(=O)(Mes)_3]$ (Mes, mesityl = 2,4,6- trimethylphenyl) onto SiO_{2-700} and SiO_{2-200} (Fig. 33). EXAFS spectroscopy revealed that vanadium supported on SiO_{2-700} provides isolated, monopodal $V=O$ surface species, while vanadium supported on SiO_{2-200} affords bipodal surface species. Compared to reported classical catalysts V_2O_5/SiO_2 , they found that the catalysts prepared by SOMC exhibit enhanced activity and selectivity to propylene, indicating the promotion of more isolated vanadium sites. Moreover, the bis-grafted species shows slightly higher activity and selectivity than the monografted one, which is accounted to the thermal stability of the bipodal structure avoiding sintering and formation of oligomeric species. Importantly, according to the literature[155,156], researchers proposed that the possible mechanism for PDH goes through the C-H activation on the V-mesityl precursor, β -H elimination, and desorption of propene and hydrogen. Furthermore, during propane activation, they proposed that the V^{III} -H formed by H_2 reduction is responsible for dehydrogenation, providing a new aspect for the mechanism of the reaction. The reduction ability of vanadium is a key for various catalytic applications and is important for NH_3 -SCR according to the proposed mechanism in literature.

As mentioned before, it is well-accepted that active species V^{III} trisiloxy was obtained after activating propane on tripodal $V^V=O$ in the case of vanadium-supported on silica[158]. However, the nature of vanadium on the surface of silica prepared by a classical method leads to a mixture of monomeric, dimeric, oligomeric species and even nanoparticles, which can hardly clarify the role of $(\equiv Si-O)_3V^V=O$. Recent and relevant work by Abou Nakad *et al.*[157] involves preparing the isolated tripodal $(\equiv Si-O)_3V^V=O$ species by grafting of $[V(=O)(OtBu)_3]$ on the partially dehydroxylated silica, followed by a thermal treatment resulting in a β -H transfer and isobutene release. The structure of the obtained catalyst was confirmed by DRIFT, solid state ^{51}V NMR, and XANES spectroscopies. These results indicate that the targeted catalysts with the desired coordination environment could be designed by purposive choosing the precursor and pretreatment of the support. The tripodal active species (Fig. 34) exhibit higher activity in PDH and lower deactivation, resulting from reduced V^{III} and less formation of V-OH. Moreover, the tripodal species show a high stability during PDH reaction, most likely due to the stable tripodal attachment avoiding sintering and gradual loss of the active

single site. Such vanadium species adapted on ceria may have a high potential as NH₃-SCR catalysts. It is indeed important that vanadium is situated next to a Ce³⁺ site, creating the necessary acid/redox pair in order to access highly active catalysts. This requires innovative synthesis methods.

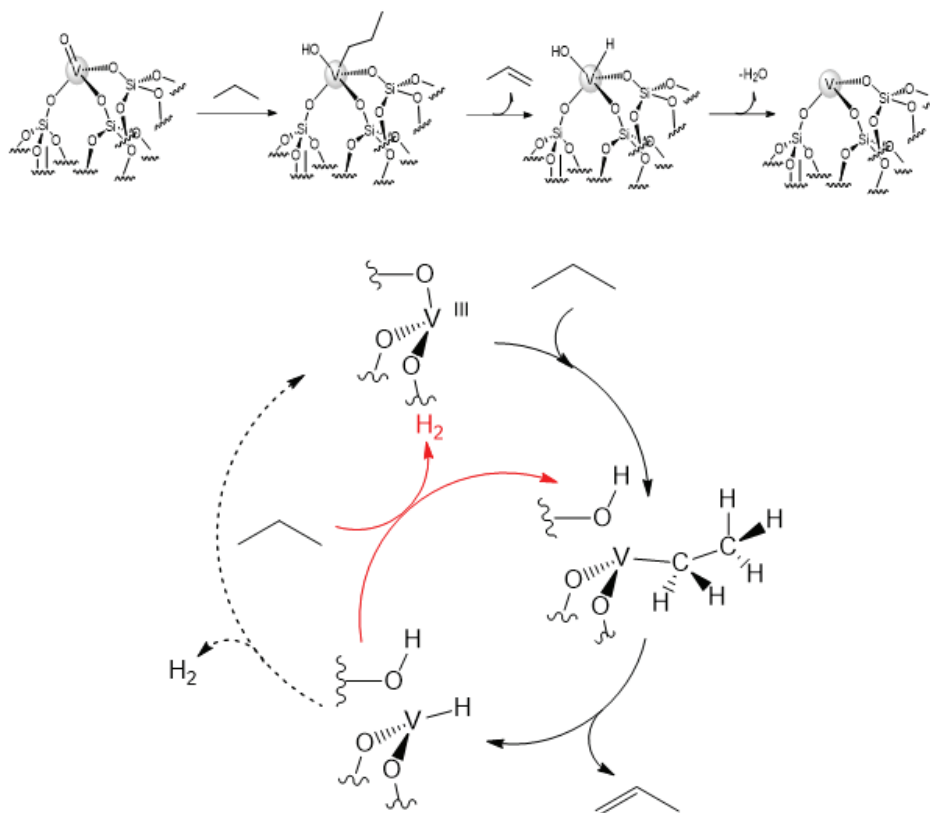


Fig. 34 Proposed mechanism for propane dehydrogenation based on V[157]

Another relevant element from group V transition state metal for NH₃-SCR is niobium. However, the niobium system is rarely employed in surface organometallic chemistry. One example [161] involves grafting of NbCl₃Me₂ on silica followed by an alkylation with ZnMe₂ leading to an active catalyst for the oligomerization of ethylene. The initiation step involves a reduction of Nb(V) into Nb(III). Thus, single Nb sites on ceria may also be relevant catalysts for NH₃-SCR.

3.3.2 Surface organometallic chemistry of Group VI

The most studied group VI elements by SOMC are Mo and W for olefin metathesis. Tungsten oxide supported on silica is an efficient catalyst for olefin metathesis used in industrial processes since the 1960s[162]. The first tungsten oxo-alkylidene derivatives and

their alkyl precursors examples were provided by Schrock *et al.*[163] They reported that $(WO)Cl_2(=CHR)(PR'_3)$ derivatives homogeneously catalyze olefin metathesis in the presence of a Lewis acid, and they found that the reaction between $(WO)Cl_2(=CHCMe_3)(PEt_3)_2$ and olefins without Lewis acid is very slow. Mazoyer *et al.*[164] reported a well-defined, silica-supported tungsten oxo alkyl species prepared by SOMC, displaying a high and sustained activity for propene self-metathesis. Remarkably, its catalytic performances vastly exceed those of the parent imido derivative, reflecting the importance of the oxo ligand in the design of robust catalysts[164]. As for the presence of isobutene byproduct over an imido derivative, they proposed as the olefin metathesis catalyst decomposition pathway that the methyltungstacyclobutane would provide the 2-methylallyl-W-hydride and afford isobutene and inactive reduced W^{IV} from a β -H transfer followed by a reductive elimination, as shown in Fig. 35.

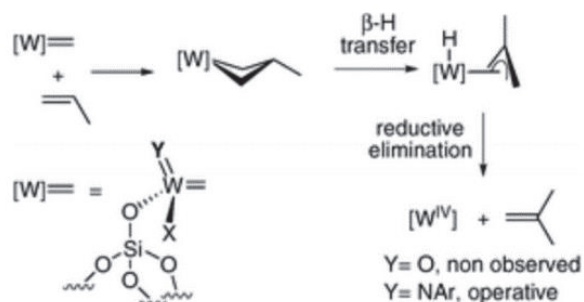


Fig. 35 Proposed deactivation mechanism via β -H elimination from the metallacyclobutane formed over WO_3/SiO_2 [164]

As an active part of C-H activation, tungsten hydride attracts considerable attention in alkane metathesis and alkane coupling reactions. Szeto *et al.*[165] reported a catalyst of non-oxidative coupling of methane (NOCM) reaction, the $[W-H]$, obtained from the $W(=CtBu)(CH_2tBu)_3$ supported on $SiO_2-Al_2O_3$ and $\gamma-Al_2O_3$ after H_2 treatment. Based on the investigation of the methane activation process by IR and SSNMR, they observed and proposed that surface species go through a partial equilibrium containing a redox conversion between $W(IV)$ and $W(VI)$. Such tungsten species adapted on ceria may have a high potential as NH_3 -SCR catalysts. It is indeed important that tungsten is situated next to Ce^{3+} site, creating the necessary acid/redox pair in order to access highly active catalyst. Another relevant element from group VI transition state metal for NH_3 -SCR is molybdenum. As molybdenum is known to be reduced at high temperature, it may also be a relevant catalyst once supported on ceria for NH_3 -SCR.

In summary, as a specific approach, surface organometallic chemistry paves the way to a well-defined and highly active catalysts, particularly for single-atom catalysis. Such materials are suitable for mechanistic studies in heterogeneous catalysis where the results can directly be associated with the single-atom nature. Typically, SOMC catalysts are always prepared using organometallic precursors (or coordination compounds) on a controlled surface to impose the targeted environment of the active single atoms (podality, density, auxiliary ligands). In this way, molecular chemistry could be applied in studying heterogeneous catalysts by grafting the specific functionalized organometallic fragments. However, it should be noted that the choice of supports, metal center, and organometallic ligands highly depends on the reaction. Moreover, SOMC can be considered a globally weak exploited technology even after decades of research within specific groups. The design of new organometallic precursors, extension to various supports, and stabilization of sensitive transition metal complexes are typically fields to be addressed in the future. Such developments will undoubtedly lead to novel applications, mechanistic insights, and even new reactions.

4 Objective of the thesis

This thesis aims to develop highly active and stable catalysts for NH_3 -SCR. Based on the bibliographic study above, ceria appears to be a promising candidate as support, owing to its oxygen storage capacity, redox properties, acidity, and textural properties. In addition, promoting metal oxides from groups V and VI have shown promising activity in NH_3 -SCR reaction. A pursued issue with conventional catalysts lies in the preparation methods that result in a mixture of different surface species. Consequently, important information, such as the structure-reactivity relationship and the mechanism, is challenging to determine since the structure of the active site is not well-established. To address the pursued issue, single-site catalysis has recently attracted much attention. Multiple reports propose that the isolated metal is the active site over traditional metal-oxide catalysts. Single-site catalysts generally exhibit a higher atom efficiency and are suitable for active site probing and mechanistic studies. Surface organometallic chemistry (SOMC) is considered an efficient method for immobilizing the single-site moieties on the surface of oxides, mainly via protonolysis of specific organometallic complexes. It has paved the way for researching the nature of active sites, determining elementary steps of catalytic reactions, discovering new reactions, and acts as a bridge between homogeneous and heterogeneous catalysis. The choice of the promoting element is important. In the literature, most transition state metals have been applied, giving

indeed different catalytic performances. This work is focused on the early transition state metal of groups V and VI, owing to their high oxophilicity, redox capability, since they may bring acidity (both Lewis and Bronsted types) and can lead selectively to isolated metal oxo species. However, to the best of our knowledge, report of single-site catalyst supported on metal oxides for NH₃-SCR reaction is rare[166,167]. Moreover, surface organometallic chemistry on ceria is unknown. Thus, this thesis starts with the study of the surface of ceria, followed by the preparation and characterization of metal-oxo (group V and VI) species supported on ceria by SOMC (as shown in Fig. 36) and their application in the NH₃-SCR reaction.

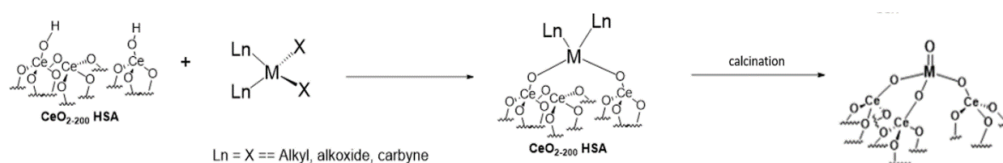


Fig. 36 General approach to synthesize M-oxo/CeO₂ (for example M = W, Mo, Nb, V)

Chapter II is first dedicated to investigation of ceria. In-situ DRIFT and XRD investigate the optimized temperatures for calcination and dehydroxylation. The number of active surface hydroxyls and the mobility of lattice oxygen in ceria structure are studied. To synthesize the predicted active species W-oxo on the surface of ceria, a novel strategy is designed where [W(\equiv C*t*Bu)(CH₂*t*Bu)₃] is grafted onto a ceria dehydroxylated at 200 °C followed by a controlled oxidation under air. The W complex resulting from the grafting reaction and the species resulting from the oxidation process are disclosed. The catalytic performances in NH₃-SCR and structural stability are compared to those of bulk ceria and WO_x/CeO₂ synthesized by the impregnation method.

Chapter III is directed to catalysts based on vanadium supported on ceria prepared by SOMC. Catalysts prepared from different vanadium precursors and with different vanadium loadings have been synthesized, characterized, and tested for NH₃-SCR reaction. In order to prepare the isolated V-oxo/CeO₂ catalysts, different precursors ([V(=O)(OEt)₃]₂, [V(CH₂SiMe₃)₄], and [V(=O)(O*t*Bu)₃]) are used and immobilized on the dehydroxylated ceria from a protonolysis reaction, followed by calcination at 500 °C. These materials have been structurally characterized and investigated in NH₃-SCR reaction.

Chapter IV is dedicated to extending this new synthetic approach based on SOMC to obtain niobium-oxo supported on CeO₂ by grafting [Nb(OEt)₅]₂ on the support and calcining the

resulting material under air at 500 °C. The obtained materials have been characterized, and the calcined sample has been submitted to NH₃-SCR reaction. The catalytic activity of different metal oxo of group V (V, Nb) and VI (W, Mo) supported on ceria catalysts synthesized during this thesis has been compared, and the most promising system has been identified.

Finally, **Chapter V** brings a general conclusion and perspectives suggested for future researches.

Reference

- [1] G. Haxel, J. Hedrick and G. Orris, Rare earth elements— critical resources for high technology, US Geological Survey, US Geological Survey, 2002. <https://pubs.usgs.gov/fs/2002/fs087-02>.
- [2] F. Czerwinski, J.A. Szpunar, The Nanocrystalline ceria sol-gel coatings for high temperature applications, *Journal of Sol-Gel Science and Technology*. 9 (1997) 103–114. <https://doi.org/10.1007/bf02439341>.
- [3] Y. Zhang, S. Zhao, J. Feng, S. Song, W. Shi, D. Wang, II Review Unraveling the physical chemistry and materials science of CeO₂-based nanostructures, *CHEMPR*. (2021) 1–38. <https://doi.org/10.1016/j.chempr.2021.02.015>.
- [4] Y. Ma, W. Gao, Z. Zhang, S. Zhang, Z. Tian, Y. Liu, J.C. Ho, Y. Qu, Regulating the surface of nanoceria and its applications in heterogeneous catalysis, *Surface Science Reports*. 73 (2018) 1–36. <https://doi.org/10.1016/j.surfrep.2018.02.001>.
- [5] A. Kotani, H. Mizuta, T. Jo, J.C. Parlebas, Theory of core photoemission spectra in CeO₂, *solid State Communications*, 53 (1985) 805-810. [https://doi.org/10.1016/0038-1098\(85\)90223-6](https://doi.org/10.1016/0038-1098(85)90223-6).
- [6] J. Paier, C. Penschke, J. Sauer, Oxygen defects and surface chemistry of ceria: Quantum chemical studies compared to experiment, *Chemical Reviews*. 113 (2013) 3949–3985. <https://doi.org/10.1021/cr3004949>.
- [7] D.R. Mullins, The surface chemistry of cerium oxide, *Surface Science Reports*. 70 (2015) 42–85. <https://doi.org/10.1016/j.surfrep.2014.12.001>.
- [8] Y. Zhang, S. Zhao, J. Feng, S. Song, W. Shi, D. Wang, H. Zhang, Unraveling the physical chemistry and materials science of CeO₂-based nanostructures, *Chem*. 7 (2021) 2022–2059. <https://doi.org/10.1016/j.chempr.2021.02.015>.
- [9] A. Trovarelli, J. Llorca, Ceria Catalysts at Nanoscale: How Do Crystal Shapes Shape Catalysis? *ACS Catalysis*. 7 (2017) 4716–4735. <https://doi.org/10.1021/acscatal.7b01246>.
- [10] H.F. Wardenga, A. Klein, Surface potentials of (111), (110) and (100) oriented CeO_{2-x} thin films, *Applied Surface Science*. 377 (2016) 1–8. <https://doi.org/10.1016/j.apsusc.2016.03.091>.
- [11] G.S. Herman, Surface structure determination of (formula presented) by angle-resolved mass spectroscopy of recoiled ions, *Physical Review B - Condensed Matter and Materials Physics*. 59 (1999) 14899–14902. <https://doi.org/10.1103/PhysRevB.59.14899>.
- [12] Y. Lin, Z. Wu, J. Wen, K.R. Poepelmeier, L.D. Marks, Imaging the atomic surface structures of CeO₂ nanoparticles, *Nano Letters*. 14 (2014) 191–196. <https://doi.org/10.1021/nl403713b>.

- [13] S. Gritschneider, M. Reichling, Structural elements of CeO₂(111) surfaces, *Nanotechnology*. 18 (2007) 2–7. <https://doi.org/10.1088/0957-4484/18/4/044024>.
- [14] D.R. Mullins, P.M. Albrecht, F. Calaza, Variations in reactivity on different crystallographic orientations of cerium oxide, *Topics in Catalysis*. 56 (2013) 1345–1362. <https://doi.org/10.1007/s11244-013-0146-7>.
- [15] M. Molinari, S.C. Parker, D.C. Sayle, M.S. Islam, Water adsorption and its effect on the stability of low index stoichiometric and reduced surfaces of ceria, *Journal of Physical Chemistry C*. 116 (2012) 7073–7082. <https://doi.org/10.1021/jp300576b>.
- [16] Z. Wu, M. Li, J. Howe, H.M. Meyer, S.H. Overbury, Probing defect sites on CeO₂ nanocrystals with well-defined surface planes by raman spectroscopy and O₂ adsorption, *Langmuir*. 26 (2010) 16595–16606. <https://doi.org/10.1021/la101723w>.
- [17] M. Wang, F. Wang, J. Ma, M. Li, Z. Zhang, Y. Wang, X. Zhang, J. Xu, Investigations on the crystal plane effect of ceria on gold catalysis in the oxidative dehydrogenation of alcohols and amines in the liquid phase, *Chemical Communications*. 50 (2014) 292–294. <https://doi.org/10.1039/c3cc46180g>.
- [18] N. V. Skorodumova, S.I. Simak, B.I. Lundqvist, I.A. Abrikosov, B. Johansson, Quantum origin of the oxygen storage capability of ceria, *Physical Review Letters*. 89 (2002) 166601/1-166601/4. <https://doi.org/10.1103/PhysRevLett.89.166601>.
- [19] K. K. Jeong, W. Han Mechanistic study for enhanced CO oxidation activity on (Mn,Fe) co-doped CeO₂(111). 293-294 (2017) 82-88. <https://doi.org/10.1016/j.cattod.2016.11.046>.
- [20] C. Sun, H. Li, L. Chen, Nanostructured ceria-based materials: Synthesis, properties, and applications, *Energy and Environmental Science*. 5 (2012) 8475–8505. <https://doi.org/10.1039/c2ee22310d>.
- [21] Y. Madier, C. Descorme, A.M. Le Govic, D. Duprez, Oxygen mobility in CeO₂ and Ce_xZr_(1-x)O₂ compounds: Study by CO transient oxidation and ¹⁸O/¹⁶O isotopic exchange, *Journal of Physical Chemistry B*. 103 (1999) 10999–11006. <https://doi.org/10.1021/jp991270a>.
- [22] F. Esch, S. Fabris, L. Zhou, T. Montini, C. Africh, P. Fornasiero, G. Comelli, R. Rosei, Chemistry: Electron localization determines defect formation on ceria substrates, *Science*. 309 (2005) 752–755. <https://doi.org/10.1126/science.1111568>.
- [23] A. Holmgren, B. Andersson, Oxygen Storage Dynamics in Pt/CeO₂/Al₂O₃ Catalysts, *Journal of Catalysis*. 178 (1998) 14–25. <https://doi.org/10.1006/JCAT.1998.2114>.
- [24] D. Duprez, Study of surface mobility by isotopic exchange: recent developments and perspectives, *Studies in Surface Science and Catalysis*. 112 (1997) 13–28. [https://doi.org/10.1016/S0167-2991\(97\)80820-8](https://doi.org/10.1016/S0167-2991(97)80820-8).
- [25] H. Song, U.S. Ozkan, Changing the oxygen mobility in Co/ceria catalysts by Ca incorporation: Implications for ethanol steam reforming, *Journal of Physical Chemistry A*. 114 (2010) 3796–3801. <https://doi.org/10.1021/jp905608e>.
- [26] Z. Yang, T.K. Woo, K. Hermansson, Adsorption of NO on unreduced and reduced CeO₂ surfaces: A plane-wave DFT study, *Surface Science*. 600 (2006) 4953–4960. <https://doi.org/10.1016/j.susc.2006.08.018>.
- [27] J. Zhang, X.Q. Gong, G. Lu, A DFT + U study of NO evolution at reduced CeO₂(110), *Physical Chemistry Chemical Physics*. 16 (2014) 16904–16908. <https://doi.org/10.1039/c4cp02235a>.

- [28] M. Nolan, Molecular adsorption on the doped (110) ceria surface, *Journal of Physical Chemistry C*. 113 (2009) 2425–2432. <https://doi.org/10.1021/jp809292u>.
- [29] Q. Fu, H. Saltsburg, M. Flytzani-Stephanopoulos, Active nonmetallic Au and Pt species on ceria-based water-gas shift catalysts, *Science*. 301 (2003) 935–938. <https://doi.org/10.1126/science.1085721>.
- [30] R. Heinzmann, I. Issac, J.P. Eufinger, G. Ulbrich, M. Lerch, J. Janek, S. Indris, Observing local oxygen interstitial diffusion in donor-Doped ceria by ^{17}O NMR relaxometry, *Journal of Physical Chemistry C*. 120 (2016) 8568–8577. <https://doi.org/10.1021/acs.jpcc.6b03341>.
- [31] R. Schmitt, A. Nenning, O. Kraynis, R. Korobko, A.I. Frenkel, I. Lubomirsky, S.M. Haile, J.L.M. Rupp, A review of defect structure and chemistry in ceria and its solid solutions, *Chemical Society Reviews*. 49 (2020) 554–592. <https://doi.org/10.1039/c9cs00588a>.
- [32] T. Charoonsuk, N. Vittayakorn, T. Kolodiaznyi, Lattice evolution and point defect chemistry in Ta-doped ceria, *Journal of Alloys and Compounds*. 695 (2017) 1317–1323. <https://doi.org/10.1016/j.jallcom.2016.10.272>.
- [33] Y. Hao, C.K. Yang, S.M. Haile, ceria-zirconia solid solutions ($\text{Ce}_{1-x}\text{Zr}_x\text{O}_{2-\delta}$, $x \leq 0.2$) for solar thermochemical water splitting: A thermodynamic study, *Chemistry of Materials*. 26 (2014) 6073–6082. <https://doi.org/10.1021/cm503131p>.
- [34] L. Cheng, X. Yue, J. Fan, Q. Xiang, Site-Specific Electron-Driving Observations of CO_2 -to- CH_4 Photoreduction on Co-Doped CeO_2 /Crystalline Carbon Nitride S-Scheme Heterojunctions, *Advanced Materials*. 34 (2022) 1–11. <https://doi.org/10.1002/adma.202200929>.
- [35] B. Goris, S. Turner, S. Bals, G. Van Tendeloo, Three-dimensional valency mapping in ceria nanocrystals, *ACS Nano*. 8 (2014) 10878–10884. <https://doi.org/10.1021/nn5047053>.
- [36] S. Turner, S. Lazar, B. Freitag, R. Egoavil, J. Verbeeck, S. Put, Y. Strauven, G. Van Tendeloo, High resolution mapping of surface reduction in ceria nanoparticles, *Nanoscale*. 3 (2011) 3385–3390. <https://doi.org/10.1039/c1nr10510h>.
- [37] J. Qin, Y. Long, W. Wu, W. Zhang, Z. Gao, J. Ma, Amorphous Fe_2O_3 improved [O] transfer cycle of $\text{Ce}^{4+}/\text{Ce}^{3+}$ in CeO_2 for atom economy synthesis of imines at low temperature, *Journal of Catalysis*. 371 (2019) 161–174. <https://doi.org/10.1016/j.jcat.2019.01.032>.
- [38] P. Daw, S. Chakraborty, J.A. Garg, Y. Ben-David, D. Milstein, Direct synthesis of pyrroles by dehydrogenative coupling of diols and amines catalyzed by cobalt pincer complexes, *Angewandte Chemie - International Edition*. 55 (2016) 14373–14377. <https://doi.org/10.1002/anie.201607742>.
- [39] T. Kamachi, S.M.A.H. Siddiki, Y. Morita, M.N. Rashed, K. Kon, T. Toyao, K. ichi Shimizu, K. Yoshizawa, Combined theoretical and experimental study on alcoholysis of amides on CeO_2 surface: A catalytic interplay between Lewis acid and base sites, *Catalysis Today*. 303 (2018) 256–262. <https://doi.org/10.1016/j.cattod.2017.09.006>.
- [40] X. Huang, K. Zhang, B. Peng, G. Wang, M. Muhler, F. Wang, ceria-Based Materials for Thermocatalytic and Photocatalytic Organic Synthesis, *ACS Catalysis*. 11 (2021) 9618–9678. <https://doi.org/10.1021/acscatal.1c02443>.
- [41] M. Capdevila-Cortada, G. Vilé, D. Teschner, J. Pérez-Ramírez, N. López, Reactivity descriptors for ceria in catalysis, *Applied Catalysis B: Environmental*. 197 (2016) 299–312. <https://doi.org/10.1016/j.apcatb.2016.02.035>.
- [42] C. Sanchez, J. Livage, G. Lucazeau, Infrared and Raman Study of Amorphous V_2O_5 , 12 (1982)

- 3–7. <https://doi.org/10.1002/jrs.1250120110>
- [43] X. Yao, Z. Wang, S. Yu, F. Yang, L. Dong, Acid pretreatment effect on the physico-chemical property and catalytic performance of CeO₂ for NH₃-SCR, *Applied Catalysis A: General*. 542 (2017) 282–288. <https://doi.org/10.1016/j.apcata.2017.06.003>.
- [44] T. Yi, Y. Zhang, J. Li, X. Yang, Promotional effect of H₃PO₄ on ceria catalyst for selective catalytic reduction of NO by NH₃, *Cuihua Xuebao/Chinese Journal of Catalysis*. 37 (2016) 300–307. [https://doi.org/10.1016/S1872-2067\(15\)60977-9](https://doi.org/10.1016/S1872-2067(15)60977-9).
- [45] J. An, Y. Wang, J. Lu, J. Zhang, Z. Zhang, S. Xu, X. Liu, T. Zhang, M. Gocyla, M. Heggen, R.E. Dunin-Borkowski, P. Fornasiero, F. Wang, Acid-promoter-free ethylene methoxycarbonylation over Ru-clusters/ceria: The catalysis of interfacial Lewis acid-base pair, *Journal of the American Chemical Society*. 140 (2018) 4172–4181. <https://doi.org/10.1021/jacs.8b01742>.
- [46] S. Cai, D. Zhang, L. Zhang, L. Huang, H. Li, R. Gao, L. Shi, J. Zhang, Comparative study of 3D ordered macroporous Ce_{0.75}Zr_{0.2}M_{0.05}O_{2-δ} (M = Fe, Cu, Mn, Co) for selective catalytic reduction of NO with NH₃, *Catalysis Science and Technology*. 4 (2014) 93–101. <https://doi.org/10.1039/c3cy00398a>.
- [47] G. Postole, B. Chowdhury, B. Karmakar, K. Pinki, J. Banerji, A. Auroux, Knoevenagel condensation reaction over acid-base bifunctional nanocrystalline Ce_xZr_{1-x}O₂ solid solutions, *Journal of Catalysis*. 269 (2010) 110–121. <https://doi.org/10.1016/j.jcat.2009.10.022>.
- [48] H.J. Lee, S. Park, I.K. Song, J.C. Jung, Direct synthesis of dimethyl carbonate from methanol and carbon dioxide over Ga₂O₃/Ce_{0.6}Zr_{0.4}O₂ catalysts: Effect of acidity and basicity of the catalysts, *Catalysis Letters*. 141 (2011) 531–537. <https://doi.org/10.1007/s10562-010-0544-4>.
- [49] N.C. Nelson, Z. Wang, P. Naik, J.S. Manzano, M. Pruski, I.I. Slowing, Phosphate modified ceria as a Brønsted acidic/redox multifunctional catalyst, *Journal of Materials Chemistry A*. 5 (2017) 4455–4466. <https://doi.org/10.1039/c6ta08703e>.
- [50] M. Tamura, R. Kishi, Y. Nakagawa, K. Tomishige, Self-assembled hybrid metal oxide base catalysts prepared by simply mixing with organic modifiers, *Nature Communications*. 6 (2015) 1–9. <https://doi.org/10.1038/ncomms9580>.
- [51] S. Xie, Z. Wang, F. Cheng, P. Zhang, W. Mai, Y. Tong, ceria and ceria-based nanostructured materials for photoenergy applications, *Nano Energy*. 34 (2017) 313–337. <https://doi.org/10.1016/j.nanoen.2017.02.029>.
- [52] R. Ma, S. Zhang, T. Wen, P. Gu, L. Li, G. Zhao, F. Niu, Q. Huang, Z. Tang, X. Wang, A critical review on visible-light-response CeO₂-based photocatalysts with enhanced photooxidation of organic pollutants, *Catalysis Today*. 335 (2019) 20–30. <https://doi.org/10.1016/j.cattod.2018.11.016>.
- [53] Z. Shen, Y. Hu, B. Li, Y. Zou, S. Li, G. Wilma Busser, X. Wang, G. Zhao, M. Muhler, State-of-the-art progress in the selective photo-oxidation of alcohols, *Journal of Energy Chemistry*. 62 (2021) 338–350. <https://doi.org/10.1016/j.jechem.2021.03.033>.
- [54] Y. Liu, Y. Chen, W. Zhou, B. Jiang, X. Zhang, G. Tian, Hydrogenated Cu₂O\Au@CeO₂ Z-scheme catalyst for photocatalytic oxidation of amines to imines, *Catalysis Science and Technology*. 8 (2018) 5535–5543. <https://doi.org/10.1039/c8cy01689e>.
- [55] D. Yu, Y. Jia, Z. Yang, H. Zhang, J. Zhao, Y. Zhao, B. Weng, W. Dai, Z. Li, P. Wang, J.A. Steele, M.B.J. Roeffaers, S. Dai, H. Huang, J. Long, Solar photocatalytic oxidation of methane

- to methanol with water over RuOx/ZnO/CeO₂ nanorods, *ACS Sustainable Chemistry and Engineering*. 10 (2022) 16–22. <https://doi.org/10.1021/acssuschemeng.1c07162>.
- [56] J. Wang, B. Li, T. Gu, T. Ming, J. Wang, P. Wang, J.C. Yu, (Gold core) @ (Ceria shell) nanostructures for plasmon-enhanced catalytic reactions under visible light, *ACS Nano*. 8 (2014) 8152–8162. <https://doi.org/10.1021/nn502303h>.
- [57] Y. Chai, L. Zhang, Q. Liu, F. Yang, W.L. Dai, Insights into the Relationship of the Heterojunction Structure and Excellent Activity: Photo-Oxidative Coupling of Benzylamine on CeO₂-rod/g-C₃N₄ Hybrid under Mild Reaction Conditions, *ACS Sustainable Chemistry and Engineering*. 6 (2018) 10526–10535. <https://doi.org/10.1021/acssuschemeng.8b01865>.
- [58] P. Sudarsanam, B. Hillary, M.H. Amin, S.B.A. Hamid, S.K. Bhargava, Structure-activity relationships of nanoscale MnOx/CeO₂ heterostructured catalysts for selective oxidation of amines under eco-friendly conditions, *Applied Catalysis B: Environmental*. 185 (2016) 213–224. <https://doi.org/10.1016/j.apcatb.2015.12.026>.
- [59] M. Wang, M. Shen, X. Jin, J. Tian, M. Li, Y. Zhou, L. Zhang, Y. Li, J. Shi, Oxygen Vacancy Generation and Stabilization in CeO_{2-x} by Cu Introduction with Improved CO₂ Photocatalytic Reduction Activity, *ACS Catalysis*. 9 (2019) 4573–4581. <https://doi.org/10.1021/acscatal.8b03975>.
- [60] S. Gao, B. Gu, X. Jiao, Y. Sun, X. Zu, F. Yang, W. Zhu, C. Wang, Z. Feng, B. Ye, Y. Xie, Highly Efficient and Exceptionally Durable CO₂ Photoreduction to Methanol over Freestanding Defective Single-Unit-Cell Bismuth Vanadate Layers, *Journal of the American Chemical Society*. 139 (2017) 3438–3445. <https://doi.org/10.1021/jacs.6b11263>.
- [61] Y. Wang, J. Zhao, T. Wang, Y. Li, X. Li, J. Yin, C. Wang, CO₂ photoreduction with H₂O vapor on highly dispersed CeO₂/TiO₂ catalysts: Surface species and their reactivity, *Journal of Catalysis*. 337 (2016) 293–302. <https://doi.org/10.1016/j.jcat.2015.12.030>.
- [62] J.B. Park, J. Graciani, J. Evans, D. Stacchiola, S. Ma, P. Liu, A. Nambu, J.F. Sanz, J. Hrbek, J.A. Rodriguez, High catalytic activity of Au/CeOx/TiO₂(110) controlled by the nature of the mixed-metal oxide at the nanometer level, *Proceedings of the National Academy of Sciences of the United States of America*. 106 (2009) 4975–4980. <https://doi.org/10.1073/pnas.0812604106>.
- [63] G. Spezzati, A.D. Benavidez, A.T. DeLaRiva, Y. Su, J.P. Hofmann, S. Asahina, E.J. Olivier, J.H. Neethling, J.T. Miller, A.K. Datye, E.J.M. Hensen, CO oxidation by Pd supported on CeO₂(100) and CeO₂(111) facets, *Applied Catalysis B: Environmental*. 243 (2019) 36–46. <https://doi.org/10.1016/j.apcatb.2018.10.015>.
- [64] K. Kim, J. Do Yoo, S. Lee, M. Bae, J. Bae, W.C. Jung, J.W. Han, A Simple Descriptor to Rapidly Screen CO Oxidation Activity on Rare-Earth Metal-Doped CeO₂: From Experiment to First-Principles, *ACS Applied Materials and Interfaces*. 9 (2017) 15449–15458. <https://doi.org/10.1021/acsami.7b01844>.
- [65] H. Ha, S. Yoon, K. An, H.Y. Kim, Catalytic CO Oxidation over Au Nanoparticles Supported on CeO₂ Nanocrystals: Effect of the Au-CeO₂ Interface, *ACS Catalysis*. 8 (2018) 11491–11501. <https://doi.org/10.1021/acscatal.8b03539>.
- [66] B. Liu, J. Liu, T. Li, Z. Zhao, X.Q. Gong, Y. Chen, A. Duan, G. Jiang, Y. Wei, Interfacial Effects of CeO₂-Supported Pd Nanorod in Catalytic CO Oxidation: A Theoretical Study, *Journal of Physical Chemistry C*. 119 (2015) 12923–12934. <https://doi.org/10.1021/acs.jpcc.5b00267>.
- [67] M.E. Strayer, T.P. Senftle, J.P. Winterstein, N.M. Vargas-Barbosa, R. Sharma, R.M. Rioux,

- M.J. Janik, T.E. Mallouk, Charge Transfer Stabilization of Late Transition Metal Oxide Nanoparticles on a Layered Niobate Support, *Journal of the American Chemical Society*. 137 (2015) 16216–16224. <https://doi.org/10.1021/jacs.5b11230>.
- [68] F. Yang, J. Graciani, J. Evans, P. Liu, J. Hrbek, J.F. Sanz, J.A. Rodriguez, CO oxidation on inverse CeOx/Cu(111) catalysts: High catalytic activity and ceria-promoted dissociation of O₂, *Journal of the American Chemical Society*. 133 (2011) 3444–3451.
- [69] L. Nie, D. Mei, H. Xiong, B. Peng, Z. Ren, X.I.P. Hernandez, A. DeLaRiva, M. Wang, M.H. Engelhard, L. Kovarik, A.K. Datye, Y. Wang, Activation of surface lattice oxygen in single-atom Pt/CeO₂ for low-temperature CO oxidation, *Science*. 358 (2017) 1419–1423. <https://doi.org/10.1126/science.aao2109>.
- [70] X. Guo, R. Zhou, A new insight into the morphology effect of ceria on CuO/CeO₂ catalysts for CO selective oxidation in hydrogen-rich gas, *Catalysis Science and Technology*. 6 (2016) 3862–3871. <https://doi.org/10.1039/c5cy01816a>.
- [71] M. Tamura, T. Tonomura, K.I. Shimizu, A. Satsuma, Transamidation of amides with amines under solvent-free conditions using a CeO₂ catalyst, *Green Chemistry*. 14 (2012) 717–724. <https://doi.org/10.1039/c2gc16316k>.
- [72] J. An, Y. Wang, Z. Zhang, Z. Zhao, J. Zhang, F. Wang, The Synthesis of Quinazolin-ones from Olefins, CO, and Amines over a Heterogeneous Ru-clusters/ceria Catalyst, *Angewandte Chemie*. 130 (2018) 12488–12492. <https://doi.org/10.1002/ange.201806266>.
- [73] L. Al-Hmoud, C.W. Jones, Reaction pathways over copper and cerium oxide catalysts for direct synthesis of imines from amines under aerobic conditions, *Journal of Catalysis*. 301 (2013) 116–124. <https://doi.org/10.1016/j.jcat.2013.01.027>.
- [74] S. Putla, M.H. Amin, B.M. Reddy, A. Nafady, K.A. Al Farhan, S.K. Bhargava, MnOx Nanoparticle-Dispersed CeO₂ Nanocubes: A Remarkable Heteronanostructured System with Unusual Structural Characteristics and Superior Catalytic Performance, *ACS Applied Materials and Interfaces*. 7 (2015) 16525–16535. <https://doi.org/10.1021/acsami.5b03988>.
- [75] S.C. Yang, S.H. Pang, T.P. Sulmonetti, W.N. Su, J.F. Lee, B.J. Hwang, C.W. Jones, Synergy between ceria oxygen vacancies and Cu nanoparticles facilitates the catalytic conversion of CO₂ to CO under mild conditions, *ACS Catalysis*. 8 (2018) 12056–12066. <https://doi.org/10.1021/acscatal.8b04219>.
- [76] K. Chang, H. Zhang, M.J. Cheng, Q. Lu, Application of ceria in CO₂ Conversion Catalysis, *ACS Catalysis*. 10 (2020) 613–631. <https://doi.org/10.1021/acscatal.9b03935>.
- [77] Y. Wang, H. Arandiyani, J. Scott, K.F. Aguey-Zinsou, R. Amal, Single Atom and Nanoclustered Pt Catalysts for Selective CO₂ Reduction, *ACS Applied Energy Materials*. 1 (2018) 6781–6789. <https://doi.org/10.1021/acsaem.8b00817>.
- [78] R. Mrad, A. Aissat, R. Cousin, D. Courcot, S. Siffert, Catalysts for NOx selective catalytic reduction by hydrocarbons (HC-SCR), *Applied Catalysis A: General*. 504 (2015) 542–548. <https://doi.org/10.1016/j.apcata.2014.10.021>.
- [79] Z. Lian, W. Shan, Y. Zhang, M. Wang, H. He, Morphology-Dependent Catalytic Performance of NbOx/CeO₂ Catalysts for Selective Catalytic Reduction of NOx with NH₃, *Industrial and Engineering Chemistry Research*. 57 (2018) 12736–12741. <https://doi.org/10.1021/acs.iecr.8b02553>.
- [80] D. Zengel, M. Stehle, O. Deutschmann, M. Casapu, J.D. Grunwaldt, Impact of gas phase

- reactions and catalyst poisons on the NH₃-SCR activity of a V₂O₅-WO₃/TiO₂ catalyst at pre-turbine position, *Applied Catalysis B: Environmental*. 288 (2021) 119991. <https://doi.org/10.1016/j.apcatb.2021.119991>.
- [81] D.E. Doronkin, F. Benzi, L. Zheng, D.I. Sharapa, L. Amidani, F. Studt, P.W. Roesky, M. Casapu, O. Deutschmann, J.D. Grunwaldt, NH₃-SCR over V-W/TiO₂ Investigated by Operando X-ray Absorption and Emission Spectroscopy, *Journal of Physical Chemistry C*. 123 (2019) 14338–14349. <https://doi.org/10.1021/acs.jpcc.9b00804>.
- [82] J. Xu, H. Yu, C. Zhang, F. Guo, J. Xie, Development of cerium-based catalysts for selective catalytic reduction of nitrogen oxides: a review, *New Journal of Chemistry*. 43 (2019) 3996–4007. <https://doi.org/10.1039/c8nj05420g>.
- [83] C. Paolucci, A.A. Verma, S.A. Bates, V.F. Kispersky, J.T. Miller, R. Gounder, W.N. Delgass, F.H. Ribeiro, W.F. Schneider, Isolation of the copper redox steps in the standard selective catalytic reduction on Cu-SSZ-13, *Angewandte Chemie - International Edition*. 53 (2014) 11828–11833. <https://doi.org/10.1002/anie.201407030>.
- [84] P. Chen, M. Jabłońska, P. Weide, T. Caumanns, T. Weirich, M. Muhler, R. Moos, R. Palkovits, U. Simon, Formation and Effect of NH₄⁺ Intermediates in NH₃-SCR over Fe-ZSM-5 Zeolite Catalysts, *ACS Catalysis*. 6 (2016) 7696–7700. <https://doi.org/10.1021/acscatal.6b02496>.
- [85] L. Han, S. Cai, M. Gao, J.Y. Hasegawa, P. Wang, J. Zhang, L. Shi, D. Zhang, Selective Catalytic Reduction of NO_x with NH₃ by Using Novel Catalysts: State of the Art and Future Prospects, *Chemical Reviews*. 119 (2019) 10916–10976. <https://doi.org/10.1021/acs.chemrev.9b00202>.
- [86] J.H. Park, H.J. Park, J.H. Baik, I.S. Nam, C.H. Shin, J.H. Lee, B.K. Cho, S.H. Oh, Hydrothermal stability of Cu-ZSM5 catalyst in reducing NO by NH₃ for the urea selective catalytic reduction process, *Journal of Catalysis*. 240 (2006) 47–57. <https://doi.org/10.1016/j.jcat.2006.03.001>.
- [87] Y. Shan, J. Du, Y. Zhang, W. Shan, X. Shi, Y. Yu, R. Zhang, X. Meng, F.S. Xiao, H. He, Selective catalytic reduction of NO_x with NH₃: Opportunities and challenges of Cu-based small-pore zeolites, *National Science Review*. 8 (2021) nwab010. <https://doi.org/10.1093/nsr/nwab010>.
- [88] C. Tang, H. Zhang, L. Dong, ceria-based catalysts for low-temperature selective catalytic reduction of NO with NH₃, *Catalysis Science and Technology*. 6 (2016) 1248–1264. <https://doi.org/10.1039/c5cy01487e>.
- [89] J. Arfaoui, A. Ghorbel, C. Petitto, G. Delahay, Novel V₂O₅-CeO₂-TiO₂-SO₄²⁻ nanostructured aerogel catalyst for the low temperature selective catalytic reduction of NO by NH₃ in excess O₂, *Applied Catalysis B: Environmental*. 224 (2018) 264–275. <https://doi.org/10.1016/j.apcatb.2017.10.059>.
- [90] Y. Peng, K. Li, J. Li, Identification of the active sites on CeO₂-WO₃ catalysts for SCR of NO_x with NH₃: An in situ IR and Raman spectroscopy study, *Applied Catalysis B: Environmental*. 140–141 (2013) 483–492. <https://doi.org/10.1016/j.apcatb.2013.04.043>.
- [91] B. Liu, J. Liu, S. Ma, Z. Zhao, Y. Chen, X.Q. Gong, W. Song, A. Duan, G. Jiang, Mechanistic study of selective catalytic reduction of NO with NH₃ on W-doped CeO₂ catalysts: Unraveling the catalytic cycle and the role of oxygen vacancy, *Journal of Physical Chemistry C*. 120 (2016) 2271–2283. <https://doi.org/10.1021/acs.jpcc.5b11355>.
- [92] X. Liu, P. Jiang, Y. Chen, Y. Wang, Q. Ding, Z. Sui, H. Chen, Z. Shen, X. Wu, A basic

- comprehensive study on synergetic effects among the metal oxides in CeO₂-WO₃/TiO₂ NH₃-SCR catalyst, *Chemical Engineering Journal*. 421 (2021) 127833. <https://doi.org/10.1016/j.ccej.2020.127833>.
- [93] J. Liu, B. Liu, Y. Fang, Z. Zhao, Y. Wei, X.Q. Gong, C. Xu, A. Duan, G. Jiang, Preparation, characterization and origin of highly active and thermally stable Pd-Ce_{0.8}Zr_{0.2}O₂ catalysts via sol-evaporation induced self-assembly method, *Environmental Science and Technology*. 48 (2014) 12403–12410. <https://doi.org/10.1021/es5027008>.
- [94] H. Jiang, J. Zhao, D. Jiang, M. Zhang, Hollow MnOx-CeO₂ nanospheres prepared by a green route: A novel low-temperature NH₃-SCR catalyst, *Catalysis Letters*. 144 (2014) 325–332. <https://doi.org/10.1007/s10562-013-1113-4>.
- [95] X. Yao, L. Chen, J. Cao, F. Yang, W. Tan, L. Dong, Morphology and crystal-plane effects of CeO₂ on TiO₂/CeO₂ catalysts during NH₃-SCR reaction, *Industrial and Engineering Chemistry Research*. 57 (2018) 12407–12419. <https://doi.org/10.1021/acs.iecr.8b02830>.
- [96] Y. Cheng, W. Song, J. Liu, H. Zheng, Z. Zhao, C. Xu, Y. Wei, E.J.M. Hensen, Simultaneous NO_x and particulate matter removal from diesel exhaust by hierarchical Fe-doped Ce-Zr oxide, *ACS Catalysis*. 7 (2017) 3883–3892. <https://doi.org/10.1021/acscatal.6b03387>.
- [97] H. Liu, Z. Fan, C. Sun, S. Yu, S. Feng, W. Chen, D. Chen, C. Tang, F. Gao, L. Dong, Improved activity and significant SO₂ tolerance of samarium modified CeO₂-TiO₂ catalyst for NO selective catalytic reduction with NH₃, *Applied Catalysis B: Environmental*. 244 (2019) 671–683. <https://doi.org/10.1016/j.apcatb.2018.12.001>.
- [98] L. Wei, Y. Liu, H. Dai, S. Cui, C. Wang, H.C. Hsi, E. Duan, Y. Peng, J. Deng, Electronic structure tailoring of Al³⁺- and Ta⁵⁺-doped CeO₂ for the synergistic removal of NO and chlorinated organics, *Applied Catalysis B: Environmental*. 304 (2022) 120939. <https://doi.org/10.1016/j.apcatb.2021.120939>.
- [99] G. Zhang, W. Han, H. Zhao, L. Zong, Z. Tang, Solvothermal synthesis of well-designed ceria-titanium catalysts with enhanced catalytic performance for wide temperature NH₃-SCR reaction, *Applied Catalysis B: Environmental*. 226 (2018) 117–126. <https://doi.org/10.1016/j.apcatb.2017.12.030>.
- [100] J. Liu, X. Li, Q. Zhao, J. Ke, H. Xiao, X. Lv, S. Liu, M. Tadé, S. Wang, Mechanistic investigation of the enhanced NH₃-SCR on cobalt-decorated Ce-Ti mixed oxide: In situ FTIR analysis for structure-activity correlation, *Applied Catalysis B: Environmental*. 200 (2017) 297–308. <https://doi.org/10.1016/j.apcatb.2016.07.020>.
- [101] Z. Liu, Y. Yi, J. Li, S.I. Woo, B. Wang, X. Cao, Z. Li, A superior catalyst with dual redox cycles for the selective reduction of NO_x by ammonia, *Chemical Communications*. 49 (2013) 7726–7728. <https://doi.org/10.1039/c3cc43041c>.
- [102] Z. Ma, D. Weng, X. Wu, Z. Si, Effects of WO_x modification on the activity, adsorption and redox properties of CeO₂ catalyst for NO_x reduction with ammonia, *Journal of Environmental Sciences (China)*. 24 (2012) 1305–1316. [https://doi.org/10.1016/S1001-0742\(11\)60925-X](https://doi.org/10.1016/S1001-0742(11)60925-X).
- [103] S. Yang, Y. Liao, S. Xiong, F. Qi, H. Dang, X. Xiao, J. Li, N₂ selectivity of NO reduction by NH₃ over MnOx-CeO₂: Mechanism and key factors, *Journal of Physical Chemistry C*. 118 (2014) 21500–21508. <https://doi.org/10.1021/jp5062489>.
- [104] H. Chang, L. Ma, S. Yang, J. Li, L. Chen, W. Wang, J. Hao, Comparison of preparation methods for ceria catalyst and the effect of surface and bulk sulfates on its activity toward NH₃-SCR, *Journal of Hazardous Materials*. 262 (2013) 782–788.

<https://doi.org/10.1016/j.jhazmat.2013.09.043>.

- [105] N.Z. Yang, R.T. Guo, Y. Tian, W.G. Pan, Q.L. Chen, Q.S. Wang, C.Z. Lu, S.X. Wang, The enhanced performance of ceria by HF treatment for selective catalytic reduction of NO with NH₃, *Fuel*. 179 (2016) 305–311. <https://doi.org/10.1016/j.fuel.2016.04.002>.
- [106] X. Chen, S. Gao, H. Wang, Y. Liu, Z. Wu, Selective catalytic reduction of NO over carbon nanotubes supported CeO₂, *Catalysis Communications*. 14 (2011) 1–5. <https://doi.org/10.1016/j.catcom.2011.07.005>.
- [107] L. Zhang, J. Sun, L. Li, S. Ran, G. Li, C. Li, C. Ge, L. Dong, Selective Catalytic Reduction of NO by NH₃ on CeO₂-MO_x (M = Ti, Si, and Al) Dual Composite Catalysts: Impact of Surface Acidity, *Industrial and Engineering Chemistry Research*. 57 (2018) 490–497. <https://doi.org/10.1021/acs.iecr.7b03652>.
- [108] Y. Li, H. Cheng, D. Li, Y. Qin, Y. Xie, S. Wang, WO₃/CeO₂-ZrO₂, a promising catalyst for selective catalytic reduction (SCR) of NO_x with NH₃ in diesel exhaust, *Chemical Communications*. (2008) 1470–1472. <https://doi.org/10.1039/b717873e>.
- [109] S. Zhan, H. Zhang, Y. Zhang, Q. Shi, Y. Li, X.J. Li, Efficient NH₃-SCR removal of NO_x with highly ordered mesoporous WO₃(χ)-CeO₂ at low temperatures, *Applied Catalysis B: Environmental*. 203 (2017) 199–209. <https://doi.org/10.1016/j.apcatb.2016.10.010>.
- [110] Z. Ma, X. Wu, Z. Si, D. Weng, J. Ma, T. Xu, Impacts of niobia loading on active sites and surface acidity in NbO_x/CeO₂-ZrO₂ NH₃-SCR catalysts, *Applied Catalysis B: Environmental*. 179 (2015) 380–394. <https://doi.org/10.1016/j.apcatb.2015.05.038>.
- [111] Z. Lian, F. Liu, H. He, K. Liu, Nb-doped VO_x/CeO₂ catalyst for NH₃-SCR of NO_x at low temperatures, *RSC Advances*. 5 (2015) 37675–37681. <https://doi.org/10.1039/c5ra02752g>.
- [112] Z. Xiong, W. Wang, J. Li, L. Huang, W. Lu, The synergistic promotional effect of W doping and sulfate modification on the NH₃-SCR activity of CeO₂ catalyst, *Molecular Catalysis*. 522 (2022) 112250. <https://doi.org/10.1016/j.mcat.2022.112250>.
- [113] Y. Peng, C. Wang, J. Li, Structure–activity relationship of VO_x/CeO₂ nanorod for NO removal with ammonia, *Applied Catalysis B: Environmental*. 144 (2014) 538–546. <http://dx.doi.org/10.1016/j.apcatb.2013.07.059>
- [114] L. Yan, Y. Liu, K. Zha, H. Li, L. Shi, D. Zhang, Deep insight into the structure-activity relationship of Nb modified SnO₂-CeO₂ catalysts for low-temperature selective catalytic reduction of NO by NH₃, *Catalysis Science and Technology*. 7 (2017) 502–514. <https://doi.org/10.1039/c6cy02242a>.
- [115] I. El Arrouji, C. Chen, J. Toyir, C. Larabi, K.C. Szeto, A. de Mallmann, M. Taoufik, A. Oulmekki, NH₃-selective catalytic reduction of nox to N₂ over ceria supported wox based catalysts: Influence of tungsten content, *Catalysts*. 11 (2021) 1–12. <https://doi.org/10.3390/catal11080950>.
- [116] C. Li, Q. Li, P. Lu, H. Cui, G. Zeng, Characterization and performance of V₂O₅/CeO₂ for NH₃-SCR of NO at low temperatures, *Frontiers of Environmental Science and Engineering in China*. 6 (2012) 156–161. <https://doi.org/10.1007/s11783-010-0295-x>.
- [117] Z. Lian, F. Liu, H. He, Effect of preparation methods on the activity of VO_x/CeO₂ catalysts for the selective catalytic reduction of NO_x with NH₃, *Catalysis Science and Technology*. 5 (2015) 389–396. <https://doi.org/10.1039/c4cy00935e>.
- [118] X. Yao, L. Chen, J. Cao, F. Yang, W. Tan, L. Dong, Morphology and Crystal-Plane Effects of

- CeO₂ on TiO₂/CeO₂ Catalysts during NH₃-SCR Reaction, *Industrial and Engineering Chemistry Research*. 57 (2018) 12407–12419. <https://doi.org/10.1021/acs.iecr.8b02830>.
- [119] Y. Zhou, S. Ren, M. Wang, J. Yang, Z. Chen, L. Chen, Mn and Fe oxides co-effect on nanopolyhedron CeO₂ catalyst for NH₃-SCR of NO, *Journal of the Energy Institute*. 99 (2021) 97–104. <https://doi.org/10.1016/j.joei.2021.08.003>.
- [120] Z. Chen, S. Ren, Y. Zhou, X. Li, M. Wang, L. Chen, Comparison of Mn doped CeO₂ with different exposed facets for NH₃-SCR at low temperature, *Journal of the Energy Institute*. 105 (2022) 114–120. <https://doi.org/10.1016/j.joei.2022.08.007>.
- [121] X. Zhang, J. Wang, Z. Song, H. Zhao, Y. Xing, M. Zhao, J. Zhao, Z. Ma, P. Zhang, N. Tsubaki, Promotion of surface acidity and surface species of doped Fe and SO₄²⁻ over CeO₂ catalytic for NH₃-SCR reaction, *Molecular Catalysis*. 463 (2019) 1–7. <https://doi.org/10.1016/j.mcat.2018.11.002>.
- [122] X. Yao, J. Cao, L. Chen, K. Kang, Y. Chen, M. Tian, F. Yang, Doping effect of cations (Zr⁴⁺, Al³⁺, and Si⁴⁺) on MnOx/CeO₂ nano-rod catalyst for NH₃-SCR reaction at low temperature, *Cuihua Xuebao/Chinese Journal of Catalysis*. 40 (2019) 733–743. [https://doi.org/10.1016/s1872-2067\(18\)63204-8](https://doi.org/10.1016/s1872-2067(18)63204-8).
- [123] N. Akter, S. Zhang, J. Lee, D.H. Kim, J.A. Boscoboinik, T. Kim, Selective catalytic reduction of NO by ammonia and NO oxidation Over CoOx/CeO₂ catalysts, *Molecular Catalysis*. 482 (2020) 110664. <https://doi.org/10.1016/j.mcat.2019.110664>.
- [124] K. Ni, Y. Peng, Y. Wang, Z. Huang, H. Zhao, X. Wu, G. Jing, Enhancement of SO₂ resistance on submonolayer V₂O₅-MnO₂/CeO₂ catalyst by three-dimensional ordered mesoporous CeO₂ in low-temperature NH₃-SCR, *Energy and Fuels*. 36 (2022) 2787–2798. <https://doi.org/10.1021/acs.energyfuels.1c04379>.
- [125] Z. Lian, W. Shan, Y. Zhang, M. Wang, H. He, Morphology-dependent catalytic performance of NbOx/CeO₂ catalysts for selective catalytic reduction of NOx with NH₃, *Industrial and Engineering Chemistry Research*. 57 (2018) 12736–12741. <https://doi.org/10.1021/acs.iecr.8b02553>.
- [126] W. Tan, J. Wang, Y. Cai, L. Li, S. Xie, F. Gao, F. Liu, L. Dong, Molybdenum oxide as an efficient promoter to enhance the NH₃-SCR performance of CeO₂-SiO₂ catalyst for NOx removal, *Catalysis Today*. 397–399 (2022) 475–483. <https://doi.org/10.1016/j.cattod.2021.07.007>.
- [127] H. Zhang, G. Liu, L. Shi, J. Ye, Single-atom catalysts: Emerging multifunctional materials in heterogeneous catalysis, *Advanced Energy Materials*. 8 (2018) 1701343. <https://doi.org/10.1002/aenm.201701343>.
- [128] W. Guo, Z. Wang, X. Wang, Y. Wu, General Design Concept for Single-Atom Catalysts toward Heterogeneous Catalysis, *Advanced Materials*. 33 (2021) 27–29. <https://doi.org/10.1002/adma.202004287>.
- [129] H. Lv, W. Guo, M. Chen, H. Zhou, Y. Wu, Rational construction of thermally stable single atom catalysts: From atomic structure to practical applications, *Chinese Journal of Catalysis*. 43 (2022) 71–91. [https://doi.org/10.1016/S1872-2067\(21\)63888-3](https://doi.org/10.1016/S1872-2067(21)63888-3).
- [130] J. Wang, Z. Li, Y. Wu, Y. Li, Fabrication of single-atom catalysts with precise structure and high metal loading, *Advanced Materials*. 30 (2018) 1–5. <https://doi.org/10.1002/adma.201801649>.

- [131] M.K. Samantaray, E. Pump, A. Bendjeriou-Sedjerari, V. D'Elia, J.D.A. Pelletier, M. Guidotti, R. Psaro, J.M. Basset, Surface organometallic chemistry in heterogeneous catalysis, *Chemical Society Reviews*. 47 (2018) 8403–8437. <https://doi.org/10.1039/c8cs00356d>.
- [132] S. Liang, C. Hao, Y. Shi, The Power of single-atom catalysis, *ChemCatChem*. 7 (2015) 2559–2567. <https://doi.org/10.1002/cctc.201500363>.
- [133] V. D'Elia, H. Dong, A.J. Rossini, C.M. Widdifield, S.V.C. Vummaleti, Y. Minenkov, A. Poater, E. Abou-Hamad, J.D.A. Pelletier, L. Cavallo, L. Emsley, J.M. Basset, Cooperative effect of monopodal silica-supported niobium complex pairs enhancing catalytic cyclic carbonate production, *Journal of the American Chemical Society*. 137 (2015) 7728–7739. <https://doi.org/10.1021/jacs.5b02872>.
- [134] M.K. Samantaray, S.K. Mishra, A. Saidi, J.M. Basset, Surface organometallic chemistry: A sustainable approach in modern catalysis, *Journal of Organometallic Chemistry*. 945 (2021) 121864. <https://doi.org/10.1016/j.jorganchem.2021.121864>.
- [135] R.P. Saint-Arroman, M. Chabanas, A. Baudouin, C. Copéret, J.M. Basset, A. Lesage, L. Emsley, Characterization of surface organometallic complexes using high resolution 2D solid state NMR spectroscopy. Application to the full characterization of a silica supported metal carbyne: $\equiv\text{SiO-Mo}(\equiv\text{CtBu})(\text{CH}_2\text{tBu})_2$, *Journal of the American Chemical Society*. 123 (2001) 3820–3821. <https://doi.org/10.1021/ja002259n>.
- [136] S.E. Ashbrook, S. Seddon, New methods and applications in solid state NMR spectroscopy of quadrupolar nuclei, *Journal of the American Chemical Society*. 136 (2014) 15440–15456. <https://doi.org/10.1021/ja504734p>.
- [137] A.I. Frenkel, J.A. Rodriguez, J.G. Chen, Synchrotron techniques for in situ catalytic studies: Capabilities, challenges, and opportunities, *ACS Catalysis*. 2 (2012) 2269–2280. <https://doi.org/10.1021/cs3004006>.
- [138] P. Serna, B.C. Gates, Molecular metal catalysts on supports: Organometallic chemistry meets surface science, *Accounts of Chemical Research*. 47 (2014) 2612–2620. <https://doi.org/10.1021/ar500170k>.
- [139] R.J. Witzke, A. Chapovetsky, M.P. Conley, D.M. Kaphan, M. Delferro, Nontraditional catalyst supports in surface organometallic chemistry, *ACS Catalysis*. 10 (2020) 11822–11840. <https://doi.org/10.1021/acscatal.0c03350>.
- [140] S.L. Scott, J.-M. Basset, Stoichiometric and catalytic reactivity of organometallic fragments supported on inorganic oxides, *Journal of Molecular Catalysis*: 86 (1994) 5–22 [https://doi.org/10.1016/0304-5102\(93\)E0163-B](https://doi.org/10.1016/0304-5102(93)E0163-B)
- [141] J. Estephane, E. Groppo, A. Damin, J.G. Vitillo, D. Gianolio, C. Lamberti, S. Bordiga, C. Prestipino, S. Nikitenko, E.A. Quadrelli, M. Taoufik, J.M. Basset, A. Zecchina, Structure and enhanced reactivity of Chromocene carbonyl confined inside cavities of NaY zeolite, *Journal of Physical Chemistry C*. 113 (2009) 7305–7315. <https://doi.org/10.1021/jp811240m>.
- [142] Y.A. Ryndin, J.P. Candy, B. Didillon, L. Savary, J.M. Basset, Surface organometallic chemistry on metals applied to the environment: Hydrogenolysis of AsPh_3 with nickel supported on alumina, *Journal of Catalysis*. 198 (2001) 103–108. <https://doi.org/10.1006/jcat.2000.3116>.
- [143] Z. Thiam, E. Abou-Hamad, B. Dereli, L. Liu, A.H. Emwas, R. Ahmad, H. Jiang, A.A. Isah, P.B. Ndiaye, M. Taoufik, Y. Han, L. Cavallo, J.M. Basset, M. Eddaoudi, Extension of surface organometallic chemistry to metal–organic frameworks: Development of a well-defined single

- site [(=Zr-O-)W(=O)(CH₂tBu)₃] olefin metathesis catalyst, *Journal of the American Chemical Society*. 142 (2020) 16690–16703. <https://doi.org/10.1021/jacs.0c06925>.
- [144] N. Millot, C.C. Santini, F. Lefebvre, J.M. Basset, Surface organometallic chemistry: A route to well-defined boron heterogeneous co-catalyst for olefin polymerisation, *Comptes Rendus Chimie*. 7 (2004) 725–736. <https://doi.org/10.1016/j.crci.2004.03.011>.
- [145] N. Merle, J. Trébosc, A. Baudouin, I. Del Rosal, L. Maron, K. Szeto, M. Genelot, A. Mortreux, M. Taoufik, L. Delevoye, R.M. Gauvin, ¹⁷O NMR gives unprecedented insights into the structure of supported catalysts and their interaction with the silica carrier, *Journal of the American Chemical Society*. 134 (2012) 9263–9275. <https://doi.org/10.1021/ja301085m>.
- [146] M. Delgado, F. Delbecq, C. C. Santini, F. Lefebvre, S. Norsic, P. Putaj, P. Sautet, J.-M. Basset, Evolution of Structure and of Grafting Properties of γ -Alumina with Pretreatment Temperature. 116 (2012), 834-843. <https://doi.org/10.1021/jp208709x>
- [147] M. Taoufik, K.C. Szeto, N. Merle, I. Del Rosal, L. Maron, J. Trébosc, G. Tricot, R.M. Gauvin, L. Delevoye, Heteronuclear NMR spectroscopy as a surface-selective technique: A unique look at the hydroxyl groups of γ -alumina. *Chemistry - A European Journal*. 20 (2014) 4038–4046. <https://doi.org/10.1002/chem.201304883>.
- [148] A. T. F. Batista, D. Wisser, T. Pigeon, D. Gajan, F. Diehl, M. Rivallan, L. Catita, A.-S. Gay, A. Lesage, C. Chizallet, P. Raybaud, Beyond γ -Al₂O₃ crystallite surfaces: The hidden features of edges revealed by solid-state ¹H NMR and DFT calculations. *Journal of Catalysis*. 378 (2019), 140-143. <https://doi.org/10.1016/j.jcat.2019.08.009>.
- [149] N. Merle, T. Tabassum, S. L. Scott, A. Motta, K. Szeto, M. Taoufik, * R. M. Gauvin, and L. Delevoye, High-field NMR, reactivity, and DFT modeling reveal the γ -Al₂O₃ surface hydroxyl network. *Angewandte Chemie International Edition*. 61 (2022) e202207316. <https://doi.org/10.26434/chemrxiv-2022-mghvd>
- [150] J. Joubert, F. Delbecq, P. Sautet, E. Le Roux, M. Taoufik, C. Thieuleux, F. Blanc, C. Copéret, J. Thivolle-Cazat, J.M. Basset, Molecular understanding of alumina supported single-site catalysts by a combination of experiment and theory, *Journal of the American Chemical Society*. 128 (2006) 9157–9169. <https://doi.org/10.1021/ja0616736>.
- [151] G. Busca, Structural, Surface, and Catalytic Properties of Aluminas, *Advances in Catalysis*. 57(2014), 319-404. <https://doi.org/10.1016/B978-0-12-800127-1.00003-5>.
- [152] F. Zhang, K.C. Szeto, M. Taoufik, L. Delevoye, R.M. Gauvin, S.L. Scott, Enhanced Metathesis Activity and Stability of Methyltrioxorhenium on a Mostly Amorphous Alumina: Role of the Local Grafting Environment, *Journal of the American Chemical Society*. 140 (2018) 13854–13868. <https://doi.org/10.1021/jacs.8b08630>.
- [153] K.C. Szeto, B. Loges, N. Merle, N. Popoff, A. Quadrelli, H. Jia, E. Berrier, A. De Mallmann, L. Delevoye, R.M. Gauvin, M. Taoufik, Vanadium oxo organometallic species supported on silica for the selective non-oxidative dehydrogenation of propane, *Organometallics*. 32 (2013) 6452–6460. <https://doi.org/10.1021/om400795s>.
- [154] R.R. Langeslay, D.M. Kaphan, C.L. Marshall, P.C. Stair, A.P. Sattelberger, M. Delferro, Catalytic applications of vanadium: A mechanistic perspective, *Chemical Reviews*. 119 (2019) 2128–2191. <https://doi.org/10.1021/acs.chemrev.8b00245>.
- [155] M.E. Harlin, V.M. Niemi, A.O.I. Krause, Alumina-supported vanadium oxide in the dehydrogenation of butanes, *Journal of Catalysis*. 195 (2000) 67–78. <https://doi.org/10.1006/jcat.2000.2969>.

- [156] S. Chen, Z. Qin, G. Wang, M. Dong, J. Wang, Promoting effect of carbon dioxide on the dehydrogenation of ethylbenzene over silica-supported vanadium catalysts, *Fuel*. 109 (2013) 43–48. <https://doi.org/10.1016/j.fuel.2012.06.004>.
- [157] J. Abou Nakad, N. Berthet, K.C. Szeto, A. De Mallmann, M. Taoufik, Direct conversion of trans-2-butene into a mixture of monomers with different composition over vanadium supported catalysts, *Catalysis Communications*. 169 (2022) 106469. <https://doi.org/10.1016/j.catcom.2022.106469>.
- [158] Y.L. Wu, Z.F. Han, X. Yan, W.Z. Lang, Y.J. Guo, Effective synthesis of vanadium-doped mesoporous silica nanospheres by sol-gel method for propane dehydrogenation reaction, *Microporous and Mesoporous Materials*. 330 (2022) 111616. <https://doi.org/10.1016/j.micromeso.2021.111616>.
- [159] J. Abou Nakad, R. Rajapaksha, K.C. Szeto, A. De Mallmann, M. Taoufik, Preparation of tripodal vanadium oxo-organometallic species supported on silica, $[(\equiv\text{SiO})_3\text{V}(=\text{O})]$, for selective nonoxidative dehydrogenation of propane, *Organometallics*. 41 (2022) 2784–2797. <https://doi.org/10.1021/acs.organomet.2c00377>.
- [160] D.M. Kaphan, M.S. Ferrandon, R.R. Langeslay, G. Celik, E.C. Wegener, C. Liu, J. Niklas, O.G. Poluektov, M. Delferro, Mechanistic aspects of a surface organo-vanadium(III) catalyst for hydrocarbon hydrogenation and dehydrogenation, *ACS Catalysis*. 9 (2019) 11055–11066. <https://doi.org/10.1021/acscatal.9b02800>.
- [161] A. Hamieh, R. Dey, B. Nekoueishahraki, M. K. Samantaray, Y. Chen, E. Abou-Hamad, J.M. Basset, Single site silica supported tetramethyl niobium by the SOMC strategy: synthesis, characterization and structure–activity relationship in the ethylene oligomerization reaction, *Chemical Communication*. 53 (2017) 7068–7071. <https://doi.org/10.1039/c7cc02585h>
- [162] J.C. Mol, Industrial applications of olefin metathesis, *Journal of Molecular Catalysis A: Chemical*. 213 (2004) 39–45. <https://doi.org/10.1016/j.molcata.2003.10.049>.
- [163] R. Schrock, S. Rocklage, J. Wengrovius, G. Rupprecht, J. Fellmann, Preparation and characterization of active niobium, tantalum and tungsten metathesis catalysts, *Preprints*. 25 (1980) 382–391.
- [164] E. Mazoyer, N. Merle, A. De Mallmann, J.M. Basset, E. Berrier, L. Delevoye, J.F. Paul, C.P. Nicholas, R.M. Gauvin, M. Taoufik, Development of the first well-defined tungsten oxo alkyl derivatives supported on silica by SOMC: Towards a model of WO_3/SiO_2 olefin metathesis catalyst, *Chemical Communications*. 46 (2010) 8944–8946. <https://doi.org/10.1039/c0cc02507k>.
- [165] K.C. Szeto, S. Norsic, L. Hardou, E. Le Roux, S. Chakka, J. Thivolle-Cazat, A. Baudouin, C. Papaioannou, J.M. Basset, M. Taoufik, Non-oxidative coupling of methane catalysed by supported tungsten hydride onto alumina and silica-alumina in classical and H_2 permeable membrane fixed-bed reactors, *Chemical Communications*. 46 (2010) 3985–3987. <https://doi.org/10.1039/c0cc00007h>.
- [166] W. Qu, X. Liu, J. Chen, Y. Dong, X. Tang, Y. Chen, Single-atom catalysts reveal the dinuclear characteristic of active sites in NO selective reduction with NH_3 , *Nature Communications*. 11 (2020) 1–7. <https://doi.org/10.1038/s41467-020-15261-5>.
- [167] S. Xie, W. Tan, Y. Li, L. Ma, S.N. Ehrlich, J. Deng, P. Xu, F. Gao, L. Dong, F. Liu, Copper single atom-triggered niobia-ceria catalyst for efficient low-temperature reduction of nitrogen oxides, *ACS Catalysis*. 12 (2022) 2441–2453. <https://doi.org/10.1021/acscatal.1c05661>.

CHAPTER II

**Surface Organometallic Chemistry of
[W(\equiv C*t*Bu)(CH₂*t*Bu)₃] on CeO₂ for the development
of highly active NH₃-SCR catalysts**

1 Introduction

A significant worldwide increase in stationary thermal power plants and mobile combustion engines culminates with the production of a large amounts of carbon dioxide and nitrogen oxides (NO_x). However, NO_x contribute to ecosystem damage, serious health issues, and worsens the climate changes, through the greenhouse effect, acid rains, and ozone destruction[1]. Therefore, the emission legislation of NO_x has been drastically going down[2,3]. The three-way catalyst system was implemented in the exhaust gas after-treatment systems to meet the stringent harmful emission limits[4]. Yet the diesel exhaust composition brings new challenges in mobilized industries. The most effective and useful method for NO_x removal without compromising the engine performance is the selective catalytic reduction (SCR) assisted by reducing agents[5,6]. Among them, NH₃-SCR leads to high NO_x conversions at low temperatures and in large temperature ranges[7,8].

A wide range of SCR catalysts has been developed[7]. V₂O₅-WO₃(MoO₃)/TiO₂ (TiO₂ supported V₂O₅ associated with WO₃ or MoO₃ materials) has been commercially viable and utilized[7,9]. Though the catalytic activity of this class of materials is acceptable, they suffer however from lots of weaknesses such as the formation of N₂O at high temperature, narrow operation temperature ranges, lack of thermal robustness triggering phase transition of TiO₂ and then may result in the active phase structure destruction at high temperature. Another central environmental issue for the state-of-the-art system is the gradual release of deleterious and toxic V₂O₅, highly volatile species under typical operation temperatures[10]. It has been a non-stop story since then, and several efficient catalysts based on transition metals (W, Nb, Mo, Zr, Ta) and rare earth metals (Ce, Y) have been well described [7]. The most discussed mechanistic pathway for NH₃-SCR involves acidic and redox sites. CeO₂-based catalysts have been extensively studied due to their superior redox properties. However, the surface acidity of CeO₂ is relatively weak, which leads to a low activity when pure CeO₂ is used as catalyst[11]. To improve the catalytic performance of CeO₂-based materials, the easiest way is to introduce another component to promote the acidity and eventually the redox properties. Tungsten has frequently been used as a promoter with CeO₂ and has shown encouraging results[12].

Shan *et al.*[13] prepared CeO₂/TiO₂ and CeO₂-WO₃/TiO₂ catalysts by sol-gel method using ammonium paratungstate, cerium nitrate, and tetrabutyl titanate for NH₃-SCR investigations. The results revealed that the doping of CeO₂/TiO₂ with tungsten enhanced the catalytic

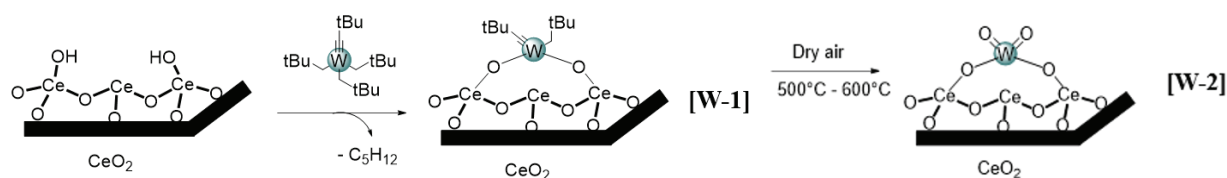
activity. Further characterization showed that the presence of polymeric tungsten oxides favors the formation of Ce^{3+} and offers Brønsted acid sites which were reported to enhance the catalytic activity. The role of tungsten in CeO_2 - WO_x has been elucidated by in-situ IR and Raman for a sample prepared by co-precipitation[14]. It was found that the presence of tungsten can easily activate NH_3 and facilitate the reaction with NO. Moreover, Zhan and co-workers[15] have performed NH_3 -TPD studies on CeO_2 - WO_x and have found that the larger amount of Lewis acidity is beneficial to the targeted reaction. Although no concrete information regarding the reaction mechanism can be withdrawn from previous studies, it has clearly been demonstrated that the presence of Lewis acidity and redox properties is necessary to access highly active NH_3 -SCR catalysts based on tungsten. Recently, a series of tungsten-based catalysts with different loadings has been prepared by impregnation of HPW on ceria and characterized by N_2 physisorption, XRD, FT-IR, Raman and UV-Vis spectroscopies[16]. Evidently, a low tungsten loading (< 4 wt%) resulted in mainly isolated tungsten oxo sites, while higher loadings led to polymeric tungsten oxides. A similar tendency has also been observed in another independent study of WO_3/CeO_2 system[17]. The catalytic performance of the series of catalysts showed that the polymeric tungsten species enhance the activity in the low temperature region (< 300 °C) and the isolated tungsten species is mainly responsible for the catalytic activity at higher temperature (> 450 °C). The increased activity in the low temperature region for the highly loaded sample is believed to be directly related to the Brønsted acidity originated from the polymeric tungsten oxides. The best performing catalyst was identified to be with a 2 wt% tungsten loading and was attributed to a synergetic effect between major surface species, isolated tungsten-oxo (supposed to exhibit high Lewis acidity) and the redox support, ceria. However, the structure of the active species in the latter catalyst remained unidentified at atomic level (monomeric vs oligomeric, bis-oxo vs mono-oxo). Nevertheless, latter works strongly suggested that isolated tungsten species exhibited high activity and may be the active site for NH_3 -SCR, similar to olefin metathesis catalysts[18,19].

Commonly reported catalysts are prepared by uncontrolled impregnation, resulting in different tungsten oxides species, including isolated surface tungsten sites, W_xO_y clusters, amorphous WO_3 , and $Ce_2(WO_4)_3$. However, this complexity in the surface species makes it difficult to identify the active site and draw a structure-activity relationship. In addition, commercial NH_3 -SCR catalysts are loaded with high amounts of WO_3 [20,21], to ensure higher stability and sufficient acidity, thus increasing the NH_3 adsorption strength which improves the activity and the selectivity by inhibiting the oxidation of NH_3 [22]. This

phenomenon is also found in the case of industrial metathesis catalysts, where a high amount of metal such as tungsten, ca. 10 wt%, is required to reach high catalytic activities while only a low fraction of the metal sites is active[23]. Extensive work by Bell and co-workers has successively shown that the optimal tungsten density is 0.6 W/nm²[19], in which tungsten is mainly under the form of isolated mono-oxo site after calcination. Nevertheless, the mono-oxo species exhibited far lower activity in propene metathesis compared to the bis-oxo species, that can be concentrated after a high thermal treatment under an inert atmosphere. The difference in activity is probably due to the facility of propene to coordinate Lewis acidic tungsten with a bis-oxo tetrahedral configuration. This finding is supported by DFT calculation and EXAFS. Hence, the importance of bis-oxo tungsten species in olefin metathesis is related to a facile coordination of the reactant prior to the reaction. Similar phenomenon can be assumed for NH₃-SCR, where the activity can be enhanced if NH₃ can easily coordinate a Lewis acidic site and NO coordinates a redox site. Therefore, the bis-oxo tungsten species immobilized onto ceria will in principle be a promising formulation for a NH₃-SCR catalyst. A powerful approach known as surface organometallic chemistry (SOMC) can be applied to prepare such single-site species. This methodology involves the controlled grafting of a suitable organometallic precursor on a support, thus creating a firmly bonded surface organometallic fragment. Previous studies have shown that catalytic materials prepared through this approach can lead to enhanced activity and facilitate further mechanistic studies[24]. A particular strength of SOMC is the capability to unravel the structure of the active species[25,26] and this can thereby lead to the development of well-defined highly active catalysts that contain only the active site with an overall low metal content[27–31]. To our best knowledge, using the SOMC strategy with a ceria support for the NH₃-SCR reaction is unknown.

In this Chapter, we present a well-controlled surface isolated tungsten species bearing oxo ligands on ceria by grafting the Schrock-type $W(\equiv C tBu)(CH_2 tBu)_3$ complex followed by calcination. The resulting material is characterized by DRIFT, elemental analysis, XPS, Raman, EPR, SSNMR, BET, NH₃-TPD, H₂-TPR, TEM and EXAFS, confirming the single-site nature and its suitability for mechanistic investigations. This strategy provides a general method to fabricate single-site catalysts with relatively low metal loadings and high dispersions. The latter material has been investigated in the selective reduction of NO assisted by NH₃ under typical combustion conditions. In order to situate the activity of the current catalyst, a comparison with the same catalyst formula prepared by conventional aqueous

impregnation has been made. Moreover, the necessity of the ceria support is confirmed. Finally, the Mo analogue has been prepared through SOMC using the same type of precursor and tested for SCR of NO with the aim to reveal the effect of different metal in the same group.



Scheme 1 Illustration of the strategy used for preparing isolated tungsten-oxo species supported on ceria.

2 Preparation and characterization of CeO₂ support

2.1 Preparation of CeO₂ dehydroxylated at 200 °C

Ceria support (CeO₂) is pre-treated by calcination under air in order to remove impurities (such as carbonates), followed by hydration and dehydroxylation steps. The latter process is essential in SOMC allowing to control the density of surface OH groups on the support and the structure of the resulting species after a grafting reaction. Erwan le Roux and his co-workers[32] have shown that dehydroxylation of silica at 200 °C and 700 °C resulted in different OH densities, leading to different surface species. When [W(≡CtBu)(CH₂tBu)₃] is supported on SiO₂₋₂₀₀, the bipodal grafted surfaces species [(≡SiO)₂W(≡CtBu)(CH₂tBu)₃] is obtained, while reaction with SiO₂₋₇₀₀ gives the monopodal species [(≡SiO)W(≡CtBu)(CH₂tBu)₃]. From researches in our laboratory[33] it has been found that the podality has impacts on the electrophilicity and stability of tungsten-oxo species supported onto silica, thus affecting the catalytic activity for olefin metathesis.

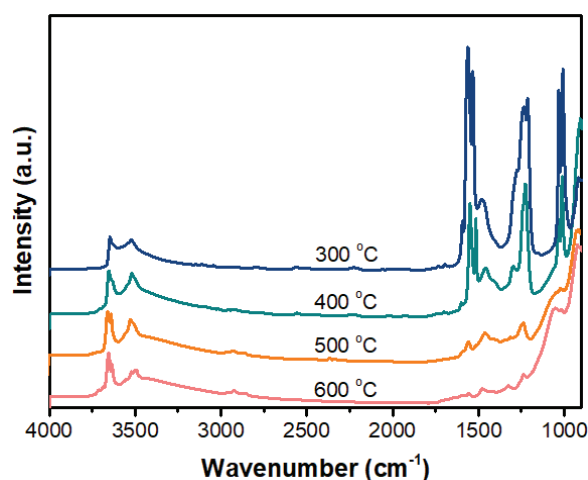


Fig. 1 DRIFT spectra of ceria calcinated at different temperatures for 16 h under a continuous flow of dry air.

Ceria calcined at different temperature was screened in order to determine the necessary pre-treatment conditions to obtain a clean surface (without carbonates) suitable for a well-controlled functionalization. The calcination process at different temperatures (300 - 600 °C) is followed by DRIFT. As depicted in Fig. 1, the DRIFT spectra obtained show the presence of two sets of bands in the 3700-3480 cm^{-1} and 1600-1050 cm^{-1} ranges, attributable respectively to the stretching vibrations of ceria O-H groups and adsorbed carbonates CO_3^- [34]. The intensities of these bands decrease with the rise of the calcination temperature, due to condensation of nearby OH-groups and thermal decomposition of carbonates to CO_2 . For temperatures above 500 °C, the signals of carbonates disappear and some surface OH groups are still preserved.

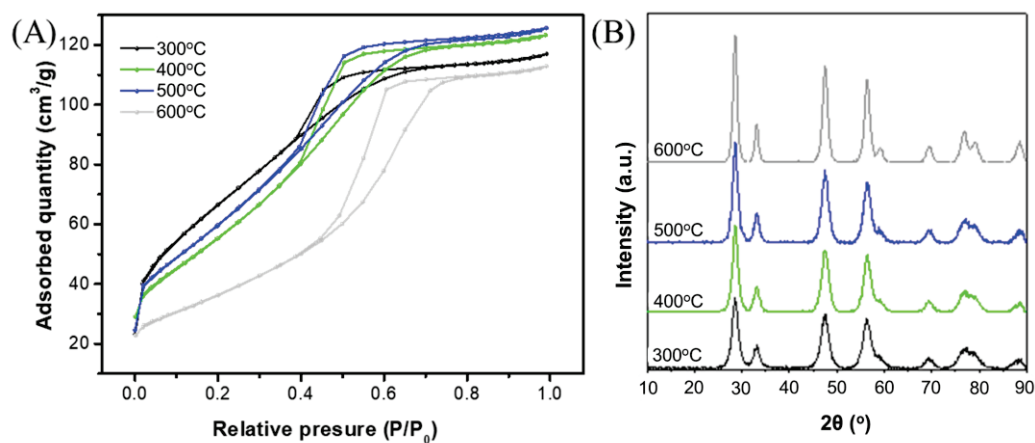


Fig. 2 (A) Evolution of nitrogen physisorption isotherms and (B) Powder X-Ray diffraction of ceria with calcination temperature (300, 400, 500 and 600 °C) for 16 h under a continuous flow of dry air.

The specific surface area of these samples has been also measured. Upon increasing the calcination temperature up to 600 °C, the BET surface area decreases from 247 $\text{m}^2\cdot\text{g}^{-1}$ to 132 $\text{m}^2\cdot\text{g}^{-1}$. As shown in Table 1, the loss of surface area is more pronounced above 500 °C, from 207 $\text{m}^2\cdot\text{g}^{-1}$ to 132 $\text{m}^2\cdot\text{g}^{-1}$. This decrease is attributed to aggregation of ceria crystallites. The X-ray diffraction analyses revealed that the crystalline structure (cubic fluorite)[17,35] is preserved and becomes more crystalline after higher temperature treatments (Fig. 2B). From the diffraction pattern, the mean size of microcrystals can be evaluated by Scherrer's equation[36]. The average crystallite sizes are summarized in Table 1, indicating that the ceria particles tend to agglomerate upon heating. This phenomenon is more accentuated for temperatures higher than 500 °C and can explain the substantial loss of BET surface area at high temperatures. Consequently, the optimal calcination temperature needed to carry out a well-suited surface organometallic chemistry on ceria is 500 °C.

Table 1 Average particle size of ceria samples calcined at various temperatures, estimated from Scherrer's equation

Sample	Calcination temperature	Average particle size ^{a)}	Surface area ^{b)}	BET surface area
CeO ₂₋₃₀₀	300 °C	39 (Å)	214 m ² ·g ⁻¹	247 m ² ·g ⁻¹
CeO ₂₋₄₀₀	400 °C	42 (Å)	198 m ² ·g ⁻¹	226 m ² ·g ⁻¹
CeO ₂₋₅₀₀	500 °C	45 (Å)	173 m ² ·g ⁻¹	207 m ² ·g ⁻¹
CeO ₂₋₆₀₀	600 °C	59 (Å)	140 m ² ·g ⁻¹	132 m ² ·g ⁻¹

^{a)} The average size of the particles was calculated using the following equation (Scherrer's equation):

$$T = \frac{0.9 \times \lambda}{\cos \theta \times \sqrt{H^2 - H'^2}}, \text{ where:}$$

T - the size of the particles (Å)

λ - X-Ray wavelength (Å).

θ - Bragg angle.

H - full width at half maximum (FWHM) of the measured line.

H' - full width at half maximum (FWHM) of the instrument's response.

^{b)} The surface area is calculated assuming that the particles have a perfectly spherical shape, $S = 60000/\rho \times d$ where:

ρ- Specific gravity of ceria (7.215 g·cm⁻³)

d- Particle diameter (Å).

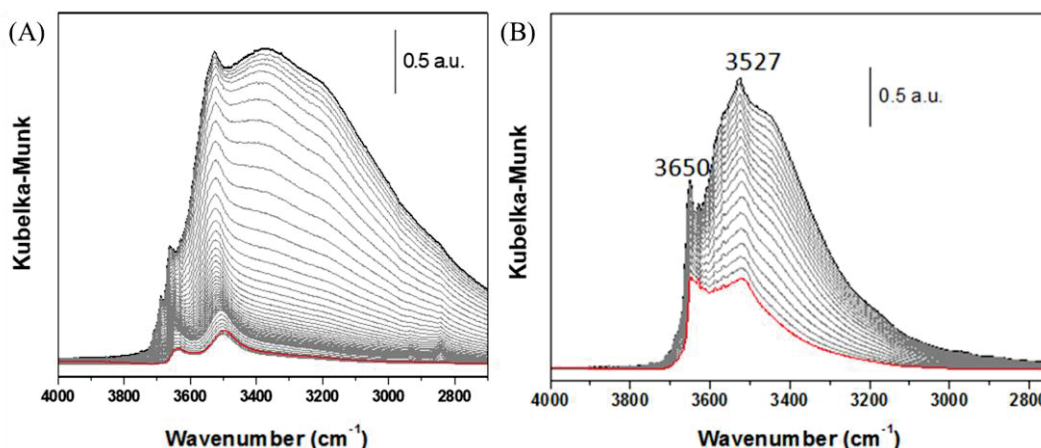


Fig. 3 Temperature-resolved DRIFT spectra of ceria highlighting the ν(O-H) region: (A) dehydroxylation at different temperatures (heating rate: 5 °C/min from 20 – 500 °C). (B) dehydroxylation at 200 °C versus time (heating rate: 5 °C/min from 20 – 200 °C, then 2 hours at 200 °C).

In order to optimize the number of anchoring sites (surface hydroxyl groups), the material calcined at 500 °C is hydrated in the presence of water vapor pressure of and then dehydroxylated. The temperature of the dehydroxylation process is optimized by conducting an operando DRIFT study (Fig. 3). The effect of the dehydroxylation temperature on the nature and the number of surface hydroxyls (anchoring sites) is studied by following the stretching vibration of ν(O-H). The DRIFT study depicted in Fig. 3B shows that the relative intensity of physisorbed water decreased upon increasing temperature. At 200 °C,

physiosorbed water is practically removed and mainly shows the presence of bridged OH groups and minor amount of terminal OH groups. This temperature has therefore been chosen for the dehydroxylation in order to keep a maximum amount of available hydroxyl groups for grafting.

2.2 Characterization of CeO₂₋₂₀₀ by DRIFT spectroscopy

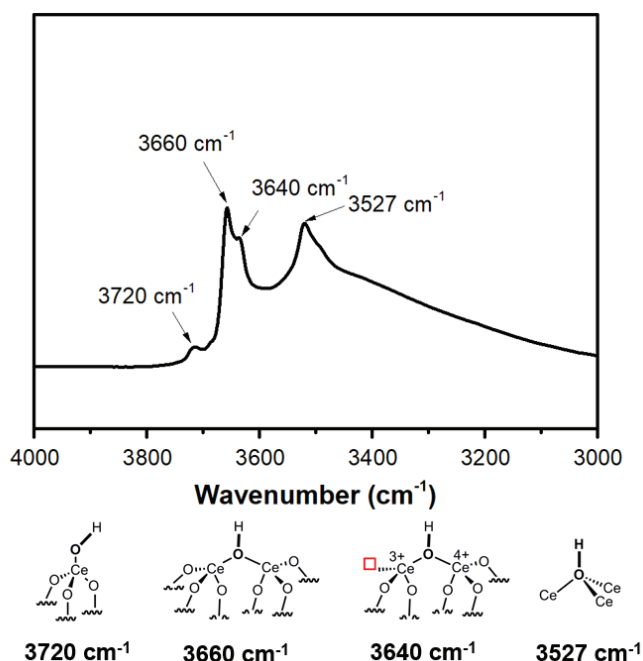


Fig. 4 Attribution of (CeO-H) stretching vibrations according to literature[6,37].

The IR spectrum of ceria dehydroxylated at 200 °C pictured in Fig. 4 shows four ν(O-H) vibration bands which are attributed to different structures of cerium hydroxyl on the surface (terminal and bridging O-H)[6,38]. The intensity of the band at 3720 cm⁻¹ associated with isolated OH groups (μ¹-OH) is weak, and the spectrum is rather dominated by the broad signal centered at 3660 cm⁻¹ with a shoulder at 3640 cm⁻¹, attributed to bridged hydroxyl groups (μ²-OH). The large band centered at 3527 cm⁻¹ is initially attributed to tridentate OH groups (μ³-OH) by Ahmed Badri[37]. Later, the same author proposed that this band is rather due to an inaccessible residual cerium oxy-hydroxide phase located within the pores[6,38]. Such kind of hydroxyl groups have also been reported for a γ-alumina support[39].

2.3 Characterization of OH groups in CeO₂₋₂₀₀ by titration with Al(*i*Bu)₃

To achieve the functionalization of surface hydroxides by a grafting reaction under controlled conditions, it is desirable to know their amount. Among different quantification methods, the

chemical titration using highly reactive $\text{Al}(i\text{Bu})_3$, developed in our laboratory has shown to be reliable[40]. Contrary to conventional Grignard reagents that can trigger alkylation and coupling reactions, $\text{Al}(i\text{Bu})_3$ reacts selectively with hydroxyls groups by a protonolysis followed by a release of isobutane. The titration reaction is monitored by DRIFT spectroscopy (Fig. 5), and it shows that all kinds of available OH groups are consumed. This suggests that all OH-groups including the band centered at 3527 cm^{-1} are accessible and can readily react with $\text{Al}(i\text{Bu})_3$, which suggests that the band centered at 3527 cm^{-1} is associated with the active tridentate OH groups ($\mu^3\text{-OH}$) rather than inert fragments located within the pores.

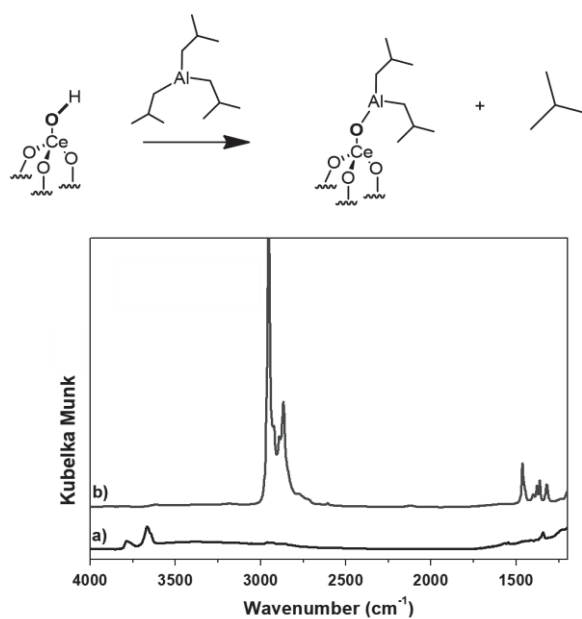


Fig. 5 DRIFT spectra of CeO_{2-200} a) before and b) after the grafting of $\text{Al}(i\text{Bu})_3$ (surface OH titration).

After the reaction of the ceria surface with $\text{Al}(i\text{Bu})_3$ (see the Experiment section), new bands appearing in the $3100\text{-}2850\text{ cm}^{-1}$ and $1620\text{-}1400\text{ cm}^{-1}$ regions (Fig. 5) are characteristic of aliphatic $\nu(\text{CH}_x)$, and $\delta(\text{CH}_x)$ vibrations of the perhydrocarbyl ligands. The ^1H MAS NMR (Fig. 6A) and ^{13}C CP MAS NMR (Fig. 6B) spectra of $\text{Al}(i\text{Bu})_3/\text{CeO}_{2-200}$ show broad signals. Moreover, the observed chemical shifts have significantly shifted with respect to the molecular precursor, consistent with the presence of paramagnetism. Combined with the results from DRIFT, these signals are assigned to the presence of an isobutyl group, which indicates the successful grafting. Noteworthy, all the $\nu(\text{CeO-H})$ bands between $4000\text{-}3500\text{ cm}^{-1}$ disappeared, confirming that all the OH groups are consumed by reaction with $\text{Al}(i\text{Bu})_3$. This latter, diluted in pentane, reacts quantitatively with surface hydroxyl groups by releasing one equivalent of isobutane per OH group (Fig. 5). The quantification of the released isobutane by GC shows that CeO_{2-200} contains $0.7\text{ mmol OH}\cdot\text{g}^{-1}$ ($2.2\text{ site}/\text{nm}^2$).

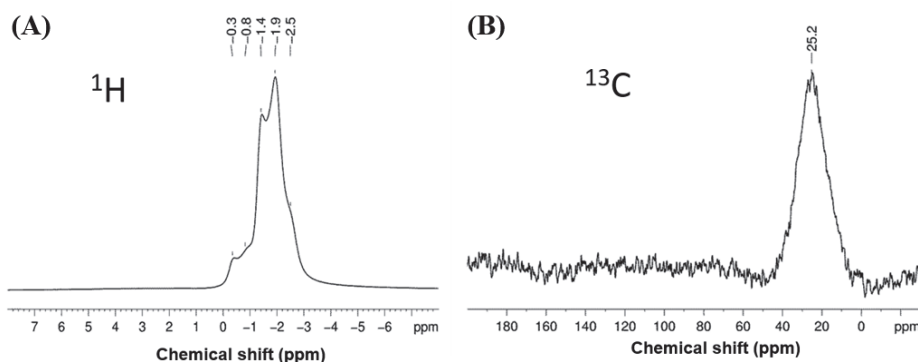


Fig. 6 (A) ^1H MAS and (B) ^{13}C CP MAS NMR spectra of $\text{Al}(i\text{Bu})_3/\text{CeO}_2\text{-200}$

2.4 Characterization of $\text{CeO}_2\text{-200}$ by solid state NMR

To achieve more insights about OH groups on CeO_2 support, ^1H and ^{17}O MAS NMR are conducted with CeO_2 enriched with ^{17}O prepared from ^{17}O labeled water through hydration and dehydroxylation at $200\text{ }^\circ\text{C}$. The results are shown in Fig. 7A. The ^1H MAS NMR spectrum of CeO_2 shows 3 major features: i) weak but resolved peaks around 1.4 ppm; ii) a large resonance at 5.0 ppm; iii) a broad signal at 6.6 ppm. In the literature, only few solid state ^1H NMR studies on CeO_2 have been published[41,42]. Gill and co-workers[41] have studied the evolution of water desorption on CeO_2 nano-cubes with low surface area ($S_{\text{BET}} = 17\text{ m}^2/\text{g}$) in function of temperature. Water adsorbed on ceria is characterized by a peak around 5 ppm. After treatment at $200\text{ }^\circ\text{C}$, no water is observed on the surface and the spectrum shows only two weak peaks at 8 and 3 ppm, assigned to hydroxyl groups without further precision[41]. A more recent work by Chen *et al.*[42] also shows that physisorbed water on CeO_2 nano-rods ($S_{\text{BET}} = 110\text{ m}^2/\text{g}$) leads to a peak at 5 ppm in the ^1H NMR spectrum. Interestingly, CeO_2 nano-rods with higher surface area exhibit two signals around 1.6 ppm and 8.4 ppm after drying. Those peaks are attributed (by DFT calculation on CeO_2 (111) surface model) to terminal and bridged OH-groups on CeO_2 . Combining the latter findings with DRIFT spectrum (Fig. 4), the weak and resolved peaks around 1.5 ppm are attributed to terminal OH groups ($\nu(\mu^1\text{-OH}) = 3720\text{ cm}^{-1}$) with a slightly different environment. The most intense signal is located at 5.0 ppm. Such chemical shift has previously been assigned to physisorbed water on ceria[41,42]. Nevertheless, DRIFT data (Fig. 4) of this sample suggests the absence of water. In addition, physisorbed water (^{17}O labelled) on ceria gives a characteristic peak at 32 ppm in the ^{17}O NMR spectrum[43], which is absent in our case (Fig. 7B). Thus, the signal at 5.0 ppm is tentatively assigned to $\mu^2\text{-OH}$ ($\nu(\mu^2\text{-OH}) = 3660\text{ cm}^{-1}$ and 3640 cm^{-1} in DRIFT).

This peak is somewhat shifted to higher fields with respect to the calculated value for bridged hydroxyl groups on CeO₂ (111) and may be due to the presence of para magnetism in the sample (confirmed by XPS, *vide infra*). Consequently, the last peak at 6.6 ppm is ambitiously attributed to μ^3 -OH, based on the intensity distribution observed by DRIFT.

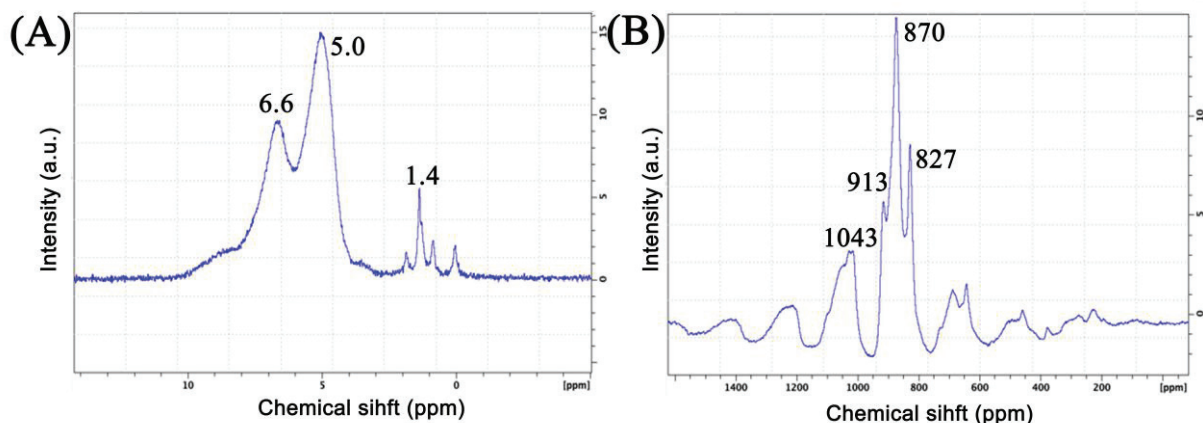


Fig. 7 (A) ¹H MAS NMR and (B) ¹⁷O MAS NMR spectra of CeO₂ enriched in ¹⁷O and dehydroxylated at 200 °C.

For in depth understanding of the ceria support, CeO₂ enriched in ¹⁷O has been prepared by hydration of the calcined sample by 90% ¹⁷O labelled water followed by dehydroxylation at 200 °C. This procedure has been frequently applied[44], and has particularly shown success to selectively enrich surface silanol in silica[45]. The ¹⁷O MAS NMR spectrum of this labelled sample, collected with a high field spectrometer (800 MHz) shows main peaks centered at 870 ppm (Fig. 7B), attributed to O in bulk ceria. The less intense, but well-resolved peaks at 1043 ppm, 913 ppm, and 827 ppm are related to surface and subsurface oxygen sites[43,46] or other defect sites (for example, sites near oxygen vacancies)[43]. Signals between 200-300 ppm are typically assigned to bridged OH groups[47]. The terminal OH group, μ^1 -OH, expected to appear around 70 ppm[47] is not visible in the present case, probably due to a relatively small amount of this species (indicated by DRIFT and ¹H MAS NMR) and the extremely high mobility of oxygen. The fact that the main peak in the ¹⁷O MAS NMR spectrum belongs to bulk oxygen strongly suggests that the oxygen atoms of the ¹⁷O enriched surface hydroxyl groups are extremely mobile and can readily migrate into the bulk structure of ceria during the dehydroxylation process at 200 °C.

2.5 Characterization of CeO₂₋₂₀₀ by XPS spectroscopy

X-Ray photoelectronic spectroscopy is used to characterize the elemental composition and the corresponding electronic states of Ce and O in dehydroxylated CeO₂. Due to the pairs of spin

orbit doublet, ten features are usually found in the Ce 3d region. Ce ion should not be considered as a pure Ce⁴⁺, but a mixture of Ce⁴⁺ and Ce³⁺ which mixes with a 4f Lⁿ⁻¹ configuration due to the similar energies of 4f and orbital ligand valence level[48]. As presented in Fig. 8A, three peaks labelled v (882.3 eV), v'' (888.8 eV), v''' (898.1 eV) in green line are attributed to 3d_{5/2} of Ce⁴⁺ and peaks u (900.8 eV), u'' (908.3 eV), u''' (916.7 eV) in blue line are assigned to 3d_{3/2} of Ce⁴⁺. The other 4 peaks v₀, v', u₀, u' in orange line which appeared at 881.4 eV, 884.3 eV, 898.7 eV and 902.3 eV respectively, belongs to the contribution of Ce³⁺. Thus, the co-existence of Ce³⁺ and Ce⁴⁺ is evidenced, and the proportion of Ce³⁺ in CeO₂ is calculated to be 20.6% according to the formula (Ce³⁺ % = Ce³⁺ / (Ce⁴⁺ + Ce³⁺)). The O 1s spectrum for CeO₂₋₂₀₀ is presented in Fig. 8B. The O 1s peak could be split into two contributions: 529.0 eV and 530.3 eV, which are attributed to surface oxygen (denoted as O_α) and lattice oxygen in bulk ceria (denoted as O_β). The ratio O_α/(O_α+ O_β) for CeO₂₋₂₀₀ is estimated to be 19.1%.

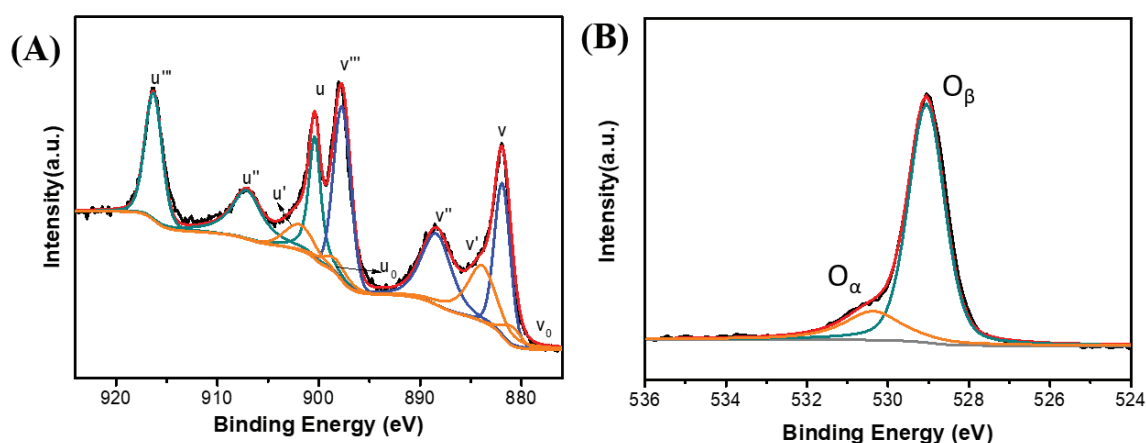


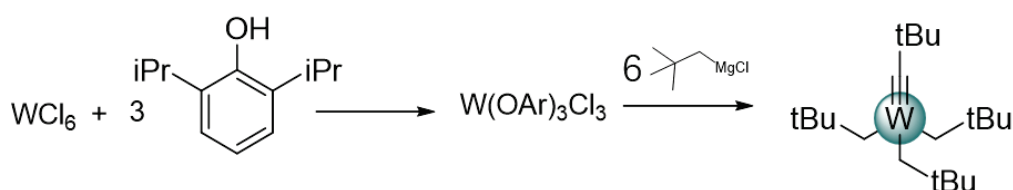
Fig. 8 (A) Ce 3d and (B) O 1s XPS spectra of CeO₂₋₂₀₀.

In summary, a series of experiments allows to determine the desired pre-treatment conditions, being calcination at 500 °C, followed by hydration and dehydroxylation at 200 °C, affording a water-free surface with substantial amounts of hydroxyl groups suitable for grafting. The resulting material is further characterized by XRD, BET, DRIFT, XPS, and solid state NMR (¹H and ¹⁷O), revealing a relatively high surface area containing different hydroxyls group (μ^1 -OH, μ^2 -OH, and μ^3 -OH). Attribution of the different hydroxyl groups has tentatively been made inspired by literature data. Among the published results, there are significant inconsistencies regarding the assignment of OH-groups. A reasonable explanation is that the spectroscopic features (IR, NMR) of OH-groups are dependent on the nature of ceria (nano

materials, textural properties, crystallinity) and the dominating crystalline face exposed to the surface. Such a complex surface with different OH-groups is expected to exhibit different reactivity towards a selected organometallic precursor upon grafting. Herein, $W(\equiv C tBu)(CH_2 tBu)_3$ has been selected as precursor to functionalize ceria with tungsten. The grafting of $W(\equiv C tBu)(CH_2 tBu)_3$ is expected to occur through a protonolysis reaction.

3 Preparation and characterization of $W(\equiv C tBu)(CH_2 tBu)_3$ supported on CeO_{2-200}

3.1 Preparation of $[W(\equiv C tBu)(CH_2 tBu)_3]/CeO_{2-200}$ [W-a]



Scheme 2 Schematic illustration of the synthesis process of $W(\equiv C tBu)(CH_2 tBu)_3$

$W(\equiv C tBu)(CH_2 tBu)_3$ is synthesized according to the procedure in [Scheme 2](#), which is described in detail in the experimental section. The first step consists of the reaction between 2,6-diisopropylphenol and WCl_6 in toluene at room temperature leading to $W(OAr)_3Cl_3$ (Ar=2,6 diisopropylphenyl) in a good yield of 90%. This intermediate is characterized by NMR (1H and ^{13}C) in solution in C_6D_6 . This complex, $W(OAr)_3Cl_3$, reacted with 6 equivalent of $NpMgCl$ in Et_2O at room temperature, allowing to obtain the tungsten carbyne $W(\equiv C tBu)(CH_2 tBu)_3$ in 50% yield after sublimation. This complex is characterized by NMR (1H and ^{13}C , solution in C_6D_6), as shown in [Fig. 9](#).

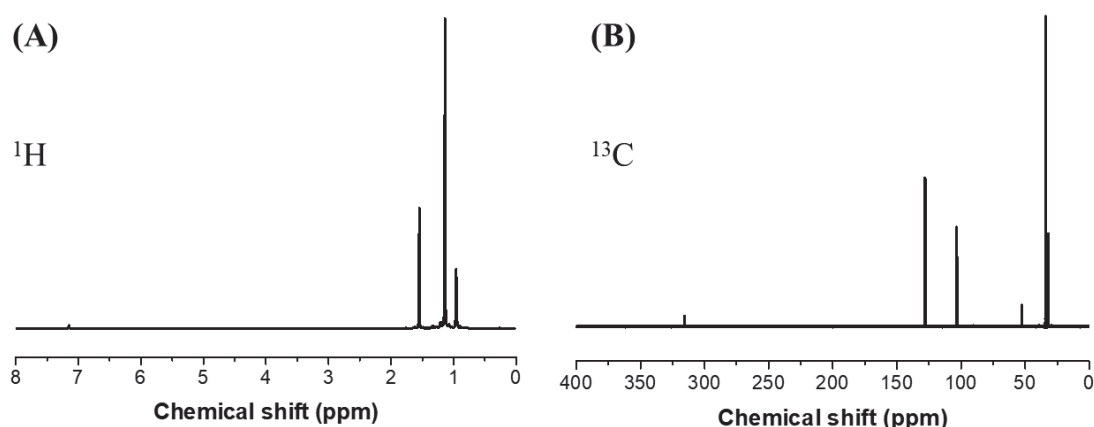
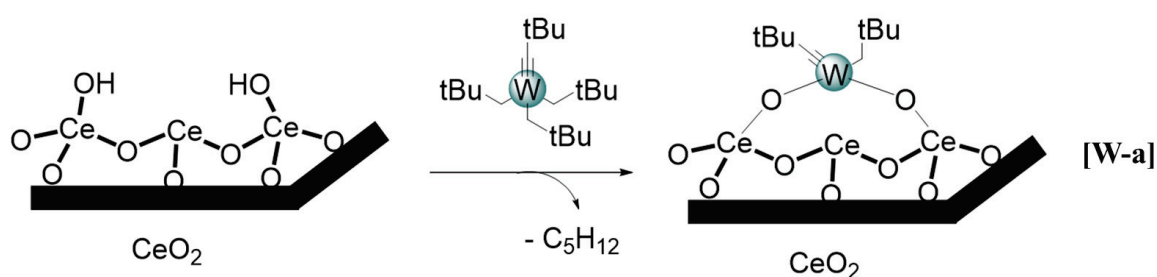


Fig. 9 (A) 1H and (B) ^{13}C $\{^1H\}$ of $W(\equiv C tBu)(CH_2 tBu)_3$

The grafting reaction of $[W(\equiv CtBu)(CH_2tBu)_3]$ on CeO_{2-200} is carried out in pentane at room temperature during 12 h. The resulting materials are washed three times with pentane via filtration to remove all the unreacted complex $[W(\equiv CtBu)(CH_2tBu)_3]$. After evaporation of the solvent, the supported tungsten complex, $[W(\equiv CtBu)(CH_2tBu)_3]/CeO_{2-200}$, **[W-a]**, is isolated as a grey powder after drying under vacuum and then characterized by Elemental analysis, Nitrogen adsorption-desorption isotherm measurements, DRIFT, SSMASNMR, XPS, EPR, EXAFS, TEM.

3.2 Characterization of **[W-a]** by Mass balance analysis

Elemental analysis of **[W-a]** shows the presence of 3.30 wt% W, which correspond to ca. 0.18 mmolW.g⁻¹. The evaluation of the amount of carbon reveals the presence of 2.16 wt% C (1.79 mmolC.g⁻¹), which gives a C/W ratio of 9.95. Furthermore, a quantitative GC analysis of the gas released during the grafting process, shows the formation of 0.38 mmol of neopentane which corresponds to 1.9 *t*BuCH₃ per W. This should correspond to a partial consumption of surface hydroxyls (ca. 55 % of the initial surface O-H groups compared with the number of surface hydroxyls calculated from a chemical titration using Al(*i*Bu)₃). Overall, the data are consistent with the formation of bipodal surface species bearing two ligands, by protonolysis with surface hydroxyls leading to a concomitant release of ca. two neopentane per tungsten atom grafted, as highlighted in [Scheme 3](#).



Scheme 3 Schematic illustration of the grafting of $W(\equiv CtBu)(CH_2tBu)_3$ on CeO_{2-200} .

3.3 Characterization of **[W-a]** by DRIFT spectroscopy

The grafting reaction is monitored by DRIFT spectroscopy ([Fig. 10](#)). We observed that the peak at 3720 cm⁻¹ assigned to terminal $\nu(CeO-H)$ disappears, which suggests that it is consumed during the reaction. The details of the (O-H) region is highlighted in [Fig. 10B](#), showing partial consumed OH groups, including the terminal μ^1-OH and bridged μ^2-OH . On the other hand, the peak at 3527 cm⁻¹, attributed to bridged μ^3-OH is preserved during the

grafting progress. This phenomenon indicates that protonolysis of $[\text{W}(\equiv\text{CtBu})(\text{CH}_2\text{tBu})_3]$ with surface hydroxyls on ceria occurs completely on terminal OH groups, which is similar to the reaction between $\text{W}(\equiv\text{CtBu})(\text{CH}_2\text{tBu})_3$ and alumina dehydroxylated at 500 °C where only terminal tetrahedral Al-OH sites is reacted completely[49]. As elemental analysis suggests that the grafted surface species comprises a bipodal attachment, it is reasonable to believe that the initial protonolysis occurs on terminal hydroxyl groups. Moreover, the surface tungsten species may readily react with a bridged hydroxyl group in proximity to form the proposed structure, resulting in a partial consumption of the less reactive bridged μ^2 -OH. In addition, after the surface functionalization of ceria with $\text{W}(\equiv\text{CtBu})(\text{CH}_2\text{tBu})_3$, the new bands appearing in the 3100-2850 cm^{-1} and 1620-1400 cm^{-1} ranges are characteristic of aliphatic $\nu(\text{CH})$, $\delta(\text{CH}_2)$ and $\delta(\text{CH}_3)$ vibrations of the perhydrocarbyl ligands bonded to surface tungsten. Noteworthy, a band at 2120 cm^{-1} , which is absent in the neat ceria sample (line a in Fig. 10A) is observed in [W-a] (line b in Fig. 10A). This signal has already been found and ascribed to the forbidden $2\text{F}_{5/2} \rightarrow 2\text{F}_{7/2}$ electronic transition of the subsurface Ce^{3+} (due to the partial reduction of ceria)[50].

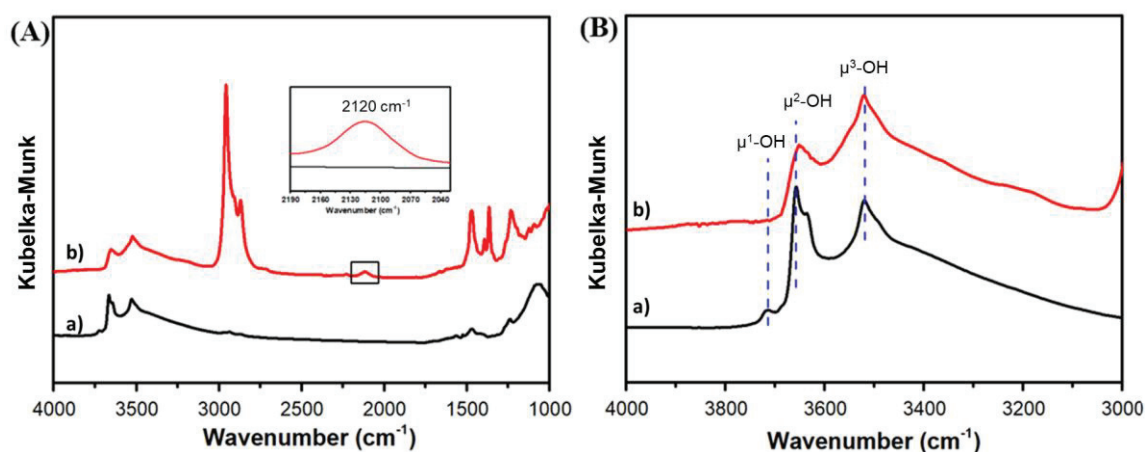


Fig. 10 (A) (4000-1000 cm^{-1}) DRIFT spectra and (B) specific attribution of (O-H) stretching vibration bands of a) CeO_{2-200} and b) [W-a].

3.4 Characterization of [W-a] by Nitrogen adsorption-desorption isotherm measurements

The textural properties of CeO_{2-200} and [W-a] are examined by nitrogen adsorption-desorption isotherm measurements. The physisorption isotherms and the pore size distribution are depicted in Fig. 11. As shown, the shape of these material isotherms corresponds to type IV according to IUPAC classification and show an H2 type hysteresis loop (characteristic of

capillary condensation between the aggregates constituting the solid)[51]. The initial increase in adsorption capacity at low relative pressure is due to a monolayer adsorption. The upward deviation in the range of $P/P_0 = 0.5 - 0.7$ for the support and the catalyst is associated with the progressive filling of space between the aggregates of particles. The dehydroxylated ceria has a specific surface area of $ca. 188 \pm 10 \text{ m}^2 \cdot \text{g}^{-1}$. The surface area was slightly decreased upon functionalization with the transition metal complex by reducing the value to $166 \pm 10 \text{ m}^2 \cdot \text{g}^{-1}$. The pore volumes also decreased from 0.24 ± 0.01 to $0.21 \pm 0.01 \text{ cm}^3 \cdot \text{g}^{-1}$.

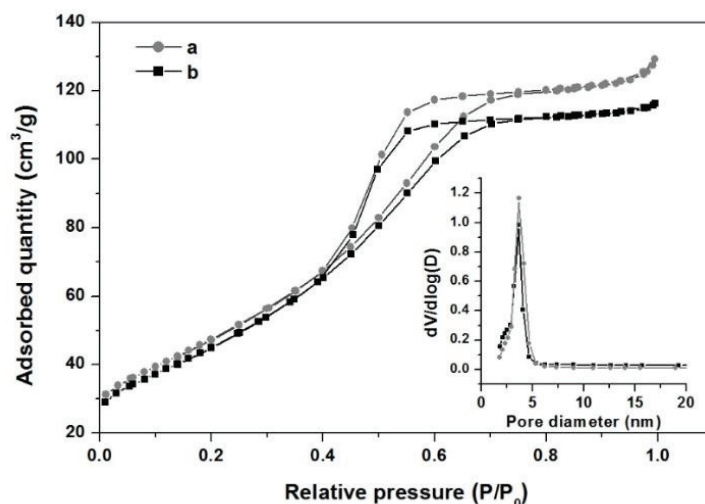


Fig. 11 Nitrogen physisorption isotherms and corresponding pore size distribution (inset) of (a) CeO_{2-200} and (b) [W-a]

3.5 Characterization of [W-a] by solid state MAS NMR

^1H MAS NMR spectrum of the resulting material [W-a], depicted in Fig. 12A, shows large signals at -3 and 0.1 ppm, tentatively attributed to the methyl of neopentyl and neopentylidyne ligands, respectively. A significant shift (with respect to the pure complex, Fig. 6) and a broadening of the signals are due to the presence of paramagnetic species (Ce^{3+})[42,52]. In addition, a 30% ^{13}C labeled molecular complex $[\text{W}(\equiv^*\text{C}t\text{Bu})(^*\text{CH}_2t\text{Bu})_3]$ [53] grafted onto ceria dehydroxylated at 200 °C is employed in order to extract useful information in the ^{13}C CP MAS NMR analysis. Fig. 12B shows the latter result and displays an intense and broad signal centered at 26 ppm assigned to the methyl of the *t*-Bu fragments and a broad, albeit weak-signal at 80 ppm, which can be assigned to the methylene carbons of the neopentyl fragment (CH_2tBu). A weak signal at 287 ppm can be ambitiously attributed to the quaternary carbons of carbyne ligands. Compared to the signals of molecular complex in Fig.9, all the observed resonances of grafting material are shifted to higher fields (also observed in ^1H

MAS NMR) with a notable broadness and are presumably due to paramagnetic Ce^{3+} ions in trigonal and cubic sites present in the ceria support as already identified[42,52].

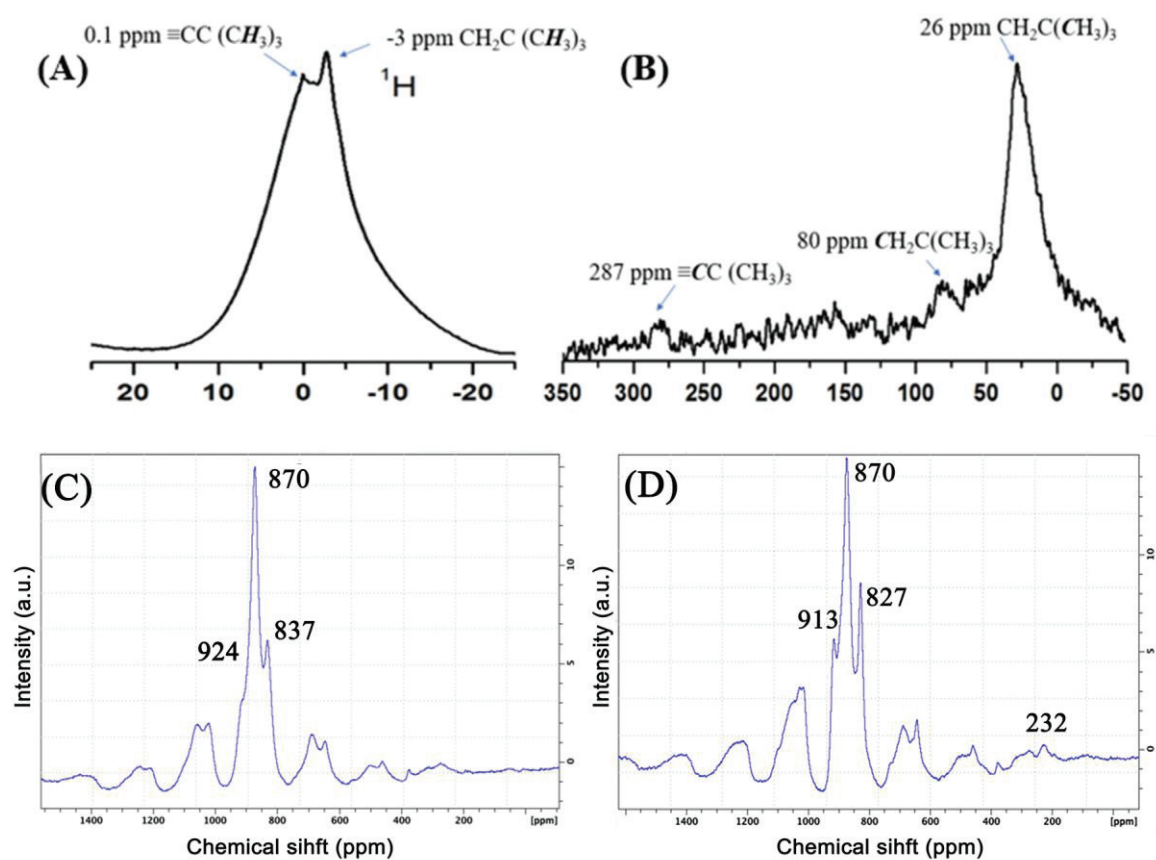


Fig. 12 (A) ^1H MAS and (B) ^{13}C CP MAS NMR spectra of $\text{W}(\equiv\text{CtBu})(\text{CH}_2\text{tBu})_3/\text{CeO}_2\text{-200}$; ^{17}O MAS NMR spectra of (C) $\text{W}(\equiv\text{CtBu})(\text{CH}_2\text{tBu})_3/\text{CeO}_2\text{-200}$ and (D) CeO_2 enriched in ^{17}O .

^{17}O solid state MAS NMR is a powerful approach to characterize the local structure of inorganic metal oxides and provides details of metal-support interactions in heterogeneous catalysts after selective surface labeling[45,47]. Previous research in our laboratory has successfully created a surface ^{17}O silanol enriched silica ($\text{SiO}_2\text{-200}$ and $\text{SiO}_2\text{-700}$ labeled with ^{17}O on the surface) and used as support to host diamagnetic organometallic fragments ($[\text{Zr}(\text{CH}_2\text{tBu})_4]$ and $[\text{W}(\equiv\text{CtBu})(\text{CH}_2\text{tBu})_3]$). It appeared in this work that ^{17}O NMR is powerful to probe the local structure in various oxygen environments: silanols, siloxanes, and metal-bound siloxides[45]. ^{17}O NMR has been shown to be extremely sensitive to CeO_2 , where it can distinguish oxygen in the first and second surface layers from the bulk[43,46]. We prepare an ^{17}O labeled ceria with H_2^{17}O as used for silica with the aim to enhance the understanding for surface Ce-OH groups and its reactivity with $[\text{W}(\equiv\text{CtBu})(\text{CH}_2\text{tBu})_3]$. Unfortunately, as described in section 2.4, such treatment results in diffusion of the surface

exchange ^{17}O into the bulk material. Nevertheless, some information can be extracted from the ^{17}O MAS NMR spectrum upon grafting of $[\text{W}(\equiv\text{C}t\text{Bu})(\text{CH}_2t\text{Bu})_3]$ on labeled CeO_2 (Fig. 12). The major signal at 870 ppm has previously been attributed to bulk ceria. Furthermore, resolved peaks at 914 ppm and 827 ppm, related to surface and subsurface sites[46] are still observed with insignificant shifts with respect to pure ceria. Noteworthy, the small peak at 232 ppm in CeO_2 attributed to bridged $\mu^2\text{-OH}$ groups is not presented in **[W-a]**, consistently with the consumption of these OH groups during the grafting process. The same behavior is also observed by DRIFT.

3.6 Characterization of **[W-a]** by X-ray diffraction analysis

The X-ray diffraction analyses before and after grafting are shown in Fig. 13, and reveals that both samples exhibit the same diffraction peaks at 28.5° , 33.1° , 47.5° , 56.4° , 59.1° , 69.7° , and 79.1° characteristic of the cubic fluorite structure of CeO_2 [49,51]. This observation suggests that the functionalization did not affect the crystalline structure of ceria. From the diffraction pattern, the mean size of microcrystals can be evaluated from Scherrer's equation. The average crystal sizes consequently estimated are as summarized in Table 2. It seems that the ceria particles have a tendency to agglomerate during the grafting of $[\text{W}(\equiv\text{C}t\text{Bu})(\text{CH}_2t\text{Bu})_3]$, which corroborates the marginal reduction in the surface area.

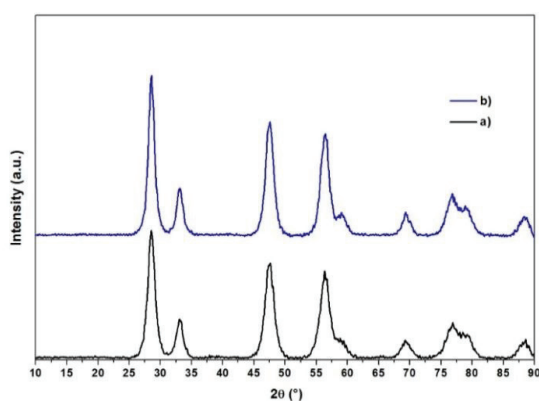


Fig. 13 Powder X-Ray diffraction of (a) CeO_{2-200} and (b) **[W-a]**.

Table 2 Average particle size of CeO_{2-200} and **[W-a]** (estimated measured using Scherrer's equation)

Sample	Average particle size ^{a)}	Surface area ^{b)}	BET
CeO_{2-200}	45 (Å)	173 $\text{m}^2\cdot\text{g}^{-1}$	188 $\text{m}^2\cdot\text{g}^{-1}$
[W-a]	52 (Å)	155 $\text{m}^2\cdot\text{g}^{-1}$	166 $\text{m}^2\cdot\text{g}^{-1}$

^{a)}The average size of the particles was calculated using the following equation (Scherrer's equation):

$$T = \frac{0.9 \times \lambda}{\cos \theta \times \sqrt{H^2 - H'^2}}, \text{ where:}$$

T – the size of the particles (Å)

λ – X-Ray wavelength (Å).

Θ – Bragg angle.
 H – full width at half maximum (FWHM) of the measured line.
 H' – full width at half maximum (FWHM) of the instrument's response.

^{b)} The surface area is calculated assuming that the particles have a perfectly spherical shape, $S = 60000/\rho \times d$ where:
 ρ - Specific gravity of ceria (7.215 g.cm⁻³)
 d- Particle diameter (Å).

3.7 Characterization of [W-a] by X-ray photoelectron spectroscopy analysis and Electron paramagnetic resonance

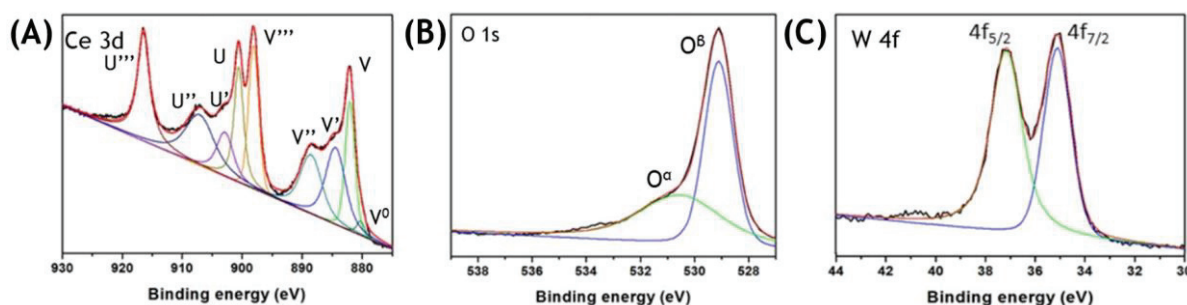


Fig. 14 XPS spectra of [W-a]: (a) Ce 3d, (b) O 1s, (c) W 4f.

X-ray photoelectron spectroscopy (XPS) analyses are carried out in order to provide more information on the oxidation state of the constituent elements in the sample: (W, Ce, O). Fig. 14 shows the representative XPS spectra for the Ce 3d, O 1s, and W 4f. The total fraction of Ce³⁺ is estimated by taking the fitted Ce³⁺ peaks areas to the total deconvolved spectra ($\%Ce^{3+} = (Ce^{3+}/(Ce^{4+} + Ce^{3+}))$)[54]. After the grafting of the organometallic complex [W(\equiv C*t*Bu)(CH₂*t*Bu)₃], the ratio of Ce³⁺ is 34% which is higher than that of CeO₂₋₂₀₀(20.6% in section 2.5). It is widely reported that the concomitant presence of Ce³⁺ and Ce⁴⁺ offers an oxygen-buffering capacity and redox properties that can promote NO_x dissociation[53,55]. The O 1s spectra is described by a large peak at 531 eV and a shoulder at 532.5 eV, assigned to lattice oxygen of CeO₂ (denoted O_β)[56] and surface oxygen (denoted as O_α) such as oxygen in defect-oxide CeO_{2-x} or hydroxyl group[13]. The relative amounts of calculated O_α ($\%O_{\alpha} = O_{\alpha}/(O_{\alpha} + O_{\beta})$) is estimated as 37%. Compared to the CeO₂₋₂₀₀(19.1% in section 2.5), more surface oxygen may promote the oxidation of NO to NO₂, inducing the “Fast SCR”, and resulting in a higher overall SCR catalytic activity[56]. Simultaneously, it can also promote the high-temperature oxidation of NH₃ and affect the selectivity[57]. Thus, an optimal amount of O_α is desirable in order to increase the reaction rate[58].

XPS analysis is also used to investigate the oxidation state of supported tungsten. The W 4f signal is depicted in Fig. 14e. It shows the presence of two signals attributable to W 4f_{5/2} and W 4f_{7/2} at 37.5 and 35.3 eV respectively, after deconvolution. These values are characteristic

of W(VI) for the grafted complex. Indeed, the W 4f peaks overlap with the Ce 5s peaks, as shown in Fig. 14f and may cause discrepancies for the curve deconvolution. Nevertheless, these results are consistent with the presence of W(VI), but may contain marginal structural heterogeneities. Electron paramagnetic resonance (EPR) spectroscopy of the [W-a] material (Fig. 15) did not show any signal of isolated W(V) ions expected with a g factor between 1.84 and 1.51[59]. This supports the XPS findings that all tungsten atoms are present in the oxidation state of W(VI).

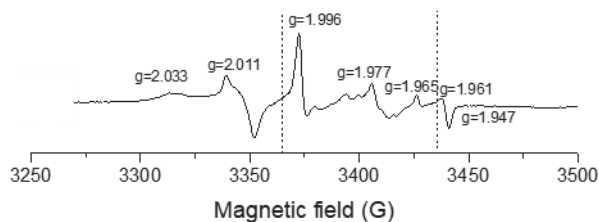


Fig. 15 EPR spectra of [W-a] recorded at room temperature with a microwave power of 1.6 mW.

3.8 Characterization of [W-a] by X-ray absorption spectroscopy

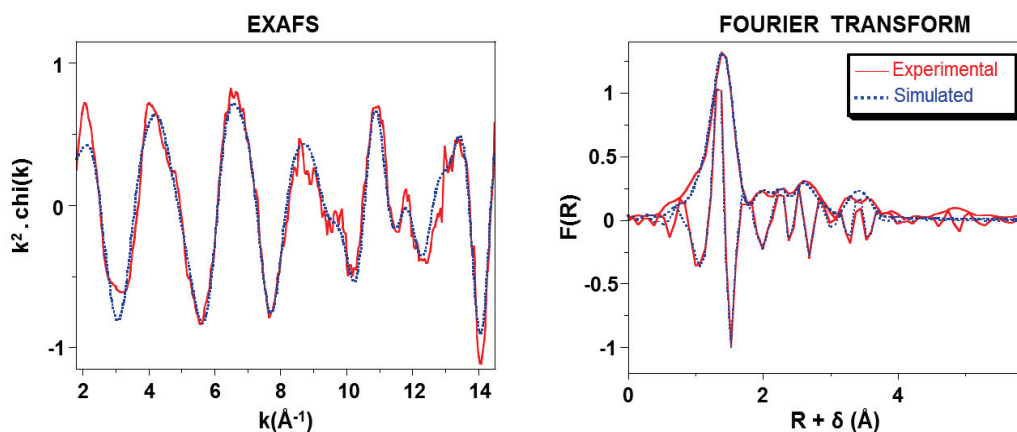


Fig. 16 W L_{III} -edge k^2 -weighted EXAFS (left) and its Fourier transform (right, modulus and imaginary part of the FT) for [W-a]. Solid lines: experimental; dashed lines: spherical wave theory.

Table 3 EXAFS parameters for [W-a]. The errors generated by the EXAFS fitting program “Round Midnight” are indicated between parentheses.

Type of Neighbor	Number of Neighbors	Distance (Å)	σ^2 (Å ²)
W≡CCMe ₃	1.1(2)	1.78(1)	0.0011(6)
W-O _{ce}	1.9(3)	1.78 ^(b)	0.0011 ^(b)
W-CH ₂ CMe ₃	1.0(2)	2.26(3)	0.0011 ^(b)
W-Q(Ce)	1.9(5)	2.69(2)	0.0015(10)
W-Q(Ce)	3.0(8)	2.94(3)	0.0015 ^(b)
W≡CCMe ₃	1.1 ^(b)	3.25(6)	0.0015 ^(b)
W-OCe	1.0(4)	3.57(3)	0.0015 ^(b)

Δk : [1.8 – 14.5 Å⁻¹] – ΔR : [0.5-4.0 Å]; $S_0^2 = 0.94$; $\Delta E_0 = 4.7 \pm 1.2$ eV (the same for all shells); Fit residue: $\rho = 5.6$ %; Quality factor: $(\Delta\chi)^2/\nu = 2.36$ ($\nu = 15/30$). (b) Shell constrained to a parameter above.

[W-a] is studied by X-ray absorption spectroscopy (Fig. 16 and Table 3), in order to shed light on the structure of the supported species. For the first peak of the Fourier transform (right in Fig. 16), two levels of coordinated light atom back-scatterers can be evidenced at ca. 1.78 Å and 2.25 Å. Considering the level at 1.78 Å, two types of atoms, O and C are considered: oxygen coming from the ceria surface and carbon from a carbyne ligand. The parameters thus extracted from the fit of the EXAFS signal are in agreement with a bipodal structure, $(\equiv\text{Ce}-\text{O})_2\text{W}(\equiv\text{C}t\text{Bu})(\text{CH}_2t\text{Bu})_3$, with ca. two oxygen atoms at 1.78(1) Å, ca. one carbon atom at 1.78(1) Å, and another one at 2.25(3) Å, attributed most probably to carbon atoms of neopentylidyne and neopentyl ligands respectively. The W-O distance seems marginally short but tungsten has been found to be surrounded by around six oxygen atoms at 1.787(1) Å in a $\text{W}_{0.2}\text{Ce}_{0.8}\text{O}_2$ mixed metal oxide[60]. Moreover, the two carbon back-scatterers are located at distances in the range of $\text{W}\equiv\text{C}$ and $\text{W}-\text{C}$ triple and single bonds respectively, as observed for $[\text{W}(\equiv\text{CCMe}_3)(=\text{CHCMe}_3)(\text{CH}_2\text{CMe}_3)(\text{dmpe})]$ molecular complex (1.785(8) Å for $\text{W}\equiv\text{C}t\text{Bu}$ and 2.258(9) Å for $\text{W}-\text{CH}_2t\text{Bu}$)[61]. Similar parameters are obtained when fitting the $k^3\chi(k)$ spectrum. The fit can be also improved by adding further layers of back-scatters, in particular two types of oxygen atoms at 2.69(2) and 2.94(2) Å and only around one cerium atom at 3.57(3) Å. The inclusion of tungsten as a second neighbor is not statistically validated. Therefore, this EXAFS study suggests a single-site structure $[(\equiv\text{Ce}-\text{O})_2\text{W}(\equiv\text{C}t\text{Bu})(\text{CH}_2t\text{Bu})]$, as the one represented in Fig. 17, where the tungsten atom is in a pseudo-octahedral environment, can be tentatively proposed (in the cerium oxide crystal[62], the Ce-O bond distance is ca. 2.34 Å and the shortest Ce-Ce distance is ca. 3.83 Å).

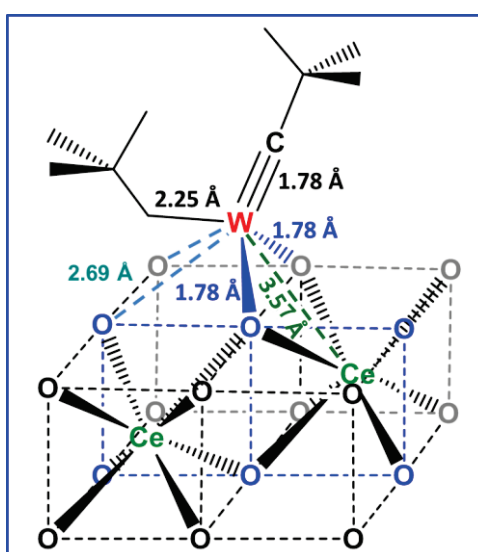


Fig. 17 Proposed structure for [W-a].

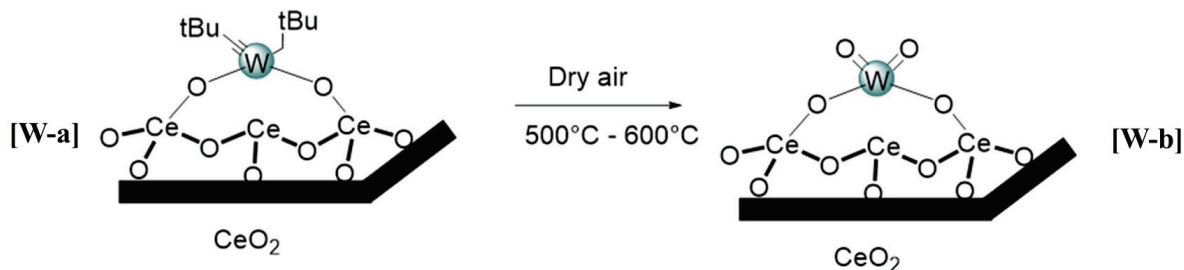
In summary, $[W(\equiv C*t*Bu)(CH_2*t*Bu)_3]$ has successfully been grafted on ceria dehydroxylated at 200 °C. Combination of different techniques, such as mass balance analysis, BET, DRIFT, solid state NMR, XPS, EPR and EXAFS suggests that the grafted species possesses a bipodal attachment to ceria bearing one neopentylidyne and one neopentane ligand in the closest coordination sphere. There are in addition two surface oxygen atoms that act as coordinating ligands, as revealed by EXAFS giving in a deformed octahedral configuration around tungsten. The grafting process proceeds via protonolysis on terminal (total consumption) and bridged (partial consumption) hydroxyl groups on the surface of ceria, as indicated by DRIFT and ^{17}O NMR, along with the release of neopentane (two equivalents). No substantial change in textural properties and crystallinity is observed after grafting. Extensive investigations by XPS, EPR and XAS confirm the existence of solely W^{VI} and a mixture of Ce^{III} and Ce^{IV} on the surface.

4 Preparation and characterization of W-oxo supported on CeO₂₋₂₀₀

4.1 Preparation of W-oxo/CeO₂ [W-b]

As the commercial tungsten-based NH₃-SCR catalyst (V₂O₅/WO₃ supported on titania) comprises tungsten bearing terminal oxo and bridge W-O-W, most of the research activities are focused on acidic properties of tungsten oxide species. Although the real active site for this system is still a matter of debate, it is a general agreement that highly dispersed tungsten is beneficial for the reaction and bulk WO₃ is practically inactive[57]. Current work aims to synthesize highly dispersed isolated tungsten oxo on ceria. Such species are expected to be highly active in NH₃-SCR based on published reports (see section 1). In the literature, different methods to prepare tungsten-based catalysts can be found. Their main objectives are to enhance the catalytic activity, frequently prepared by impregnation[58], sol-gel[63] or co-precipitation[14] techniques. Although the effects of tungsten loading and dispersion have been reported[57,64], no particular work is dedicated to the synthesis of isolated tungsten oxo species on ceria. There are indeed publications reporting low tungsten loading with presumably isolated tungsten sites as the major species, nevertheless, the isolated nature of those species is never confirmed due to a lack of detailed characterization. In order to achieve the pre-defined target, we hereby employ a unique oxidation approach, comprising low temperature oxidation of a reactive surface organometallic fragment. Previous studies in solution have shown that a tungsten alkylidyne complex, being in equilibrium with the corresponding tungsten bis alkylidene complex, yielded a tungsten mono oxo complex upon

O₂ exposure[65]. Hence, the pre-catalyst [W(=CtBu)(CH₂tBu)₃]/CeO₂ [**W-a**] is treated with dry air at different temperatures (500 °C, 600 °C), with the aim to achieve W-oxo/CeO₂₋₅₀₀ [**W-b1**] and W-oxo/CeO₂₋₆₀₀ [**W-b2**]. The oxidation process is illustrated in Scheme 4, highlighting the formation of the targeted isolated bis-oxo tungsten species.



Scheme 4 Schematic illustration of the preparation of targeted bis-oxo tungsten species [(=Ce-O)₂W(=O)₂].

4.2 Characterization of [W-b] by Elemental analysis and DRIFT spectroscopy

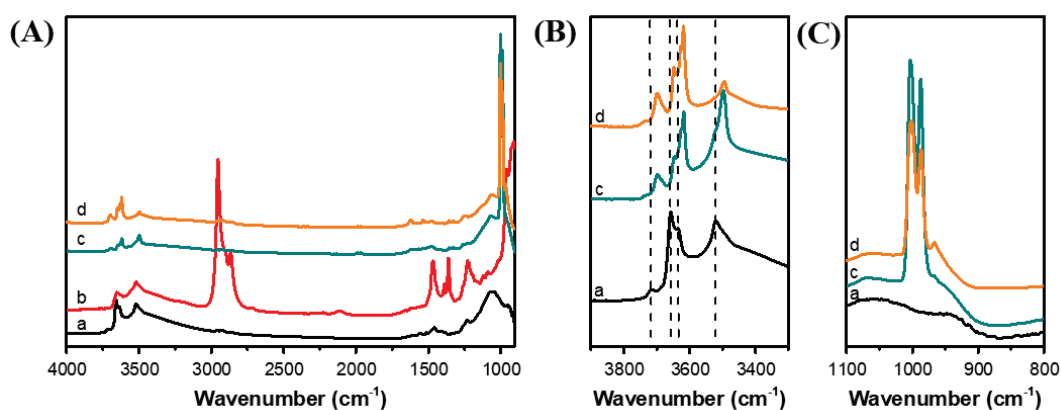


Fig. 18 DRIFT spectra in different ranges (A) 4000 – 950 cm⁻¹; (B) 3900 – 3300 cm⁻¹; (C) 1100 – 800 cm⁻¹ over samples: a) CeO₂₋₂₀₀; b) [W-a]; c) [W-b1]; d) [W-b2].

Elemental analysis of the resulting materials (calcined from 25 to 500 or 600 °C) shows the same tungsten content of 3.2 wt%, and no carbon was detected, suggesting that calcination under the given temperatures can readily remove the organic ligands from the tungsten Schrock complex without loss of the transition metal. The materials have been exposed to such high temperature since the catalytic reaction is carried out at such temperatures.

FT-IR analysis is further carried out to monitor surface changes upon the oxidation process. A series of DRIFT spectra highlighting each step is presented in Fig. 18: pure CeO₂ after dehydroxylation (line a), sample after the grafting process, [W-a] (line b), oxidated sample followed by calcination at 500 °C, [W-b1] (line c), and oxidated sample calcined at 600 °C,

[W-b2] (line d). As discussed in section 3.3, **[W-a]** features characteristic peaks around 3000 cm^{-1} and 1500 cm^{-1} for aliphatic $\nu(\text{CH})$ and $\delta(\text{CH}_2)$ and $\delta(\text{CH}_3)$ vibrations of the perhydrocarbyl ligands. These peaks disappear after calcination (Fig. 18A). Likewise, the peak at 2120 cm^{-1} , which belongs to the forbidden $2F_{5/2} \rightarrow 2F_{7/2}$ electronic transition of the subsurface Ce^{3+} , also disappeared during the oxidation process. The remaining features lie in the $\nu(\text{O-H})$ and $\nu(\text{W=O})$ regions. The oxidation at room temperature of **[W-a]** shows the disappearance of almost all alkyl bands revealing the removal of all alkyl groups even at low temperature (Fig. 19). This result can be explained by a [2+2] cycloaddition of the carbenes fragments $\text{W}=\text{CH}/\text{Bu}_3$ intermediates with O_2 leading to the formation of W-oxo fragments and the corresponding aldehyde (Scheme 5). Such reactivity is important to obtain the targeted isolated tungsten oxo after calcination as most of the organic fragments have already been removed at low temperature, avoiding combustion reaction and formation of water which will cause agglomeration of tungsten.

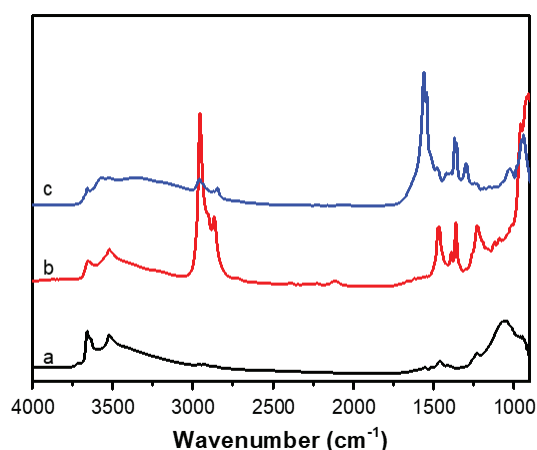
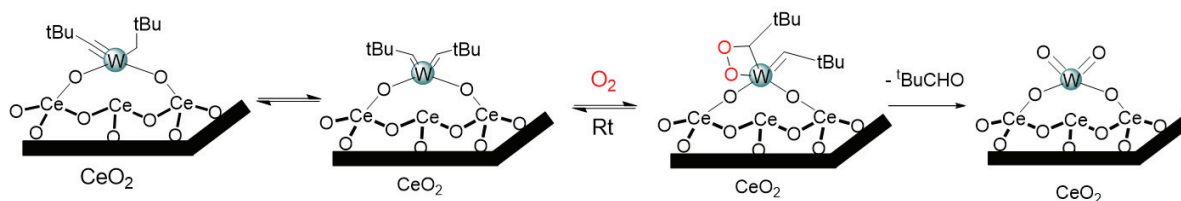


Fig. 19 DRIFT spectrum of (a) CeO_2 -200, **[W-a]** (b) before and (c) after oxidation at room temperature.



Scheme 5 Schematic illustration of **[W-a]** oxidated at room temperature.

To clarify the spectroscopic features of the samples after calcination, the $\nu(\text{O-H})$ and $\nu(\text{W=O})$ have been highlighted in Fig. 18B and 18C. In the (O-H) stretching region, we observe that the IR band attributed to terminal OH groups at 3720 cm^{-1} ($\mu^1\text{-OH}$) which should have been

consumed during the grafting progress appear to be more intense after calcination (lines c and d) with a minor 25 cm^{-1} shift (new band at 3695 cm^{-1}). Although it is very difficult to perform quantitative analysis based on DRIFT, it seems that the total amount of OH groups has decreased after calcination (comparison of a and c in Fig. 18A). There are also evolutions of the μ^2 -OH and μ^3 -OH after calcination. Similarly, a slight red shift has been observed in both cases. Interestingly, the relative intensities between different OH-group IR bands seems to be modified. The most pronounced change involves reduction of the μ^3 -OH peak intensity and a slight increase in the intensity of the other OH-group bands, in particular μ^1 -OH. Such results may suggest that there is a redistribution of surface OH-groups upon heat treatment. During the calcination study of pure ceria (Fig. 1), a similar reduction of the μ^3 -OH peak has been observed. Hence, for [W-b2], the reduction of the μ^3 -OH may be most likely due to the high temperature treatment, causing further condensation of such OH-groups. Nevertheless, the presence of tungsten bis-oxo species may also cause a consumption of adjacent OH-groups by condensation with the oxo ligand, giving the tetrapodal mono-oxo species (Fig. 20).

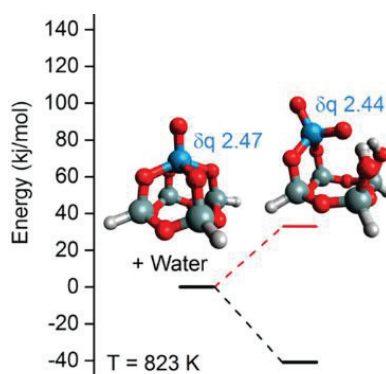


Fig. 20 DFT calculated enthalpy and Gibbs free energy changes for the conversion of $(\equiv\text{SiO})_4\text{W}=\text{O}$ to $(\equiv\text{SiO})_2\text{W}(=\text{O})_2$ at 823 K[19]

Lessons from the similar tungsten oxo system supported on silica have revealed a tungsten mono-oxo species can readily be formed by calcination. However, this species can be transformed to a bis-oxo species when treated under helium at high temperature[19] (Fig. 20). It further indicates that the penta-coordinated tungsten mono-oxo species is more stable under calcination. It is then reasonable to believe that the penta-coordinated tungsten mono-oxo species supported on ceria will be the major surface complex under the given conditions. The somewhat increase of the μ^1 -OH intensity along with a slight shift may be attributed to a restructuring and de-coordination of μ^2 -OH and μ^3 -OH at high temperature. In fact, creation

of small amount of μ^1 -OH seems also observed by DRIFT during the calcination studies of ceria (Fig. 1).

The other obvious difference between pure CeO_{2-200} and [W-b1], [W-b2] is in the region 900 - 1100 cm^{-1} , which is characteristic of supported metal oxo species. As already mentioned, the ceria supported tungsten species can be present as mono-oxo $(\equiv\text{CeO})_4\text{W}=\text{O}$ and bis-oxo $(\equiv\text{CeO})_2\text{W}(=\text{O})_2$ species after calcination. These species feature representative absorption bands in the DRIFT spectrum where the mono-oxo species usually gives a signal above 1000 cm^{-1} while the bis-oxo species are characterized by two peaks below 1000 cm^{-1} (symmetric and asymmetric vibration modes, splitted by $\Delta \approx 25\text{ cm}^{-1}$).[23][27] In Fig. 18C, [W-b] is shown three distinguishable peaks at 1002 cm^{-1} , 986 cm^{-1} and 968 cm^{-1} , which are attributed to tungsten mono-oxo, and bis-oxo ($\nu_s(\text{W}=\text{O})$ and $\nu_{as}(\text{W}=\text{O})$), respectively. The presence of these peaks indicates the co-existence of tungsten mono-oxo and bis-oxo in [W-b1] and [W-b2].

4.3 Characterization of [W-b] by Raman spectroscopy

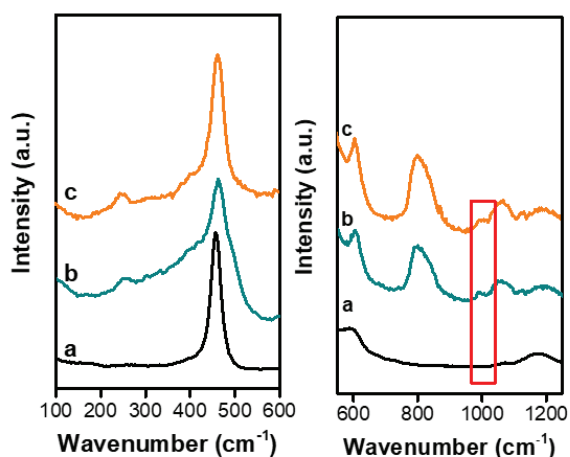


Fig. 21 Raman spectroscopy of a) CeO_{2-200} ; b) W-oxo/ CeO_{2-500} [W-b1]; c) W-oxo/ CeO_{2-600} [W-b2].

Raman spectroscopy is a sensitive technique to study supported metal oxide and is complementary to FT-IR investigation. The Raman spectra of W-oxo/ CeO_{2-500} [W-b1] (line b), W-oxo/ CeO_{2-600} (line c) [W-b2] and support CeO_{2-200} are displayed in Fig. 21. All samples show the characteristic peak at 459 cm^{-1} , which is attributable to F2g mode of the symmetric breathing mode of cubic CeO_2 (fluorite structure).[59] The peak at 599 cm^{-1} is attributed to the defect-induced mode. The broadband centered at 1179 cm^{-1} is ascribed to the second order longitudinal optical mode (2LO) of CeO_2 . The peak at 252 cm^{-1} is assigned to a second order

transverse acoustic mode (2TA)[66]. For the tungsten-containing samples, [W-b1] and [W-b2], a peak at 802 cm^{-1} appeared, which is associated with the W-O stretching vibration modes. However, the characteristic $\nu(\text{W}=\text{O})$ mode appears as a weak and broad peak around 1000 cm^{-1} , suggesting the presence of tungsten-oxo. However, it is hard to distinguish the mono-oxo and bis-oxo structure due to a lack of sensibility and a fairly low concentration. Thus, the results from Raman spectroscopy are in agreement with those from DRIFT and literature data, showcasing the formation of highly dispersed tetrapodal tungsten mono-oxo species as the dominating species after calcination at high temperature.

4.4 Characterization of [W-b] by Nitrogen adsorption-desorption isotherm measurements

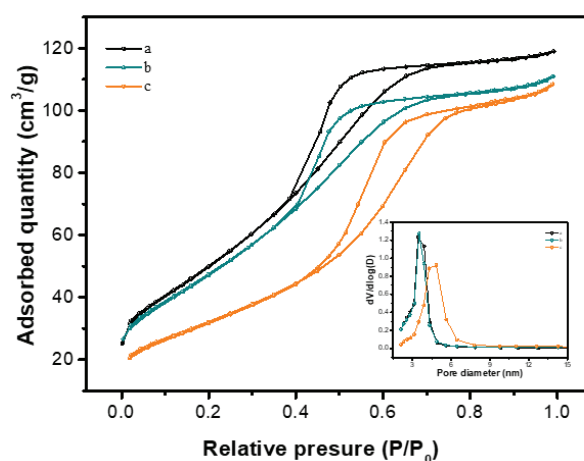


Fig. 22 Nitrogen physisorption isotherms and corresponding pore size distribution (inset) of (a) CeO_2 , (b) [W-b1], (c) [W-b2]

Table 4 Results obtained from nitrogen physisorption isotherms

Sample	Surface area (m^2/g)	Average particle Size (nm)	Total pore volume(cm^3/g)	Surface tungsten density(W/nm^2)
$\text{CeO}_2\text{-200}$	188	3.36	0.23	0
[W-a]	166	3.19	0.16	0.65
[W-b1]	178	3.40	0.20	0.61
[W-b2]	118	4.41	0.20	0.92

Fig. 22 illustrates the N_2 adsorption-desorption isotherms and BJH pore size distribution plots determined from the adsorption branch of the N_2 isotherms of [W-b1] and [W-b2]. Similar to pure CeO_2 , the adsorption/desorption isotherms belong to type IV profile under IUPAC classification, which display H2 type hysteresis loop characteristic of capillary condensation between the aggregates constituting the solid. The BET surface area of each sample is listed in Table 4. After calcination at $500\text{ }^\circ\text{C}$, a slight gain in BET surface area is observed and is

probably due to the removal of organic ligands. Further heating (600 °C) causes a notable decrease in BET surface area, due to the segregation of the ceria, as already observed during the calcination of pure ceria prior to grafting (Table 1). The pore sizes given in Table 4, derived from desorption data and calculated from the isotherm using the BJH model, shows that most of the average pore sizes fall into the range of 3 to 5 nm, while the [W-b2] exhibited a minor shift towards a larger average pore size, which can be ascribed to the agglomeration and distortion of ceria crystalline at high temperature.

4.5 Characterization of [W-b] by HRTEM and STEM

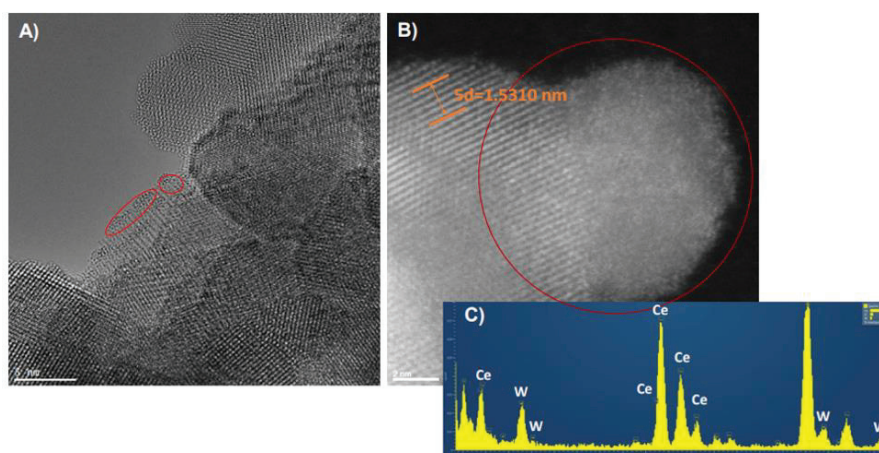


Fig. 23. HRTEM (A), STEM (B) and EDX analysis (C) of [W-b1].

The composition and distribution of different elements on W-oxo/CeO₂ are analyzed using High-resolution transmission electron microscopy (HRTEM) and Scanning Transmission Electron Microscopy (STEM) (Fig. 23). STEM/EDX analyses showed a homogeneous distribution of tungsten and cerium through the sample. The regular lattice distance of 0.30 nm is characteristic of (111) reticular planes of ceria[67], consistent with XRD study where the (111) facets are dominant. HRTEM and STEM also reveal that ceria is still present as highly crystalline, while tungsten deposited on ceria is rather amorphous (Fig. 23). No evident clusters or nanoparticles of WO₃ are observed even under extensive magnification (~1 nm in resolution). In addition, the images also visualize that tungsten seems to localize preferably on the surface/border of ceria with high dispersion, in agreement with energy-dispersive X-ray spectroscopy (EDX) in Fig. 23C. Although the single atom nature of the sample cannot be directly revealed by HRTEM, current results clearly show the absence of clusters or nanoparticles and may indicate an atomic distribution of tungsten on the surface of ceria.

4.6 Characterization of [W-b] by X-ray photoelectron spectroscopy

W-oxo/CeO₂₋₆₀₀ has further been analyzed by XPS to determine the surface composition and oxidation state of different elements. The spectrum of Ce 3d, O 1s, and W 4f of W-oxo/CeO₂₋₆₀₀ are depicted in Fig. 24. The surface Ce³⁺ proportion ($Ce^{3+}/(Ce^{3+}+Ce^{4+})$) is estimated to be 26.8%, which is somewhat higher than 20.6% in support CeO₂₋₂₀₀ (see section 2.5). The slight increase in the surface Ce³⁺ concentration after immobilization of tungsten is most likely due to the thermal treatment causing a restructuring of the surface. Notably the formation of the major tetrapodal mono oxo species (*vide infra*) may necessitate opening of Ce-O-Ce bridges and can thereby create additional Ce³⁺ close to the tungsten center. O 1s spectrum presents two binding energies at 529.6 and 531 eV, previously assigned to lattice oxygen and to surface oxygen (O²⁻ hydroxide) respectively[55]. The ratio of surface oxygen ($O_{\alpha}\% = O_{\alpha}/(O_{\alpha}+O_{\beta})$) is 35.2 % in W-oxo/CeO₂₋₆₀₀, and it is notably higher than that in support CeO₂₋₂₀₀(19.1%), confirming the existence of more surface oxygen in [W-b2]. Generally, a higher surface oxygen content is positive since it has been reported to be favorable for NH₃-SCR[68].

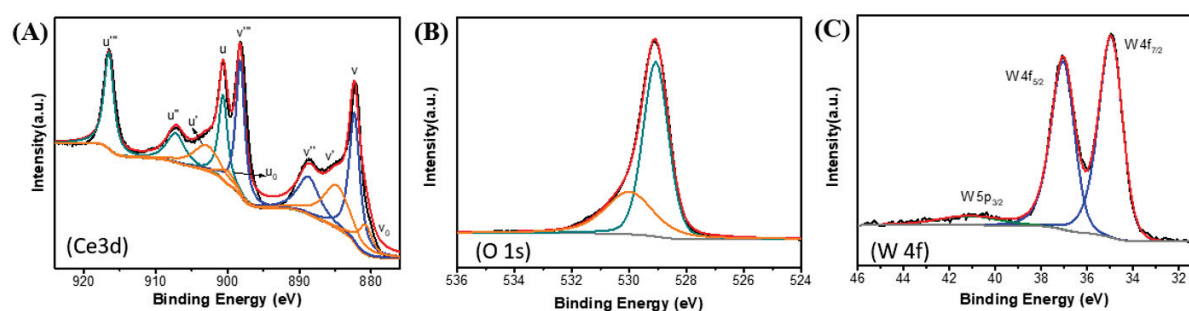


Fig. 24 XPS spectra of [W-b2]; (A) Ce 3d, (B) O 1s, (C) W 4f and W 5p.

4.7 Characterization of [W-b2] by X-ray absorption spectroscopy

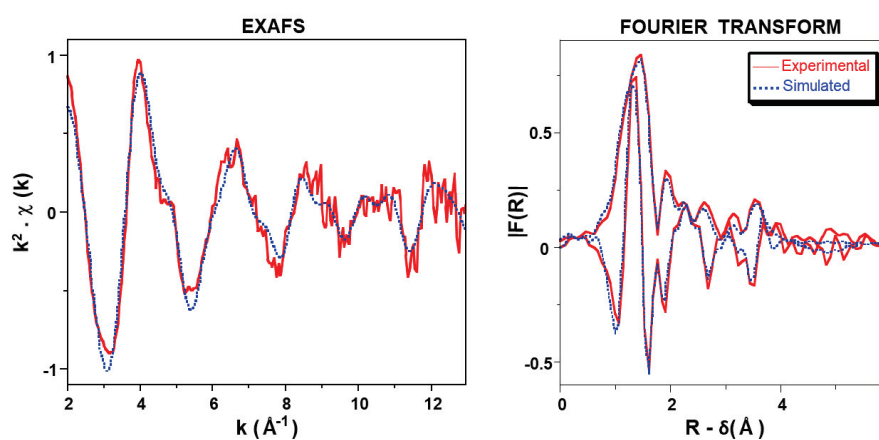


Fig. 25 W L_{III}-edge k^2 -weighted EXAFS (left) and its Fourier transform (right, modulus and imaginary part of the FT) for [W-b] material. Solid lines: experimental; dashed lines: spherical wave theory

X-ray absorption spectroscopy study at the W L_{III} edge is conducted to reveal the tungsten coordination environment in [W-b2]. EXAFS spectroscopy and corresponding Fourier transform magnitude and imaginary are shown in Fig. 25. The structural parameters extracted from the fit of the EXAFS signal are listed in Table 5. The first peak observed in the Fourier transform (maximum in R - δ at ca. 1.55 Å) can be fitted by three levels of oxygen back-scatters, with distances of 1.69 Å and 1.86 Å and 2.11 Å from the W scatterer, which can be attributed to W=O and W-O bonds, respectively[33]. Besides, the fit of the EXAFS signal could be much improved by considering further levels of O and Ce back-scatterers as indicated in Table 5. The introduction of a W--W contribution in the fit led to much worse simulations, indicating that most probably mainly isolated tungsten sites are present in the sample.

Table 5 EXAFS structural parameters obtained for [W-b].^(a) The errors generated by the fitting program “RoundMidnight” are indicated between parentheses^(a)

Type of Neighbor	Number of Neighbors	Distance (Å)	σ^2 (Å ²)
W=O	1.30(15)	1.69(1)	0.0028(15)
W-O Ce	2.40(3)	1.86(2)	0.0028 ^(b)
W-O (Ce)	1.0 ^(b)	2.11(3)	0.0028 ^(b)
W-O (Ce)	0.9(5)	2.71(4)	0.0028 ^(b)
W-O (Ce)	1.4(8)	2.93(4)	0.0028 ^(b)
W-Ce	0.3 ^(b)	3.58(5)	0.0101(41)
W-Ce	2.8 ^(b)	3.81(3)	0.0101 ^(b)

^(a) Δk : [2.0 - 13.0 Å⁻¹] - ΔR : [0.5 - 4.2 Å]; $S_0^2 = 0.94$; $\Delta E_0 = 6.5 \pm 0.7$ eV (the same for all shells); Fit residue: $\rho = 6.8$ %; Quality factor: $(\Delta\chi)^2/\nu = 2.90$ ($\nu = 14/28$). ^(b) Shell constrained to a parameter above.

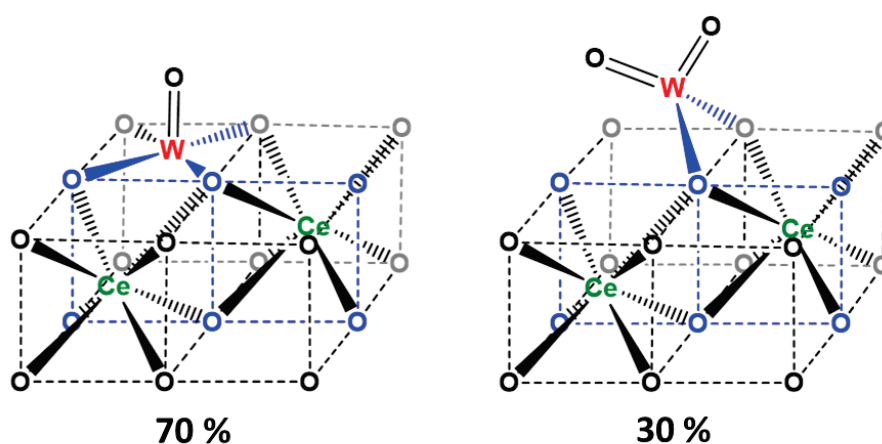


Fig. 26 Proposed structure for [W-b2]

Detailed analysis of the first coordination sphere indicates that there is a mixture of tungsten mono-oxo and bis-oxo, as shown in the structures proposed in Fig. 26 agreeing with the

EXAFS results. The same conclusion has also been provided by DRIFT and Raman spectroscopy earlier. According to the fitted data for numbers of neighbors, the proportion of these species is estimated to be roughly $70 \pm 15\%$ for tungsten mono-oxo and $30 \pm 15\%$ for tungsten bis-oxo. The dominating mono-oxo species is presumably formed through a condensation of the bis-oxo species with adjacent OH-groups, as described by Bell *et al.* (Fig. 20).

In summary, the calcination of [W-a] at high temperatures offers [W-b], which turns out to contain a mixture of isolated tungsten mono-oxo and bis-oxo species supported on ceria. This conclusion is based on a series of characterizations, for instance by XPS, DRIFT, Raman, EXAFS, BET, and TEM. No proximate W-W is found by EXAFS, suggesting that the W-oxo species presents as isolated after calcination at 600 °C. Such a result can only be obtained via the current strategy, involving surface organometallic chemistry on oxide and low temperature oxidation prior to calcination. As observed, most of the alkyl groups on the surface have already been removed in contact with oxygen, avoiding the production of water at high temperature which will promote agglomeration of tungsten.

5 Catalytic performance investigation

5.1 Catalytic performance in NO conversion and N₂ Selectivity

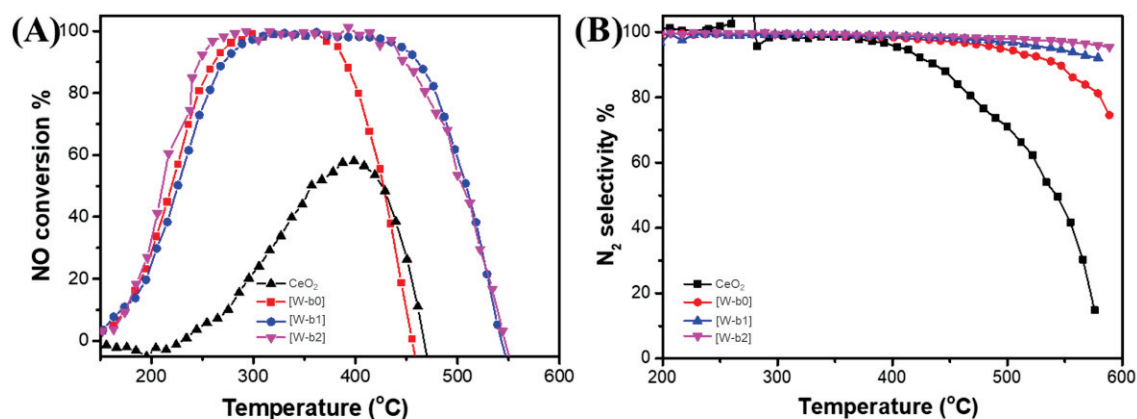


Fig. 27 (A) NO conversion and (B) N₂ selectivity observed for CeO₂₋₂₀₀ and W-oxo/CeO₂ at different temperatures.

The prepared materials ([W-a] exposed to O₂ at room temperature [W-b0], 500 °C [W-b1] and 600 °C [W-b2]) are submitted to catalytic studies for deNO_x reaction through NH₃-SCR and compared to pure CeO₂ under a simulated feed from typical combustion outlet under continuous flow (mixture of 300 ppm NO, 350 ppm of NH₃, 12% O₂ in He). The NO

conversion and N_2 selectivity are presented as a function of temperature in Fig. 27. CeO_2 itself exhibits moderate activity with a maximum conversion of 58% (at 400 °C). Once functionalized with isolated tungsten oxo species, the catalysts show outstanding catalytic performances with practically total conversion even at 300 °C, which extend up to at least 450 °C before a drop of conversion is observed. The latter is due to the oxidation of ammonia (*vide infra*) rather than the deactivation of the catalysts. The catalyst [W-b2] (calcined at higher temperature) shows slightly better performances than [W-b1], particularly in the low temperature region. Surprisingly, the activity of the O_2 exposed, non-calcined (at elevated temperature) catalyst displays a similar activity (as [W-b1] and [W-b2]) in the low temperature region, but a poor activity in the high temperature region. The selectivity for N_2 has notably improved after addition of isolated tungsten oxo species on ceria, especially at high temperatures region above 400°C (Fig. 27B).

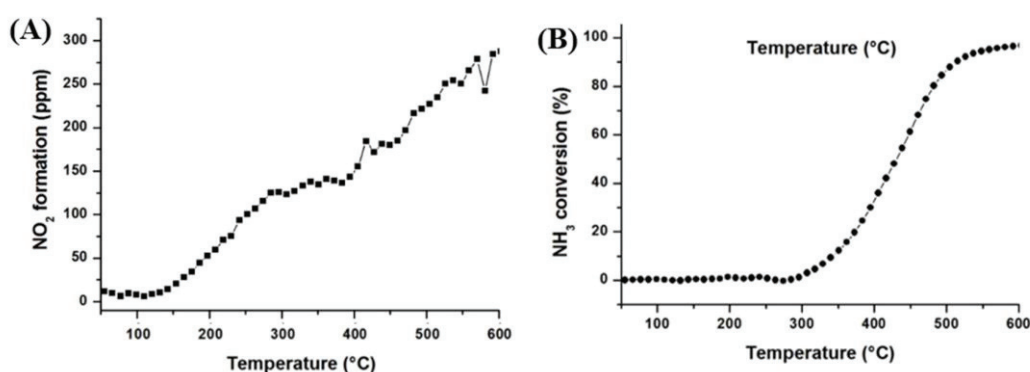


Fig. 28 Separate oxidation reaction of NO into NO₂ (A) and of NH₃ into NO_x (B) with [W-a] as catalyst.

To extend the behavior of these catalysts for deNO_x related reactions, two experiments with a separate (NO + O₂) and (NH₃ + O₂) feed are performed on [W-a] exposed to O₂ at room temperature. The results concerning NO and NH₃ oxidation versus temperature, presented in Fig. 28, show that the oxidation of NO into NO₂ starts at low temperature, ca. 150 °C, with a NO conversion increasing linearly with temperature to reach a pseudo-plateau between 280 and 380 °C before increasing gradually again. The first part of the curve can be explained by the role of the surface oxygen available that can promote the oxidation of the NO into NO₂. After the plateau, thermal oxidation is presumably dominating. In contrast, the oxidation of NH₃ do not take place before the reaction temperature reaches 300 °C, where a sharp increase is observed for temperatures higher than 300 °C. This result suggests that the exceptional performance of the synthesized isolated tungsten oxo supported on ceria catalysts may be

related to the NO oxidation capability as NO₂ can promote fast SCR. Such properties are particularly important in the low temperature region (< 300 °C) where NH₃ remains resistant to oxidation. On the other hand, Fig. 28 clearly shows that NH₃ oxidation becomes more important from temperatures higher than 450 °C, explaining the gradual loss of conversion and selectivity above this temperature (Fig. 27).

5.2 Recycling and tolerance of H₂O of ceria supported tungsten-oxo catalysts

The catalyst robustness is generally important, particularly in an economic and sustainable society. For potential NH₃-SCR uses, it is essential to provide the resistance data towards thermal treatment, the presence of water and the catalytic behaviors after several cycles, as well as the long-term stability. Thus, the pre-catalyst W(\equiv C*t*Bu)(CH₂*t*Bu)₃/CeO₂₋₂₀₀, [W-a] exposed to O₂ at room temperature and W-oxo/CeO₂₋₆₀₀, [W-b2] were evaluated for the selective reduction of NO through several cycles, which are depicted in Fig. 29. [W-a] shows more than 95 % conversion of NO_x between 280 and 400 °C (Fig. 29A, 1^o cycle). Surprisingly, upon repeating SCR cycles, the catalyst performance improved, notably in high-temperature regions, which suggests that most active and stable sites are formed under the catalytic conditions (O₂, NH₃, NO, or high temperatures). Comparatively, [W-b2], already calcined at 600 °C, shows virtually a total conversion between 250 °C to 450 °C, without loss of catalytic performance after 5 cycles (Fig. 29B). Those experiments indicate that a heat treatment of [W-a] is necessary to access the most active and stable sites for NH₃-SCR, probably through surface restructuring creating supplementary acid redox pair sites. Moreover, long terms stability of the catalyst at 300 °C was also studied. The result depicted in Fig. 29C confirms that the activity of the catalysts remains stable for more than 50 h, and the total NO conversion is maintained. From the results we obtained, [W-b2] catalyst has an excellent thermal stability and resists the thermal aging.

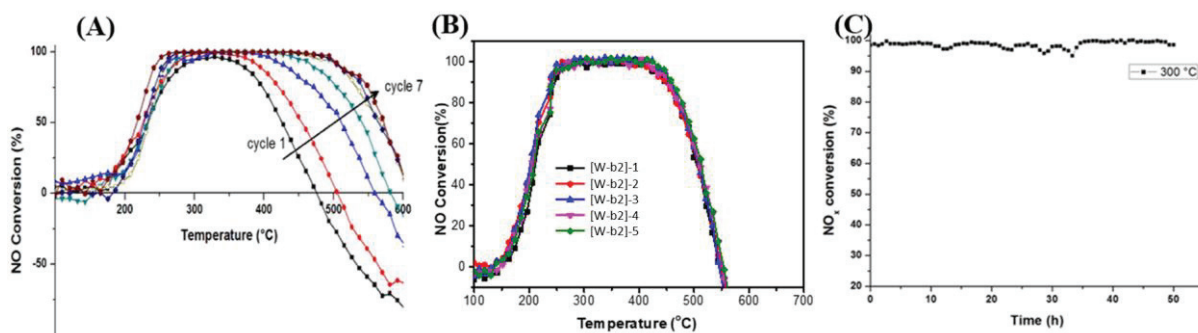


Fig. 29 Thermal stability of (A) [W-a] and (B) [W-b2]; (C) long-term stability of [W-b2].

Furthermore, in a typical combustion reaction, the outlet used to contain substantial amount of H₂O, sometimes above 5%. Water can strongly adsorb on the surface of the catalyst or at least compete with the reactant to adsorb on the active site, causing a decrease of the catalytic performance [69]. Moreover, the presence of considerable amounts of water may also accelerate migration/agglomeration of the active sites, also yielding a drop in the catalytic activity. Furthermore, it is known that surface tungsten oxo species can undergo hydrolysis to form the corresponding Bronsted acidic tungsten hydroxyl species. Hence, the resistance of [W-b2] towards water under NH₃-SCR is investigated in the presence of 5% water (Fig. 30), also reflecting more realistic conditions in combustion engines. As a primary study, W-oxo/CeO₂₋₆₀₀ is exposed to the NH₃-SCR of NO feed (same composition as mentioned in section 5.1) with 5% H₂O at two different temperatures. At 290 °C, the NO conversion decreases by 25% when 5% water is added. Importantly, the conversion is recovered when water is switched off, indicating that water acts as a competitive adsorbing reactant to the active sites rather than a deactivation poison. As for 260 °C, the NO conversion declined from 76% to 32% when 5% H₂O is added, and it recovered immediately to 65 % when water was switched off with a gradual increase. Essentially, when the temperature is brought back to 290 °C, the initial conversion is practically restored, which again supports that [W-b2] is perfectly resistant to water. Nevertheless, from a molecular point of view, current results indicate the importance of the tungsten oxo moiety for NH₃-SCR. As mentioned, the presence of such amount of water will rather favor the existence of surface tungsten hydroxyl. The fact that the catalytic performance is lower may indicate that such species have a lower activity (or is even inactive) compared to the initial tungsten oxo species.

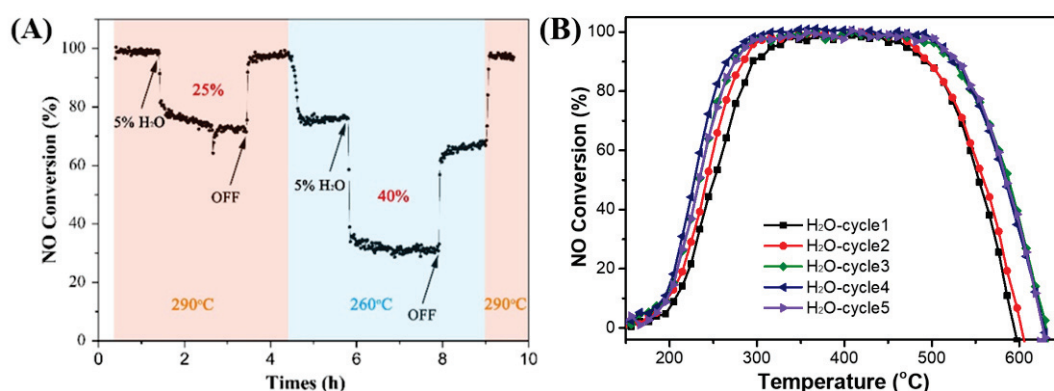


Fig. 30 H₂O resistance over [W-b2]: (A) NH₃-SCR catalytic performance at (290 °C and 260 °C) with 5% of water present in gas feed if needed; (B) NH₃-SCR catalytic performance with repeated cycles test with 5% of water present in gas feed.

In addition, standard NH₃-SCR test, including repeated cycles and with 5% of water present throughout the whole process is studied (Fig. 30B). The activity in the first cycle is somewhat lower, which can be explained by the strong adsorption of water on the surface. Upon multiple recycling tests, the conversion profile becomes stable with a slightly larger operating window. These results are rather unexpected because under the given conditions, leaching and agglomeration of tungsten are generally expected to occur, causing a gradual decrease of the activity. The fact that this catalyst is stable strongly suggests that the restructuration caused upon the heat treatment has led to a strongly anchored tungsten species on the support near a redox site. These results confirm that the effect of H₂O on the activity of the [W-b2] is minor and simultaneously confirm the robustness of [W-b2] towards water and thermal treatment.

5.3 Structure-reactivity relationship in NH₃-SCR

Generally, factors that affect the activity of NH₃-SCR catalyst are the dispersion of active sites, redox ability, and surface acidity. In order to shed light on the influence of these (widely accepted to be the most important) parameters, the catalytic performance of the synthesized isolated tungsten supported on ceria has been compared to other catalysts: i) catalyst prepared by classical impregnation using metatungstate as precursor (different dispersion); ii) tungsten-oxo supported on silica prepared through SOMC (without supplementary redox properties); iii) molybdenum oxo prepared through SOMC supported on ceria (different acidity).

5.3.1 Catalytic performance

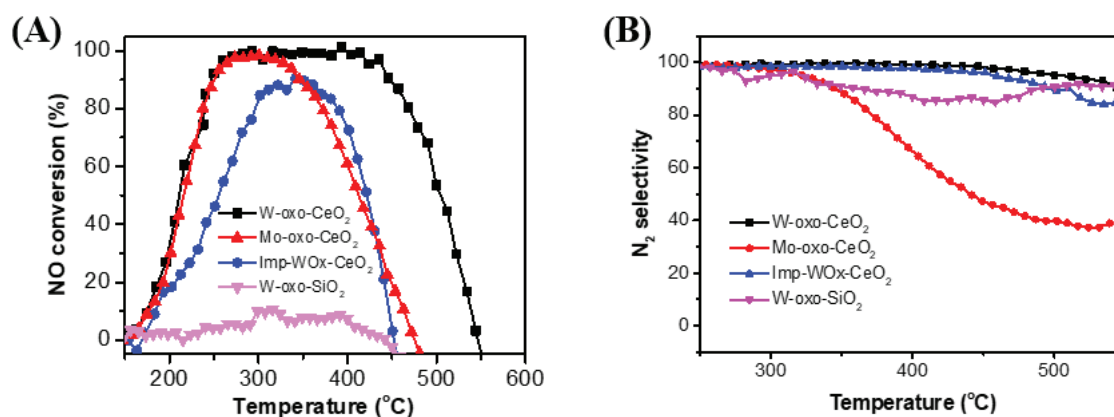


Fig. 31 (A) NO conversion and (B) N₂ selectivity performance of several compared samples.

Several comparison samples are prepared to understand the active site in W-oxo/CeO₂₋₆₀₀ [W-b2] during NH₃-SCR reaction: Imp-WO_x/CeO₂ (prepared by classical impregnation from ammonium metatungstate precursor); W-oxo/SiO₂ (W(≡CtBu)(CH₂tBu)₃ supported on SiO₂

and followed by calcination at 600 °C); Mo-oxo/CeO₂₋₆₀₀ (Mo(\equiv CtBu)(CH₂tBu)₃ supported on CeO₂ calcinated at 600 °C); The molar content of W or Mo in these samples are same with the amount of tungsten in W-oxo/CeO₂₋₆₀₀. NH₃-SCR reaction performances over these samples are displayed in Fig. 31.

To evaluate the effect of support, W-oxo/SiO₂ is prepared by grafting the same precursor W(\equiv CtBu)(CH₂tBu)₃ on SiO₂, followed by calcination at 600 °C. However, W-oxo/SiO₂ is almost inactive in the NH₃-SCR reaction, which confirms the significance of the redox support (ceria). However, the observed low conversion confirms that the tungsten-oxo supported on a neutral support may complete the NH₃-SCR cycle, even without the redox properties. As shown in Fig. 31, the catalytic performances of Mo-oxo/CeO₂₋₆₀₀ are very similar to those of [W-b2] up to 300 °C. At higher temperatures, the conversion of NO and the selectivity to N₂ obtained with this catalyst rapidly decrease. Such behavior of the latter catalyst, being presumably iso-electronic with the tungsten analogue [W-b2], is unexpected. An explanation may be related to the reducibility of the elements at high temperature. MoO₃ is known to undergo thermal reduction already at 350 °C[70], while WO₃ is perfectly stable at 500 °C[71]. Although the mechanism of NH₃-SCR is yet to be determined, among different propositions in the literature involving early transition metal, the catalytic cycle comprises d⁰ elements. The low catalytic performance of Mo-oxo/CeO₂₋₆₀₀ at high temperature is probably related to the challenge to oxidize molybdenum under the given conditions.

The short screening of different related catalysts still preserves [W-b2] as the most active and stable catalyst. This study also confirms the importance of the redox support and the stability of d⁰ transition state metal (W^{VI}) under high temperature during the NH₃-SCR. Moreover, [W-b2] also shows better catalytic behavior than Imp-WO_x/CeO₂, which suggests that catalyst performance is also dependent on the preparation method. The higher activity is probably due to the better tungsten dispersion on the ceria related to the preparation method by SOMC where only isolated tungsten sites are obtained in W-oxo/CeO₂₋₆₀₀. However, Imp-WO_x/CeO₂ prepared by impregnation generally has a surface composed of a mixture surface tungsten species[14]. To further understand the reasons for the difference in activity between Imp-WO_x/CeO₂ and [W-b2], surface acidity and redox ability (pair sites) were elucidated.

5.3.2 Surface acidity

Based on available literature data[13], acidity is essential to execute NH₃-SCR and it is generally associated with the adsorption of NH₃, which is the prerequisite for the formation of active species and subsequent reaction with active nitrites/nitrates. There are also publications reporting that a strong acidity favors this reaction[72]. Nevertheless, the type of essential acidic sites for the reaction remains unclear. Several reports insist that Bronsted acid site is favored[13] and other publications claim that the Lewis acidity is more important[15]. There is a clear disagreement in the literature. Hence, the ceria supported tungsten catalysts are submitted to acidity measurement by microcalorimetry[73], using the enthalpy change of ammonia adsorption. This technique provides qualitative and quantitative information about the acidic type (Lewis or Bronsted), acid strength and the strength distribution. The initial heats of adsorption (denoted by Q_{init}), total and irreversible amounts of NH₃ adsorbed under an equilibrium pressure of 27 Pa are summarized in Table 6 together with the strength distributions of acidic sites (Lewis or Bronsted). A rather surprising result is that [W-b2] has the lowest total uptake of NH₃, even lower than pure ceria and about three times lower than Imp-WO_x/CeO₂. On the other hand, the irreversible NH₃ uptake has risen after tungsten immobilization, reflecting that tungsten has created acidic sites. Still, the irreversible NH₃ uptake is twice as high for Imp-WO_x/CeO₂.

Table 6 Data obtained from microcalorimetric measurements for CeO₂₋₂₀₀, [W-b2], and Imp WO_x/CeO₂

Sample	NH ₃ adsorption at 110 °C		Strength distribution of acid sites (μmol NH ₃ /g sample)			
	Q _{init} ^a (kJ/mol)	NH ₃ uptake (μmol/g)		50<Q<100	100<Q<150	150<Q<200
		n _{total} ^b	n _{irrev} ^c			
CeO ₂₋₂₀₀	163	133.5	34.4	117	30	9
Imp-WO _x /CeO ₂	174	245.9	81.8	189	94	8
[W-b2]	175	89.3	40.9	37	17	8

^a Initial differential heats of NH₃ adsorption; ^b Amount of NH₃ adsorbed under an equilibrium pressure of 27 Pa; ^c Amount of irreversibly chemisorbed NH₃ under an equilibrium pressure of 27 Pa.

The strength of acid sites can be divided into three categories. For all samples, most of the acidic sites are weak (50<Q<100) and assigned to Lewis acid. The moderate acidic sites (100<Q<150) constitute about 30% of the total acidic sites for tungsten functionalized ceria.

Finally, the quantity of strong acidic sites ($150 < Q < 200$) for all samples is practically the same (Fig. 32), though rather low.

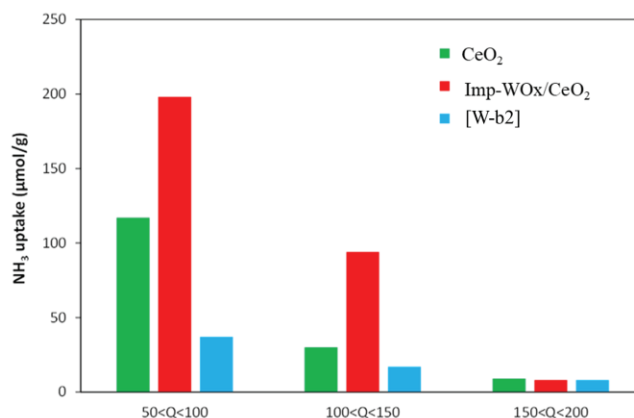


Fig. 32 Strength distributions of acidic sites.

In summary, microcalorimetry shows that tungsten-decorated ceria results in increasing surface acidity with respect to bare ceria. This technique also reveals that the acidity of Imp-WO_x/CeO₂ is far higher than [W-b2] especially in the weak and moderate acid sites. Quantitative evaluation also shows that Imp-WO_x/CeO₂ contains much more acid sites and stronger acidity than [W-b2]. As the tungsten loading is the same for both catalysts, the preparation method strongly alters the acidic properties of the materials. Interestingly, according to the catalytic results presented in section 5.3.1, [W-b2] that is less acidic than Imp-WO_x/CeO₂ exhibits higher activity. These unexpected results indicate that the quantity and the strength of acid sites in ceria supported tungsten catalysts with a low W loading are less relevant to give a highly active NH₃-SCR catalyst. It further supports that the current system may be somewhat different with respect to the proposed reaction mechanisms described in literature based on pair redox and acid (Bronsted or Lewis) sites.

5.3.3 Redox ability

H₂-TPR was performed to investigate the reducibility of CeO₂₋₂₀₀, Imp-WO_x/CeO₂, and [W-b2] via thermal gravimetric analysis (TGA) analysis. TGA can monitor the reaction under a specific carrier gas by following the mass loss with the temperature changes [69,74,75]. When H₂ is used as the carrier gas, the mass loss of materials can be associated to the reducibility of materials generally provided by the removal of oxygen by H₂ in the case of metal oxides. As shown in Fig. 33, the weight losses of the materials can be separated into three stages. The first stage (< 250 °C) is attributed to the adsorption of water. The second stage until around

500 °C corresponds to the loss of surface oxygen resulting from the reduction of surface Ce⁴⁺ to Ce³⁺. The third stage is assigned to the loss of lattice oxygen in bulk CeO₂₋₂₀₀ due to the deep reduction of Ce⁴⁺ to Ce³⁺[69]. Therefore, the second and third stages are related to reducibility.

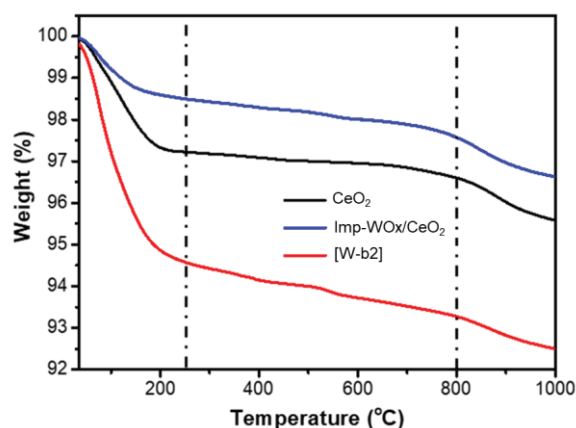


Fig. 33 TGA patterns under H₂

Table 7 O_{release} calculated from the weight loss in the second and third stages

Sampels	Mass (mg)	Mass loss (%) (total)	Mass loss (%) (stage II)	Mass loss (%) (stage III)	O _{release} (mmol/g)
CeO ₂₋₂₀₀	43.550	1.614	0.621	0.993	0.044
Imp-WO _x /CeO ₂	42.359	1.862	0.900	0.962	0.049
[W-b2]	43.485	2.079	1.304	0.776	0.057

The O_{release} is calculated from the weight loss in the second and third stages and the results are listed in Table 7. Essentially, the total weight loss and the mass loss in the second stage increase in the following order: CeO₂₋₂₀₀ < Imp-WO_x/CeO₂ < W-oxo/CeO₂₋₆₀₀. On the other hand, the mass loss in stage III varies less among the samples, as it is basically governed by the bulk support. The O_{release} in stage II may provide hints related to the catalytic performance, since this temperature window concerns surface oxygen loss and falls into the reaction temperature in NH₃-SCR. Larger oxygen loss reflects higher reducibility and may even oxidize NO to NO₂, triggering the fast SCR process. Clearly, O_{release} is improved once the ceria is decorated with tungsten. The highest O_{release} is observed for W-oxo/CeO₂₋₆₀₀, being consistent with the catalytic results (see Fig. 31). Thus, utilizing the surface organometallic chemistry approach to prepare tungsten-based NH₃-SCR catalyst has resulted in a material comprising single tungsten site being highly dispersed and with improved redox properties under the working temperature range.

6 Conclusion

Surface organometallic chemistry on ceria has been investigated and exemplified by using $W(\equiv C*t*Bu)(CH_2*t*Bu)_3$ as precursor with the aim to produce novel NH_3 -SCR catalyst. Prior to the grafting reaction, the support CeO_2 , with different pretreatments has been thoroughly characterized by DRIFT, XPS, XRD, BET, Raman and solid state NMR (1H , ^{17}O). Furthermore, chemical titration with $Al(*t*Bu)_3$ has been conducted in order to quantify the concentration of surface OH-groups of the support calcined at 500 °C and dehydroxylated at 200 °C (this appears to be the optimal pretreatment conditions).

The catalyst is synthesized in two steps. For the first step, the Schrock-type tungsten complex ($W(\equiv C*t*Bu)(CH_2*t*Bu)_3$) is grafted onto the surface of ceria with reactions through protonolysis, offering a firmly bonded surface organometallic fragment with high dispersion. And in the second step, the grafted product is calcined to form the supported tungsten-oxo species. At each step, the materials ($[W(\equiv C*t*Bu)(CH_2*t*Bu)_3]/CeO_{2-200}$ [**W-a**] and $W\text{-oxo}/CeO_2$ [**W-b**]) are characterized by FT-IR, XPS, EPR, SSNMR, Raman, and EXAFS in order to specify the structure. The grafted species [**W-a**] appears to be an isolated, bipodal tungsten complex bearing a neopentyl and neopentylidyne ligands. Moreover, EPR and XPS reveal the presence of paramagnetism and Ce^{3+} . Controlled oxidation of [**W-a**] offers the supported tungsten-oxo species [**W-b**]. Combining the aforementioned spectroscopic techniques, the local structure of [**W-b**] supported species is found to be a mixture of isolated tungsten mono-oxo and tungsten bis-oxo species. Moreover, XPS further shows the presence of Ce^{3+} , thus confirming the presence of the necessary acid redox pair (presumably the most active site for NH_3 -SCR) on the material.

The catalytic activity of [**W-b2**] shows exceptionally high activity and stability with full conversion between 250 and 450 °C under typical deNO_x conditions (with 12% O₂). The same catalytic performance is observed after several cycles. In addition, a long-term experiment (50 h) at 300 °C supports the robustness of the catalyst. Virtually the same catalytic performance in terms of conversion and stability after multiple cycles is observed in the presence of 5% water. Comparative experiments confirm that redox support CeO_2 in combination with a transition metal can boost the activity, as highlighted by $W\text{-oxo}/SiO_2$. Though only group VI transition metals (W, Mo) are investigated, current results show that tungsten is more robust than the molybdenum counterparts, especially in the high temperature region. Interestingly, $W\text{-oxo}/CeO_2$ shows higher activity than WO_x/CeO_2 synthesized by

impregnation catalyst on NO conversion, despite less acidity and similar redox ability. This strategy provides a general method to fabricate single-site catalysts with relatively low metal loading and high dispersion suitable for mechanistic studies and drawing the structure-reactivity relationship. Moreover, gathering different elements in this Chapter, there is a strong indication that the current reaction mechanism is somewhat different with respect to classical proposed mechanisms. First of all, the redox properties are indeed important. Nevertheless, the fact that W-oxo/SiO₂ is able to turn the catalytic cycle, though with low activity, indicates that the available sites on this catalyst (only tungsten oxo fragment supported on silica) contain the necessary elements to make the targeted reaction occur. The limited activity may be due to the kinetic limitations of certain elementary steps, in particular formation of the N-N bond during NO addition. Secondly, the acidity measurements reveal that W-oxo/CeO₂₋₆₀₀ possesses lower acidity than a corresponding sample prepared by classical impregnation, while the catalytic performance is notably higher for W-oxo/CeO₂₋₆₀₀. Moreover, the NH₃-SCR tests under 5% water indirectly prove that the Brønsted site (W-OH is expected to be the dominating surface species under this condition) has a weak inhibiting effect on the conversion compared to the tungsten oxo fragments possessing Lewis acidity. In addition, a dramatic difference in NH₃-SCR is observed between Mo-oxo/CeO₂₋₆₀₀ and W-oxo/CeO₂₋₆₀₀ at the high temperature region. Both elements present the necessary Lewis acidity, but have a different stability at high temperature. As mentioned, the initial tungsten(VI) oxo site is perfectly stable at the high temperature region. Conversely, molybdenum can undergo thermal reduction already at 350 °C, resulting in a loss of the d⁰ identity and consequently the oxo ligand. Thus, the absolute acidic content and strength do not seem to be crucial for high performance NH₃-SCR catalysts. Current results are rather directing that the active species for NH₃-SCR of NO comprise a transition metal (exemplified by tungsten) oxo sites associated to with redox site Ce³⁺.

Table 8 Summary and comparison of the catalyst preparation and catalytic performance in this chapter

Catalysts	Loading	Synthesis method	Precursor	Calcination temperature	NO conversion
CeO ₂₋₂₀₀	N.D.	N.D.	N.D.	N.D.	58% at 400 °C
W-oxo/CeO ₂₋₅₀₀	3.30 wt%	SOMC	[W(=CtBu)(CH ₂ tBu) ₃]	500 °C	T ₈₀ (256-476 °C)
W-oxo/CeO ₂₋₆₀₀	3.30 wt%	SOMC	[W(=CtBu)(CH ₂ tBu) ₃]	600 °C	T ₈₀ (236-467 °C)
Imp-WO _x /CeO ₂	3.30 wt%	Impregnation	(NH ₄) ₆ H ₂ W ₁₂ O ₄₀ *4H ₂ O	500 °C	T ₈₀ (294-391 °C)
W-oxo/SiO ₂₋₆₀₀		SOMC	[W(=CtBu)(CH ₂ tBu) ₃]	600 °C	10% at 390 °C
Mo-oxo/CeO ₂₋₆₀₀		SOMC	[Mo(=CtBu)(CH ₂ tBu) ₃]	600 °C	T ₈₀ (236-403 °C)

Reference

- [1] R.M. Doherty, M.R. Heal, F.M. O'Connor, Climate change impacts on human health over Europe through its effect on air quality, *Environmental Health: A Global Access Science Source*. 16 (2017) 34-44. <https://doi.org/10.1186/s12940-017-0325-2>.
- [2] M. Fiebig, A. Wiartalla, B. Holderbaum, S. Kiesow, Particulate emissions from diesel engines: Correlation between engine technology and emissions, *Journal of Occupational Medicine and Toxicology*. 9 (2014) 1-18. <https://doi.org/10.1186/1745-6673-9-6>.
- [3] N. Hooftman, M. Messagie, J. Van Mierlo, T. Coosemans, A review of the European passenger car regulations – Real driving emissions vs local air quality, *Renewable and Sustainable Energy Reviews*. 86 (2018) 1–21. <https://doi.org/10.1016/j.rser.2018.01.012>.
- [4] S. Ramalingam, S. Rajendran, P. Ganesan, Performance improvement and exhaust emissions reduction in biodiesel operated diesel engine through the use of operating parameters and catalytic converter: A review, *Renewable and Sustainable Energy Reviews*. 81 (2018) 3215–3222. <https://doi.org/10.1016/j.rser.2017.08.069>.
- [5] J. Xu, H. Wang, F. Guo, C. Zhang, J. Xie, Recent advances in supported molecular sieve catalysts with wide temperature range for selective catalytic reduction of NOx with C₃H₆, *RSC Advances*. 9 (2019) 824–838. <https://doi.org/10.1039/c8ra08635d>.
- [6] A. Laachir, V. Perrichon, A. Badri, J. Lamotte, E. Catherine, J. Claude Lavalley, J. El Fallah, L. Hilaire, F. le Normand, E. Quemere, G. Noel Sauvion, Reduction of CeO₂, by Hydrogen Magnetic Susceptibility and Fourier-transform Infrared, Ultraviolet and X-Ray Photoelectron Spectroscopy Measurements, *Journal of the Chemical Society, Faraday Transactions*, 87 (1991), 1601-1609. <https://doi.org/10.1039/FT9918701601>.
- [7] L. Han, S. Cai, M. Gao, J.Y. Hasegawa, P. Wang, J. Zhang, L. Shi, D. Zhang, Selective Catalytic Reduction of NOx with NH₃ by Using Novel Catalysts: State of the Art and Future Prospects, *Chemical Reviews*. 119 (2019) 10916–10976. <https://doi.org/10.1021/acs.chemrev.9b00202>.
- [8] W. Shan, H. Song, Catalysts for the selective catalytic reduction of NOx with NH₃ at low temperature, *Catalysis Science and Technology*. 5 (2015) 4280–4288. <https://doi.org/10.1039/c5cy00737b>.
- [9] G. Busca, L. Lietti, G. Ramis, F. Berti, Chemical and mechanistic aspects of the selective catalytic reduction of NOx by ammonia over oxide catalysts: A review, *Applied Catalysis B: Environmental*. 18 (1998) 1-36 [https://doi.org/10.1016/S0926-3373\(98\)00040-X](https://doi.org/10.1016/S0926-3373(98)00040-X).
- [10] Z.G. Liu, N.A. Ottinger, C.M. Creemeens, Vanadium and tungsten release from V-based selective catalytic reduction diesel aftertreatment, *Atmospheric Environment*. 104 (2015) 154–161. <https://doi.org/10.1016/j.atmosenv.2014.12.063>.
- [11] T. Montini, M. Melchionna, M. Monai, P. Fornasiero, Fundamentals and Catalytic

- Applications of CeO₂-Based Materials, *Chemical Reviews*. 116 (2016) 5987–6041. <https://doi.org/10.1021/acs.chemrev.5b00603>.
- [12] C. Tang, H. Zhang, L. Dong, Ceria-based catalysts for low-temperature selective catalytic reduction of NO with NH₃, *Catalysis Science and Technology*. 6 (2016) 1248–1264. <https://doi.org/10.1039/c5cy01487e>.
- [13] W. Shan, F. Liu, H. He, X. Shi, C. Zhang, A superior Ce-W-Ti mixed oxide catalyst for the selective catalytic reduction of NO_x with NH₃, *Applied Catalysis B: Environmental*. 115–116 (2012) 100–106. <https://doi.org/10.1016/j.apcatb.2011.12.019>.
- [14] Y. Peng, K. Li, J. Li, Identification of the active sites on CeO₂-WO₃ catalysts for SCR of NO_x with NH₃: An in situ IR and Raman spectroscopy study, *Applied Catalysis B: Environmental*. 140–141 (2013) 483–492. <https://doi.org/10.1016/j.apcatb.2013.04.043>.
- [15] S. Zhan, H. Zhang, Y. Zhang, Q. Shi, Y. Li, X.J. Li, Efficient NH₃-SCR removal of NO_x with highly ordered mesoporous WO₃(γ)-CeO₂ at low temperatures, *Applied Catalysis B: Environmental*. 203 (2017) 199–209. <https://doi.org/10.1016/j.apcatb.2016.10.010>.
- [16] I. El Arrouji, C. Chen, J. Toyir, C. Larabi, K.C. Szeto, A. de Mallmann, M. Taoufik, A. Oulmekki, NH₃ selective catalytic reduction of NO_x to N₂ over ceria supported WO₃ based catalysts: Influence of tungsten content, *Catalysts*. 11 (2021) 1–12. <https://doi.org/10.3390/catal11080950>.
- [17] Z. Ma, D. Weng, X. Wu, Z. Si, Effects of WO_x modification on the activity, adsorption and redox properties of CeO₂ catalyst for NO_x reduction with ammonia, *Journal of Environmental Sciences (China)*. 24 (2012) 1305–1316. [https://doi.org/10.1016/S1001-0742\(11\)60925-X](https://doi.org/10.1016/S1001-0742(11)60925-X).
- [18] E. Le Roux, M. Taoufik, M. Chabanas, D. Alcor, A. Baudouin, C. Coperet, J. Thivolle-Cazat, J-M. Basset, A. Lesage, S. Hediger, and L. Emsley, Well-Defined Surface Tungstenocarbonyl Complexes through the Reaction of [W(\equiv C*t*Bu)(CH₂*t*Bu)₃] with Silica, *Organometallics*. 24 (2005) 4274-4279. <https://doi.org/10.1021/om050086a>
- [19] J.G. Howell, Y.P. Li, A.T. Bell, Propene Metathesis over Supported Tungsten Oxide Catalysts: A Study of Active Site Formation, *ACS Catalysis*. 6 (2016) 7728–7738. <https://doi.org/10.1021/acscatal.6b01842>.
- [20] Y. Xu, X. Wu, L. Cao, Y. Ma, R. Ran, Z. Si, D. Weng, Z. Ma, B. Wang, Crystal orientation-dependent activity of tungsten-based catalysts for selective catalytic reduction of NO_x with NH₃, *Journal of Catalysis*. 375 (2019) 294–303. <https://doi.org/10.1016/j.jcat.2019.06.012>.
- [21] F. Can, X. Courtois, S. Berland, M. Seneque, S. Royer, D. Duprez, Composition dependent performance of alumina-based oxide supported WO₃ catalysts for the NH₃-SCR reaction and the NSR + SCR coupled process, *Catalysis Today*. 257 (2015) 41–50. <https://doi.org/10.1016/j.cattod.2015.03.024>.
- [22] M. Wang, X.P. Wu, S. Zheng, L. Zhao, L. Li, L. Shen, Y. Gao, N. Xue, X. Guo, W. Huang, Z. Gan, F. Blanc, Z. Yu, X. Ke, W. Ding, X.Q. Gong, C.P. Grey, L. Peng,

- Identification of different oxygen species in oxide nanostructures with ^{17}O solid state NMR spectroscopy, *Science Advances*. 1 (2015) 1-8. <https://doi.org/10.1126/sciadv.1400133>.
- [23] S. Lwin, Y. Li, A.I. Frenkel, I.E. Wachs, Nature of WO_x Sites on SiO_2 and Their Molecular Structure-Reactivity/Selectivity Relationships for Propylene Metathesis, *ACS Catalysis*. 6 (2016) 3061–3071. <https://doi.org/10.1021/acscatal.6b00389>.
- [24] N. Popoff, E. Mazoyer, J. Pelletier, R.M. Gauvin, M. Taoufik, Expanding the scope of metathesis: A survey of polyfunctional, single-site supported tungsten systems for hydrocarbon valorization, *Chemical Society Reviews*. 42 (2013) 9035–9054. <https://doi.org/10.1039/c3cs60115c>.
- [25] A.J. van Roosmalen, D. Koster, J.C. Mol, Infrared Spectroscopy of Some Chemisorbed Molecules on Tungsten Oxide-Silica, *The Journal of Physical Chemistry*. 84 (1980) 3075–3079. <https://doi.org/10.1021/j100460a021>.
- [26] C. Martín, P. Malet, G. Solana, V. Rives, Structural Analysis of Silica-Supported Tungstates, *The Journal of Physical Chemistry B*, 102 (1998) 2759-2768. <https://doi.org/10.1021/jp980614e>.
- [27] C. Larabi, N. Merle, F. Le Quéméner, P. Rouge, E. Berrier, R.M. Gauvin, E. Le Roux, A. de Mallmann, K.C. Szeto, M. Taoufik, New synthetic approach towards well-defined silica supported tungsten bis-oxo, active catalysts for olefin metathesis, *Catalysis Communications*. 108 (2018) 51–54. <https://doi.org/10.1016/j.catcom.2018.01.031>.
- [28] C. Larabi, K.C. Szeto, Y. Bouhoute, M.O. Charlin, N. Merle, A. De Mallmann, R.M. Gauvin, L. Delevoye, M. Taoufik, Solvent-Free Ring-Opening Metathesis Polymerization of Norbornene over Silica-Supported Tungsten–Oxo Perhydrocarbyl Catalysts, *Macromolecular Rapid Communications*. 37 (2016) 1832–1836. <https://doi.org/10.1002/marc.201600419>.
- [29] N. Merle, F. Le Quéméner, Y. Bouhoute, K.C. Szeto, A. De Mallmann, S. Barman, M.K. Samantaray, L. Delevoye, R.M. Gauvin, M. Taoufik, J.M. Basset, Well-Defined Molybdenum Oxo Alkyl Complex Supported on Silica by Surface Organometallic Chemistry: A Highly Active Olefin Metathesis Precatalyst, *Journal of the American Chemical Society*. 139 (2017) 2144–2147. <https://doi.org/10.1021/jacs.6b11220>.
- [30] N. Merle, F. Le Quéméner, S. Barman, M.K. Samantaray, K.C. Szeto, A. De Mallmann, M. Taoufik, J.M. Basset, Well-defined silica supported bipodal molybdenum oxo alkyl complexes: A model of the active sites of industrial olefin metathesis catalysts, *Chemical Communications*. 53 (2017) 11338–11341. <https://doi.org/10.1039/c7cc06041f>.
- [31] F. Zhang, K.C. Szeto, M. Taoufik, L. Delevoye, R.M. Gauvin, S.L. Scott, Enhanced Metathesis Activity and Stability of Methyltrioxorhenium on a Mostly Amorphous Alumina: Role of the Local Grafting Environment, *Journal of the American Chemical Society*. 140 (2018) 13854–13868. <https://doi.org/10.1021/jacs.8b08630>.

- [32] E. Le Roux, M. Taoufik, M. Chabanas, D. Alcor, A. Baudouin, C. Copéret, J. Thivolle-Cazat, J.M. Basset, A. Lesage, S. Hediger, L. Emsley, Well-defined surface tungstenocarbonyl complexes through the reaction of $[W(\equiv C\text{tBu})(CH_2\text{tBu})_3]$ with silica, *Organometallics*. 24 (2005) 4274–4279. <https://doi.org/10.1021/om050086a>.
- [33] D. Grekov, Y. Bouhoute, K.C. Szeto, N. Merle, A. De Mallmann, F. Lefebvre, C. Lucas, I. Del Rosal, L. Maron, R.M. Gauvin, L. Delevoye, M. Taoufik, Silica-Supported Tungsten Neosilyl Oxo Precatalysts: Impact of the Podality on Activity and Stability in Olefin Metathesis, *Organometallics*. 35 (2016) 2188–2196. <https://doi.org/10.1021/acs.organomet.6b00220>.
- [34] J.D. Rodriguez-Blanco, S. Shaw, L.G. Benning, The kinetics and mechanisms of amorphous calcium carbonate (ACC) crystallization to calcite, via vaterite., *Nanoscale*. 3 (2011) 265–271. <https://doi.org/10.1039/c0nr00589d>.
- [35] L. Chen, D. Weng, Z. Si, X. Wu, Synergistic effect between ceria and tungsten oxide on $WO_3\text{-CeO}_2\text{-TiO}_2$ catalysts for NH_3 -SCR reaction, *Progress in Natural Science: Materials International*. 22 (2012) 265–272. <https://doi.org/10.1016/j.pnsc.2012.07.004>.
- [36] A. Weibel, R. Bouchet, F. Boule'h, P. Knauth, The big problem of small particles: A comparison of methods for determination of particle size in nanocrystalline anatase powders, *Chemistry of Materials*. 17 (2005) 2378–2385. <https://doi.org/10.1021/cm0403762>.
- [37] A. Badri, C. Binet, J.-C. Lavalley, An FTIR study of surface ceria hydroxy groups during a redox process with H_2 , *Journal of the Chemical Society, Faraday Transactions*, 92 (1996) 4669–4673 <https://doi.org/10.1039/ft9969204669>
- [38] B. Beck, M. Harth, N.G. Hamilton, C. Carrero, J.J. Uhlrich, A. Trunschke, S. Shaikhutdinov, H. Schubert, H.J. Freund, R. Schlögl, J. Sauer, R. Schomäcker, Partial oxidation of ethanol on vanadia catalysts on supporting oxides with different redox properties compared to propane, *Journal of Catalysis*. 296 (2012) 120–131. <https://doi.org/10.1016/j.jcat.2012.09.008>.
- [39] M. Taoufik, K.C. Szeto, N. Merle, I. Del Rosal, L. Maron, J. Trébosc, G. Tricot, R.M. Gauvin, L. Delevoye, Heteronuclear NMR spectroscopy as a surface-selective technique: A unique look at the hydroxyl groups of γ -alumina., *Chemistry - A European Journal*. 20 (2014) 4038–4046. <https://doi.org/10.1002/chem.201304883>.
- [40] E. Mazoyer, J. Trébosc, A. Baudouin, O. Boyron, J. Pelletier, J.M. Basset, M.J. Vitorino, C.P. Nicholas, R.M. Gauvin, M. Taoufik, L. Delevoye, Heteronuclear NMR correlations to probe the local structure of catalytically active surface aluminum hydride species on γ -alumina, *Angewandte Chemie - International Edition*. 49 (2010) 9854–9858. <https://doi.org/10.1002/anie.201004310>.
- [41] L. Gill, A. Beste, B. Chen, M. Li, A.K.P. Mann, S.H. Overbury, E.W. Hagaman, Fast MAS 1H NMR study of water adsorption and dissociation on the (100) surface of ceria nanocubes: A fully hydroxylated, hydrophobic ceria surface, *Journal of Physical Chemistry C*. 121 (2017) 7450–7465. <https://doi.org/10.1021/acs.jpcc.6b12375>.

- [42] J. Chen, M.A. Hope, Z. Lin, M. Wang, T. Liu, D.M. Halat, Y. Wen, T. Chen, X. Ke, P.C.M.M. Magusin, W. Ding, X. Xia, X.P. Wu, X.Q. Gong, C.P. Grey, L. Peng, Interactions of Oxide Surfaces with Water Revealed with Solid-State NMR Spectroscopy, *Journal of the American Chemical Society*. 142 (2020) 11173–11182. <https://doi.org/10.1021/jacs.0c03760>.
- [43] M. Wang, X.P. Wu, S. Zheng, L. Zhao, L. Li, L. Shen, Y. Gao, N. Xue, X. Guo, W. Huang, Z. Gan, F. Blanc, Z. Yu, X. Ke, W. Ding, X.Q. Gong, C.P. Grey, L. Peng, Identification of different oxygen species in oxide nanostructures with ^{17}O solid state NMR spectroscopy, *Science Advances*. 1 (2015) 1-8. <https://doi.org/10.1126/sciadv.1400133>.
- [44] F.A. Perras, U. Chaudhary, I.I. Slowing, M. Pruski, Probing Surface Hydrogen Bonding and Dynamics by Natural Abundance, Multidimensional, ^{17}O DNP-NMR Spectroscopy, *Journal of Physical Chemistry C*. 120 (2016) 11535–11544. <https://doi.org/10.1021/acs.jpcc.6b02579>.
- [45] N. Merle, J. Trébosc, A. Baudouin, I. Del Rosal, L. Maron, K. Szeto, M. Genelot, A. Mortreux, M. Taoufik, L. Delevoye, R.M. Gauvin, ^{17}O NMR gives unprecedented insights into the structure of supported catalysts and their interaction with the silica carrier, *Journal of the American Chemical Society*. 134 (2012) 9263–9275. <https://doi.org/10.1021/ja301085m>.
- [46] H.Y. Li, H.F. Wang, Y.L. Guo, G.Z. Lu, P. Hu, Exchange between sub-surface and surface oxygen vacancies on $\text{CeO}_2(111)$: A new surface diffusion mechanism, *Chemical Communications*. 47 (2011) 6105–6107. <https://doi.org/10.1039/c1cc11226k>.
- [47] J. Chen, X.P. Wu, M.A. Hope, K. Qian, D.M. Halat, T. Liu, Y. Li, L. Shen, X. Ke, Y. Wen, J.H. Du, P.C.M.M. Magusin, S. Paul, W. Ding, X.Q. Gong, C.P. Grey, L. Peng, Polar surface structure of oxide nanocrystals revealed with solid state NMR spectroscopy, *Nature Communications*. 10 (2019). <https://doi.org/10.1038/s41467-019-13424-7>.
- [48] H. Wang, X. Chen, S. Gao, Z. Wu, Y. Liu, X. Weng, Deactivation mechanism of Ce/TiO_2 selective catalytic reduction catalysts by the loading of sodium and calcium salts, *Catalysis Science and Technology*. 3 (2013) 715–722. <https://doi.org/10.1039/c2cy20568h>.
- [49] J. Joubert, F. Delbecq, P. Sautet, E. Le Roux, M. Taoufik, C. Thieuleux, F. Blanc, C. Copéret, J. Thivolle-Cazat, J.M. Basset, Molecular understanding of alumina supported single-site catalysts by a combination of experiment and theory, *Journal of the American Chemical Society*. 128 (2006) 9157–9169. <https://doi.org/10.1021/ja0616736>.
- [50] C. Binet, A. Badri, J.C. Lavalley, A spectroscopic characterization of the reduction of ceria from electronic transitions of intrinsic point defects, *Journal of Physical Chemistry*. 98 (1994) 6392–6398. <https://doi.org/10.1021/j100076a025>.
- [51] B. Nematollahi, M. Rezaei, E.N. Lay, Synthesis of Nanocrystalline CeO_2 with High Surface Area by the Taguchi Method and its Application in Methanation, *Chemical Engineering and Technology*. 38 (2015) 265–273.

<https://doi.org/10.1002/ceat.201400092>.

- [52] R.M. Rakhmatullin, V. V. Pavlov, V. V. Semashko, EPR study of nanocrystalline CeO₂ exhibiting ferromagnetism at room temperature, *Physica Status Solidi (B) Basic Research*. 253 (2016) 499–503. <https://doi.org/10.1002/pssb.201552542>.
- [53] X. Yao, T. Kong, L. Chen, S. Ding, F. Yang, L. Dong, Enhanced low-temperature NH₃-SCR performance of MnO_x/CeO₂ catalysts by optimal solvent effect, *Applied Surface Science*. 420 (2017) 407–415. <https://doi.org/10.1016/j.apsusc.2017.05.156>.
- [54] X. Yao, Z. Wang, S. Yu, F. Yang, L. Dong, Acid pretreatment effect on the physicochemical property and catalytic performance of CeO₂ for NH₃-SCR, *Applied Catalysis A: General*. 542 (2017) 282–288. <https://doi.org/10.1016/j.apcata.2017.06.003>.
- [55] X. Dong, J. Wang, H. Zhao, Y. Li, The promotion effect of CeO_x on Cu-SAPO-34 catalyst for selective catalytic reduction of NO_x with ammonia, *Catalysis Today*. 258 (2015) 28–34. <https://doi.org/10.1016/j.cattod.2015.04.015>.
- [56] H. Xu, M. Sun, S. Liu, Y. Li, J. Wang, Y. Chen, Effect of the calcination temperature of cerium-zirconium mixed oxides on the structure and catalytic performance of WO₃/CeZrO₂ monolithic catalyst for selective catalytic reduction of NO_x with NH₃, *RSC Advances*. 7 (2017) 24177–24187. <https://doi.org/10.1039/c7ra03054a>.
- [57] Z. Hu, R.T. Yang, 110th anniversary: Recent progress and future challenges in selective catalytic reduction of NO by H₂ in the presence of O₂, *Industrial and Engineering Chemistry Research*. 58 (2019) 10140–10153. <https://doi.org/10.1021/acs.iecr.9b01843>.
- [58] S. Liu, R. Zhang, P. Li, H. Chen, Y. Wei, X. Liang, Morphology effect of diverse ceria with active tungsten species on NH₃-SCR behaviors, *Catalysis Today*. 339 (2020) 241–253. <https://doi.org/10.1016/j.cattod.2019.02.004>.
- [59] S. Kuba, P.C. Heydorn, R.K. Grasselli, B.C. Gates, M. Che, H. Knözinger, Redox properties of tungstated zirconia catalysts: Relevance to the activation of n-alkanes, *Physical Chemistry Chemical Physics*. 3 (2001) 146–154. <https://doi.org/10.1039/b007774g>.
- [60] Z. Liu, W. Xu, S. Yao, A.C. Johnson-Peck, F. Zhao, P. Michorczyk, A. Kubacka, E.A. Stach, M. Fernández-García, S.D. Senanayake, J.A. Rodriguez, Superior performance of Ni-W-Ce mixed-metal oxide catalysts for ethanol steam reforming: Synergistic effects of W- and Ni-dopants, *Journal of Catalysis*. 321 (2015) 90–99. <https://doi.org/10.1016/j.jcat.2014.10.017>.
- [61] M.R. Churchill, W.J. Youngs, Crystal structure and molecular geometry of W(≡CCMe₃)(=CHCMe₃)(CH₂CMe₃)(dmpe), a mononuclear Tungsten(VI) Complex with Metal Alkylidyne, and metal alkyl linkages, *Inorganic chemistry*. 18 (1979) 2454–2458. <https://doi-org/10.1021/ic50199a025>.
- [62] E.A. Kuk, G. Heger, The Structures of C-Ce₂O₃, Ce₇O₁₂, and Ce₁₁O₂₀, *Journal of Solid State Chemistry*, 147 (1999) 485–500. <https://doi.org/10.1006/jssc.1999.8403>.

- [63] C. Liu, L. Chen, H. Chang, L. Ma, Y. Peng, H. Arandiyani, J. Li, Characterization of CeO₂-WO₃ catalysts prepared by different methods for selective catalytic reduction of NO_x with NH₃, *Catalysis Communications*. 40 (2013) 145–148. <https://doi.org/10.1016/j.catcom.2013.06.017>.
- [64] X. Liu, P. Jiang, Y. Chen, Y. Wang, Q. Ding, Z. Sui, H. Chen, Z. Shen, X. Wu, A basic comprehensive study on synergetic effects among the metal oxides in CeO₂-WO₃/TiO₂ NH₃-SCR catalyst, *Chemical Engineering Journal*. 421 (2021) 127833. <https://doi.org/10.1016/j.cej.2020.127833>.
- [65] Q. Xue, J. Xie, H. Li, Y. Cheng, C. Zhu, Metal-free, highly efficient organocatalytic amination of benzylic C-H bonds, *Chemical Communications*. 49 (2013) 3700–3702. <https://doi.org/10.1039/c3cc41558a>.
- [66] M. Dave, S. Dalela, S. Kumar, P.A. Alvi, Defect induced structural and raman study of Nd-doped CeO₂ nanomaterials, in: *AIP Conference Proceedings*. 2020. <https://doi.org/10.1063/5.0017017>.
- [67] X. Wu, Z. Chen, X. Yu, Z. Huang, H. Shen, G. Jing, Mechanism by which three-dimensional ordered mesoporous CeO₂ promotes the activity of VO_x-MnO_x/CeO₂ catalysts for NO_x abatement: Atomic-scale insight into the catalytic cycle, *Chemical Engineering Journal*. 399 (2020) 125629. <https://doi.org/10.1016/j.cej.2020.125629>.
- [68] X. Fang, Y. Liu, W. Cen, Y. Cheng, Birnessite as a highly efficient catalyst for low-temperature NH₃-SCR: The vital role of surface oxygen vacancies, *Industrial and Engineering Chemistry Research*. 59 (2020) 14606–14615. <https://doi.org/10.1021/acs.iecr.0c00188>.
- [69] H. Tan, S. Ma, X. Zhao, Y. Li, C. Zhao, Y. Zhu, Excellent low-temperature NH₃-SCR of NO activity and resistance to H₂O and SO₂ over W_aCeO_x (a = 0.06, 0.12, 0.18, 0.24) catalysts: Key role of acidity derived from tungsten addition, *Applied Catalysis A: General*. 627 (2021) 118374. <https://doi.org/10.1016/j.apcata.2021.118374>.
- [70] P.A. Spevack, N.S. McIntyre, Thermal Reduction of molybdenum trioxide, *The Journal of Physical Chemistry C*, 96 (1992) 9629-9035. <https://doi.org/10.1021/j100201a062>.
- [71] J. Liu, Y. Huo, X. Shi, Z. Liu, Y. Shan, Y. Yu, W. Shan, H. He, Insight into the remarkable enhancement of NH₃-SCR performance of Ce-Sn oxide catalyst by tungsten modification, *Catalysis Today*. 15 (2022) 36-44. <https://doi.org/10.1016/j.cattod.2022.02.001>.
- [72] R.M. Yuan, G. Fu, X. Xu, H.L. Wan, Brønsted-NH₄⁺ mechanism versus nitrite mechanism: New insight into the selective catalytic reduction of NO by NH₃, *Physical Chemistry Chemical Physics*. 13 (2011) 453–460. <https://doi.org/10.1039/c0cp00256a>.
- [73] R. Farra, S. Wrabetz, M.E. Schuster, E. Stotz, N.G. Hamilton, A.P. Amrute, J. Pérez-Ramírez, N. López, D. Teschner, Understanding CeO₂ as a Deacon catalyst by probe molecule adsorption and in situ infrared characterisations, *Physical Chemistry Chemical Physics*. 15 (2013) 3454–3465. <https://doi.org/10.1039/c2cp42767b>
- [74] X. Li, X. Li, T. Zhu, Y. Peng, J. Li, J. Hao, Extraordinary Deactivation Offset Effect of

Arsenic and Calcium on CeO₂-WO₃ SCR Catalysts, *Environmental Science and Technology*. 52 (2018) 8578–8587. <https://doi.org/10.1021/acs.est.8b00746>.

- [75] B. Wang, M. Wang, L. Han, Y. Hou, W. Bao, C. Zhang, G. Feng, L. Chang, Z. Huang, J. Wang, Improved Activity and SO₂ Resistance by Sm-Modulated Redox of MnCeSmTiO_x Mesoporous Amorphous Oxides for Low-Temperature NH₃-SCR of NO, *ACS Catalysis*. 10 (2020) 9034–9045. <https://doi.org/10.1021/acscatal.0c02567>.

CHAPTER III

Novel vanadium supported on CeO₂ catalysts prepared by SOMC: Effect of precursors and vanadium loading on the activity for NH₃-SCR reaction

1 Introduction

To improve the combustion engine efficiency and minimize fuel consumption, modern diesel engine is operated at a lean fuel mixture, resulting in the emission significant amount of NO_x and causing eco-system damage[1,2]. Several engine technologies such as exhaust gas recirculation (EGR) and homogeneous charge compression ignition (HCCI), aimed to reduce the NO_x content of the upstream exhaust gas have resulted in a significant improvement in terms of NO_x diminution[3]. However, in order to meet the latest the emission standards, after-treatment devices appear to be the only solution[4]. Several downstream techniques of NO_x abatement have been developed such as NO_x storage reduction (NSR)[5], selective NO_x recirculation (SNR)[6], selective catalytic reduction (SCR) using different reducing agents (NH₃/urea or hydrocarbons)[7,8]. Japan is the first to employ NH₃-SCR technology in the 1970s. It has been widely employed for the catalytic removal of NO_x from stationary sources in the United States, Europe, and other nations and regions[2]. Lately, this technology is also implemented in mobile diesel engine vehicles.

The most common commercial catalyst, V₂O₅-WO₃/TiO₂, has been extensively investigated to gain a deeper understanding of the structure-activity relationship[9,10]. It is widely accepted that TiO₂ acts as the support, V₂O₅ (2-3 wt%) is considered to be the primary active moieties, and WO₃/MoO₃ (> 10 wt%) further promotes the thermal stability and activity[11]. As different vanadium species are found on the surface of the catalyst, their specific role in NH₃-SCR reaction is still controversial. Marberger and his co-workers[12] prepared a catalyst with 2 wt% V₂O₅, 10 wt% WO₃ supported on TiO₂ (formulation similar to the commercial catalyst) by consecutive impregnation. After investigation with time-resolved infrared and UV-visible spectroscopy, they proposed that the Lewis acid sites and the isolated mono-oxo vanadyl groups are the active acidic sites that participate in the catalytic cycle along with redox sites. On the other hand, the Brønsted acidic sites acted as the NH₃ reservoir. More specifically, isolated V⁵⁺ reduces in the presence of both NO and NH₃, the nitro-amide (NO_x-NH_x) intermediate and V-OH group were formed at the same time. After the decomposition of intermediates, V⁴⁺-OH is re-oxidized by oxygen. Choo and his co-workers[13] reported that sulfate accelerated the conversion of isolated vanadyl species to polymeric species. He and his co-workers[14] synthesized V₂O₅/TiO₂ by impregnation method using ammonium metavanadate and TiO₂ pretreated with ammonium sulfate. They demonstrated that the polymeric VO_x species dominated the NH₃-SCR instead of the monomeric vanadium species,

especially under low-temperature conditions. By DFT calculations, they explained the coupling effect of the polymeric structure shortens the reaction pathway for the regeneration of redox sites and decrease the reaction barrier.

In most vanadium-based catalysts, vanadium comprises from monomeric to polymeric vanadyl species. The distributions of the different species are thought to be closely connected to the precursors and the concentration of vanadium on the surface[12,15]. Youn and his coworkers[16] prepared a series of V_2O_5/TiO_2 catalysts by changing the oxidation state of vanadium precursors by adjusting the pH of the solutions. For catalysts with 5 wt% vanadium loading or higher, they found that precursor (V^{3+}) produced more highly coordinated polymeric vanadyl species on TiO_2 based on Raman and UV-Vis data compared to catalysts prepared from V^{4+} and V^{5+} precursors. Though the NO conversion appeared to be similar among the series of catalysts, N_2 selectivity of NH_3 -SCR reaction exhibited significant improvement when compared to [14,17] catalysts at the same loading prepared by V^{4+} and V^{5+} precursors. Bell and his colleagues[15] used in situ laser Raman to count the number of distinct VO_x species. They discovered that monomeric vanadium species (V^{5+}) accounted for 80% of the 1.3 wt% V_2O_5/TiO_2 content, while polymeric vanadium species climbed to 33% when the V loading was increased to 3.0 wt%. Their continuous investigation[14] reported that about ten times more specific activity exists with polymeric vanadate species than with monomeric vanadyl species. Moreover, polymeric species lead to a more important production of N_2O than monomeric vanadium species, and it increases with the amount of O_2 in the feed. Based on selected reports on TiO_2 supported SCR catalysts, there is already a strong contradiction between the structure-activity relationship and the assignment of the role of each species (monomeric vs polymeric).

Apart from the formulation used in the commercial catalyst, CeO_2 -based materials have largely been investigated for SCR catalytic systems, owing to the high oxygen storage capability, tunable textural properties, redox and acid/base properties[18,19]. From Chapter II, tungsten-oxo supported on ceria has been proved to be highly active and selective for NH_3 -SCR reaction. Importantly, the observed activity and selectivity can be solely assigned to the isolated tungsten bis-oxo moiety, which turns out to play the key role in NH_3 -SCR reaction over W-oxo/ CeO_2 . VO_x/CeO_2 is another encouraging system according to literatures. Pursued issues with vanadium supported on ceria systems are the volatility of V_2O_5 , this oxide being toxic once emitted and the nature of the active sites. Wu and his coworkers[20] tentatively

explored the nature of the active site on VO_x-MnO_x/CeO₂ (5 wt% VO_x) prepared by aqueous impregnation on mesoporous CeO₂. They optimistically attributed that the resulting material comprised dimeric (bridged) vanadium oxo species based on a broad ⁵¹V NMR signal and a weak Raman peak. The latter material displayed a notable enhancement of the NO conversion at low temperature compared to similar catalysts containing V₂O₅ phase (prepared similarly on lower surface area CeO₂). The authors further proposed that the improvement was due to the presence of dimeric VO_x moieties, offering abundant Brønsted and Lewis acid sites and subsequently promoting the acid cycle in the previously proposed NH₃-SCR mechanism. In a parallel work, the same groups investigated the VO_x-MnO_x system (5 wt% VO_x) supported on different ceria shapes (cube, polyhedral, rod). The preferred support was found to be ceria nano rod (with predominantly (110) facet exposed to the surface). The supported vanadium species was reported to be monomeric (based on a shoulder on the ⁵¹V MAS NMR spectrum and a weak Raman peak) and assigned it as the active site for the reaction[21]. Peng and his colleagues[22] studied highly loaded vanadium (up to 75 mol%) on ceria. Though CeO₂ was revealed as the only crystalline phase, Raman spectroscopy showed the presence of polymeric vanadium and CeVO₄ in this V_{0.75}Ce material. They further claimed that both vanadium species contribute to acidity: Lewis acid-sites (CeO₂ and polymeric VO_x) and Brønsted acid-site (defect sites on CeVO₄). Part of Lewis acid sites could convert into the Brønsted acid-sites at high temperature. Additionally, Lewis acid- sites are more stable than Brønsted acid sites under the thermal treatment used for NH₃ desorption. The authors believed that both species participate in the SCR reaction where the Lewis acidity is more important at low temperature, while the Brønsted acidity becomes essential at high temperature. Moreover, they found the presence of the different types of vanadium species depends on the vanadium content. This is consistent with the systematic investigation of the structure of vanadium oxide supported on ceria by Wu and his coworkers [23]. VO_x species interact preferably with ceria defect sites, causing reduction of such sites with respect to the neat ceria and may alter the electrical properties. Therefore, surface sites in ceria could anchor and stabilize several VO_x species, which may easily lead to complex systems with different VO_x species on the surface of ceria. On the other hand, with other supports, such as silica[24] and alumina[25,26], there was typically just one type of species visible at a particular vanadium loading.

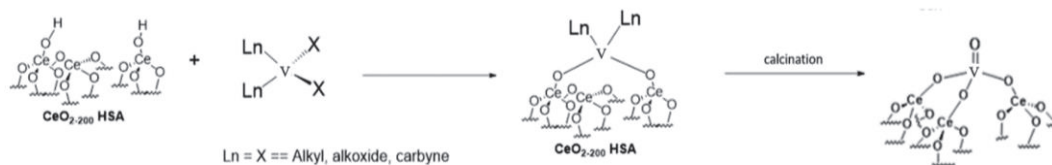
Published results have tentatively investigated the structure-reactivity relationship and the reaction mechanism. However, those reports are based on catalysts prepared by conventional

methods containing a mixture of different vanadium species (from monomeric to polymeric) on the surface during the catalytic investigations[14,27]. It is evidently impossible to assign the observed properties to a specific vanadium species. Moreover, catalysts containing mixed VO_x species are unsuitable for mechanistic investigations, especially for the study of the N-N bond formation which is rarely addressed in the literature.

More recently, catalysts comprising isolated transition metals have received substantial attention in this field. It is then reasonable to believe that a supported isolated vanadium catalyst may adapt to similar thermal resistance and simultaneously keep an exceptional SCR activity, and thereby giving a “V₂O₅” free vanadium catalyst. Avoiding V₂O₅ emission can open the way to developing sustainable and environmentally friendly vanadium-based SCR catalysts. A controlled manner to obtain isolated vanadium materials is through surface organometallic chemistry[28]. Contrarily to classical impregnation or chemical vapor deposition techniques which usually lead to uncontrollable surface species (extending from physisorbed precursors to fully decomposed species), this synthetic approach involves controlled grafting of a suitable organometallic precursor onto a given support, leaving behind a strongly anchored organometallic fragment on a solid[29]. Hence, isolated vanadium species supported on ceria can be achieved by judicious choice of the precursor on properly treated support. Moreover, low metal loading is usually sufficient to obtain highly active catalyst, which paves the way for the synthesis of well-defined vanadium species grafted on ceria and should help to elucidate a structure-reactivity relationship in NH₃-SCR of NO_x.

Owing to the inconsistency in the literature about the nature of the active site and addressing the stability of ceria supported vanadium species, this Chapter aims to synthesize several kinds of well-defined V-oxo/CeO₂ materials with low vanadium loadings through the SOMC approach. Encouraged by the positive results obtained in Chapter II, it will be ideal to employ a corresponding vanadium(V) complex as precursor. However, due to the instability of [VR₅] type homoleptic vanadium(V) complexes, heteroleptic vanadium(V) precursors and a homoleptic vanadium(IV) complexes are employed: the dimeric V⁵⁺ precursor [V(=O)(OEt)₃]₂, monomeric V⁴⁺ precursor [V(CH₂SiMe₃)₄], and monomeric V⁵⁺ precursor [V(=O)(OtBu)₃]. After calcination at 500 °C, ceria supported vanadium oxo are characterized by several techniques (DRIFT, Raman, solid state NMR, UV-Vis, XRD, XANES, HRTEM, BET, XPS, and Elemental analyses) in order to determine the structure of resulting species. The catalytic performance of V-oxo/CeO₂ in NH₃-SCR of NO_x prepared from different

precursors and with different V content have been evaluated in the temperature range of 150–600 °C.

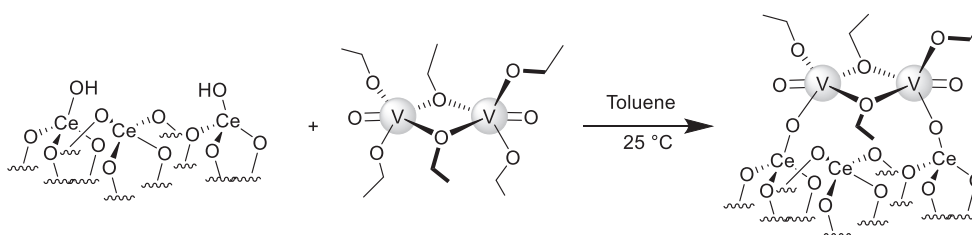


Scheme 1 Schematic illustration of the synthesized process for V-oxo/CeO₂

2 Preparation and characterization of V-oxo supported on CeO₂ using [V(=O)(OEt)₃]₂ as precursor

2.1 Preparation of [V(=O)(OEt)₃]₂/CeO₂₋₂₀₀ [V1-a]

Prior to the catalyst preparation, ceria (ceria Actalys HAS-5 Actalys 922 from Solvay (Rare Earth Laboratory, La Rochelle, France) is calcined at 500 °C, followed by rehydration and dehydroxylation at 200 °C. These experimental conditions are adapted from Chapter II, which after screening show to be the optimal ones for the pretreatment before the functionalization of CeO₂ surface with the methodology used in this study.



Scheme 2 Schematic illustration of the synthesis process of [V(=O)(OEt)₃]₂/CeO₂₋₂₀₀ [V1-a]

In the first step, a grafting reaction is performed using [V(=O)(OEt)₃]₂ precursor as shown in the [Scheme 2](#). [V(=O)(OEt)₃]₂ is commercially available. Though this precursor exhibits a dimeric structure, it is known that dimeric complexes may become monomeric once grafted onto a polar surface material[30]. The grafting reaction of [V(=O)(OEt)₃]₂ on CeO₂₋₂₀₀ is carried out in toluene at room temperature for 12 h. Unreacted complex [V(=O)(OEt)₃]₂ is washed off by filtration with toluene and rinsed with pentane. The supported vanadium complex, [V(=O)(OEt)₃]₂/CeO₂₋₂₀₀, [V1-a], is obtained as a grey powder after drying under vacuum and submitted for characterizations by Elemental analysis, DRIFT, SSNMR and EPR.

2.2 Characterization of $[V(=O)(OEt)_3]_2/CeO_{2-200}$ [V1-a]

2.2.1 Characterization of [V1-a] by Elemental analysis

Elemental analysis measurement is carried out on this material and reveals the presence of 2.16 wt% of V and 2.36 wt% of C respectively ($C/V = 4.6$). Given that the grafting reaction occurs via protonolysis, this corresponds to a partial consumption of surface hydroxyls (ca. 0.42 mmol OH/g, 60% of the initial surface O-H groups compared with the number of surface hydroxyls groups previously determined). The ethanol produced during the grafting is not evaluated, as it may remain adsorbed to the surface. Based on this result and previous experience (in Chapter II), it is reasonable to believe that the structure of the grafted vanadium ethoxy fragments in $[V(=O)(OEt)_3]_2/CeO_{2-200}$ could be a dimeric species (expected $C/V = 4$, the slightly higher experimental value is assigned to traces of strongly adsorbed ethanol derivatives) on the surface of ceria (Scheme 2).

2.2.2 Characterization of [V1-a] by DRIFT spectroscopy

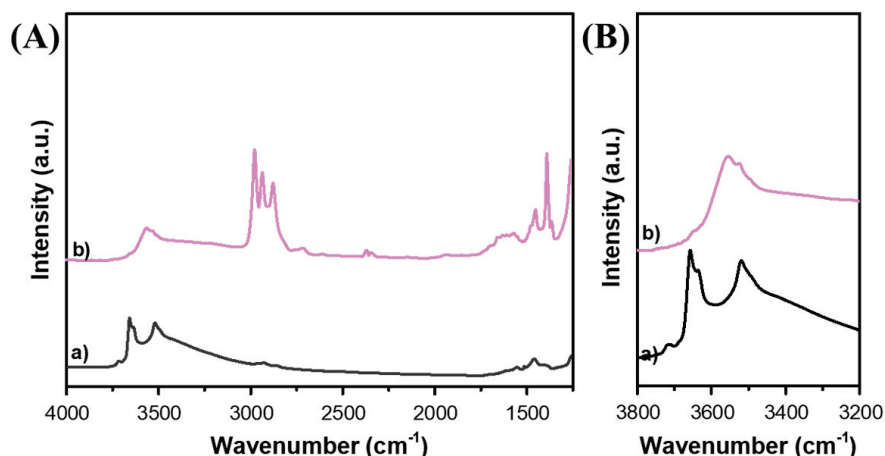


Fig. 1 (A) (4000-1250 cm^{-1}) DRIFT spectra and (B) enlarged (3800-3200 cm^{-1}) region of a) CeO_{2-200} ; b) [V1-a]

The grafting process is monitored by DRIFT spectroscopy, as shown in Fig. 1. From the enlarged infrared spectrum in the region of OH stretching vibration (Fig. 1B), ceria dehydroxylated at 200 °C, pictured in line a, shows four vibration bands previously attributed to different surface CeO-H groups. As described in Chapter II, the weak peak at 3712 cm^{-1} corresponds to isolated terminal OH group (μ^1 -OH). The dominant broad signal centered at 3660 cm^{-1} with a shoulder at 3640 cm^{-1} is assigned to bridged hydroxyl groups (μ^2 -OH), and the band at 3527 cm^{-1} corresponds to tridentate OH groups (μ^3 -OH). Upon the grafting reaction, μ^1 -OH has vanished, suggesting the high reactivity of μ^1 -OH in the protonolysis

process. In addition, part of the μ^2 -OH groups has also reacted. A component around 3550 cm^{-1} has appeared and is related to remaining μ^2 -OH in interactions with the grafted vanadium complex, resulting in a red-shift[31]. Nevertheless, the tridentate OH groups are preserved, confirming the selectivity of protonolysis on ceria support. Similar reactivity has been observed when $\text{W}(\equiv\text{C}t\text{Bu})(\text{CH}_2t\text{Bu})_3$ is grafted onto ceria dehydroxylated at 200 °C. Fig. 1A also displays new bands between 3000-2800 cm^{-1} and 1620-1400 cm^{-1} after functionalized with $[\text{V}(=\text{O})(\text{OEt})_3]_2$. They are characteristic of aliphatic $\nu(\text{C}-\text{H})$, $\delta(\text{CH}_2)$ and $\delta(\text{CH}_3)$ vibrations of the chemisorbed vanadium complex. These confirm the selective chemical reaction between surface hydroxyl groups of ceria and $[\text{V}(=\text{O})(\text{OEt})_3]_2$.

In addition, broad and unresolved IR bands extended from 1750-1550 cm^{-1} can be observed. IR absorption in this region generally corresponds to adsorbed water, aldehyde and acid molecules. In the literature, it has been reported that reduced ceria bearing reactive surface oxygen can catalyze ethanol dehydration and dehydrogenation reactions[32] giving water/ethylene/hydrogen and acetaldehyde, respectively as products. Most likely, such reaction has occurred during the grafting between the released ethanol and ceria support. To demonstrate the latter reaction, dehydroxylated ceria is reacted with dry ethanol in gas phase. Gas phase analysis reveals the presence of ethylene and traces of H_2 , which necessitates simultaneous production of water through dehydration and oxidation of the support. DRIFT analysis of ceria after reaction with ethanol shows two strong bands 1560 and 1420 cm^{-1} characteristic of carboxylate originating from total oxidation of ethanol[33,34]. Thus, the weak contribution of the unresolved absorption at 1750-1550 cm^{-1} should be related to minor amounts of water originating from the dehydration of ethanol, from acetaldehyde and acetic acid obtained after partial oxidation of ethanol. Consequently, the adsorbed water also contributes to the broad peak in the $\nu(\text{OH})$ region.

2.2.3 Characterization of [V1-a] by solid state NMR

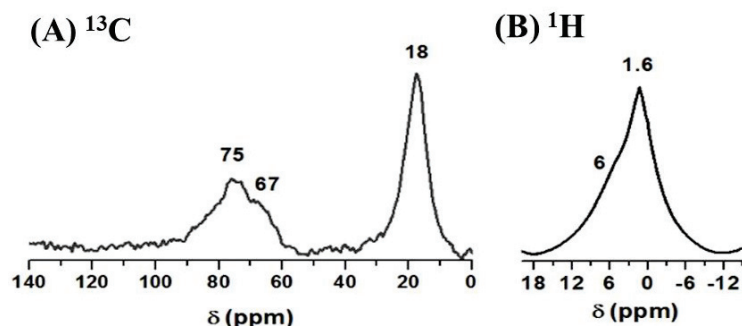


Fig. 2 (A) ^{13}C CP MAS and (B) ^1H MAS solid states NMR spectra of the [V1-a]

^1H MAS and ^{13}C CP MAS solid state NMR are used to characterize [V1-a], notably to identify the nature of the organic ligand. ^1H MAS NMR spectrum (Fig. 2B) shows a broad signal with a maximum at 1.6 ppm and a shoulder at ca. 6 ppm, tentatively attributed to methyl ($-\text{OCH}_2\text{CH}_3$) and the overlapping of methylene ($-\text{OCH}_2\text{CH}_3$) of the ethoxy ligands and unreacted ceria hydroxyls. Moreover, ^{13}C CP MAS NMR data (Fig. 2A) enable discerning between the bridging ($\mu^2-\text{OCH}_2\text{CH}_3$) and terminal ($-\text{OCH}_2\text{CH}_3$) ethoxy groups, featuring resonances at 67 and 75 ppm, respectively. In addition, an intense peak at 18 ppm is assigned to the terminal methyl groups. It should be pointed out that though all peaks are relatively broad, no significant shift with respect to the molecular complex is observed, supporting the fact that dehydration and oxidation of the ceria support have occurred. Thus, no significant perturbation of the NMR spectra (contrary to the results presented in Chapter II involving the grafting of a tungsten tris-alkyl alkylidyne complex) is most likely related to the oxidation of the paramagnetic surface Ce^{3+} species. This observation implies that vanadium oxo tris-ethoxide complex of vanadium oxo ethoxide is successfully grafted and preserves a dimeric nature, as already indicated by mass balance analysis.

2.2.4 Characterization of [V1-a] by Electron Paramagnetic Resonance

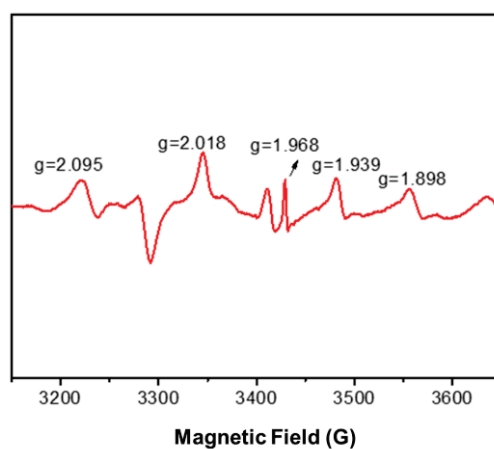


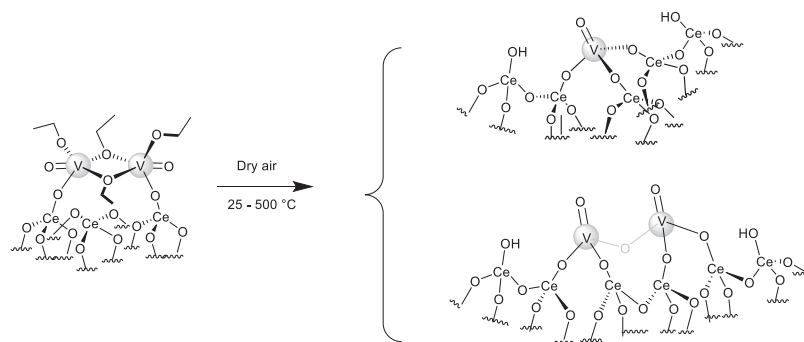
Fig. 3 EPR spectra of [V1-a] recorded at room temperature

Electron paramagnetic resonance (EPR) is carried out to probe paramagnetic species of [V1-a]. From literature[35], the ability of oxygen migration from the subsurface in ceria-containing materials is directly related to the concentration of defective sites. After functionalization with $[\text{V}(=\text{O})(\text{OEt})_3]_2/\text{CeO}_{2-200}$, the intensity of the different signals in the EPR spectrum becomes weak with several new signals assignable to different O_2^- defects[34], which show signals similar to those observed for $[\text{W}(=\text{C}t\text{Bu})(\text{CH}_2t\text{Bu})_3]/\text{CeO}_{2-200}$. As

demonstrated earlier, ethanol reacts with dehydroxylated ceria[32,36], giving ethylene and water, along with oxidation of the support. As already indicated by solid state NMR, the ethanol released upon grafting reacts with ceria oxidating Ce^{3+} , thus decreasing the paramagnetism of the sample (as evidenced by EPR in Fig. 3, which is enlarged to show the quite weak intensity) and giving water (as indicated in the DRIFT spectrum (Fig. 1B) by the broad band centered at 1620 cm^{-1}). However, [V1-a] do not exhibit any isolated V(IV) ion signal in EPR with an expected g factor between 1.94-1.99[37], suggesting that vanadium remains at the oxidation state V(V).

The grafting of $[\text{V}(=\text{O})(\text{OEt})_3]_2$ onto ceria dehydroxylated at $200\text{ }^\circ\text{C}$ occurs through protonolysis and ethanol release, resulting in vanadium oxo ethoxide surface species revealed by Elemental analysis, DRIFT and solid state NMR. Elemental analysis, EPR and solid state NMR suggested that the grafted species comprises a monopodal dimeric vanadium(V) oxo ethoxide species, as illustrated in Scheme 2. EPR and solid state NMR further indicate that the grafting reaction causes a loss of the paramagnetism of the support, which is explained by dehydration of the released ethanol.

2.3 Preparation of V-oxo/CeO₂ [V1-b] from $[\text{V}(=\text{O})(\text{OEt})_3]_2/\text{CeO}_2\text{-}200$ [V1-a]



Scheme 3 Schematic illustration of the synthesis process of V-oxo/CeO₂ [V1-b] from $[\text{V}(=\text{O})(\text{OEt})_3]_2/\text{CeO}_2\text{-}200$

From literature, supported vanadium sites surrounded by oxygen are generally used to investigate the $\text{NH}_3\text{-SCR}$ reaction. However, a reliable and convincing structure of the active species obtained from classic preparation procedures such as impregnation is hardly provided due to the presence of a mixture of different surface species. In particular, the distribution of vanadium between these different surface species varies depending on the vanadium loading which contributes to a different $\text{NH}_3\text{-SCR}$ reactivity between materials. Thus, the ultimate goal is to obtain uniquely one well-defined and stable vanadium oxo species (monomeric or dimeric in this case), though different species can hypothetically be formed after calcination

(Scheme 3). The grafted dimeric vanadium precursor on CeO₂₋₂₀₀ (pre-catalyst) are calcined under dry air, at 500 °C for 18h in the second step. The material after calcination is mentioned as [V1-b]. It is characterized by Elemental analysis, DRIFT, SSNMR, XPS, EPR and XANES.

2.4 Characterization of V-oxo/CeO₂ [V1-b]

2.4.1 Characterization of [V1-b] by Elemental analysis and DRIFT spectroscopy

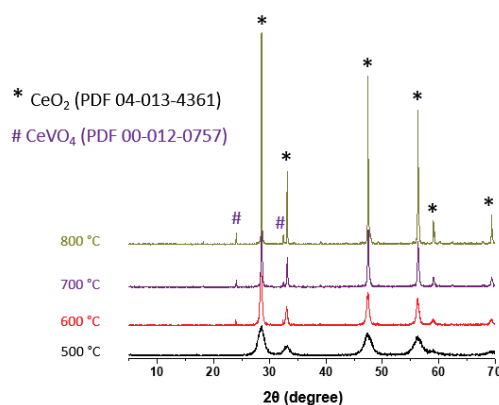


Fig. 4 XRD patterns of [V1-b] calcined at different temperature

Calcination of [V1-a] gives a yellow powder referred as [V1-b], with 2.11 wt% vanadium, and less than 0.1 wt% carbon according to the results from Elemental analysis. These results suggest that the anchored vanadium is stable during the calcination process, while the organic fragments in [V1-a] are removed during the oxidation and thermal treatment process. After extensive studies, the optimal calcination temperature for [V1-a] is 500 °C, instead of 600 °C (for W-oxo/CeO₂). Applying calcination temperatures above 500 °C results in physical changes, such as the color of the sample which turns to dark brown, characteristic of CeVO₄ and revealed by XRD (Fig. 4), and a drop in the BET surface area.

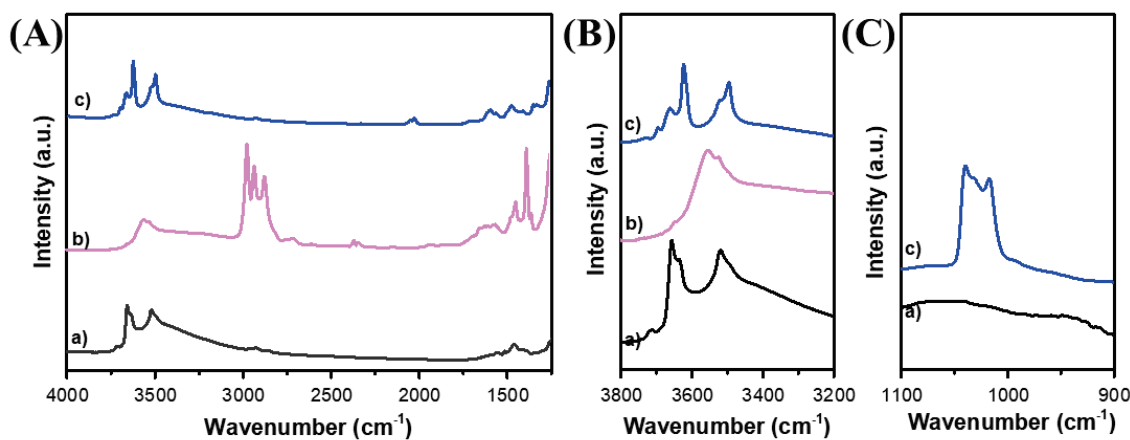


Fig. 5 (A) (4000-1250 cm⁻¹) DRIFT spectra, (B) enlarged (3800-3200 cm⁻¹) region, and (C) enlarged (1100-900 cm⁻¹) region of a) CeO₂₋₂₀₀; b) [V1-a]; c) [V1-b]

As shown in Fig. 5, DRIFT is used to investigate the oxidation and calcination process. Obviously, the absence of the $\nu(\text{C-H})$ and $\delta(\text{CH}_x)$ bands in [V1-b] indicates the total decomposition of the organic fragments. On the other hand, there is a notable change in the $\nu(\text{O-H})$ region, highlighted in Fig. 5B. After calcination, parts of the terminal OH groups at 3720 cm^{-1} ($\mu^1\text{-OH}$) that have been consumed during the grafting process are regenerated. Apart from the slight red shift in all kinds of hydroxyl groups, the relative intensities of $\mu^1\text{-OH}$, $\mu^2\text{-OH}$, $\mu^3\text{-OH}$ have changed. Similar features have also been observed in Chapter II. Moreover, new peaks have appeared around $1050\text{-}1000\text{ cm}^{-1}$ (Fig. 5C), associated with different $\nu(\text{V=O})$ modes. Detailed assignments are provided in section 3.2.

2.4.2 Characterization of [V1-b] by Raman spectroscopy

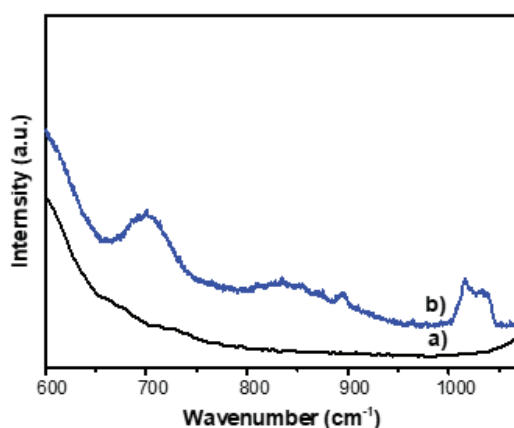


Fig. 6 Raman spectroscopy of a) $\text{CeO}_2\text{-200}$; b) [V1-b]

To gain more insights in the structure of [V1-b], the material has been analyzed by Raman spectroscopy. As shown in Fig. 6, $\text{CeO}_2\text{-200}$ shows no peak in the region between $600\text{-}1000\text{ cm}^{-1}$. For [V1-b], there is a noticeable peak at 700 cm^{-1} and a broad peak centered at 837 cm^{-1} , as reported in literature, assigned to V-O-Ce bridging modes[23,38]. The unresolved absorption at $1033\text{ - }1015\text{ cm}^{-1}$ is characteristic of V=O stretching modes (monomeric and dimeric species) of surface-dispersed vanadium[23]. In contrast, the characteristic peaks at 930 cm^{-1} (V-O-V in polyvanadate), 860 cm^{-1} (Ce-O-V in CeVO_4) and 994 cm^{-1} (V=O in V_2O_5) are not observed for [V1-b], revealing that the vanadium species after calcination in [V1-b] is mainly composed of highly-dispersed monomeric and dimeric species.

2.4.3 Characterization of [V1-b] by ^{51}V MAS solid state NMR

^{51}V MAS solid state NMR is a powerful method to identify surface vanadium species. In general, the chemical shift of vanadium(V) species is extremely large and can fall in the range of 1200 to -900 ppm, depending on the coordination environment. Matta and his co-workers[39] identified different oxidized vanadium species (distorted octahedral V–O–V chains, distorted tetrahedral sites, V_2O_5 , CeVO_4) from the isotropic chemical shift by ^{51}V NMR. The ^{51}V MAS NMR by [V1-b] is carried out under two different spinning rates (7 kHz, 10 kHz) in order to localize the ^{51}V signal of [V1-b] and spinning side bands. Fig. 7 reveals that the main signal (fairly broad) is situated at -576 ppm with a shoulder at -621 ppm. According to the literature, the nature of oxide supports, such as crystal phase, and even exposed facet, can have a significant impact on the geometric and electrical structure of the VO_4 tetrahedron[40]. For instance, monomeric vanadium (tripodal oxo moiety) supported on silica gives a shift at -670 ppm[41]. In titania, an isolated dimeric VO_4 moiety in a distorted tetrahedral configuration gives a resonance at -555 ppm, and the shoulder at about -630 ppm is assigned to disordered octahedral V^{5+} ions that are significantly interacting with titania's surface[40]. On the other hand, VO_x supported on ceria ($\text{V}/\text{Ce}=0.1$) displays a signal at -565 ppm, attributed to vanadium species in polyhedron environment with a C_{4v} symmetry[42]. Thus, the observed signal at -576 ppm is tentatively attributed to isolated (monomeric and dimeric) and oligomeric vanadium species, respectively (see section 3.2.3 for detailed assignments)[14,43]. Noteworthy, CeVO_4 , with an expected signal at -427 ppm[39], and crystalline V_2O_5 (resonance at -610 ppm[40]) are absent from [V1-b] ^{51}V spectrum. This result is consistent with those from DRIFT and Raman that [V1-b] comprises a mixture of different vanadium species where the major species are isolated.

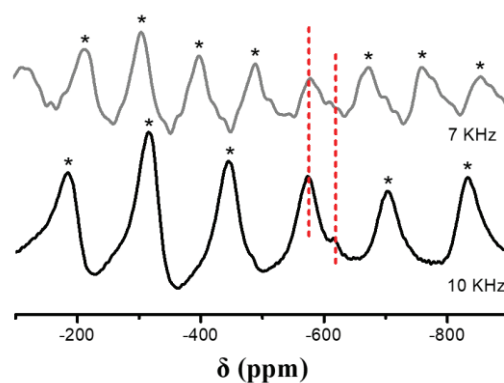


Fig. 7 ^{51}V MAS NMR spectra of [V1-b] under different spinning rates

2.4.4 Characterization of [V1-b] by X-ray photoelectron spectroscopy

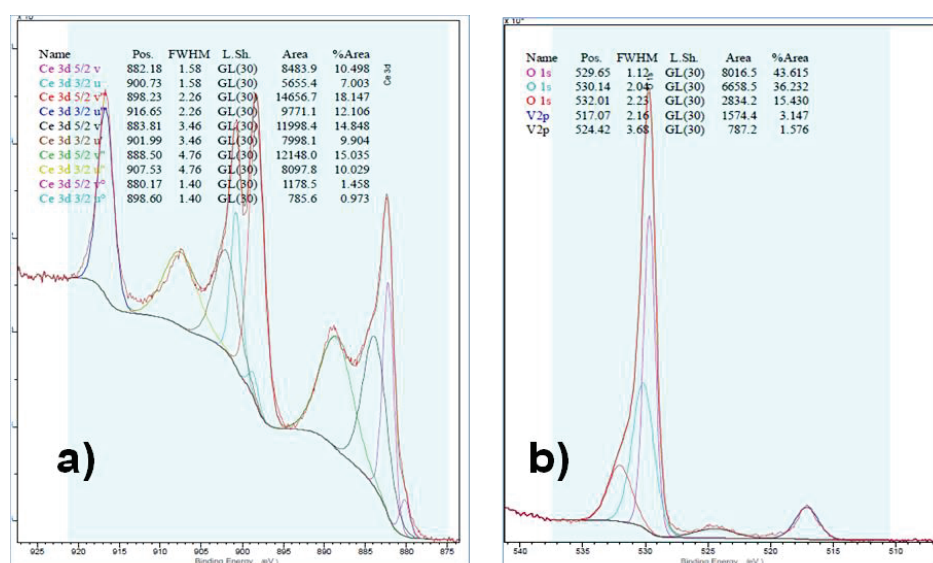


Fig. 8 XPS spectra of Ce 3d (a), O 1s and V 2p (b) of the catalyst [V1-b]

As depicted in Fig. 8, the surface composition and the oxidation states of different elements in [V1-b] (2.1 wt% loading on vanadium supported on ceria) are analyzed by XPS. Due to the pairs of spin-orbit doublet and a mixed 4f L^{n-1} configuration, the Ce 3d region shows ten features in general, consisting of Ce^{3+} and Ce^{4+} . Six of these peaks are associated with Ce^{4+} labeled v, v'', v''' ($3d_{5/2}$) and u, u'', u''' ($3d_{3/2}$). Another four peaks (u₀, u', v₀, v') are attributed to Ce^{3+} . According to literature[44,45], peak u''' at 916.5 eV is typical for Ce^{4+} and absent for Ce^{3+} . The peak area and ratio of Ce^{3+} are estimated and shown in Table 1. The percentage of u''' followed the order: $CeO_{2-200} > [V1-b]$, while evidently, the Ce^{3+} surface concentration follows the reverse order. Thus, more Ce^{3+} is presented in the [V1-b] compared to CeO_{2-200} . Such results may be caused by surface reconfiguration of cerium oxide (vanadium addition and thermal treatment). From Fig. 8b, the O 1s spectrum exhibits three binding energies at 529.6, 531, and 532 eV assigned to lattice oxygen and two different kinds of surface oxygen (O^{2-} hydroxide with different environment, which is related to oxygen vacancies)[46]. The spectrum fittings also highlight the presence of both V 2p_{3/2} and V 2p_{1/2} of V(V) with Binding energy values at 517 and 524 eV. This indicates that all vanadium species are present at the oxidation state V(V).

Table 1 Peak resulting from the deconvolution of XPS Ce 3d

Samples	u'''[a]	Ce ³⁺ [a]	O _a [a]
CeO ₂₋₂₀₀ [b]	14.2%	20.6%	19.1%
V1-b	12.1%	27.2%	54.2%

$$[a] \%Ce^{3+} = (Ce^{3+}/(Ce^{4+} + Ce^{3+}))$$

$$\% u''' = ([u'''] / ([u_0] + [u] + [u'] + [u''] + [v_0] + [v] + [v'] + [v''] + [v''']))$$

$$\%O_\alpha = (1 - (O_\beta + (O_\alpha + O_\beta + O_\gamma)))$$

$$\%V^{4+} = (V^{4+}/(V^{4+} + V^{5+})).$$

[b] CeO₂₋₂₀₀ from section 2.5 in Chapter II.

2.4.5 Characterization of [V1-b] by Electron paramagnetic resonance

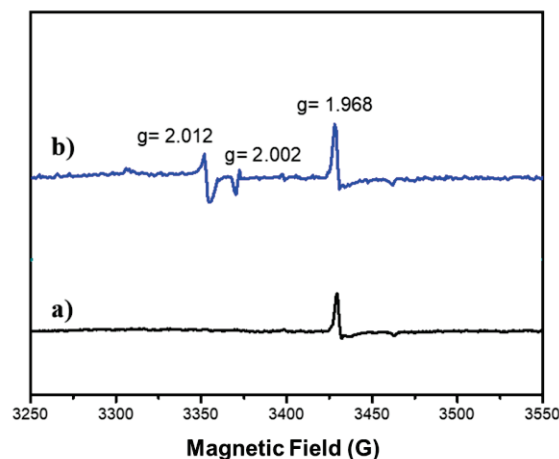


Fig. 9 EPR spectra of (a) CeO₂₋₅₀₀, (b) [V1-b]

In order to deeply investigate the paramagnetic species in the sample [V1-b], EPR analyses of reference CeO₂₋₅₀₀ and [V1-b] are compared. According to previous studies, CeO₂-based materials generally show a characteristic signal with $g=1.968$, which is related to the Ce³⁺-O-Ce⁴⁺ types of defective sites and quasi-free electrons[35]. As Ce³⁺ is generally difficult to be directly observed by EPR, its presence is usually associated with Ce⁴⁺-O₂⁻ originating from the reaction with oxygen, in which the coordinative unsaturated Ce³⁺ centers are active to oxygen adsorption[47]. Previous investigations report that the presence of other metal ions in the second coordination sphere will affect the g value ($g_e=2.0023$) of superoxide species attached to Ce centers by increasing the covalent character of the bond between π^* orbitals of the superoxide and Cerium, especially in the (111) plane[48]. Nevertheless, Fig. 9 confirms the absence of V⁴⁺ (expected with g factor between 1.94-1.99[37]) in [V1-b] and vanadium is probably present in its maximum oxidation state V⁵⁺, as also suggested by XPS. It's hard for V⁵⁺ to donate electrons to O₂ to form superoxide radicals. The approximate parameters $g=2.012$ and $g=2.002$ result from the adsorption of O₂ on cerium centers interacting with a vanadium atom.

2.4.6 Characterization of [V1-b] by X-ray absorption spectroscopy

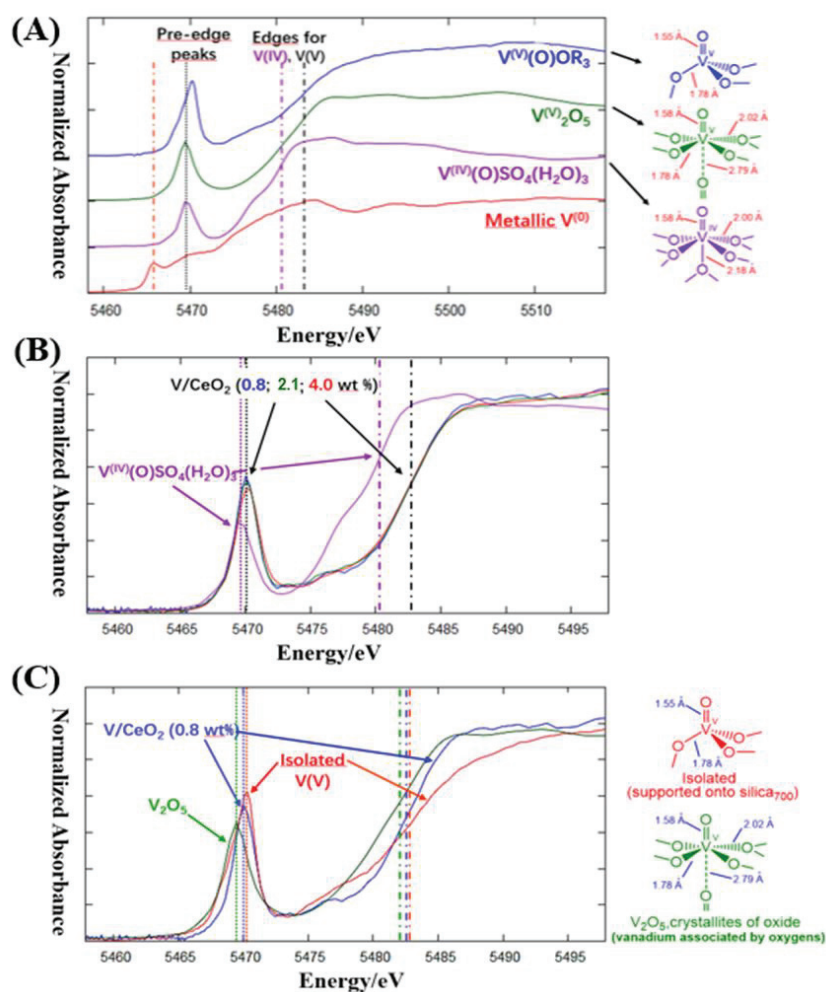


Fig. 10 (A) V K edge XANES analysis of references molecular complexes $V^V(=O)(OtBu)_3$, molecular complex $V^{IV}(=O)SO_4(H_2O)$, V_2O_5 and metallic V^0 . XANES profiles spectra of CeO_2 supported vanadium samples [V1-b] with different loading (0.8 wt%, 2.1 wt%, 4.0 wt %) compared to (B) molecular complex of V(IV) and (C) V_2O_5 and $V^V(=O)(OtBu)_3$ supported on SiO_2-700

X-ray Absorption Near Edge Structure (XANES) is conducted to extract additional information on vanadium coordination geometry (structural environment and oxidation state). For vanadium, the pre-edge peak originates from the electron transitions from 1s core levels to the empty 3d orbitals, or 4p hybridized by the ligands[49]. Fig 10A shows V K edge XANES analysis of references molecular complexes $V^V(=O)(OtBu)_3$, molecular complex $V^{IV}(=O)SO_4(H_2O)$, V_2O_5 and metallic V^0 . Previous experiences have shown that V K-edge XANES when taking into account the intensity of the pre-edge and its absolute position may provide reliable data on the oxidation state and its symmetry[50]. In Fig. 10A, the XANES

spectrum of metallic V^0 is significantly different with respect to the oxidized references. Moreover, there is a slight shift between tetrahedral V^V molecular complex $V(=O)(OtBu)_3$ versus the square pyramid V^V in V_2O_5 , which means that the coordination geometry has an effect on the peak position. Generally, the resonance edge is considered to further determine the oxidation state and symmetry. The position of K-edge for vanadium (electronic transitions from 1s to 4p) is different in molecular complex of V(V) and V(IV).

To clarify the structure of vanadium species, V K-edge XANES analyses of **[V1-b]** with different loading (prepared in the same manner) are compared in Fig. 10B. Unfortunately, it is impossible to extract the EXAFS data due to the overlap in energy with the Ce L_{III} -edge and V K-edge. Samples with different V loading give similar spectra. Compared to the given vanadium references (Fig. 10C), **[V1-b]** is situated between the isolated V(V) (molecular complex $V^V(=O)(OtBu)_3$) and $V^V_2O_5$, and notably far from the V^{IV} and V^0 references. Thus, XANES analysis suggests that the vanadium in **[V1-b]** is mainly constituted by V(V) species. However, the XANES spectrum of **[V1-b]** is somewhat different from those of V_2O_5 and isolated silica-supported tetrahedral $V^V(=O)(OtBu)_3$ complex after a careful comparison (Fig. 10C). As the EXAFS data are inhibited by the presence of Ce, the XANES analysis can only suggest that **[V1-b]** comprises V^V species (unique or mixture), most likely with low degree of polymerization of vanadium.

In summary, the calcination of the supported dimeric vanadium precursor in **[V1-a]** at 500 °C results in **[V1-b]** material containing a mixture of different vanadium species, mostly in an isolated form (monomeric and dimeric), according to DRIFT, Raman and ^{51}V MAS NMR spectroscopies. Moreover, XPS, EPR and XANES confirm that vanadium is mainly in oxidation state V. Hence, the grafted vanadium precursor seems to be mobile during the calcination process and tends to agglomerate in some extent, resulting in a mixture of different VO_x surface species, though the majority seems present as isolated sites (monomeric and dimeric). This behavior is different with respect to the tungsten system described in Chapter II, where the calcined sample still exhibits species with a monomeric nature. The different behavior is most likely related to a difference in the M-O (M = V or W) bond energy between the metal and s surface oxygen O of the ceria surface.

3 Investigation of NH₃-SCR Catalytic performance

3.1 Catalytic performance of [V1-b] for NO conversion and N₂ Selectivity

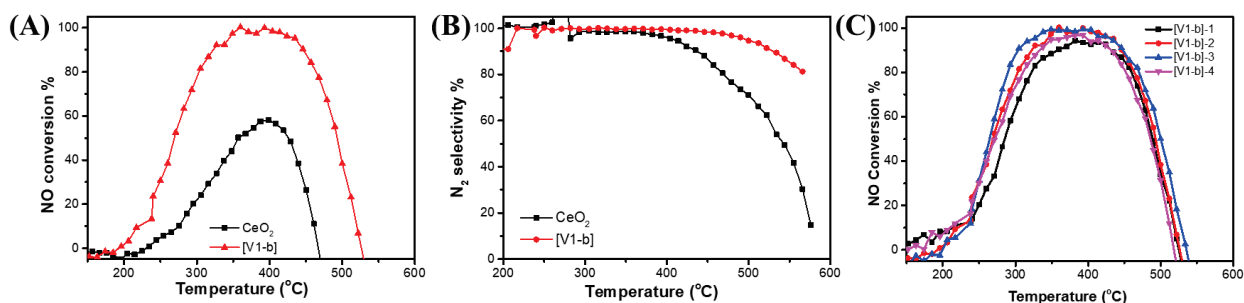


Fig. 11 (A) NO conversion, (B) N₂ selectivity and (C) cycle stability of [V1-b]

The catalytic behavior of [V1-b] (2.1 wt% loading on vanadium supported on ceria) is evaluated in NH₃-SCR reaction. A continuous fixed-bed type reactor is used under the following gas mixture: 350 ppm NH₃, 300 ppm NO and 12% O₂ in He. The reactor was heated from room temperature to 650 °C with a total flow of 300 mL/min, and the concentration of NO, NO₂, N₂O and NH₃ are recorded by gas phase FT-IR (from a calibration). From Fig. 11A, bulk ceria only shows 58% NO conversion at 400 °C, while [V1-b] exhibits an obvious enhancement of the activity and a broader operation temperature window (over 90% NO conversion between 300-400 °C). Also, N₂ selectivity with [V1-b] is improved, especially in the high temperature region (> 400 °C), suggesting that the oxidation of NH₃ is reduced after the addition of V. Furthermore, no significant change in the conversion profile is observed for [V1-b] after 4 consecutive cycles (catalytic test according to the given conditions; cooling under a flow of Ar; repeated catalytic test), indicating that the catalytic activity of [V1-b] is stable under the given conditions without apparent loss of vanadium.

3.2 Effects of vanadium loading

Current results are indeed encouraging. However, due to a lack of strong evidences for the structural description of the surface sites (notably by EXAFS) and reasonable comparison of the catalytic activity, it is difficult to establish a structure-activity relationship for [V1-b]. Hence, a series of catalysts prepared in the same manner (utilizing [V(=O)(OEt)₃]₂ as precursor), but with different vanadium loadings (0.2, 1.2 and 4 wt% vanadium) has been synthesized and investigated (structure and catalytic performance).

3.2.1 Effects of vanadium loading on catalytic activity

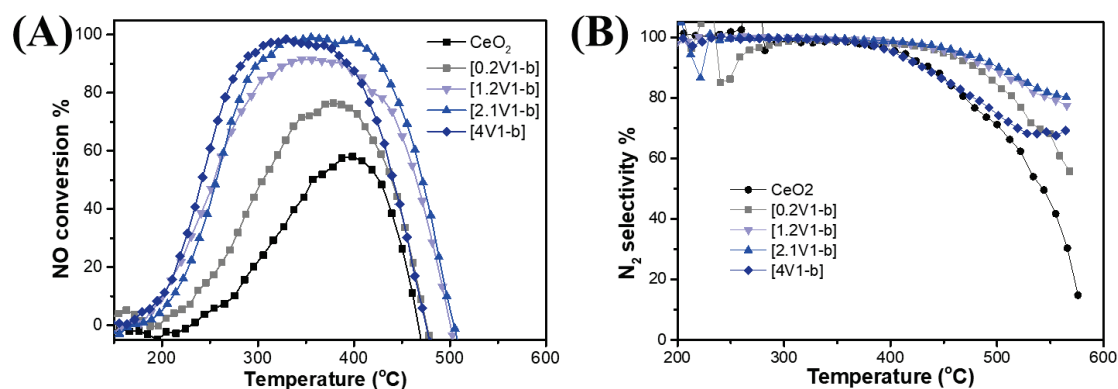


Fig. 12 (A) NO conversion and (B) N₂ selectivity of various vanadium loading of [V1-b]

NH₃-SCR activities of bulk CeO₂, [0.2V1-b], [1.2V1-b], [2.1V1-b] and [4V1-b] catalysts as a function of temperature are presented Fig. 12A. Obviously, the series of [V1-b] catalysts show better catalytic performance than bulk CeO₂, confirming that the addition of vanadium improves the NH₃-SCR activity. Nevertheless, a clear tendency is observed as a function of vanadium loading (under the same GHSV). For instance, only 72% and 91% of NO conversion are obtained at 350 °C over [0.2V1-b] and [1.2V1-b], while full NO conversion are registered over [2.1V1-b] and [4V1-b]. Noteworthy, when the amount of V increased from 0.2 wt% to 4 wt %, the mainly enhancement in catalytic activities lies in the low temperature region. [4V1-b] exhibits the best catalytic performance before 300 °C. However, NO conversion starts to decay from about 400 °C, featuring a slightly lower thermal robustness than [2.1V1-b]. Also, [2.1V1-b] shows the broadest operation temperature window (>90% NO conversion in the 290-430°C temperature range). In addition, the N₂ selectivity is promoted with the increase of vanadium loading upto [2.1V1-b]. [4V1-b] shows the lowest N₂ selectivity, which is even inferior to that of CeO₂. Referring to reports in literature, bulk VO_x usually shows low catalytic performances at high temperatures, and gives a narrow operation temperature window[51]. It seems that increasing the vanadium loading will enlarge the supported VO_x phase (or favors the polymerization degree of vanadium species), which is expected. The observed results also show that increasing the vanadium loading enhances the NH₃-SCR activity at low temperature. However, [4V1-b] shows a decreased activity in a high temperatures domain ($\theta > 350^{\circ}\text{C}$) than [2.1V1-b], which is found to be the optimal loading for this system since it exhibits the best catalytic performance in both ranges of temperature. To shed light on the structure-activity relationship in V-oxo/CeO₂ system, this series of vanadium-based catalysts has been submitted to further characterization studies.

3.2.2 Investigation of surface species by DRIFT spectroscopy

IR spectroscopy is a sensible technique to probe local structures. Concerning the series of [V1-b] with different vanadium loadings, clear evolutions in the $\nu(\text{O-H})$ and $\nu(\text{V=O})$ regions are observed, as shown in Fig. 13. Upon calcination, several Ce-OH groups have been regenerated due to the decomposition of alkoxide ligands, most likely through V-OH intermediates followed by a transfer of OH-groups to the support[41]. The population of OH-groups after calcination is dependent on the vanadium loading. μ^1 -type OH is hardly regenerated and μ^2 and μ^3 types Ce-OH are clearly visible. There are further two kinds of μ^2 and μ^3 types Ce-OH, with bands at 3640 cm^{-1} (μ^2) and 3501 cm^{-1} (μ^3) that seem to be more persistent upon increasing the vanadium content. These results suggest that bridged hydroxyls are preferably regenerated after calcination. In the case of [4V1-b], more μ^3 -OH are found than μ^2 -OH, suggesting the formation of polymeric species.

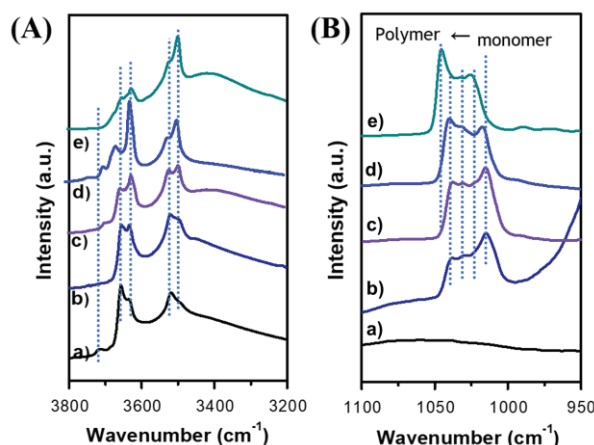


Fig. 13 (A) DRIFT spectra in region (A) $3800\text{--}3200\text{ cm}^{-1}$ and (B) $1100\text{--}950\text{ cm}^{-1}$ for catalysts: (a) CeO_{2-200} , (b) [0.2V1-b], (c) [1.2V1-b], (d) [2.1V1-b], (e) [4V1-b]

Important information can be extracted from the unresolved bands around $1050\text{--}1000\text{ cm}^{-1}$, assigned to $\nu(\text{V=O})$, Fig. 13B. According to previous studies[23,52], absorptions in this region can be associated with $\nu(\text{V=O})$ of vanadium mono oxo moieties with different degree of V-O-V aggregation. As increasing the degree of polymerization used to increase the energy of the absorption maximum. The unresolved bands are ambitiously decomposed to five peaks at $1046, 1039, 1032, 1024$ and 1016 cm^{-1} , attributed to surface mono-oxo O=VO_3 sites of polymeric, oligomeric, trimeric, dimeric and monomeric structures, respectively[23]. Deconvolution of the $\nu(\text{V=O})$ signals is shown in Fig. 14. Generally, the intensities increase with the rise of vanadium content, reflecting that more surface oxo species are formed. When comparing the relative intensities of the signals, it practically appears that the component at

1016 cm^{-1} is the major species in the samples with 0.2 and 1.2 wt% of vanadium. Upon increase of the vanadium amount, the peaks at 1032 cm^{-1} and 1039 cm^{-1} steadily grow, which suggests that oligomeric species are formed when adding vanadium. The polymeric vanadyl species only appears in the case of [4V1-b], indicating an oversaturation of the surface with vanadium (with respect to the surface area) results in polymeric vanadium species. The ratio between different species has been tentatively estimated from the deconvoluted data (assuming the same extinction coefficient and normalized with respect to $\text{O}=\text{VO}_3$ groups). The results are shown in Table 2. Despite the rough estimation, a clear and reasonable tendency is observed. At vanadium loading lower than 2.1 wt%, monomeric $\text{O}=\text{VO}_3$ is the major species. In the case of over-saturation, in [4V1-b], the vanadium tends to agglomerate, giving different surface species (from monomeric to polymeric) with the dimeric $\text{O}=\text{VO}_3$ as the major species. Moreover, these results indicate that vanadium is extremely mobile on ceria during the calcination, as minor amounts of agglomerates are observed even for low vanadium loadings.

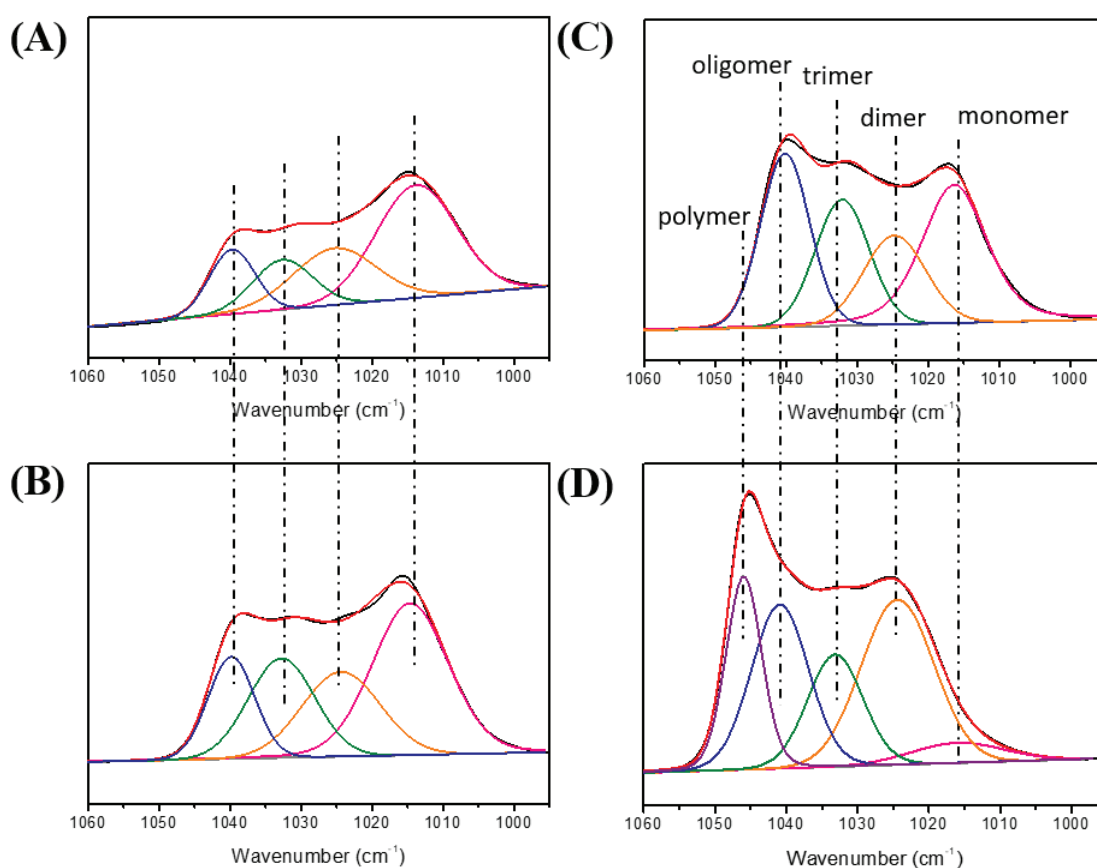
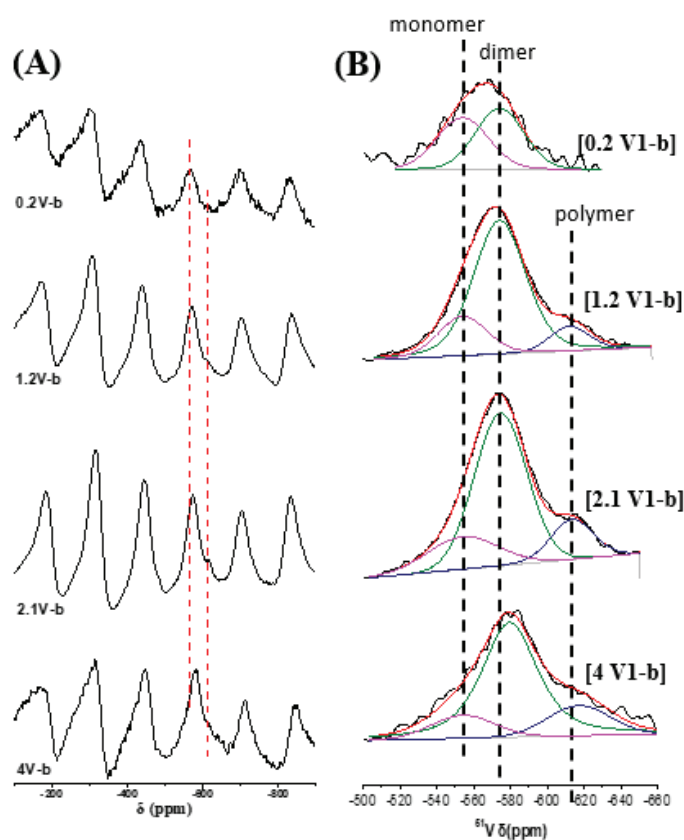


Fig. 14 Decomposition of DRIFT spectra of catalysts with different V loading, (A) [0.2V1-b], (B) [1.2V1-b], (C) [2.1V1-b], (D) [4V1-b]

Table 2 Relative ratio of different vanadium species in deconvolution of DRIFT

V loading	Monomer (1016 cm ⁻¹)	Dimer (1024 cm ⁻¹)	Trimer (1032 cm ⁻¹)	Oligomer (1039 cm ⁻¹)	Polymer (1046 cm ⁻¹)
0.2	68.4%	18.6%	7.5%	5.5%	N
1.2	64.9%	17.0%	11.7%	6.4%	N
2.1	59.0%	15.9%	12.9%	12.2%	N
4	6.2%	48.1%	14.6%	17.4%	13.6%

3.2.3 Investigation of surface species by ⁵¹V MAS NMR

**Fig. 15** (A) ⁵¹V MAS NMR spectra and (B) the corresponding deconvolution of [V1-b] with different loading

⁵¹V MAS NMR is a powerful technique to shed light on the coordinating sphere and geometry of supported vanadium species. He and his colleagues[27] used ⁵¹V MAS NMR to calculate the relative percentage of the different surface vanadium species after introduction of different ammonium sulfate concentration for V₂O₅/TiO₂ catalysts. Higher degree of vanadium polymerization results in a shift of ⁵¹V signal towards higher fields. Thus, the series of [V1-b] catalysts has been analyzed by ⁵¹V MAS NMR for complementary quantifications of the different vanadium surface species and to correlate the spectroscopic features with the

structures. From Fig. 14A, it can be seen that the chemical shift of the main peak shifts significantly to high field with the rise of vanadium surface densities. In addition, the shoulder at high field becomes more pronounced. A similar shift towards higher field upon increasing vanadium loading has already been observed for V₂O₅/CeO₂ and V₂O₅/TiO₂ materials[40]. Applying the same assumption as for DRIFT, three components have been defined and associated with monomeric, dimeric, trimeric, oligomeric and polymeric vanadium species. The proportion of the different components can similarly be estimated after deconvolution. Although the absolute values obtained by ⁵¹V MAS NMR are somewhat different from those obtained by DRIFT. Deconvolution of the main ⁵¹V NMR signal is frequently applied in literature and appears to be more reliable than DRIFT. The monomeric species is the major one at low vanadium contents. Increasing the vanadium loading results in a gradual increase of dimeric and oligomeric species. Polymeric species are only found for [4V1-b].

Table 3 Relative ratio of different vanadium species from deconvolution of ⁵¹V MAS NMR[14,40]

V loading	Monomer (-551 ppm)	Dimer (-572 ppm)	Oligomer (-615 ppm)
0.2	63.4%	35.6%	N
1.2	35.2%	60.5%	5.8%
2.1	33.6%	57.7%	8.7%
4	23.6%	66.4%	10.8%

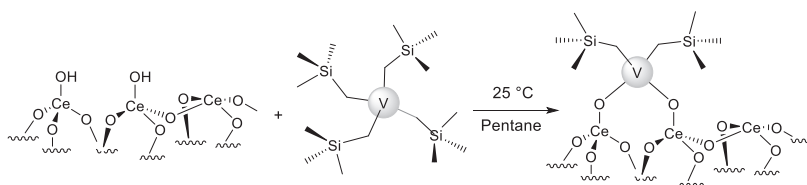
In summary, [V(=O)(OEt)₃]₂ has been successfully grafted as a dimeric bipodal V(V) species on ceria dehydroxylated at 200 °C, characterized by Elemental analysis, DRIFT, Raman, solid state NMR, XPS, EPR and XANES. The grafted material [V1-a] has been calcined and investigated for NH₃-SCR of NO_x. The catalytic result is promising, showing a high conversion, selectivity and robustness. In order to correlate the structure-activity relationship, a series of vanadium-based catalysts, prepared in the same manner with different loadings [xV1-b, x=0.2, 1.2, 2.1, 4] have been synthesized, characterized and catalytically investigated. A combination of different techniques, such as Elemental analysis, DRIFT, solid state NMR, and XANES suggests that the calcined products always exhibit a mixture of various V^V oxo species supported on ceria. Estimation of the quantities of the different species is done by the deconvolution of DRIFT and ⁵¹V MAS NMR data. The monomeric species dominate the mixture until the loading of 2.1 wt% V. Nevertheless, the oligomeric vanadyl species are constantly increasing with the loading. Polymeric vanadyl species are identified in [4V1-b]. Formation of different vanadium oxo species on ceria is proposed in Scheme 3. Current findings suggest that vanadium is rather mobile on a ceria surface under a calcination at

500 °C, resulting in different degrees of agglomeration, depending on the loading. Noteworthy, catalytic activity increases with the rise of vanadium loading, notably in the low temperature region. However, the catalytic performance in high temperature region decreases for [4V1-b]. Although it is difficult to correlate the structure-activity relationship due to the presence of different surface species, it is clear that polymeric vanadium species enhance the NH₃-SCR activity in the low temperature region. The same conclusion has been recently reported for tungsten systems prepared by impregnation method[53]. In Chapter II involving tungsten-based catalysts, the isolated tungsten species is found to offer the best catalytic performances and structure stability. It is then reasonable to believe that isolated vanadium species will also give a higher-performing catalyst. As the chosen dimeric vanadium precursor [V(=O)(OEt)₃]₂ gives a mixture of different surface species after calcination, the next section is targeting to catalyst containing isolated monomeric vanadium species by using the monomeric homoleptic [V(CH₂SiMe₃)₄] precursor to be grafted onto ceria.

4 Preparation and characterization of V-oxo supported on CeO₂ with precursor [V(CH₂SiMe₃)₄]

4.1 Preparation of [V(CH₂SiMe₃)₄]/CeO₂₋₂₀₀ [V2-a]

According to literature[54], VN₄ was synthesized by the reaction of VCl₄ with 4 equivalents of Me₃SiCH₂Li giving dark green crystals. Prior to the grafting reaction, ceria is pretreated by calcination and dehydroxylated at 200 °C, as described in the previous section. The grafting of the monomeric vanadium (IV) precursor [V(CH₂SiMe₃)₄] is conducted in pentane at room temperature for 12 h. After washing with pentane and solvent evaporation, the resulting material is obtained as a grey powder, after drying under vacuum. It is mentioned as [V2-a] and characterized by DRIFT, SSNMR, XPS, EPR and XANES.



Scheme 4 Schematic illustration of the synthesis process of [V(CH₂SiMe₃)₄]/CeO₂₋₂₀₀ [V2-a]

4.2 Characterization of [V(CH₂SiMe₃)₄]/CeO₂₋₂₀₀ [V2-a]

4.2.1 Characterization of [V2-a] by mass balance analyses

The grafting of [V(CH₂SiMe₃)₄] presumably occurs through a protonolysis, with a release of tetramethylsilane (TMS), qualitatively detected by GC. [V2-a] is submitted to Elemental

analysis, which shows 1.29 wt% of vanadium and 2.14 wt% of carbon ($C/V = 7.1$ (th8)). The results indicate that there are still two neosilyl ligands per vanadium present on the surface of ceria in [V2-a]. This corresponds to a consumption of 0.51 mmol OH/g, since according to the surface OH groups chemical titration by $Al(iBu)_3$, there are 0.7 mmol OH/g on the neat ceria (dehydroxylated at 200 °C), this means that 73% of initial surface OH groups have reacted upon the grafting process. A similar reactivity has been reported by S. Scott *et al.* for $[V(CH_2SiMe_3)_4]$ grafting reaction on SiO_{2-200} , where only a bipodal monomeric structure, as proposed in scheme 4[55].

4.2.2 Characterization of [V2-a] by DRIFT spectroscopy

Fig. 16 shows the DRIFT spectra of materials before and after the grafting of $[V(CH_2SiMe_3)_4]$ onto ceria. The most pronounced difference between the spectra after grafting is the appearance of aliphatic stretching vibrations $\nu(C-H)$ at $3000 - 2800\text{ cm}^{-1}$, originating from the neosilyl ligand on functionalized ceria surface. It should be pointed out that the surface reaction occurs mainly on μ^1 and partially on μ^2 -type hydroxyl groups, while the μ^3 -OH seems to be persistent. The mechanism of the formation of bipodal species may occur on the presumably more reactive μ^1 -OH, followed by continuously reaction between the surface vanadium species and adjacent μ^2 -OH. On the basis of these results, we concluded that $[V(CH_2SiMe_3)_4]$ is successfully grafted on the surface of ceria. However, as reported in the case of tungsten (Chapter II), a small peak was found around 2100 cm^{-1} on [V2-a], attributed to the forbidden electronic transition from $2f_{5/2}$ to $2f_{7/2}$ of Ce^{3+} , confirming the presence of Ce^{3+} on the surface.

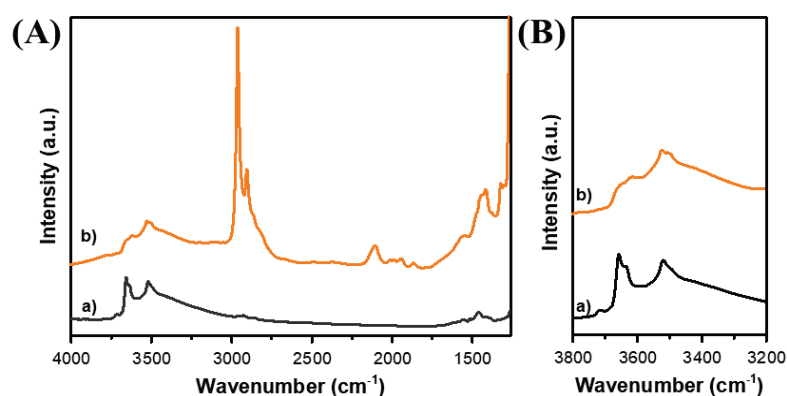


Fig. 16 (A) ($4000-1250\text{ cm}^{-1}$) DRIFT spectra and (B) enlarged ($3800-3200\text{ cm}^{-1}$) region of a) CeO_{2-200} ; b) [V2-a]

4.2.3 Characterization of [V2-a] by solid state NMR and EPR spectroscopies

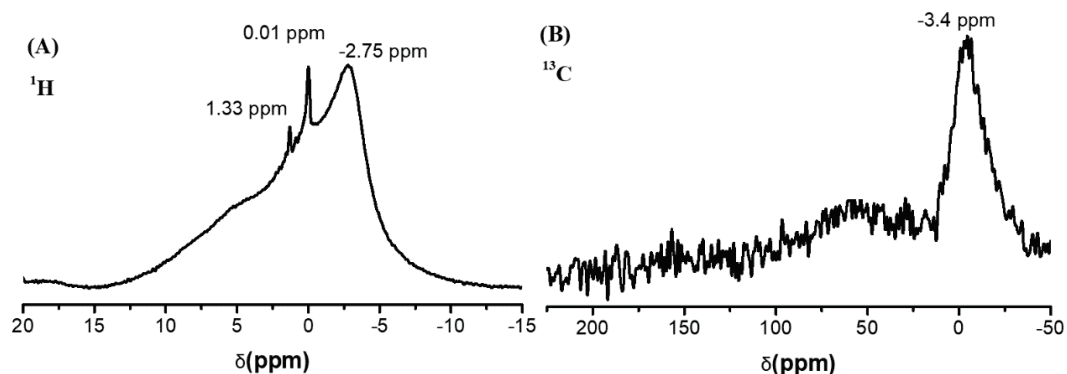


Fig. 17 (A) ^1H MAS and (B) ^{13}C CP MAS solid state NMR spectroscopies of [V2-a]

The functionalized material [V2-a] is further investigated by solid state NMR. ^1H MAS NMR in Fig. 17A shows a broad signal at -2.75 ppm along with two narrow peaks at 0 and 1.3 ppm. The broad signal may be related to the methyl ($-\text{CH}_2\text{Si}(\text{CH}_3)_3$) of neosilyl ligand in the proximity of a paramagnetic center (Ce^{3+} or V^{4+}). Such a significant shift has been observed in Chapter II and attributed to the presence of Ce^{3+} . The two narrow signals at 0.01 and 1.33 ppm are probably due to minor quantities of diamagnetic surface species V^{5+} bearing neosilyl ligand, probably obtained after oxidation during grafting (*vide infra*). Equally, the ^{13}C CP MAS NMR spectrum shows a large signal at -3.4 ppm (Fig. 17B) and an extremely broad contribution centered at 55 ppm, respectively attributed to the methyl and methylene carbons of neosilyl ligand. These results are consistent with the presence of $\nu(\text{C-H})$ aliphatic vibration bands detected by DRIFT. In order to confirm a paramagnetism of [V2-a], the sample has been investigated by EPR (Fig. 18).

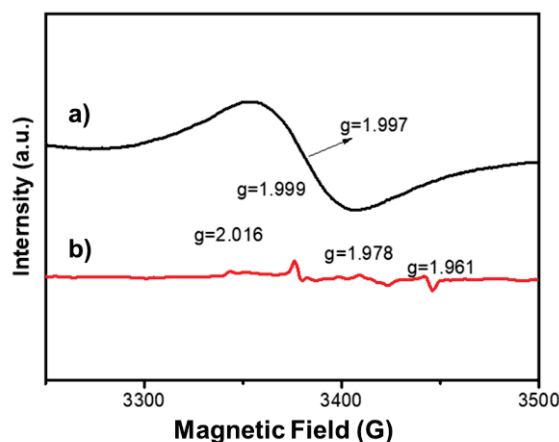


Fig. 18 EPR spectra of (a) $\text{V}(\text{CH}_2\text{SiMe}_3)_4$ diluted on Boron nitride (BN) and (b) [V2-a] recorded at room temperature (scaled for equivalent vanadium amounts)

The vanadium precursor (diluted in BN), also used as a reference, $V(\text{CH}_2\text{SiMe}_3)_4/\text{BN}$ shows a broad signal centered at $g=1.997$, characteristic of V^{4+} , without hyperfine structure (8 components) resulting from a coupling of the unpaired electron with the $7/2$ nuclear spin of ^{51}V [37]. Surprisingly, in [V2-a], no clear signal of V^{4+} (broad peak at $g \approx 1.997$) is observed. Current result suggests that oxidation of vanadium has occurred during the grafting on ceria. Similar observations have also been observed in literature when a low amount of vanadium oxalate is impregnated onto ceria[56]. Hence, the oxidation state of [V2-a] has been further investigated by XPS and XANES.

4.2.4 Characterization of [V2-a] by X-ray photoelectron spectroscopy

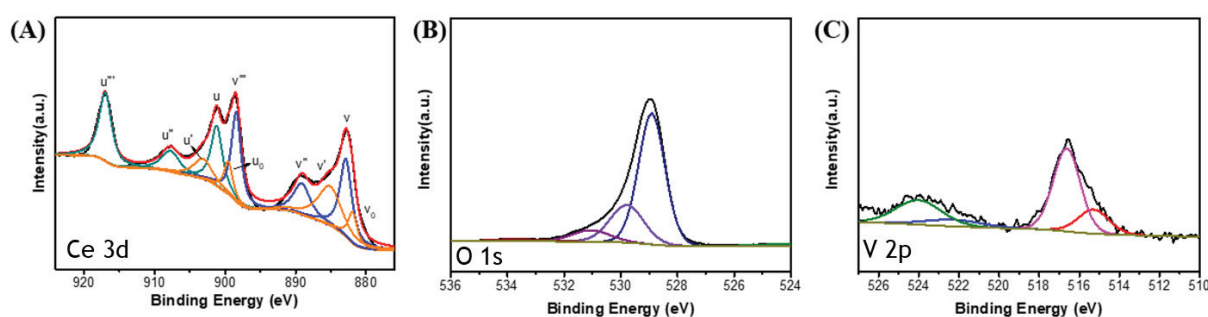


Fig. 19 XPS spectra of [V1-a]: Ce 3d (A), O 1s (B), and V 2p (C)

To further probe different oxidation states of the elements in [V2-a], XPS has been employed. Fig. 19 presents the XPS spectra along with a deconvolution of the main signals for Ce (3d), O (1s), and V (2p) in sample [V2-a]. As described in Chapter II, Ce exhibits ten characteristic peaks attributed to Ce^{3+} ($3d_{10} 4f_1$) and Ce^{4+} (Fig. 19A). Moreover, O1s spectrum comprises a major peak attributed to lattice oxygen (O_β) and other two peaks for surface oxygen O_α . In the V 2p region, two asymmetric peaks that can be decomposed into four features can be associated to the $2p_{1/2}$ and $2p_{3/2}$ of V^{5+} and V^{4+} , respectively[56]. Detection of a substantial amount of V^{5+} means that the initial $[V(\text{CH}_2\text{SiMe}_3)_4]$ precursor has been oxidized during grafting, as indicated by EPR and ^1H MAS NMR. As the experiments are conducted under a controlled atmosphere, the formation of V^{5+} is probably due to a reduction of the ceria surface. Indeed, the Ce^{3+} and the surface oxygen content seem to have increased after grafting (Table 4), thus suggesting a reduction of the support. Furthermore, there are lots of studies in the bibliography reporting a reduction of the ceria support once functionalized by a series of transition metals. Nevertheless, the reduction mechanism has never been investigated.

Table 4 Peak compositing from the deconvolution of XPS

Sample	Ce ³⁺ [a]	u''' [b]	O _α [c]	V ⁴⁺ [d]
CeO ₂₋₂₀₀	20.6%	15.5%	19.1%	N
[V2-a]	38.4%	12.5%	34.4%	24.8%

$$[a] \%Ce^{3+} = (Ce^{3+}/(Ce^{4+} + Ce^{3+}))$$

$$[b] u''' = ([u'''] / ([u_0] + [u] + [u'] + [u''] + [u'''] + [v_0] + [v] + [v'] + [v''] + [v''']))$$

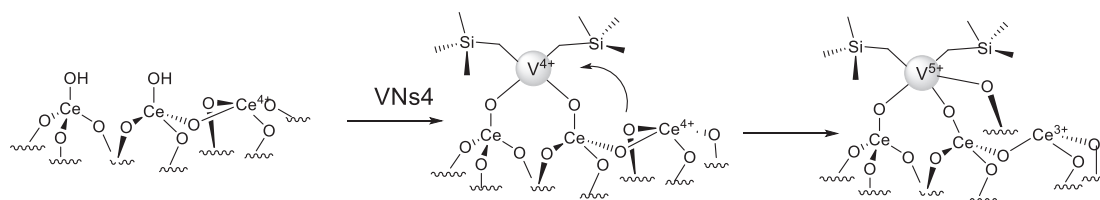
$$[c] \%O_{\alpha} = (1 - (O_{\beta} / (O_{\alpha 1} + O_{\alpha 2} + O_{\beta})))$$

$$[d] \%V^{4+} = (V^{4+} / (V^{4+} + V^{5+}))$$

4.2.5 Characterization of [V2-a] by X-ray absorption spectroscopy

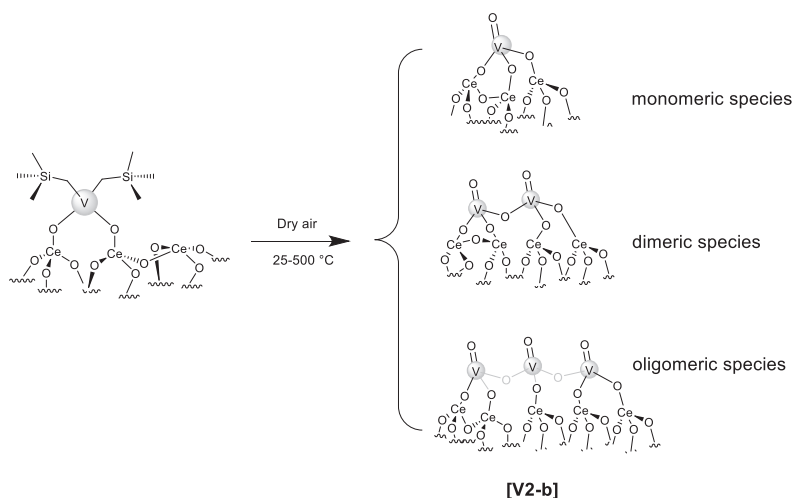
The hyperfine structure of [V(CH₂SiMe₃)₄]/CeO₂₋₂₀₀ was studied by X-ray absorption near edge structure. The results show that the oxidation state of vanadium is V^V. To have a good comparison with the following calcination products, the results are shown in section 4.4.5.

Gathering the information from different characterization techniques, the reaction between [V(CH₂SiMe₃)₄] and ceria dehydroxylated at 200 °C triggers protonolysis along with the release of tetramethylsilane. As Elemental analysis reveals that there are about two neosilyl ligands per surface vanadium, it is reasonable to propose that the structure comprises a bipodal attachment onto the support. However, the grafted species is practically EPR silent, indicating the absence of V⁴⁺. Furthermore, XPS analysis finds V⁵⁺ as the main vanadium component. In addition, a significant increase in the Ce³⁺ concentration has been observed, contrary to what was observed when vanadium(V) precursors were used. Thus, the grafting of vanadium(IV) precursor [V(CH₂SiMe₃)₄] onto ceria causes an oxidation of vanadium and a reduction of the support. Although similar phenomena have already been observed in literature, the redox mechanism has never been clearly identified. A reasonable pathway may involve an electron transfer from bridged oxygen (Ce⁴⁺-O-Ce⁴⁺) to (Ce⁴⁺-O• Ce³⁺), followed by the formation of (Ce⁴⁺-O-V⁵⁺), yielding a tripodal bis-neosilyl vanadium (Scheme 5).



Scheme 5 Proposed mechanism for the transformation of V⁴⁺ into V⁵⁺ upon grafting

4.3 Preparation of V-oxo/CeO₂ [V2-b]



Scheme 6 Schematic illustration of the synthesized process for V-oxo/CeO₂ [V2-b] from [V2-a]

In the second step, the pre-catalyst [V(CH₂SiMe₃)₄]/CeO₂₋₂₀₀, [V2-a], is calcinated under dry air at 500 °C for 18h in order to transform the surface organometallic fragment into stable vanadium oxo species on the surface of ceria. A yellow powder is recovered after this step and is referred as [V2-b]. **Scheme 6** illustrates potential species contained in [V2-b], though the targeted product is a monomeric species. The resulting material is characterized by DRIFT, Raman, SSNMR, XPS and XANES.

4.4 Characterization of V-oxo/CeO₂ [V2-b]

4.4.1 Characterization of [V2-b] by Elemental analysis and DRIFT spectroscopy

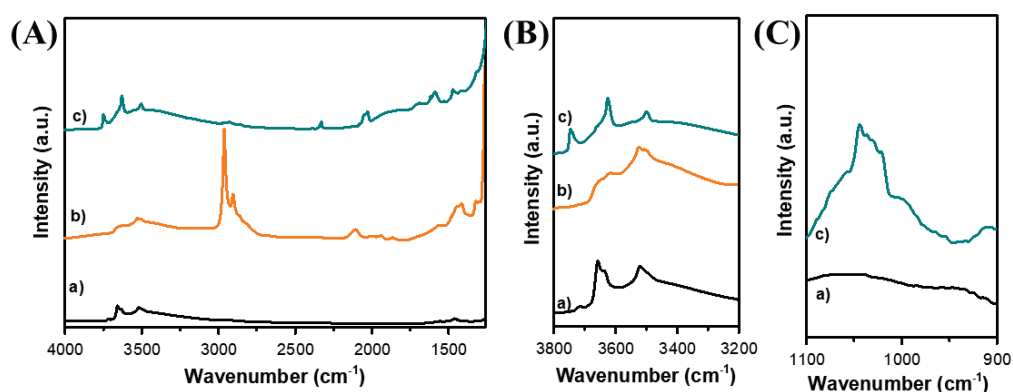


Fig. 20 (A) (4000-1250 cm⁻¹) DRIFT spectra, (B) enlarged (3800-3200 cm⁻¹) region, and (C) enlarged (1100-900 cm⁻¹) region of a) CeO₂₋₂₀₀; b) [V2-a]; c) [V2-b]

The results of Elemental analysis show that the resulting material contains 1.3 wt% vanadium, traces of silicon (0.4 wt%), and a negligible amount of carbon. This indicates that the

vanadium is perfectly stable during the thermal treatment process, while most of organic fragments were decomposed and removed. DRIFT is used to investigate the local structure changes after the oxidation and calcination processes. Compared to [V2-a], the signals corresponding to C-H stretching vibration vanished in the DRIFT spectrum of [V2-b] (Fig. 21), which is consistent with the absence of carbon found by Elemental analysis. Besides the disappearance of the organic ligands, new peaks are emerging in the 3800-3600 cm^{-1} and 1100 – 900 cm^{-1} regions. A new signal present at 3743 cm^{-1} , different from the μ^1 -OH of CeO_2 , is tentatively attributed to isolated Si-OH[57]. In fact, during the calcination, neosilyl ligands can be converted in the presence of oxygen at elevated temperature into CO_2 and $\text{Si}(\text{OH})_4$ intermediates that are deposited onto ceria. Importantly, new unresolved peaks in the later region, highlighted in Fig. 21, are attributed to different kinds of $\nu(\text{V}=\text{O})$ [23,52], suggesting the presence of mixed vanadium surface species in monomeric, dimeric, and oligomeric configuration on CeO_2 . Estimation of the proportion of these species by deconvolution has frequently been proposed in literature[23]. Hence, the DRIFT signal between 1060 and 995 cm^{-1} has been deconvoluted in the same manner as for [V1-b]. The monomeric vanadium species is still the major species, but more oligomeric species are found in this case compared to [V1-b]. In addition, the small band around 2000 cm^{-1} corresponds to $\text{V}=\text{O}$ overtone[58] as a $\text{W}=\text{O}$ overtone signal has also been observed for the tungsten system (Chapter II).

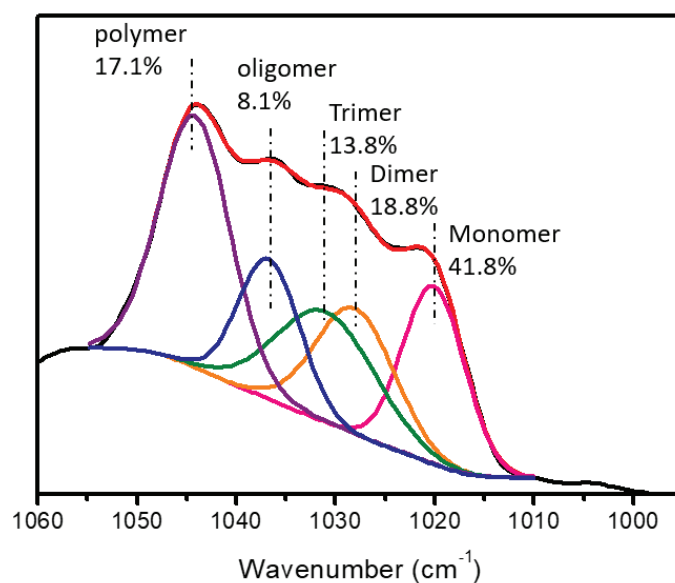


Fig. 21 DRIFT spectrum of [V2-b] in the (1060-995 cm^{-1}) region with a proposed deconvolution in order to identify different vanadium supported specie

4.4.2 Characterization of [V2-b] by Raman spectroscopy

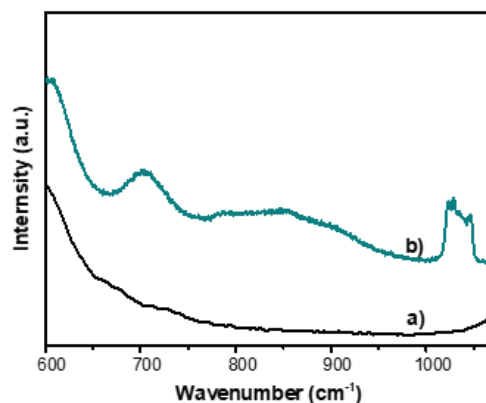


Fig. 22 Raman spectroscopy of a) CeO₂₋₂₀₀; b) [V2-b]

As the complement of DRIFT results, Raman could display more details on vanadium oxo species. Fig. 22 shows the Raman spectra of sample [V2-b] and CeO₂₋₂₀₀. The peak at 700 cm⁻¹ and a broader peak centered at 860 cm⁻¹ correspond to the vibrations of V-O and V-O-V or V-O-Ce respectively[58,59]. A combination of several signals around 1030 cm⁻¹ corresponds to the A_{2g} stretching vibrations of V=O, suggesting a mixture of vanadium species on the surface of ceria. The unresolved bands in this region are evidently composed of multiple peaks, whereas the intensities of the two signals at lowest energies are the strongest, also reflecting that the dominating vanadium species comprises a monomeric nature on the surface of ceria.

4.4.3 Characterization of [V2-b] by ⁵¹V MAS solid state NMR

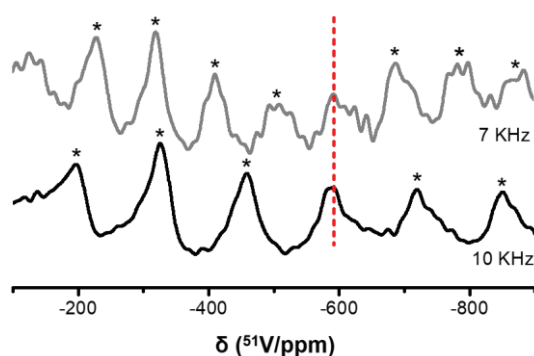


Fig. 23 ⁵¹V MAS NMR spectra of [V2-b] under different spinning rates

To further identify the vanadium species, ⁵¹V MAS NMR is employed. The spinning sidebands are identified with asterisk by varying the spinning rate. (7 KHz, 10 KHz). ⁵¹V signal of [V2-b] is centered at -587 ppm, which is slightly shifted to the high-field region

compared to [V1-b]. As justified above, increasing the content of oligomeric vanadium species tend to shift the principal ^{51}V NMR signal towards higher field. Thus, current observation indicates that [V2-b] contains more oligomeric vanadium species than [V1-b], in agreement with DRIFT results. However, this signal is too broad and weak to process a reliable deconvolution. Noteworthy, CeVO_4 with a characteristic peak at -427 ppm in the ^{51}V NMR spectrum is absent in [V2-b] and [V1-b].

4.4.4 Characterization of [V2-b] by X-ray photoelectron spectroscopy

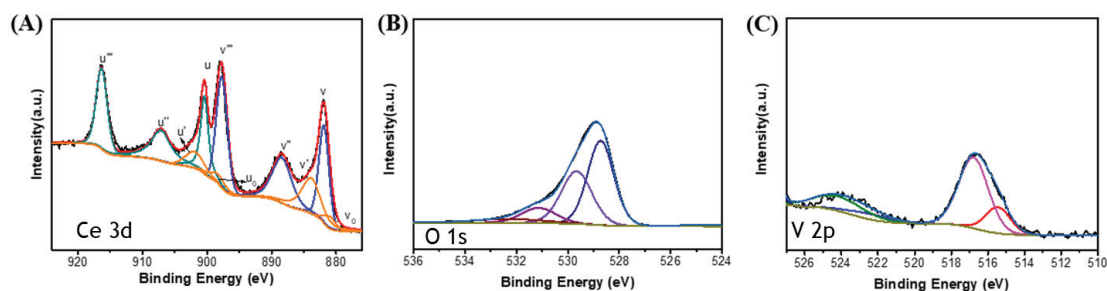


Fig. 24 XPS spectra of [V2-b]: Ce 3d (A), O 1s (B), and V 2p (C)

XPS was used to determine the oxidation states of Ce, V, and O in [V2-b] (Fig. 24). Applying the same deconvolution approach as above, the ratios of different components can be estimated and are shown in the Table 5. After calcination, the percentage of Ce^{3+} is reduced from 38.4% in [V2-a] to 30.5% in [V2-b], possibly due to the oxidation process. In addition, data extracted from the V 2p peaks (located close to the O 1s spectra signal) reveal the presence of 24.0 % V^{4+} (Fig. 24C). This result suggests that the presumably VO_2 phase (formed at the beginning of the calcination process) seems rather stable under the given calcination conditions, in agreement with literature reports[16,60]. Meanwhile, slightly more Ce^{3+} are observed in [V2-b] than in [V1-b]. Concerning O1s spectra, [V2-b] shows significantly more surface oxygen than [V1-b] which is probably associated to the presence of V^{4+} .

Table 5 Estimation of the proportion of different V surface species resulting from the deconvolution of different XPS signals

Sample	Ce^{3+}	u'''	O_α	V^{4+}
CeO_{2-200}	20.6%	15.5%	19.1%	N
[V2-b]	30.5%	14.0%	52.1%	24.0%

[a] $\% \text{Ce}^{3+} = (\text{Ce}^{3+}) / (\text{Ce}^{4+} + \text{Ce}^{3+})$

[b] $u''' = ([u''']) / ([u_0] + [u] + [u'] + [u''] + [u'''] + [v_0] + [v] + [v'] + [v''] + [v'''])$

[c] $\% \text{O}_\alpha = (1 - (\text{O}_\beta + \text{O}_\gamma) / (\text{O}_\alpha + \text{O}_\beta + \text{O}_\gamma))$

[d] $\% \text{V}^{4+} = (\text{V}^{4+}) / (\text{V}^{4+} + \text{V}^{5+})$.

4.4.5 Characterization of [V2-b] by X-ray absorption spectroscopy

Additional information on the vanadium coordination geometry, structural environment, and oxidation state in the case of the molecular complex $[\text{V}(\text{CH}_2\text{SiMe}_3)_4]$, [V2-a] and [V2-b] materials was given by X-ray absorption spectroscopy. Normalized V K-edge XANES spectra of different molecular complexes, $[\text{V}^{\text{III}}(\text{Mes})_3 \cdot \text{THF}]$, $[\text{V}(\text{CH}_2\text{SiMe}_3)_4]$, $[\text{V}^{\text{V}}(\text{=O})(\text{OtBu})_3]$, $\text{V}^{\text{V}}_2\text{O}_5$, [V2-a] obtained from the grafting of $[\text{V}(\text{CH}_2\text{SiMe}_3)_4]$ onto CeO_2 and [V2-b], obtained from the calcination of previous one and are shown in Fig. 25. In these spectra, a prominent pre-edge peak is present in the 5460-5470 eV range. This pre-edge feature arises from electronic transitions from 1s core levels to the empty 3d levels, more or less 4p hybridized by the ligands of vanadium. These electronic transitions become electric-dipolar allowed in the absence of an inversion center. In this case, the loss of symmetry permits partial overlapping and mixing of the unfilled d states of the metal with the 4p orbitals of the metal. Several studies of the V K-edge XANES features have considered the pre-edge intensity as well as its absolute position to determine both the vanadium oxidation state and its symmetry[61–63]. The only position of the pre-edge peak is generally insufficient to evaluate accurately the vanadium oxidation state. Moreover, the position of the vanadium K-edge when shifted by 16 to more than 18 eV to higher energy relative to the metal foil, is also an indication for the presence of V(V) compounds[61].

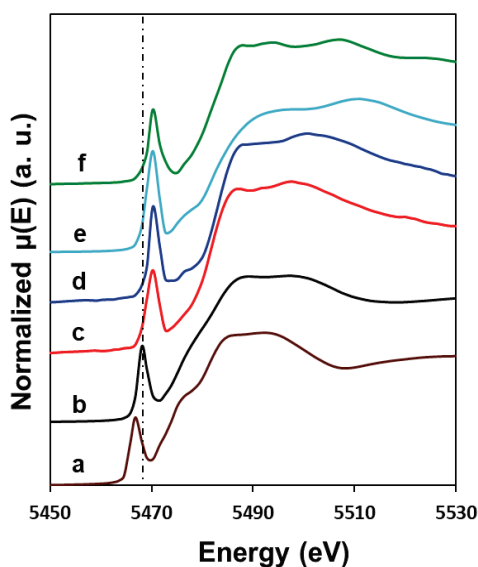


Fig. 25 XANES spectra: (a) $[\text{V}^{\text{III}}(\text{mesityl})_3]$ molecular complex, (b) $[\text{V}(\text{CH}_2\text{SiMe}_3)_4]$ molecular complex, (c) [V2-a], (d) [V2-b] material, (e) $[\text{V}^{\text{V}}(\text{O})(\text{OtBu})_3]$ molecular complex, (f) V_2O_5 (the dashed line indicates the position of the pre-edge of V^{IV})

The position and intensity of the main pre-edge peak along with the position of the edge of different vanadium compounds studied are reported Table 6. For the molecular complex,

[V(CH₂SiMe₃)₄] the position of the pre-edge peak at 5468.2 eV, its intensity of 0.61 and the edge position at 5475.2 eV are typical with those observed in other complexes or materials containing V(IV), while those characteristics of **[V2-a]** (pre-edge at 5470.3 eV, intensity of 0.72, edge at 5481.9 eV) are typical of compounds containing V(V) in a tetrahedral symmetry[62,63]. This confirms that vanadium has changed its oxidation state from V^{IV} to V^V upon its grafting onto CeO₂₋₂₀₀. After calcination, vanadium in **[V2-b]** also presents all the characteristic of tetrahedral V^V. The XANES spectra are also characteristic of V^V in a tetrahedral symmetry on both these CeO₂ supported materials.

Table 6 Positions and intensities of the pre-edge signal and edge positions in the V K-edge XANES of several samples.

Sample	Pre-edge signal position ^a (eV)	Pre-edge signal intensity ^b (a.u.)	Edge position ^a (eV)
[V ^{III} (Mes) ₃ .THF]	5466.6	0.55	5474.2
[V(CH ₂ SiMe ₃) ₄]	5468.2	0.61	5475.2
[V2-a]	5470.3	0.70	5481.9
[V2-b]	5470.4	0.77	5483.1
[V(=O)(OtBu) ₃]	5470.3	0.81	5481.9
V ₂ O ₅	5470.4	0.59	5481.4

^a Relative to a calibration with a vanadium foil (5465.1 eV); an error of ± 0.3 eV is estimated on the energy. ^b Intensity normalized to the step height of the K-edge.

In summary, the grafting of a monomeric V(IV) precursor [V(CH₂SiMe₃)₄] onto the dehydroxylated CeO₂ occurs through protonolysis and results in an oxidation process where V⁴⁺ is oxidized to V⁵⁺, while the support is reduced (Scheme 5). The main oxidation state of vanadium is confirmed by XPS, EPR and XANES. Such reactivity is unprecedented and may involve an electron transfer from a Ce⁴⁺ bridged oxygen to a Ce center, giving Ce³⁺, accompanied by an electron transfer from V⁴⁺ to the oxygen radical, creating a V-O bond. Creation of a supplementary M-O-S bond (M = grafted metal; S = support) upon grafting or heat treatment occurs frequently in surface organometallic chemistry. However, the mechanism is rather a ligand transfer by the opening of a S-O-S bridge[64,65]. In this particular case, the formation of this new bond occurs through an electron transfer, which has never been described in surface organometallic chemistry before, to the best of my knowledge.

The major species can be expressed as (≡Ce-O)₃V^V(CH₂SiMe₃)₂ based on Elemental analysis, DRIFT, SS NMR, EPR, XPS and XANES. In the second step, after calcination, a mixture of vanadium-oxo species is present on the surface of ceria, comprising monomeric, dimeric and polymeric vanadium species. From the results of DRIFT, Raman and ⁵¹V NMR, isolated vanadium species (monomer, dimer) remain as major species in **[V2-b]**, but it contains more oligomerized species than **[V1-b]**. As mentioned in the introduction, precursors at lower

oxidation state like V^{III} and V^{IV} tend to form polymeric vanadium species.[21] These results again indicate that vanadium is extremely mobile on a ceria surface during calcination. Even starting from the monomeric homoleptic precursor $[V(CH_2SiMe_3)_4]$ it yields a mixture of vanadium species with different degrees of agglomeration after calcination (Scheme 6). The reason may be related to the extremely high reactivity of the grafted vanadium neosilyl complex towards oxygen during the calcination, causing substantial heat release and formation of water to accelerate the agglomeration. Recalling that calcination of $[W(\equiv CtBu)(CH_2tBu)_3]/CeO_{2-200}$, in the same manner, gives a stable isolated tungsten species, probably due to the high stability of W-O bond, which is different from current observations. To tentatively reach the ultimate goal, the synthesis of uniquely monomeric vanadium oxo species supported on ceria, a monomeric vanadium(V) precursor $[V(=O)(OtBu)_3]$ is employed in the next section. The chosen precursor $[V(=O)(OtBu)_3]$ already contains an oxo ligand. Importantly, recent reports have described that the tert-butoxide ligand can be readily decomposed under thermolysis[41,66,67] resulting in isobutene release and formation of the corresponding isolated metal oxide surface fragment.

5 Preparation and characterization of V-oxo supported on CeO_2 with precursor $[V(=O)(OtBu)_3]$

5.1 Preparation of $[V(=O)(OtBu)_3]/CeO_{2-200}$ [V3-a]

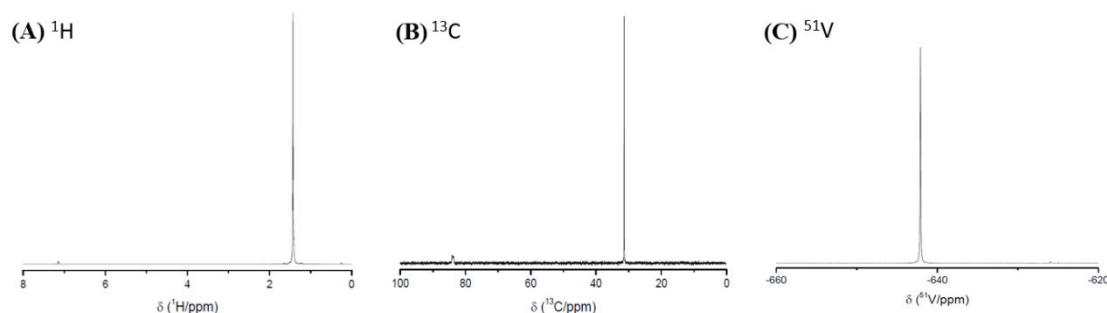
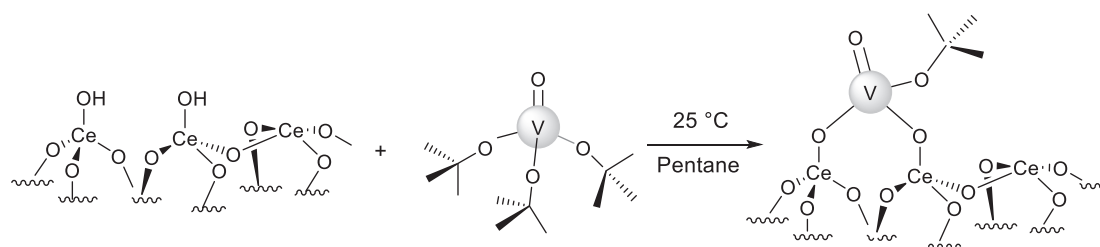


Fig. 26 (A) 1H , (B) $^{13}C\{^1H\}$, (C) ^{51}V NMR of $[V(=O)(OtBu)_3]$ in C_6D_6

$[V(=O)(OtBu)_3]$ is synthesized from the reaction between V_2O_5 and $tBuOH$ in benzene, followed by the solvent distillation and a purification by sublimation.[41] The 1H , ^{13}C and ^{51}V NMR spectra of $[V(=O)(OtBu)_3]$ in C_6D_6 are shown in Fig. 26. After purification, an intense signal at 1.43 ppm appeared in 1H NMR attributed to the methyl group in the tert-butoxide ligand. Likewise, peak at 31.8 ppm in the $^{13}C\{^1H\}$ NMR spectrum corresponds to the methyl group. A small signal at 86 ppm is assigned to the quaternary C of the $OtBu$ ligand. Moreover,

the ^{51}V NMR shows a signal at -642 ppm attributed to a tetrahedral vanadium species bearing an oxo and three alkoxide ligands[68]. CeO_2 dehydroxylated at 200 °C was used as the support to react with $[\text{V}(=\text{O})(\text{OtBu})_3]$ in toluene at room temperature overnight. After the elimination of the solvent by filtration and drying under vacuum, a yellow material, named **[V3-a]** is recovered. A schematic illustration of this synthesis process is proposed in Scheme 7. The resulting material is studied by Elemental analysis, DRIFT, SSNMR and Raman spectroscopies



Scheme 7 Schematic illustration of the synthesized process for $[\text{V}(=\text{O})(\text{OtBu})_3]/\text{CeO}_2\text{-200}$, **[V3-a]**

5.2 Characterization of $[\text{V}(=\text{O})(\text{OtBu})_3]/\text{CeO}_2\text{-200}$ **[V3-a]**

5.2.1 Characterization of **[V3-a]** by Elemental analysis and DRIFT spectroscopy

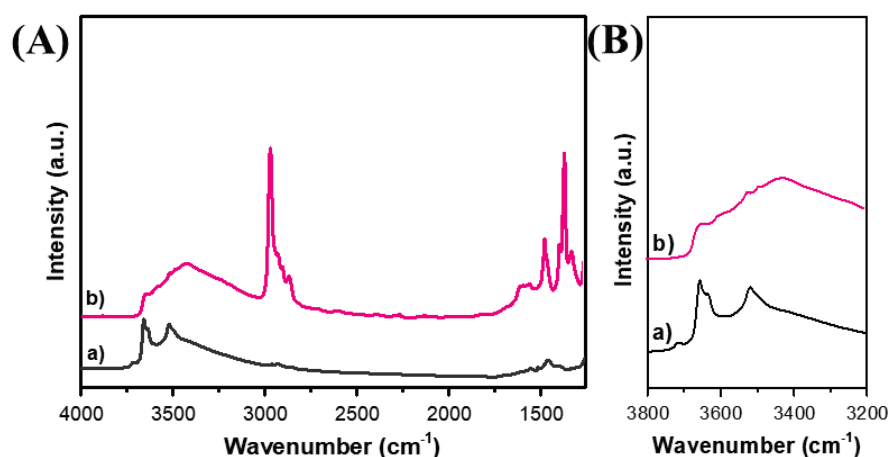


Fig. 27 (A) (4000-1250 cm^{-1}) DRIFT spectra and (B) enlarged (3800-3200 cm^{-1}) region of a) $\text{CeO}_2\text{-200}$; b) **[V3-a]**

Elemental analysis of **[V3-a]** shows the presence of 1.0 wt% V, and 1.75 wt% C, giving a C/V ratio of ca. 7.1, reflecting that 0.2 mmol V has been grafted on 1 g of support. This value is rather similar to **[V2-a]**, featuring a bipodal structure. However, the C/V ratio is somewhat far from the expected value (4) for a bipodal structure. Nevertheless, taking into account the relative instability of 4-coordinated surface vanadium species and the strong coordination ability of the released tert-butanol, it is reasonable to admit that the excess carbon is

originated from adsorbed tert-butanol, which gives the broader $\nu(\text{O-H})$ band around 3300 cm^{-1} . Similarly to the grafting process of $[\text{V}(=\text{O})(\text{OEt})_3]_2$ and $[\text{V}(\text{CH}_2\text{SiMe}_3)_4]$, the protonolysis happened predominantly on terminal OH groups and partially on bridged hydroxyls (Fig. 27). Moreover, the resulting material exhibits aliphatic stretching $\nu(\text{C-H})$ vibration bands at $3000\text{--}2800\text{ cm}^{-1}$ and bending $\delta(\text{CH}_x)$ vibration bands at $1500\text{--}1300\text{ cm}^{-1}$, attributed to the tert-butyl fragments grafted on the surface of ceria. This should result from the formation of bipodal vanadium surface species bearing one tert-butoxide and one oxo ligand with a tert-butanol molecule coordinated to V or strongly physisorbed onto ceria. Similar to **[V1-a]**, a weak and broad contribution at $1700\text{--}1600\text{ cm}^{-1}$ is also observed. This IR band was previously assigned to water generated through the dehydration of released tert-butanol into isobutene and carbonyl compounds originating from isomerization/oxidation of tert-butanol.

5.2.2 Characterization of **[V3-a]** by solid state NMR

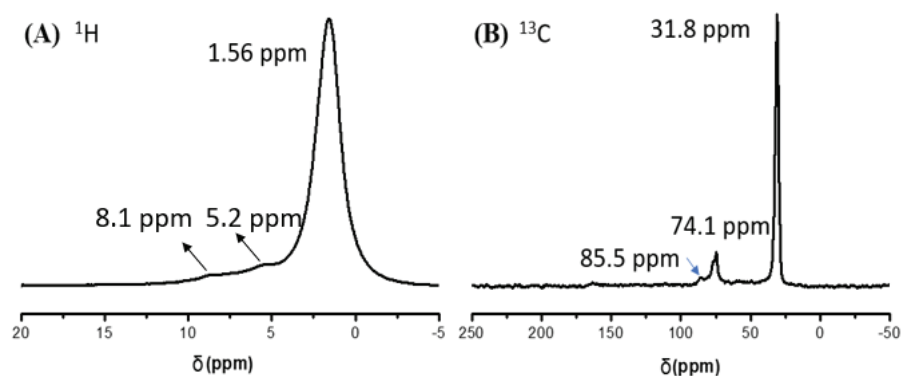
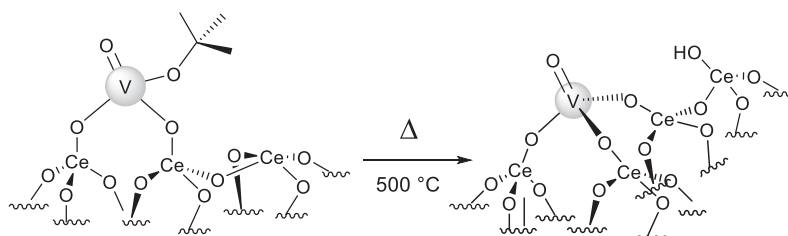


Fig. 28 (A) ^1H and (B) ^{13}C CP MAS NMR of **[V3-a]**

As shown in Fig. 28, ^1H MAS solid state NMR spectrum of **[V3-a]** exhibits a relative broad signal at 1.56 ppm, corresponding to the methyl group of the tert-butoxide ligand. There are also minor features at 5.2 and 8.1 ppm, that may originate from adsorbed isobutene (formed after dehydration of tert-butanol, as observed by DRIFT) and butanal (generated after isomerization and dehydrogenation of 1-butanol). An intense peak at 31.8 ppm shown in the ^{13}C CP MAS NMR spectrum is associated with the methyl groups of the ligand. Noteworthy, there are further two signals at 74.1 ppm and 85.5 ppm. The former is rather narrow and probably originated from coordinated or physisorbed tert-butanol, while the latter is weak and attributed to the quaternary CCH_3 in **[V3-a]**. Noteworthy, no clear sign of paramagnetism is observed in the NMR spectra, thus supporting the fact that dehydration/oxidation catalyzed by Ce^{3+} of tert-butanol has taken place upon the grafting. This reaction occurred during the preparation of **[V1-a]**, by using $[\text{V}(=\text{O})(\text{OEt})_3]_2$ as precursor. NMR results support the

proposition by DRIFT and Elemental analysis, in which the grafted product is a bipodal vanadium $[(\equiv\text{Ce}-\text{O})_2\text{V}(=\text{O})(\text{OtBu})]$ having tert-butanol coordinated to vanadium or physisorbed on the surface.

5.3 Preparation of V-oxo/CeO₂ [V3-b] from [V(=O)(OtBu)₃]/CeO₂₋₂₀₀ [V3-a]



Scheme 8 Schematic illustration of the synthesis process of V-oxo/CeO₂ [V3-b] from [V3-a]

In the second step, the calcination process, the pre-catalyst [V(=O)(OtBu)₃]/CeO₂ was calcined under dry air at 500 °C for 18 h to form vanadium-oxo on the surface of ceria. The oxidation process is illustrated in [Scheme 8](#), and the product, named [V3-b], was characterized by DRIFT, Raman and SSNMR.

5.4 characterization of V-oxo/CeO₂ [V3-b]

5.4.1 Characterization of [V3-b] by DRIFT spectroscopy

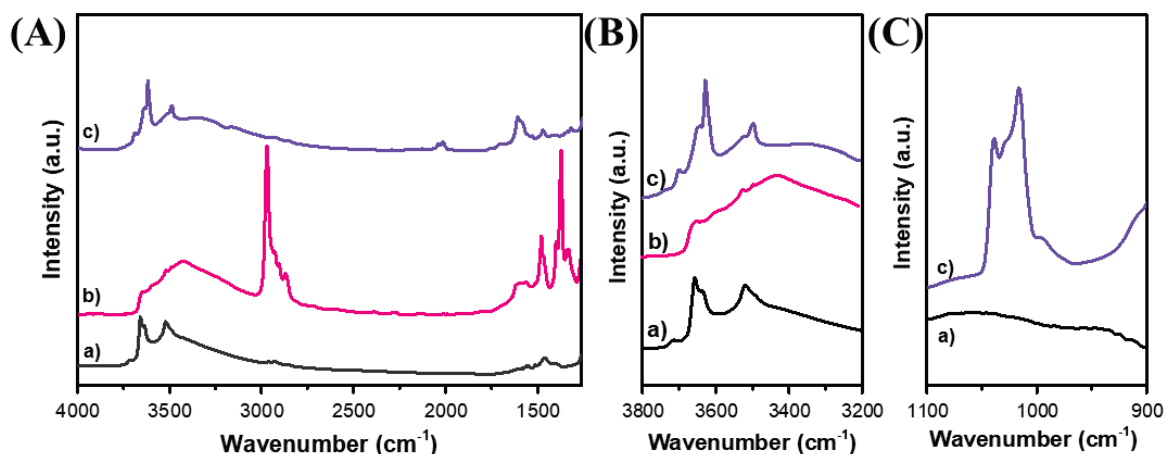


Fig. 29 (A) (4000-1250 cm⁻¹) DRIFT spectra, (B) enlarged (3800-3200 cm⁻¹) region, and (C) enlarged (1100-900 cm⁻¹) region of a) CeO₂₋₂₀₀; b) [V3-a]; c) [V3-b]

Surface species changes during the calcination process were monitored by DRIFT ([Fig. 29](#)). As we mentioned before, $\nu(\text{C}-\text{H})$ and $\delta(\text{CH}_x)$ vibration bands linked to aliphatic alkyls, located around 2800 cm⁻¹ and 1500 cm⁻¹ are absent in [V3-b], suggesting the removal of -OtBu ligands during the thermal treatment. The (O-H) stretching region is highlighted in [Fig.](#)

29B, revealing the regeneration of certain Ce-OH groups with a slight red shift, as observed before for [V1-b] and [W-b]. The vanadium oxo fragments revealed by a $\nu(\text{V}=\text{O})$ vibration band have been highlighted in Fig. 30. As mentioned before, different degrees of vanadium agglomeration are revealed in the DRIFT spectrum. After deconvolution similarly conducted as above, [V3-b] features the highest content of monomeric vanadium oxo species among the vanadium catalysts synthesized in this Chapter. Moreover, a broad peak at 995 cm^{-1} is observed, tentatively attributed to the presence of V_2O_5 [69,70].

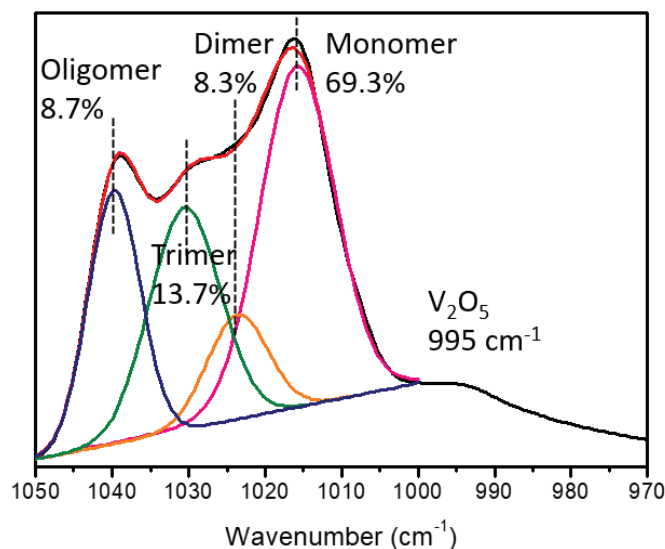


Fig. 30 Decomposition of DRIFT spectroscopy of enlarged region of $1050\text{-}970\text{ cm}^{-1}$

5.4.2 Characterization of [V3-b] by Raman

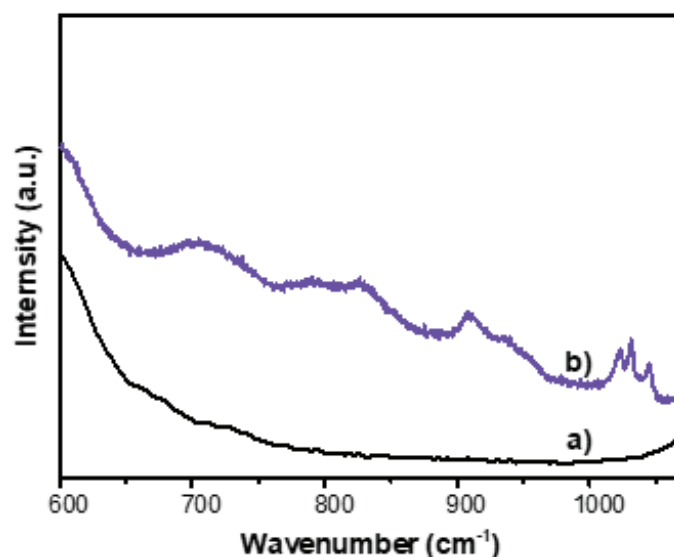


Fig. 31 Raman spectra of a) CeO₂; b) [V3-b]

Raman spectroscopy is used to further clarify the surface vanadium species in [V3-b]. From Fig. 31, the signals at 700 cm⁻¹ and 860 cm⁻¹ are assigned to different vibrations of V-O-M (M=V, Ce), similar to the case of [V2-b] and [V1-b]. Noteworthy, a new band at 906 cm⁻¹ and a shoulder at 935 cm⁻¹ are observed for [V3-b], which are tentatively attributed to the presence of pyrovanadate (V₂O₇)[23]. In the region of the A_{2g} stretching vibrations of V=O, three resolved peaks are shown at 1021 cm⁻¹, 1030 cm⁻¹, and 1044 cm⁻¹, assigned to the different polymerized vanadium species. This is consistent with the DRIFT results.

5.4.3 Characterization of [V3-b] by ⁵¹V MAS solid -state NMR

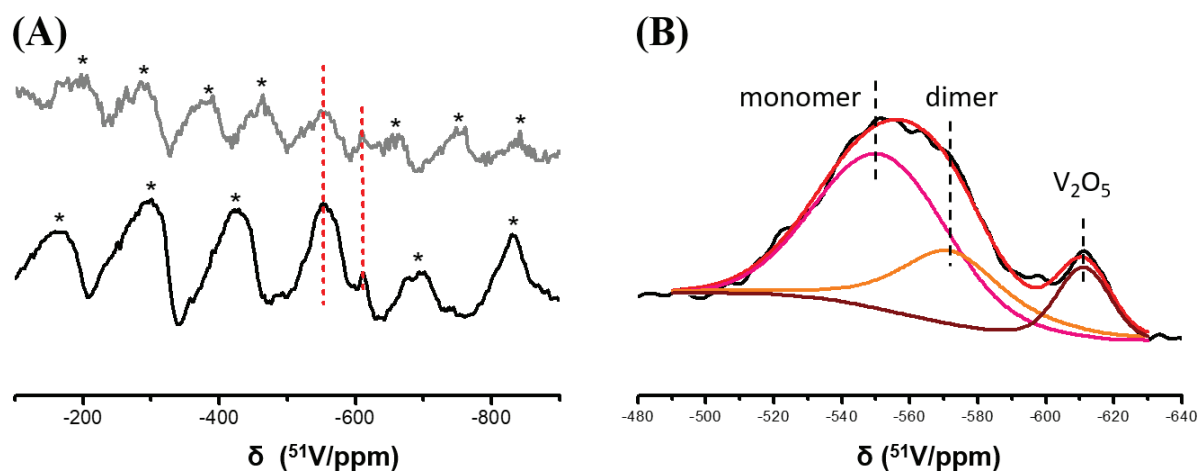


Fig. 32 (A) ⁵¹V MAS NMR spectra and (B) decomposition of [V3-b]

⁵¹V MAS SSNMR is conducted to further investigate the coordination environment of the supported vanadium species. The spinning sidebands are identified by running the acquisition in two different conditions (7 KHz and 10 KHz spinning rates). Deconvolution of ⁵¹V NMR spectrum conducted similarly as mentioned before is shown in Fig. 32B, with the signal of the major monomeric vanadium species at -550 ppm. Noteworthy, the signal attributed to CeVO₄ is absent in [V3-b] similar to the case of [V1-b] and [V2-b], while a minor amount of V₂O₅ is detected from the ⁵¹V resonance at -610 cm⁻¹.

In summary, the grafting of the monomeric V(V) precursor [V(=O)(OBu)₃] onto ceria gives the corresponding monomeric bipodal species [(≡Ce-O)₂V(=O)(OtBu)] with tert-butanol coordinated to vanadium or adsorbed on the ceria surface. This structure is deduced from data based on Elemental analysis, DRIFT and solid state NMR. After calcination, DRIFT, Raman and ⁵¹V NMR suggest that the major part of surface species is a monomeric vanadium oxo species.

6 Effects of precursor for V-oxo/CeO₂ on NH₃-SCR Catalytic performance

6.1 Catalytic performance in the NO conversion and N₂ Selectivity

The catalytic performance of NH₃-SCR of NO is evaluated at 1 bar with a mass of 30 mg of catalyst and the following gas mixture: 350 ppm NH₃, 300 ppm NO, 12% O₂, in He. Fig. 33A shows the NO_x conversion through NH₃-SCR on a series of ceria supported 1.2 wt% vanadium loaded catalysts. VO_x/CeO₂ synthesized by a conventional impregnation method (mentioned as IMPV-CeO₂)[22] is compared to the V-oxo/CeO₂ catalysts synthesized by SOMC approach with [V(=O)(OEt)₃]₂, [V(CH₂SiMe₃)₄], and [V(=O)(OtBu)₃] molecular precursors. The introduction of vanadium enhances the NO conversion and enlarges the operating temperature window compared to pure support CeO₂₋₂₀₀. It must be noticed that NO_x conversion with VO_x/CeO₂ samples synthesized by SOMC exhibit higher performances than the VO_x/CeO₂ samples synthesized by a classical impregnation. Since the vanadium loading is the same, current results suggest that the SOMC approach offers more active sites in the final catalysts.

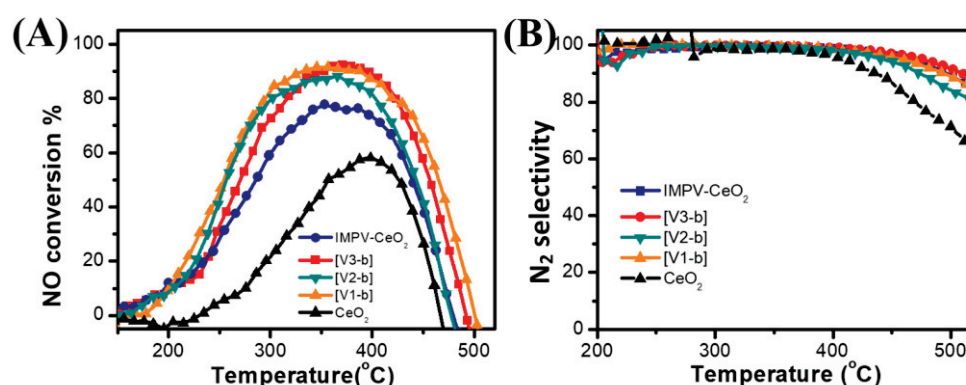


Fig. 33 (A) NO conversion and (B) N₂ selectivity over different catalysts

Concerning the series of catalysts prepared by SOMC, the most promising catalyst is [V1-b] in terms of NO conversion and the operating temperature window. The slight, but notable difference among the SOMC catalysts is necessarily linked to the surface vanadium species. Recalling the results from structure characterization, there is a difference in the proportion of isolated (monomeric and dimeric) and oligomeric vanadium species in [V1-b], [V2-b], and [V3-b]. Detailed analysis of Fig. 33A seems that [V3-b], containing the highest ratio of monomeric vanadium oxo species shows the lowest NO conversion in the low temperature range (<350 °C). In the high temperature region, substantial variation of the catalytic performance is observed. [V2-b] displays the lowest activity, and [V1-b] features a slightly higher activity than [V3-b].

As described in the introduction part, there is a continuous debate on the structure-activity relationship on VOx supported on ceria catalysts for ammonia SCR. There are reports claiming that the isolated vanadium species is the main active site at low temperature, while other groups conclude that it is rather the oligomeric vanadium species that are active at low temperature. Such inconsistency prompted current investigation, using a novel approach for SCR catalyst synthesis, namely SOMC. The present results indicate that the isolated vanadium oxo sites govern the high temperature activity, while the oligomeric species exhibit higher activity in the low temperature region. Similar observations have also been found in the tungsten supported on ceria system[53]. Referring to Chapter II, where the corresponding tungsten system has been extensively studied, it is found that the most active catalyst comprises an isolated tungsten oxo supported on ceria. Interestingly, after acid/base and redox characterizations, it appears that the acidity and the redox capability constitute only a minor effect on the activity.

6.2 Structure-reactivity relationship in NH₃-SCR

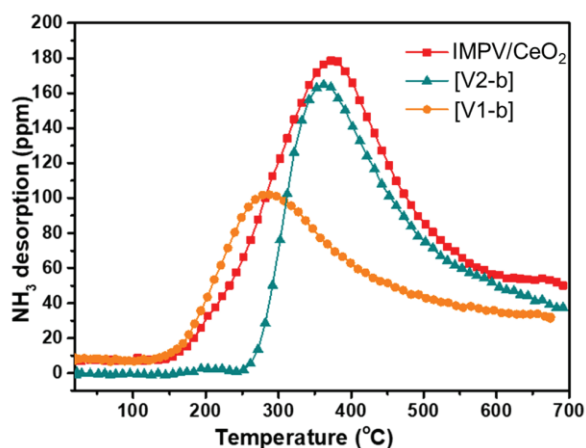


Fig. 34 NH₃-TPD profiles of [IMPV-CeO₂], [V1-b] and [V2-b]

It is generally accepted that surface acidity and redox property are crucial in the NH₃-SCR reaction. In order to evaluate the surface acidity, [IMPV-CeO₂], [V1-b] and [V2-b] have been submitted to NH₃-TPD analysis and the results are shown in Fig. 34. The order of the total calculated amount of released NH₃ is: [IMPV-CeO₂] (104.4 μmol/g) > [V2-b] (91.2 μmol/g) > [V1-b] (61.7 μmol/g). The results show that VOx/CeO₂ synthesized by impregnation method with the same loading exhibits a higher surface acidity than samples obtained from SOMC approach. Comparing the SOMC catalysts, [V1-b], being more active, shows less overall acidity than [V2-b]. This can be explained by the fact that [V2-b] contains

more polymeric vanadium oxo species that generate the acidity. Interestingly, the NH₃-TPD experiments revealed that the acidity is inversely proportional to the observed activity, which is completely different with respect to literature reports. A similar tendency is found for the corresponding tungsten system. Nevertheless, taking into account that most of the vanadium sites present in the SOMC catalysts are isolated, the reaction mechanism may differ from classically proposed pathways. To gain further insights into these catalysts, the redox capability of the samples has been conducted by H₂-TPR.

The redox properties of bulk ceria IMPV/CeO₂, [V1-b] and [V2-b] are determined by H₂ temperature programmed reduction in a thermobalance. The results are shown in Fig. 35, and the weight loss is due to a release of oxygen from the solid and thereby reflects the reducibility of vanadium or of the ceria support. The total oxygen release decreases in the order: [IMPV-CeO₂] (65 μmol/g) > [V1-b] (61 μmol/g) > [V2-b] (57 μmol/g) > CeO₂₋₂₀₀ (44 μmol/g). These values are rather similar and it is thereby difficult to distinguish among the redox properties of these catalysts. Although [IMPV-CeO₂] exhibits the highest value, this catalyst shows the lowest performance. Reminding that the results from NH₃-TPD also indicate that [IMPV-CeO₂] has the highest acidity, it also indicates that the reaction mechanism for SOMC catalysts (consisting mainly in isolated supported vanadium sites) may be different from the classically proposed pathways.

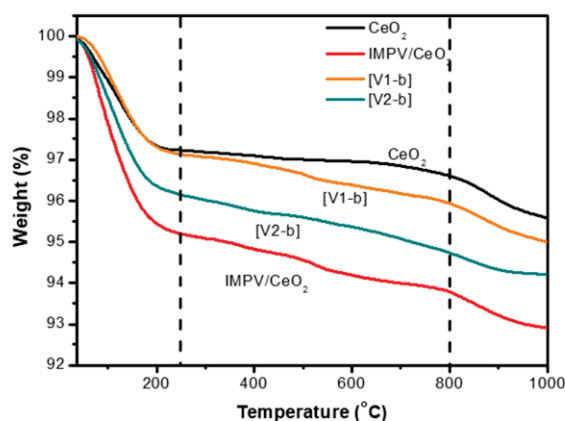


Fig. 35 TGA patterns under H₂ over CeO₂₋₂₀₀, IMPV/CeO₂, [V1-b] and [V2-b]

7 Conclusion

In the previous chapter, surface organometallic chemistry of tungsten on ceria has been developed and the resulting material appears to be a highly active and stable NH₃-SCR catalyst within a broad temperature range. Encouraged by the discovery that isolated tungsten

species supported on ceria possess such exceptionally high activity, this chapter is intended to develop similar isolated vanadium species supported on ceria. Hence Surface Organometallic Chemistry on ceria has been extended to the case of vanadium, which is a frequently used element for NH₃-SCR. The targeted product is synthesized according to surface organometallic chemistry practices in two steps: i) grafting a suitable precursor onto a ceria surface previously dehydroxylated; ii) calcination of the grafted materials at 500 °C to form the targeted isolated vanadium-oxo species supported on ceria. The materials have been characterized by Elemental analysis, FT-IR, XPS, EPR, SSNMR, Raman, and XANES. As homoleptic VR₅ type complexes are unstable, commercially available [V(=O)(OEt)₃]₂ has initially been employed as precursor. Although the calcined material possesses fairly high activity and selectivity for NH₃-SCR, structural characterization of the catalyst by DRIFT, Raman and ⁵¹V MAS NMR reveals that it contains a mixture of monomeric (major species), dimeric and oligomeric vanadium oxo species. In the second and the third attempt, the homoleptic [V(CH₂SiMe₃)₄] and [V(=O)(OtBu)₃] molecular complexes have been used respectively. Despite these materials showing relatively high NH₃-SCR activity, the structural characterizations also suggest that the catalysts contain a mixture of monomeric, dimeric and oligomeric vanadium oxo species. These experiments confirm that vanadium is extremely mobile on a ceria surface. To shed light on the structure-activity relationship, a series of ceria supported vanadium catalysts prepared from [V(=O)(OEt)₃]₂ with different loadings were prepared. Structural characterizations indicate that the degree of agglomeration of vanadium increases with the loading. The catalytic performances of this series of catalysts clearly show an enhancement in the activity at low temperature upon increasing the loading. On the other hand, the activity at high temperature improves by increasing the proportion of isolated vanadium species (low loading). The best catalyst [**V1-b**] has been studied by NH₃-TPD and H₂-TPR. Surprisingly, the determined acidity and redox properties were weaker than for the catalyst prepared by conventional impregnation which presented far lower catalytic activity. The generally higher activity observed for the SOMC catalysts may be related to the higher dispersion of vanadium species. Gathering the information in this chapter, it seems like the reaction mechanism for NH₃-SCR is somewhat different for isolated system compared to the already proposed mechanism (L-H, or E-R). As the acidity and redox properties appear to have less influence on the catalytic activity, the dominating mechanism for isolated group V and VI transition state metal catalysts may involve Lewis acid/redox pair involving a new

elementary step during the N-N formation. Prior to proposing a new mechanism, additional elements (Nb, Mo) have been equally investigated in order to confirm the observed tendency.

Table 7 Summary and comparison of the catalyst preparation and catalytic performance in this chapter

Catalysts	Loading	Synthesis method	Precursor	Calcination temperature	NO conversion
CeO ₂ -200	N.D.	N.D.	N.D.	N.D.	58% at 400 °C
[0.2V1-b]	0.2 wt%	SOMC	[V(=O)(OEt) ₃]	500 °C	76% at 377 °C
[1.2V1-b]	1.2 wt%	SOMC	[V(=O)(OEt) ₃]	500 °C	T ₈₀ (295-442 °C)
[2.1V1-b]	2.1 wt%	SOMC	[V(=O)(OEt) ₃]	500 °C	T ₈₀ (283-419 °C)
[4V1-b]	4.0 wt%	SOMC	[V(=O)(OEt) ₃]	500 °C	T ₈₀ (272-416 °C)
[V2-b]	1.3 wt%	SOMC	[V(CH ₂ SiMe ₃) ₄]	500 °C	T ₈₀ (298-404 °C)
[V3-b]	1.0 wt%	SOMC	[V(=O)(OtBu) ₃]	500 °C	T ₈₀ (314-423 °C)
IMPV	1.2 wt%	Impregnation	NH ₄ VO ₄	500 °C	80% at 370 °C

Reference

- [1] J. N. Armor, Catalytic removal of nitrogen oxides: where are the opportunities? *Catalysis today*, 26 (1995) 99-105. [https://doi.org/10.1016/0920-5861\(95\)00132-Y](https://doi.org/10.1016/0920-5861(95)00132-Y)
- [2] G. Busca, L. Lietti, G. Ramis, F. Berti, Chemical and mechanistic aspects of the selective catalytic reduction of NO_x by ammonia over oxide catalysts: A review, *Applied Catalysis B: Environmental* 18 (1998) 1-36. [https://doi.org/10.1016/S0926-3373\(98\)00040-X](https://doi.org/10.1016/S0926-3373(98)00040-X)
- [3] R. Verschaeren, W. Schaepdryver, T. Serruys, M. Bastiaen, L. Vervaeke, S. Verhelst, Experimental study of NO_x reduction on a medium speed heavy duty diesel engine by the application of EGR (exhaust gas recirculation) and Miller timing, *Energy*. 76 (2014) 614–621. <https://doi.org/10.1016/j.energy.2014.08.059>.
- [4] T. V. Johnson, Review of diesel emissions and control, *International Journal of Engine Research*. 10 (2009) 275–285. <https://doi.org/10.1243/14680874JER04009>.
- [5] L. Masdrag, X. Courtois, F. Can, S. Royer, E. Rohart, G. Blanchard, P. Marecot, D. Duprez, Understanding the role of C₃H₆, CO and H₂ on efficiency and selectivity of NO_x storage reduction (NSR) process, in: *Catalysis Today*, 3 (2012) 70–76. <https://doi.org/10.1016/j.cattod.2012.03.053>.
- [6] S. Hodjati, K. Vaezzadeh, C. Petit, V. Pitchon, A. Kiennemann, NO_x sorption-desorption study: application to diesel and lean-burn exhaust gas (selective NO_x recirculation technique), *Catalysis Today*. 59 (2000) 323–334. [https://doi.org/10.1016/S0920-5861\(00\)00298-4](https://doi.org/10.1016/S0920-5861(00)00298-4).
- [7] R. Burch, J.P. Breen, F.C. Meunier, A review of the selective reduction of NO_x with hydrocarbons under lean-burn conditions with non-zeolitic oxide and platinum group metal catalysts, 39 (2002) 283-303. [https://doi.org/10.1016/S0926-3373\(02\)00118-2](https://doi.org/10.1016/S0926-3373(02)00118-2)
- [8] P.G. Savva, C.N. Costa, Hydrogen lean-DeNO_x as an alternative to the ammonia and hydrocarbon selective catalytic reduction (SCR), *Catalysis Reviews - Science and Engineering*. 53 (2011) 91–151. <https://doi.org/10.1080/01614940.2011.557964>.
- [9] Q. Zhang , Y. Wu , H. Yuan, Recycling strategies of spent V₂O₅-WO₃/TiO₂ catalyst: A review, *Resources, Conservation and Recycling*, 161 (2020) 104983. <https://doi.org/10.1016/j.resconrec.2020.104983>
- [10] M. Zhu, J.K. Lai, U. Tumuluri, Z. Wu, I.E. Wachs, Nature of Active Sites and Surface

Intermediates during SCR of NO with NH₃ by Supported V₂O₅-WO₃/TiO₂ Catalysts, *Journal of the American Chemical Society*. 139 (2017) 15624–15627. <https://doi.org/10.1021/jacs.7b09646>.

- [11] D.W. Kwon, K.H. Park, S.C. Hong, Influence of VO_x surface density and vanadyl species on the selective catalytic reduction of NO by NH₃ over VO_x/TiO₂ for superior catalytic activity, *Applied Catalysis A: General*. 499 (2015) 1–12. <https://doi.org/10.1016/j.apcata.2015.04.005>.
- [12] A. Marberger, D. Ferri, M. Elsener, O. Kröcher, The Significance of Lewis Acid Sites for the Selective Catalytic Reduction of Nitric Oxide on Vanadium-Based Catalysts, *Angewandte Chemie*. 128 (2016) 12168–12173. <https://doi.org/10.1002/ange.201605397>.
- [13] S.T. Choo, Y.G. Lee, I.-S. Nam, S.-W. Ham, J.-B. Lee, Characteristics of V₂O₅ supported on sulfated TiO₂ for selective catalytic reduction of NO by NH₃, *Applied Catalysis A: General*, 200 (2000) 177-188. [https://doi.org/10.1016/S0926-860X\(00\)00636-0](https://doi.org/10.1016/S0926-860X(00)00636-0)
- [14] G. He, Z. Lian, Y. Yu, Y. Yang, K. Liu, X. Shi, Z. Yan, W. Shan, H. He, Polymeric vanadyl species determine the low-temperature activity of V-based catalysts for the SCR of NO_x with NH₃, *Science Advance*, 4 (2018) 11. <https://doi.org/10.1126/sciadv.aau4637>.
- [15] G.T. Went, L.-J. Leu, A.T. Bell, Quantitative Structural Analysis of Dispersed Vanadia Species in TiO₂(Anatase)-Supported V₂O₅, *Journal of Catalysis*, 134 (1992) 479-491. [https://doi.org/10.1016/0021-9517\(92\)90336-G](https://doi.org/10.1016/0021-9517(92)90336-G)
- [16] S. Youn, S. Jeong, D.H. Kim, Effect of oxidation states of vanadium precursor solution in V₂O₅/TiO₂ catalysts for low temperature NH₃ selective catalytic reduction, *Catalysis Today*. 232 (2014) 185–191. <https://doi.org/10.1016/j.cattod.2014.01.025>.
- [17] G.-J. Dong, Y.-F. Zhang, Z. Yuan, B. Yang, Effect of the pH value of precursor solution on the catalytic performance of V₂O₅-WO₃ /TiO₂ in the low temperature NH₃-SCR of NO_x, 12 (2014) 1455-1463. [https://doi.org/10.1016/S1872-5813\(15\)60003-2](https://doi.org/10.1016/S1872-5813(15)60003-2).
- [18] T. Zhang, H. Chang, K. Li, Y. Peng, X. Li, J. Li, Different exposed facets VO_x/CeO₂ catalysts for the selective catalytic reduction of NO with NH₃, *Chemical Engineering Journal*. 349 (2018) 184–191. <https://doi.org/10.1016/j.cej.2018.05.049>.
- [19] C. Tang, H. Zhang, L. Dong, Ceria-based catalysts for low-temperature selective catalytic reduction of NO with NH₃, *Catalysis Science and Technology*. 6 (2016) 1248–1264. <https://doi.org/10.1039/c5cy01487e>.
- [20] X. Wu, Z. Chen, X. Yu, Z. Huang, H. Shen, G. Jing, Mechanism by which three-dimensional ordered mesoporous CeO₂ promotes the activity of VO_x-MnO_x/CeO₂ catalysts for NO_x abatement: Atomic-scale insight into the catalytic cycle, *Chemical Engineering Journal*. 399 (2020). 125629. <https://doi.org/10.1016/j.cej.2020.125629>.
- [21] X. Wu, X. Yu, Z. Huang, H. Shen, G. Jing, MnO_x-decorated VO_x/CeO₂ catalysts with preferentially exposed {110} facets for selective catalytic reduction of NO_x by NH₃, *Applied Catalysis B: Environmental*. 268 (2020) 118419. <https://doi.org/10.1016/j.apcatb.2019.118419>.
- [22] Y. Peng, C. Wang, J. Li, Structure-activity relationship of VO_x/CeO₂ nanorod for NO removal with ammonia, *Applied Catalysis B: Environmental*. 144 (2014) 538–546. <https://doi.org/10.1016/j.apcatb.2013.07.059>.
- [23] Z. Wu, A.J. Rondinone, I.N. Ivanov, S.H. Overbury, Structure of vanadium oxide supported on ceria by multiwavelength Raman spectroscopy, *Journal of Physical Chemistry C*. 115 (2011) 25368–25378. <https://doi.org/10.1021/jp2084605>.
- [24] Z. Wu, S. Dai, S.H. Overbury, Multiwavelength Raman spectroscopic study of silica-supported vanadium oxide catalysts, *Journal of Physical Chemistry C*. 114 (2010) 412–422.

<https://doi.org/10.1021/jp9084876>.

- [25] Z. Wu, H.S. Kim, P.C. Stair, S. Rugmini, S.D. Jackson, On the structure of vanadium oxide supported on aluminas: UV and visible Raman spectroscopy, UV-visible diffuse reflectance spectroscopy, and temperature-programmed reduction studies, *Journal of Physical Chemistry B*. 109 (2005) 2793–2800. <https://doi.org/10.1021/jp046011m>.
- [26] M.A. Bañares, I.E. Wachs, Molecular structures of supported metal oxide catalysts under different environments, *Journal of Raman Spectroscopy*. 33 (2002) 359–380. <https://doi.org/10.1002/jrs.866>.
- [27] Z. Shi, Q. Peng, J. E, B. Xie, J. Wei, R. Yin, G. Fu, Mechanism, performance and modification methods for NH₃-SCR catalysts: A review, *Fuel*. 331 (2023) 125885. <https://doi.org/10.1016/j.fuel.2022.125885>.
- [28] M.K. Samantaray, S.K. Mishra, A. Saidi, J.M. Basset, Surface organometallic chemistry: A sustainable approach in modern catalysis, *Journal of Organometallic Chemistry*. 945 (2021) 121864. <https://doi.org/10.1016/j.jorganchem.2021.121864>.
- [29] J. Abou Nakad, N. Berthet, K.C. Szeto, A. De Mallmann, M. Taoufik, Direct conversion of trans-2-butene into a mixture of monomers with different composition over vanadium supported catalysts, *Catalysis Communications*. 169 (2022) 106469. <https://doi.org/10.1016/j.catcom.2022.106469>.
- [30] K.C. Szeto, Z.R. Jones, N. Merle, C. Rios, A. Gallo, F. Le Quemener, L. Delevoye, R.M. Gauvin, S.L. Scott, M. Taoufik, A Strong Support Effect in Selective Propane Dehydrogenation Catalyzed by Ga(*i*Bu)₃ Grafted onto γ -Alumina and Silica, *ACS Catalysis*. 8 (2018) 7566–7577. <https://doi.org/10.1021/acscatal.8b00936>.
- [31] K.C. Szeto, A. Gallo, S. Hernández-Morejudo, U. Olsbye, A. De Mallmann, F. Lefebvre, R.M. Gauvin, L. Delevoye, S.L. Scott, M. Taoufik, Selective Grafting of Ga(*i*Bu)₃ on the Silanols of Mesoporous H-ZSM-5 by Surface Organometallic Chemistry, *Journal of Physical Chemistry C*. 119 (2015) 26611–26619. <https://doi.org/10.1021/acs.jpcc.5b09289>.
- [32] D.R. Mullins, S.D. Senanayake, T.L. Chen, Adsorption and reaction of C₁-C₃ alcohols over CeO_x(111) thin films, *Journal of Physical Chemistry C*. 114 (2010) 17112–17119. <https://doi.org/10.1021/jp103905e>.
- [33] Q. Cheng, M. Du, G. Ramanoudjame, V. Jayaraman, Evolution of Glutamate Interactions During Binding to a Glutamate Receptor, *Nature Chemical Biology*. 1 (2005) 329–332. <https://doi.org/10.1038/nchembio738>.
- [34] L. Wang, Y. Yu, H. He, Y. Zhang, X. Qin, B. Wang, Oxygen vacancy clusters essential for the catalytic activity of CeO₂ nanocubes for o-xylene oxidation, *Scientific Reports*. 7 (2017). <https://doi.org/10.1038/s41598-017-13178-6>.
- [35] B. Murugan, A. V. Ramaswamy, Defect-site promoted surface reorganization in nanocrystalline ceria for the low-temperature activation of ethylbenzene, *Journal of the American Chemical Society*. 129 (2007) 3062–3063. <https://doi.org/10.1021/ja066834k>.
- [36] Z. Pászti, O. Hakkel, G.P. Szíjjártó, A. Tompos, Adsorption and transformations of ethanol over ceria based model catalysts, *Catalysis Today*. 306 (2018) 145–153. <https://doi.org/10.1016/j.cattod.2017.01.026>.
- [37] C.J. Magon, J.F. Lima, J.P. Donoso, V. Lavayen, E. Benavente, D. Navas, G. Gonzalez, Deconvolution of the EPR spectra of vanadium oxide nanotubes, *Journal of Magnetic Resonance*. 222 (2012) 26–33. <https://doi.org/10.1016/j.jmr.2012.06.004>.
- [38] C. Popa, M.V. Ganduglia-Pirovano, J. Sauer, Periodic density functional theory study of VOn

- species supported on the CeO₂(111) surface, *Journal of Physical Chemistry C*. 115 (2011) 7399–7410. <https://doi.org/10.1021/jp108185y>.
- [39] J. Matta, D. Courcot, E. Abi-Aad, A. Aboukaïs, Identification of vanadium oxide species and trapped single electrons in interaction with the CeVO₄ phase in vanadium-cerium oxide systems. ⁵¹V MAS NMR, EPR, Raman, and thermal analysis studies, *Chemistry of Materials*. 14 (2002) 4118–4125. <https://doi.org/10.1021/cm010396t>.
- [40] J.Z. Hu, S. Xu, W.Z. Li, M.Y. Hu, X. Deng, D.A. Dixon, M. Vasiliu, R. Craciun, Y. Wang, X. Bao, C.H.F. Peden, Investigation of the Structure and Active Sites of TiO₂ Nanorod Supported VO_x Catalysts by High-Field and Fast-Spinning ⁵¹V MAS NMR, *ACS Catalysis*. 5 (2015) 3945–3952. <https://doi.org/10.1021/acscatal.5b00286>.
- [41] J. Abou Nakad, R. Rajapaksha, K.C. Szeto, A. De Mallmann, M. Taoufik, Preparation of Tripodal Vanadium Oxo-Organometallic Species Supported on Silica, [(=SiO)₃V(=O)], for Selective Nonoxidative Dehydrogenation of Propane, *Organometallics*. 41 (2022) 2784–2797. <https://doi.org/10.1021/acs.organomet.2c00377>.
- [42] R. Cousin, D. Courcot, E. Abi-Aad, S. Capelle, J.P. Amoureux, M. Dourdin, M. Guelton, A.A. Aboukaïs, ⁵¹V MAS NMR characterization of V-Ce-O catalysts, *Colloids and Surfaces A: Physicochemical and Engineering Aspects*, 158 (1999) 43–49. [https://doi.org/10.1016/S0927-7757\(99\)00129-6](https://doi.org/10.1016/S0927-7757(99)00129-6)
- [43] T. Yan, Q. Liu, S. Wang, G. Xu, M. Wu, J. Chen, J. Li, Promoter rather than Inhibitor: Phosphorus Incorporation Accelerates the Activity of V₂O₅-WO₃/TiO₂ Catalyst for Selective Catalytic Reduction of NO_x by NH₃, *ACS Catalysis*. 10 (2020) 2747–2753. <https://doi.org/10.1021/acscatal.9b05549>.
- [44] E. Abi-aad, R. Bechara, J. Grimblot, A. Aboukaïs, Preparation and Characterization of CeO₂ under an Oxidizing Atmosphere. Thermal Analysis, XPS, and EPR Study, *Chemistry of Materials*. 5 (1993) 793–797. <https://doi.org/10.1021/cm00030a013>.
- [45] G. M. Ingo, R. Dal Maschino and L. Scoppio, Thermal and surface characterizations of 25.5 (wt.%) CeO₂-2.5 Y₂O₃-72 ZrO₂ Fine powder, *Surface and interface analysis*, 18 (1992) 661–666. <https://doi.org/10.1002/sia.740180905>
- [46] S. Jain, J. Shah, N.S. Negi, C. Sharma, R.K. Kotnala, Significance of interface barrier at electrode of hematite hydroelectric cell for generating ecopower by water splitting, *International Journal of Energy Research*. 43 (2019) 4743–4755. <https://doi.org/10.1002/er.4613>.
- [47] A. Martínez-Arias, J.C. Conesa, J. Soria, O₂-probe EPR as a method for characterization of surface oxygen vacancies in ceria-based catalysts, *Research on Chemical Intermediates*. 33 (2007) 775–791. <https://doi.org/10.1163/156856707782169345>
- [48] M. V. Martínez-Huerta, J.M. Coronado, M. Fernández-García, A. Iglesias-Juez, G. Deo, J.L.G. Fierro, M.A. Bañares, Nature of the vanadia-ceria interface in V⁵⁺/CeO₂ catalysts and its relevance for the solid state reaction toward CeVO₄ and catalytic properties, *Journal of Catalysis*. 225 (2004) 240–248. <https://doi.org/10.1016/j.jcat.2004.04.005>.
- [49] P. Chaurand, J. Rose, V. Briois, M. Salome, O. Proux, V. Nassif, L. Olivi, J. Susini, J.L. Hazemann, J.Y. Bottero, New methodological approach for the vanadium K-edge X-ray absorption near-edge structure interpretation: Application to the speciation of vanadium in oxide phases from steel slag, *Journal of Physical Chemistry B*. 111 (2007) 5101–5110. <https://doi.org/10.1021/jp063186i>.
- [50] K.C. Szeto, B. Loges, N. Merle, N. Popoff, A. Quadrelli, H. Jia, E. Berrier, A. De Mallmann, L. Delevoye, R.M. Gauvin, M. Taoufik, Vanadium oxo organometallic species supported on silica

- for the selective non-oxidative dehydrogenation of propane, *Organometallics*. 32 (2013) 6452–6460. <https://doi.org/10.1021/om400795s>.
- [51] S. Liu, H. Wang, Y. Wei, R. Zhang, S. Royer, Morphology-Oriented ZrO₂-Supported Vanadium Oxide for the NH₃-SCR Process: Importance of Structural and Textural Properties, *ACS Applied Materials and Interfaces*. 11 (2019) 22240–22254. <https://doi.org/10.1021/acsami.9b03429>.
- [52] N.Y. Topsøe, M. Anstrom, J.A. Dumesic, Raman, FTIR and theoretical evidence for dynamic structural rearrangements of vanadia/titania DeNO_x catalysts, *Catalytic letters*. 76 (2001) 11–20. <https://doi.org/10.1023/A:1016715823630>
- [53] I. El Arrouji, C. Chen, J. Toyir, C. Larabi, K.C. Szeto, A. de Mallmann, M. Taoufik, A. Oulmekki, NH₃-selective catalytic reduction of NO_x to N₂ over Ceria supported WO_x based catalysts: Influence of tungsten content, *Catalysts*. 11 (2021) 1–12. <https://doi.org/10.3390/catal11080950>.
- [54] G.A. Razuvaev, V.N. Latyaeva, V. V Drobotenko, Synthesis and properties of covalent tri- and tetravalent vanadium, *Journal of Organometallic Chemistry*, 208 (1981) 169–182. [https://doi.org/10.1016/S0022-328X\(00\)82672-8](https://doi.org/10.1016/S0022-328X(00)82672-8)
- [55] J.A.N. Ajjou, G.L. Rice, S.L. Scott, Kinetics and mechanisms of thermally induced alkane eliminations from silica-supported bis(alkyl)chromium(IV) and -vanadium(IV) complexes, *Journal of the American Chemical Society*. 120 (1998) 13436–13443. <https://doi.org/10.1021/ja9831507>.
- [56] J. Matta, D. Courcot, E. Abi-Aad, A. Aboukaïs, Thermal Analysis, EPR and XPS study of Vanadyl(IV) oxalate behavior on the ceria surface, *Journal of Thermal Analysis and Calorimetry* 66 (2001) 717–727. <https://doi.org/10.1023/A:1013131819569>.
- [57] N.J. Abreu, H. Valdés, C.A. Zaror, F. Azzolina-Jury, M.F. Meléndrez, Ethylene adsorption onto natural and transition metal modified Chilean zeolite: An operando DRIFTS approach, *Microporous and Mesoporous Materials*. 274 (2019) 138–148. <https://doi.org/10.1016/j.micromeso.2018.07.043>.
- [58] H. Huang, Y. Gu, J. Zhao, X. Wang, Catalytic combustion of chlorobenzene over VO_x/CeO₂ catalysts, *Journal of Catalysis*. 326 (2015) 54–68. <https://doi.org/10.1016/j.jcat.2015.02.016>.
- [59] M. V. Bosco, M.A. Bañares, M. V. Martínez-Huerta, A.L. Bonivardi, S.E. Collins, In situ FTIR and Raman study on the distribution and reactivity of surface vanadia species in V₂O₅/CeO₂ catalysts, *Journal of Molecular Catalysis A: Chemical*. 408 (2015) 75–84. <https://doi.org/10.1016/j.molcata.2015.07.012>.
- [60] G. Silversmit, D. Depla, H. Poelman, G.B. Marin, R. De Gryse, Determination of the V2p XPS binding energies for different vanadium oxidation states (V⁵⁺ to V⁰⁺), *Journal of Electron Spectroscopy and Related Phenomena*. 135 (2004) 167–175. <https://doi.org/10.1016/j.elspec.2004.03.004>.
- [61] J. Wong, F.W. Lytle, R.P. Messmer, D.H. Maylotte, X-edge absorption spectra of selected vanadium compounds, *Physical review*, 8 (1984) 5596–5610. <https://doi.org/10.1103/PhysRevB.30.5596>
- [62] M. Nabavi, F. Taulelle, C. Sanchez, M. Verdager, Xanes and 51V Nmr study of vanadium-oxygen compounds, *Journal of Physics and Chemistry of Solids*. 51 (1990) 1375–1382. [https://doi.org/10.1016/0022-3697\(90\)90020-G](https://doi.org/10.1016/0022-3697(90)90020-G).
- [63] P. Chaurand, J. Rose, V. Briois, M. Salome, O. Proux, V. Nassif, L. Olivi, J. Susini, J.L. Hazemann, J.Y. Bottero, New methodological approach for the vanadium K-edge X-ray

- absorption near-edge structure interpretation: Application to the speciation of vanadium in oxide phases from steel slag, *Journal of Physical Chemistry B*. 111 (2007) 5101–5110. <https://doi.org/10.1021/jp063186i>.
- [64] J. Pelletier, J. Espinas, N. Vu, S. Norsic, A. Baudouin, L. Delevoye, J. Trébosc, E. Le Roux, C. Santini, J.M. Basset, R.M. Gauvin, M. Taoufik, A well-defined silica-supported aluminium alkyl through an unprecedented, consecutive two-step protonolysis-alkyl transfer mechanism, *Chemical Communications*. 47 (2011) 2979–2981. <https://doi.org/10.1039/c0cc04986g>.
- [65] S. Soignier, M. Taoufik, E. Le Roux, G. Saggio, C. Dablemont, A. Baudouin, F. Lefebvre, A. De Mallmann, J. Thivolle-Cazat, J.M. Basset, G. Sunley, B.M. Maunders, Tantalum hydrides supported on MCM-41 mesoporous silica: Activation of methane and thermal evolution of the tantalum-methyl species, *Organometallics*. 25 (2006) 1569–1577. <https://doi.org/10.1021/om050609e>.
- [66] F. Le Quémener, S. Barman, N. Merle, M.A. Aljuhani, M.K. Samantaray, Y. Saih, K.C. Szeto, A. De Mallmann, Y. Minenkov, K.W. Huang, L. Cavallo, M. Taoufik, J.M. Basset, Metathetic Oxidation of 2-Butenes to Acetaldehyde by Molecular Oxygen Using the Single-Site Olefin Metathesis Catalyst ($\equiv\text{SiO}$)₂Mo(=O)₂, *ACS Catalysis*. 8 (2018) 7549–7555. <https://doi.org/10.1021/acscatal.8b01767>.
- [67] C. Larabi, N. Merle, F. Le Quémener, P. Rouge, E. Berrier, R.M. Gauvin, E. Le Roux, A. de Mallmann, K.C. Szeto, M. Taoufik, New synthetic approach towards well-defined silica supported tungsten bis-oxo, active catalysts for olefin metathesis, *Catalysis Communications*. 108 (2018) 51–54. <https://doi.org/10.1016/j.catcom.2018.01.031>.
- [68] M.P. Högerl, L.M. Serena Goh, E. Abou-Hamad, S. Barman, O. Dachwald, F.A. Pasha, J. Pelletier, K. Köhler, V. D’Elia, L. Cavallo, J.M. Basset, SOMC grafting of vanadium oxytriisopropoxide (VO(OiPr)₃) on dehydroxylated silica; Analysis of surface complexes and thermal restructuring mechanism, *RSC Advances*. 8 (2018) 20801–20808. <https://doi.org/10.1039/c8ra02419g>.
- [69] F. Chiker, J.P. Nogier, J.L. Bonardet, Sub-monolayer V₂O₅-anatase TiO₂ and Eurocat catalysts: IR, Raman and XPS characterisation of VO_x dispersion, *Catalysis Today*. 78 (2003) 139–147. [https://doi.org/10.1016/S0920-5861\(02\)00317-6](https://doi.org/10.1016/S0920-5861(02)00317-6).
- [70] S. Besselmann, E. Löffler, M. Muhler, On the role of monomeric vanadyl species in toluene adsorption and oxidation on V₂O₅/TiO₂ catalysts: A Raman and in situ DRIFTS study, *Journal of Molecular Catalysis A: Chemical*. 162 (2000) 401–411. [https://doi.org/10.1016/s1381-1169\(00\)00307-1](https://doi.org/10.1016/s1381-1169(00)00307-1).

CHAPTER IV

**Selective Catalytic Reduction of NO_x with NH₃ over
niobium supported on CeO₂ prepared by Surface
Organometallic Chemistry**

1 Introduction

Fossil fuels are still the primary energy source for industries, vehicles, and ships. The combustion process to extract energy simultaneously emits large amounts of NO_x (mainly including NO and NO₂). The presence of such gasses in the atmosphere causes acid rain, photochemical pollution, and human damage[1]. Therefore, governments have started regulating NO_x emissions. The NO_x treatment methods are divided into the pretreatment, combustion treatment, and post-treatment[2]. The pretreatment mainly modifies the fuel with physical or chemical processes, such as hydrogen denitrification, washing, or coal blending technology to reduce the formation of nitrogen oxides. Combustion treatment reduces NO_x production by changing combustion conditions, such as low nitrogen combustion, low oxygen combustion, graded combustion, etc.[2,3] However, these two methods show difficulties, high cost, and low efficiency in industrial production and automobile exhaust treatment. Post-treatment, especially selective catalytic reduction (SCR) with NH₃ is one of the promising methods to remove nitrogen oxides, which produces only N₂ and H₂O[4]. Although SCR units have been implemented in industrial plants and in recent mobile vehicles, the commercial catalysts still need improvements in the applicable temperature window, thermal stability, recycling, reuse ability, and catalytic conversion efficiency[5]. Therefore, designing a novel efficient NH₃-SCR catalyst is essential in NO_x emissions control.

Ceria-based materials have been intensively investigated for NH₃-SCR, as CeO₂ possesses advantages like low cost, high oxygen storage capacity, acid/base and redox properties necessary for the reaction[6]. Nevertheless, the relatively low acidity and inefficient active sites limit the activity of pure CeO₂[7]. Researchers have developed several methods to improve the catalytic activity of NH₃-SCR in ceria-based catalysts. For instance, 1) structuring different morphology to alter the specific surface area[8]; 2) identification and preparation of ceria material with the more active crystal facet exposed to the surface[9]; 3) introduction of heteroelements (bimetallic oxide catalysts and multiplex system) to improve the oxygen storage capacity or enhance acidity[7,10–12]. Among these methods, the introduction of metal promoters has attracted more attention owing to their convenience and high efficiency.

Recently, Niobium is regarded as an alternative promoter to enhance the catalytic performance of NH₃-SCR over metal oxides-based catalysts. Zhang[13]*et al.* found that the

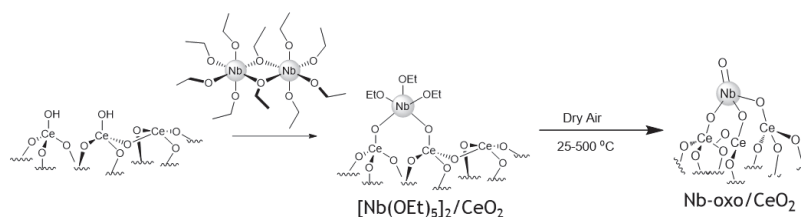
introduction of Niobium into CuCe mixed oxide broadens the operation temperature window from (180-240 °C) to (150-390 °C). They attributed the higher NO conversion at high temperatures (> 300 °C) to the improved acidity by niobium doping. Qu[14] *et al.* reported the abundant surface oxygen species on the surface of CeO₂-Nb₂O₅ prepared by co-precipitation: Nb-OH and Nb=O, which can be regarded as the Brønsted acid site and Lewis acid site. A similar structure was reported by Liu[15] and his co-workers on the surface of the 15% Nb₂O₅ supported on CeO₂/TiO₂ catalyst via impregnation of NbCl₅. They performed the in-situ DRIFT and found that NH₄⁺ is the major reactive intermediate at low temperature (< 200 °C), and the adsorbed NH₂ species become the dominating intermediate at high temperature, which are in agreement with the L-H mechanism at low temperature and E-R mechanism at high temperature.

Even though most of the strategies enhanced the macro activity of NH₃-SCR reaction, identifying the exact active sites and how the different active sites are associated with the mechanism is still challenging[5]. This information is essential in order to design a catalyst at atomic scale, resulting in a ceria-based NH₃-SCR catalyst with improved catalytic performance. Reported Nb/CeO₂ catalysts are synthesized by conventional methods yielding a mixture of different NbO_x species on the surface after the preparation. Hence, it is impossible to attribute the role of each surface specie in the SCR reaction. On the other hand, work dedicated to the synthesis of single Niobium species is difficult, and the corresponding reports are rare. Guo[16] and his co-workers prepared single-atom niobium in graphitic layers by an arc-discharge method. Wu and his co-workers[17] reported 20% Tungsten and 1% Niobium incorporated KIT-6 (WNb-KIT-6) material prepared by the one-pot sol-gel method. They claimed to have incorporated isolated Nb into the ordered silica material (KIT-6) and tuned the electronic environment by W deposition onto these sites, which resulted in enhanced propene yield during 2-butene+ethylene metathesis.

Surface organometallic chemistry is a powerful approach to controllably immobilize metal species onto a support[18]. It is for instance an efficient strategy to prepare well-defined catalysts with tailored moieties on the surface, notably isolated species, which offers solid catalysts suitable for extensive characterization, investigation of reaction mechanisms and determination the structure-reactivity relationship. Yet the development of niobium-based catalysts prepared by SOMC is rare. Jean-Marie Basset and his co-workers[19] reported silica supported the tetramethyl niobium complex, [≡(SiO)NbMe₄] for the trimerization of ethylene.

This catalyst is prepared in two steps: 1) grafting NbCl_3Me_2 on the surface of silica to form $[(\equiv\text{SiO})\text{NbCl}_3\text{Me}]$; 2) surface methylation between $[(\equiv\text{SiO})\text{NbCl}_3\text{Me}]$ and ZnMe_2 . Another example involves the grafting of $\text{Nb}(=\text{N}t\text{Bu})(\text{CH}_2\text{CMe}_2\text{Ph})_3$ on silica leading to a catalyst for the imidation of ketones $[(\text{SiO}_2)_2\text{Nb}(=\text{N}t\text{Bu})(\text{CH}_2\text{CMe}_2\text{Ph})]$.^[20] To our best knowledge, using the SOMC strategy for ceria support with niobium for NH_3 -SCR reaction is unknown.

The organometallic chemistry of Nb^{V} is rather limited due to the homoleptic NbR_5 type complexes instability. Therefore, $\text{Nb}(\text{OEt})_5$ is chosen as precursor, which will simultaneously allow to directly compare with the results obtained with catalyst based on vanadium counterpart described in Chapter III. Herein, surface organometallic chemistry has been applied with the aim to synthesize well-defined Nb supported on ceria as NH_3 -SCR catalyst. More specifically, the targeted niobium-oxo supported on ceria is tentatively synthesized by grafting of $\text{Nb}(\text{OEt})_5$ on the surface of ceria followed by calcination, similarly to the vanadium system described in Chapter III. The structure of the resulting materials is characterized by DRIFT, Elemental analysis, XPS, SSNMR, TOF-SIMS, BET, TEM, and EXAFS. The NO conversion and N_2 selectivity of these catalysts are also investigated with NH_3 -SCR conditions.



Scheme 1 Illustration of the preparing niobium-oxo supported on ceria

2 Preparation and characterization of $[\text{Nb}(\text{OEt})_5]_2/\text{CeO}_2$ -200

2.1 Preparation of $[\text{Nb}(\text{OEt})_5]_2/\text{CeO}_2$ -200 [Nb-a]

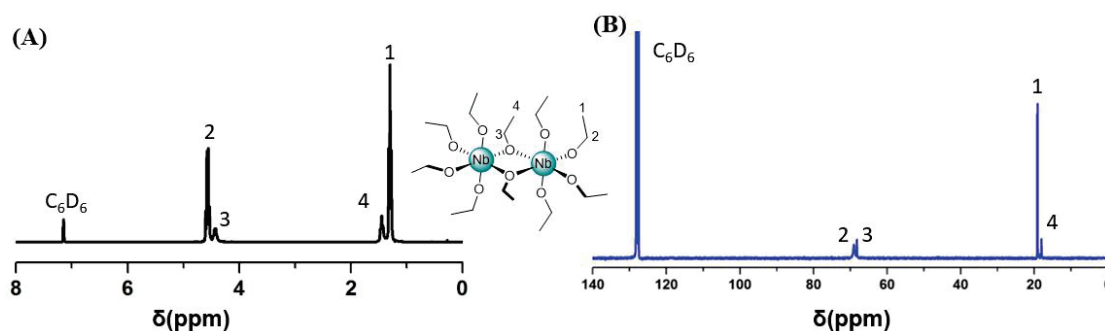
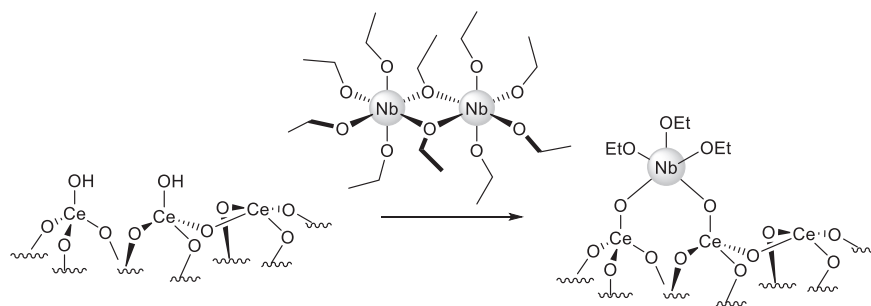


Fig. 1 Liquid NMR (A) ^1H and (B) $^{13}\text{C} \{^1\text{H}\}$ of $[\text{Nb}(\text{OEt})_5]_2$

The ceria support (CeO_2) was treated by calcination at 500 °C under air, followed by hydration and dehydroxylation at 200 °C (see Chapter II section 2.1) before use. $[\text{Nb}(\text{OEt})_5]_2$ is commercial and purchased from Strem. The purity is confirmed by ^1H and $^{13}\text{C}\{^1\text{H}\}$ NMR (Fig. 1), displaying the characteristic signals of the dimeric $[\text{Nb}(\text{OEt})_5]_2$ complex without visible organic impurities. The grafting reaction of $[\text{Nb}(\text{OEt})_5]_2$ on CeO_2 was conducted in toluene at room temperature during 12 h. The resulting materials were washed three times with toluene and rinsed with pentane to remove unreacted precursor. After evaporation of the solvent and drying under vacuum, the resulting materials were obtained as light grey powder. The $[\text{Nb}(\text{OEt})_5]_2/\text{CeO}_2$ sample was named **[Nb-a]**. Then, it is characterized by Elemental analysis, BET, DRIFT, SSNMR.

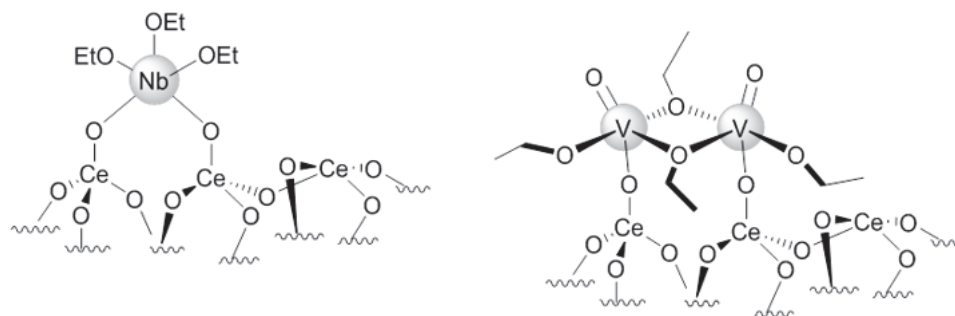
2.2 Characterization of [Nb-a] by Elemental analysis



Scheme 2 Schematic illustration of the grafting of $[\text{Nb}(\text{OEt})_5]_2$ on CeO_{2-200} .

Results of Elemental analysis of **[Nb-a]** show the presence of 1.8% Nb and 1.4% C, which correspond to $0.19 \text{ mmolNb}\cdot\text{g}^{-1}$ and $1.18 \text{ mmolC}\cdot\text{g}^{-1}$, or $\text{C/Nb} = 6.2$. These results suggest that three ethoxide ligands remain per Nb in the product, which means two equivalents of ethanol have been produced during the protonolysis process. Therefore, 0.38 mmol OH/g of hydroxyls on the surface of ceria have been consumed. According to the chemical titration of OH groups in CeO_2 dehydroxylated at 200 °C, $0.7 \text{ mmol OH}\cdot\text{g}^{-1}$ is found on the surface of CeO_{2-200} , meaning that around 54% of initial surface O-H has reacted when $[\text{Nb}(\text{OEt})_5]_2$ is grafted onto the surface of CeO_2 . Unfortunately, the released ethanol is difficult to be quantified. According to the literature, there are examples demonstrating that dimeric complexes can be cleaved upon grafting, notably onto a polar support, giving monomeric grafted species[21]. Based on our previous experiences (Chapter II and III) and Elemental analysis, the structure of $[\text{Nb}(\text{OEt})_5]_2/\text{CeO}_{2-200}$ is tentatively proposed to be a monomeric bipodal species (expected $\text{C/V} = 6$), expressed as $[(\equiv\text{CeO})_2\text{Nb}(\text{OEt})_3]$ (Scheme 2). There is a

notably different reactivity between $[\text{Nb}(\text{OEt})_5]_2$ and $[\text{V}(=\text{O})(\text{OEt})_3]_2$ with ceria (Scheme 3). In this case, the final structure appears to be a monomeric bipodal species containing 0.19 mmol Nb per gram of support. While in Chapter II, the final structure is rather described by a dimeric species containing 0.42 mmol V per gram of support. The difference in reactivity can be related to the diameter of the transition metal, as Nb is larger and may therefore be monomeric in toluene. Conversely, vanadium is smaller and may keep a dimeric nature for stabilization.



Scheme 3 Resulting species after grafting of dimeric vanadium (right) or niobium (left) ethoxide precursors on ceria.

2.3 Characterization of [Nb-a] by DRIFT spectroscopy

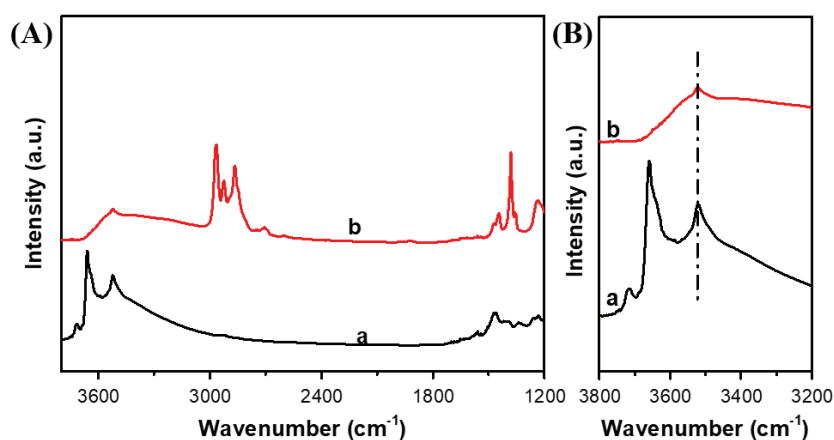


Fig. 2 (A) ($3800\text{-}1200\text{ cm}^{-1}$) DRIFT spectra and (B) specific enlargements ($3800\text{-}3200\text{ cm}^{-1}$) for the attribution of $\nu(\text{O-H})$ stretching vibration bands of a) CeO_{2-200} and b) [Nb-a].

As shown in Fig. 2, DRIFT spectroscopy is used to examine the grafting process. Pronounced changes are observed in the $\nu(\text{OH})$, $\nu(\text{CHx})$, and $\delta(\text{CH})$ regions. In fact, the appearance of bands at $3000\text{-}2700\text{ cm}^{-1}$ and $1500\text{-}1200\text{ cm}^{-1}$ (Fig. 2A) is attributed to aliphatic $\nu(\text{CHx})$, and $\delta(\text{CHx})$ vibrations of the ethoxy ligands bonded to Nb on the surface of CeO_2 . Enlarged infrared spectra in the $\nu(\text{O-H})$ region are shown in Fig. 2B. After grafting, the terminal $\mu^1\text{-OH}$ totally disappeared. On the other hand, the $\mu^3\text{-type OH}$ (3527 cm^{-1}) seems to be less reactive.

Importantly, the DRIFT spectrum in this region is rather dominated by a broad peak, indicating the presence of interactions between remaining Ce-OH groups and the grafted surface organometallic fragment. Similar features are observed when $[V(=O)(OEt)_3]_2$ and $[W(\equiv C tBu)(CH_2 tBu)_3]$ are grafted on the surface of ceria. Thus, the results of DRIFT confirm the successful grafting of $[Nb(OEt)_5]_2$ onto the surface of ceria.

2.4 Characterization of [Nb-a] by Nitrogen adsorption-desorption isotherm measurements

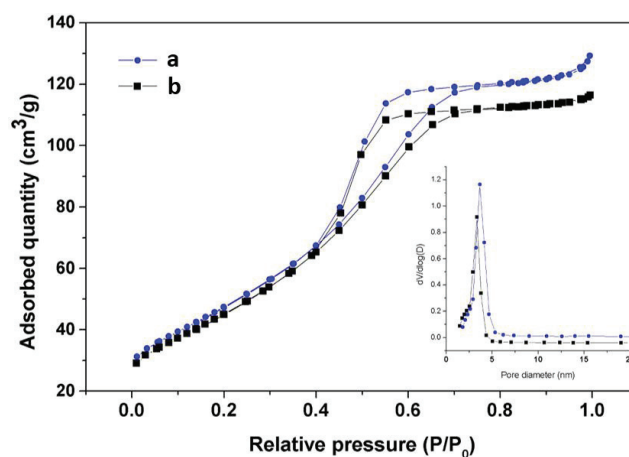


Fig. 3 Nitrogen physisorption isotherms and corresponding pore size distribution (BJH during desorption, inset) of (a) CeO_2 -200 and (b) [Nb-a].

Nitrogen adsorption-desorption isotherm measurement for CeO_2 and [Nb-a] are employed to evaluate the effects of the grafting on the textural properties of the material. The physisorption isotherms and the pore size distribution is depicted in Fig. 3 and its inset. CeO_2 and [Nb-a] exhibit the same type of adsorption/desorption isotherms, classified as type IV according to IUPAC nomenclature and show a H2-type hysteresis loop. [Nb-a] has a specific surface area of $175 \text{ m}^2 \cdot \text{g}^{-1}$, which shows a marginal decrease with respect to bulk CeO_2 ($188 \text{ m}^2 \cdot \text{g}^{-1}$). In addition, [Nb-a] shows a similar pore size distribution to bulk ceria, as depicted in the inset of Fig. 3. These observations suggest that the functionalization with $[Nb(OEt)_5]_2$ of the surface of ceria has limited impact on the textural properties of CeO_2 .

2.5 Characterization of [Nb-a] by solid state NMR

Solid state NMR (1H and ^{13}C) is used to characterize the nature of organic moieties in the grafting material [Nb-a]. As depicted in Fig. 4A, a main 1H signal at 1.2 and a shoulder

around 4.6 ppm are observed, assigned to (-OCH₂CH₃) and (-OCH₂CH₃) respectively. Furthermore, ¹³C CP MAS NMR spectrum features significantly broader peaks at 19 and 67 ppm, attributed to (-OCH₂CH₃) and (-OCH₂CH₃) respectively. In addition, there are also two narrower components at 17 and 63 ppm, tentatively attributed to strongly adsorbed ethanol on the surface[22]. Furthermore, there is a small shoulder at 72 ppm characteristic of bridged ethoxide ligands. The latter indicates that [Nb-a] comprises mainly a monomeric species with minor amounts of dimeric species. Noteworthy, no broadening or shift in the NMR spectra is observed, suggesting the absence of paramagnetism. Based on these results, grafting [Nb(OEt)₅]₂ onto ceria gives mainly an isolated bipodal Nb species bearing three ethoxide ligands.

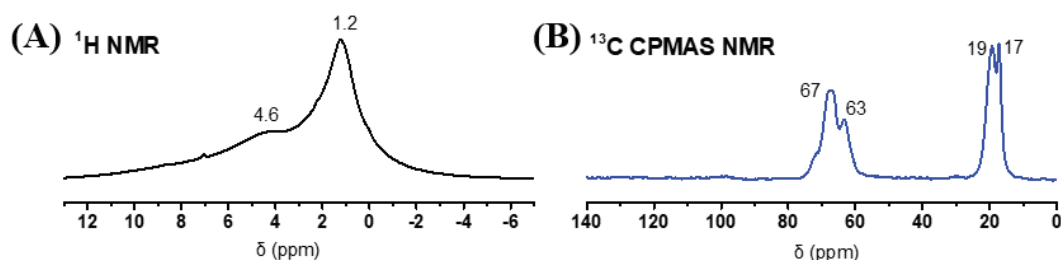


Fig. 4 (A) ¹H MAS NMR and (B) ¹³C CP MAS NMR of [Nb-a].

3 Preparation and characterization of Nb-oxo supported on CeO₂

3.1 Preparation of Nb-oxo/CeO₂ [Nb-b]

The grafted material [Nb-a] is calcined under dry air for 18 h to obtain niobium-oxo species on the surface of ceria. The resulting material is mentioned as [Nb-b], and is characterized by DRIFT, ToF-SIMS, XPS, TEM, and EXAFS.

3.2 Characterization of [Nb-b] by Elemental analysis and DRIFT spectroscopy

The Nb content in [Nb-b] is found to be 1.8 wt% from Elemental analysis, confirming no loss of Nb during the calcination process. Moreover, no carbon is detected, indicating that the organic ligands are completely removed. FT-IR analysis is further carried out to follow the surface structure upon calcination. As shown in Fig. 5, the initially presented ν(CH_x) and δ(CH_x) vibrations of the ethoxide ligands in [Nb-a] are absent in Nb-oxo/CeO₂, [Nb-b], which suggests that organic fragments have totally decomposed during the calcination process. Moreover, several hydroxyl groups are regenerated with a slight red shift with respect to the

initial ceria material, suggesting a re-distribution of hydroxyls on the surface occurs during the calcination process, similar to the W and V systems on ceria described in the previous Chapters. Another pronounced change in the DRIFT spectrum is in the 900-1100 cm^{-1} region, which corresponds to the frequency of Nb=O stretching modes. Fig. 5C highlights this region where three bands can be identified at 976 cm^{-1} , 969 cm^{-1} , and 955 cm^{-1} , and assigned to different Nb=O species[23,24].

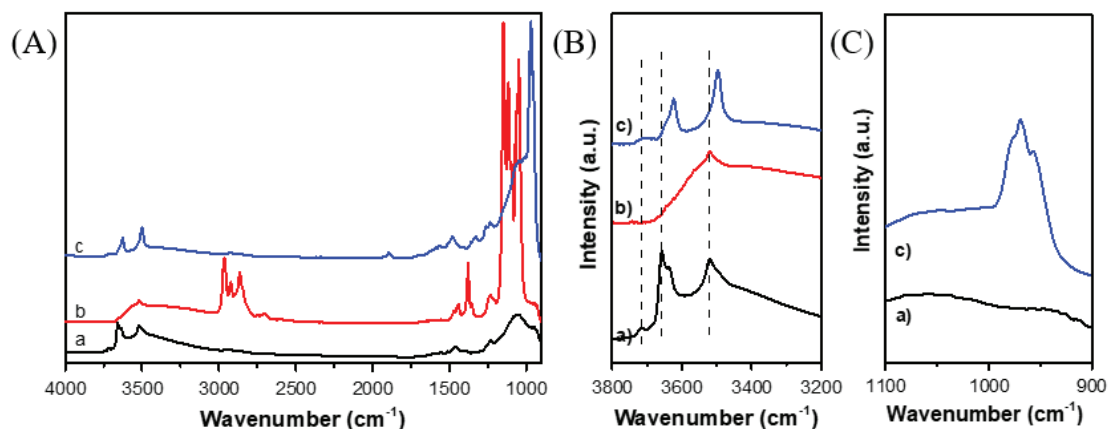


Fig. 5 DRIFT spectra in different region (A) 4000 cm^{-1} -1000 cm^{-1} ; (B) 3800 cm^{-1} -3200 cm^{-1} ; (C) 1100 cm^{-1} -900 cm^{-1} over samples: a) $\text{CeO}_2\text{-200}$; b) [Nb-a]; c) [Nb-b].

3.3 Characterization of [Nb-b] by Time-of-flight secondary ion mass spectrometry

To further investigate the population of different Nb oxo species on the surface, Time of Flight Secondary Ion Mass Spectrometry is applied to [Nb-b]. A. Benninghoven was the first to propose this method to discriminate different surface species[25]. When the primary ion dose is applied to the surface, different surface fragments will be extracted from the material and analyzed by MS. The ion dose used to be low to minimize the destruction of chemical bonds[26]. Mass spectrometry analysis of the chemical composition of these fragments provides access to the surface composition of the material. Therefore, this is a powerful technique to determine the presence of different Nb species (monomeric, dimeric, oligomeric) in [Nb-b]. According to the observed mass distributions (Fig. 6), there are mainly monomeric species (Nb^+ , $\text{NbO}_x^{+/-}$, $\text{CeNbO}_y^{+/-}$), minor amounts of dimeric species (Nb_2O_5^- , Nb_2O_6^- , $\text{CeNb}_2\text{O}_6^+$, $\text{Ce}_2\text{Nb}_2\text{O}_7^+$, $\text{Ce}_3\text{Nb}_2\text{O}_9^+$) and importantly no oligomeric species in [Nb-b]. These results indicate that most of the species observed in Time of Flight Secondary Ion Mass Spectra are monomeric along with smaller amounts of dimeric species, which is consistent with the observation in EXAFS (*vide infra*).

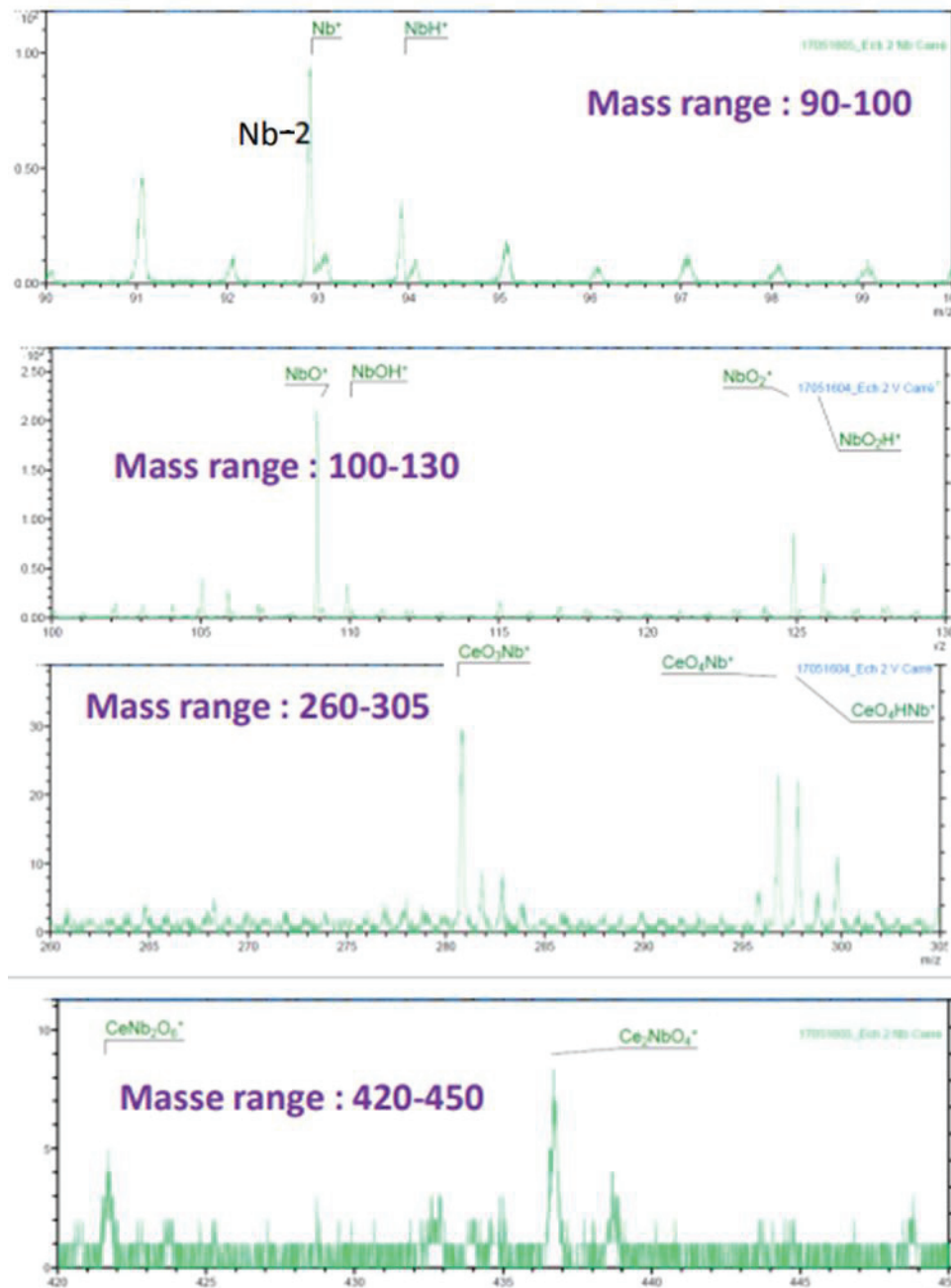


Fig. 6 Mass distribution of clusters released from ToF-SIMS irradiation

3.4 Characterization of [Nb-b] by X-ray photoelectron spectroscopy and EDX Mapping

The distribution of different elements on [Nb-b] is visualized by STEM/EDX (energy-dispersive X-ray spectroscopy) mapping. Transmission electron microscopy is a general technique to determine the presence of foreign clusters or nano particles on a support. However, due to the high atomic weight of Ce, eventual particles of Nb are expected to be masked. Nevertheless, large particles of Nb or NbOx, even supported on ceria, can be

revealed by STEM/EDX. Fig. 7 displays a STEM image and the corresponding EDX mapping of an object. The expected elements (Ce, Nb, O) are equally distributed throughout the object, indicating the Nb is well dispersed on the surface of ceria. In addition, the oxidation state of surface Ce in [Nb-b] is analyzed by XPS. As shown in Fig. 7E, 10 characterized peaks can be identified, originating from Ce³⁺ and Ce⁴⁺ on the surface. Peaks labeled v, v'', v''' (3d_{5/2}) and u, u'', u''' (3d_{3/2}) are assigned to the Ce⁴⁺, while u₀, u', v₀, v' are attributed to Ce³⁺. Based on the formula $\%Ce^{3+} = 100 * [Ce^{3+} / (Ce^{4+} + Ce^{3+})]$, the ratio of Ce³⁺ is estimated to be 29.5% which shows a significant increase with respect to bulk CeO₂₋₂₀₀ (20.6%). An increase in Ce³⁺ concentration after the introduction of a hetero element has previously been observed for tungsten (Chapter II) and vanadium (Chapter III). This result thus confirms the presence of Ce³⁺ in [Nb-b]. Unfortunately, the oxidation state of Nb is not analyzed by XPS. However, the oxidation state of [Nb-b] is determined by XANES in the next section.

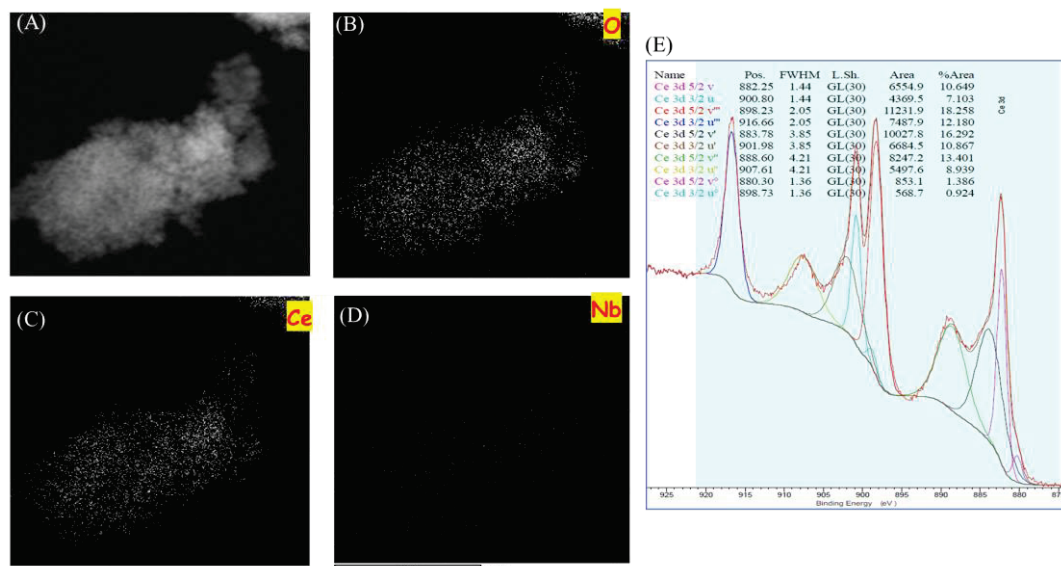


Fig. 7 STEM (A, B, C, D) and XPS ϵ spectra of Ce 3d of the catalyst [Nb-b]

3.5 Characterization of [Nb-b] by X-ray Adsorption spectroscopy

The sample with a Nb loading of 1.8 wt% was studied by X-ray absorption spectroscopy in order to precise the structure of the supported species. The XANES results (Fig. 8) suggested that the Nb species on the cerium oxide surface, with a spectrum showing an important pre-edge signal, are in a tetrahedral environment.

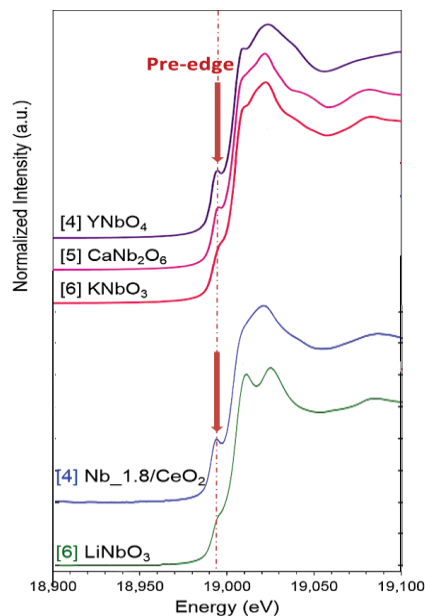


Fig. 8 Niobium K-edge XANES for sample with 1.8 wt% Nb loading (down blue) compared with known crystal where Nb is in coordination 4 ([4], tetrahedral), 5 ([5], square based pyramid) or 6 ([6], octahedral)

The parameters extracted from the fit of the EXAFS (Fig. 9 and Table 1) of the 1.8 wt % loaded sample are in agreement with a $(\text{O})_3\text{Nb}(=\text{O})$ structure, with ca. one oxygen atom at 1.74(2) Å, attributed to an oxo ligand and ca. three oxygen atoms at 1.997(12) Å, attributed most probably to two surface oxide ligands and one hydroxyl ligand. The fit could be also improved by adding a further layer of back-scatterers, with only ca. one cerium atom at 3.50(2) Å and ca. two oxygen atoms at 2.56(4) Å. The inclusion of niobium as a second neighbor was not statistically validated. Therefore, this EXAFS study is in agreement with the $(\text{O})_3\text{Nb}(=\text{O})$ tetrahedral structure of an isolated site as the one represented below in Fig. 10, with one Ce atom from the surface as a second neighbor.

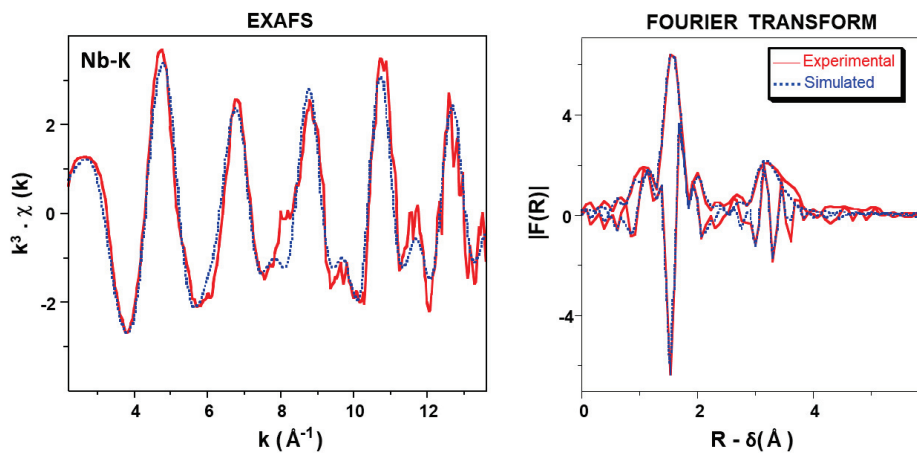


Fig. 9 Niobium K-edge k^3 -weighted EXAFS for [Nb-b] (left) and corresponding modulus and imaginary part of the Fourier transform (right). Solid lines: experimental; dashed lines: spherical wave theory

Table 1 EXAFS parameters for the niobium species at the surface of cerium oxide ^a

Type of neighbor	Number of neighbours	Distance (Å)	σ^2 (Å ²)
Nb= <u>O</u>	0.8(3)	1.74(2)	0.0051(22)
Nb- <u>O</u> Ce _x or Nb- <u>OH</u>	2.8(3)	1.997(12)	0.0043(14)
-b- <u>O</u> _s	2.3(7)	2.56(4)	0.0148(59)
Nb-O- <u>Ce</u>	1.1(4)	3.50(2)	0.0052(24)

^a The errors generated by the EXAFS fitting program “RoundMidnight” are indicated in parentheses. ^a Δk : [2.1-14.3 Å⁻¹] - ΔR : [0.4-3.6 Å]; $S_0^2 = 0.92$; $\Delta E_0 = 1.2 \pm 1.4$ eV; Fit residue: $\rho = 8.6$ %; $(\Delta\chi)^2/\nu = 2.84$ with $\nu = 13/26$

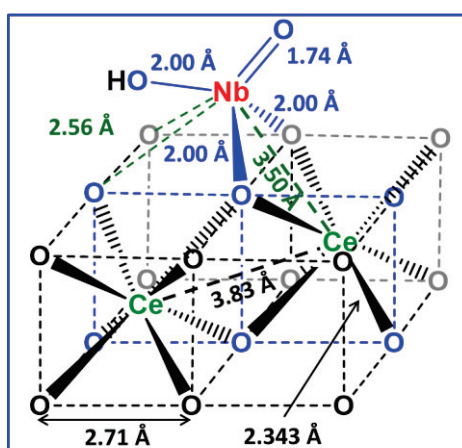


Fig. 10 Structure in agreement with the fit of the EXAFS (distances in blue or green are deduced from the fit, distances in black are those of the CeO₂ crystal)

4 Catalytic performance investigation

4.1 Catalytic performance (NO conversion and N₂ selectivity) of [Nb-b]

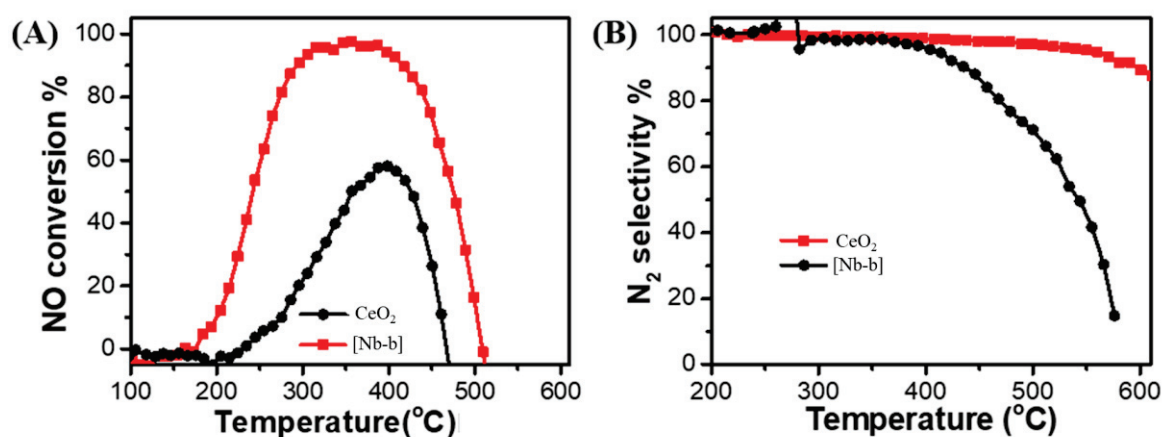


Fig. 11 (A) NO conversion and (B) N₂ selectivity performance of CeO₂ and Nb-oxo/CeO₂ at different temperatures

Bulk CeO₂ and [Nb-b] were evaluated for the NH₃-SCR reaction in a continuous flow reactor. The temperature dependencies of the NO_x conversion and N₂ selectivity are shown in Fig. 11. The catalyst [Nb-b] synthesized by SOMC shows more than 90 % conversion of NO_x between 300 to 400 °C, while a maximum 58 % was observed at 350 °C for CeO₂. It was obvious that niobium improved the NO_x conversion. Moreover, the selectivity for N₂ is outstandingly increased with the addition of Niobium onto ceria.

4.2 Effect of Nb loading on catalytic performance over [xNb-b] (x=0.2 wt%, 0.5 wt%, 1.0 wt%, and 1.8 wt%)

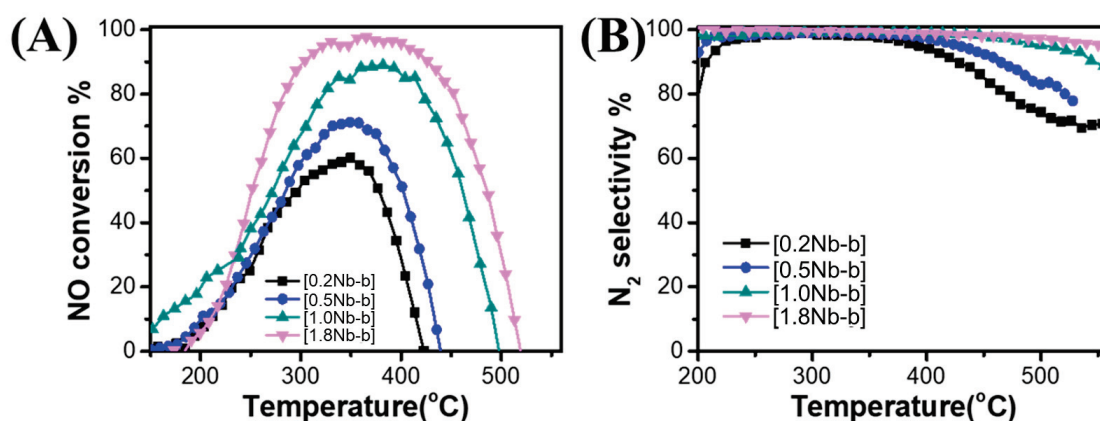


Fig. 12 (A) NO conversion and (B) N₂ selectivity performance of different loading of [xNb-b] (x=0.2 wt%, 0.5wt%, 1.0wt%, 1.8wt%)

The prepared series of [xNb-b] catalysts with various niobium loadings (x, wt%), (x=0.2 wt%, 0.5 wt%, 1.0 wt%, and 1.8 wt%) as a function of temperature are presented in Fig. 12. Obviously, the catalytic conversion of NO increases with the niobium loading using the same GHSV. [0.2Nb-b] exhibits 60% NO conversion at 350 °C, which is similar to bulk CeO₂, while 71% and 86% NO conversions are obtained over [0.5Nb-b] and [1.0Nb-b]. Noteworthy, full NO conversion and the broadest operation temperature window were provided by [1.8Nb-b]. Additionally, N₂ selectivity in Fig. 12B is also improved by increasing the niobium loading. These results confirm the positive effect provided by the addition of isolated niobium centers on ceria. Increasing the Nb loading as mostly isolated sites also expands the operating temperature window in the NH₃-SCR reaction.

5 Comparison of different group V and VI transition metals supported on ceria

5.1 Structure of catalysts based on CeO₂ supported metals (M=V, Nb, Mo, W)

Inconveniences with conventional NH_3 -SCR catalysts lie in the preparation methods, as described earlier, which inevitably lead to a mixture of different surface species. Such complex surfaces are difficult to characterize at molecular level and make it impossible to associate the role of each specie in the catalytic reaction. A prerequisite to develop novel catalysts exceeding the performance of the state-of-the-art catalysts is to determine the structure-reactivity relationship. In addition, an alternative synthetic method for such catalysts needs to be introduced, featuring unique and controllable active sites. This thesis is targeted towards ceria supported monomeric transition metals (Group V and VI) species. Such transition metals modified ceria have already been reported to be promising catalysts for NH_3 -SCR. Furthermore, monomeric species have recently been postulated to be the real active sites of classically known metal-oxide catalysts in industrially important reactions[27–30]. The employed synthetic method is surface organometallic chemistry, which after judicious choice of the organometallic precursors and pre-treatment of the support may provide uniquely isolated sites. Evidently, a thorough characterization and determination of the optimal pretreatment conditions are extremely important prior to the grafting process.

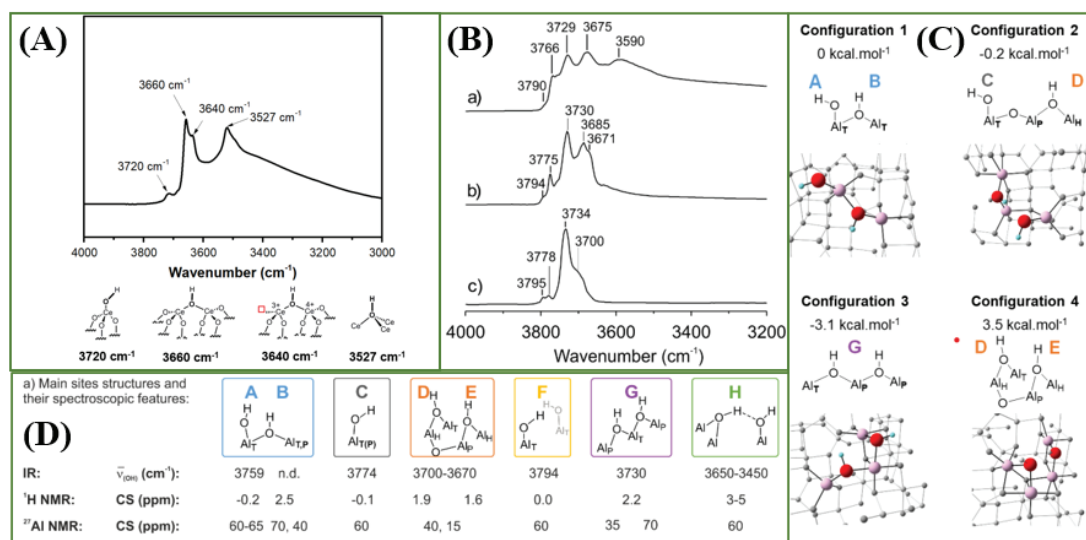


Fig. 13 (A) Attribution of (CeO-H) stretching vibration bands in this thesis; (B) DRIFTS spectra in the hydroxyl stretching region for a) Al_2O_3 -300, b) Al_2O_3 -500, c) Al_2O_3 -700; (C) structures of the main hydroxyl sites and their spectroscopic features (values shown for Al_2O_3 -500); (D) Calculated hydroxyl group configurations and their relative energies, for the partially hydroxylated (110) surface of γ - Al_2O_3 with $\theta = 0.7 \text{ OH/nm}^2$

As discussed in Chapter II, the surface of CeO_2 dehydroxylated at 200 °C contains 0.7 mmol $\text{OH}\cdot\text{g}^{-1}$ after calculation by a chemical titration using $\text{Al}(i\text{Bu})_3$. The DRIFT spectrum of CeO_2 -200 exhibits different hydroxyl groups (μ^1 -OH, μ^2 -OH, and μ^3 -OH), as shown in Fig. 13A.

Similar types of hydroxyls are reported to the surface of Al_2O_3 (Fig. 13B)[31]. Based on a DFT calculation, Merle *et al.* proposed four kinds of hydroxyl group configurations after water adsorption on either an (Al atoms in trigonal symmetry) site or an Al_T (Al atoms in pseudo-tetrahydro symmetry) surface site. Combining the information from experimental studies (selective reaction with HCl and CO_2), characterization (high-field ^1H and ^{27}Al solid state NMR, IR spectroscopy), and DFT calculations, they proposed the structure-property correlations (Fig. 13D). Similar to Al_2O_3 , various hydroxyls on ceria surface may possess different reactivity, and the co-presence of Ce^{3+} and Ce^{4+} makes the surface even more complex than the surface of Al_2O_3 .

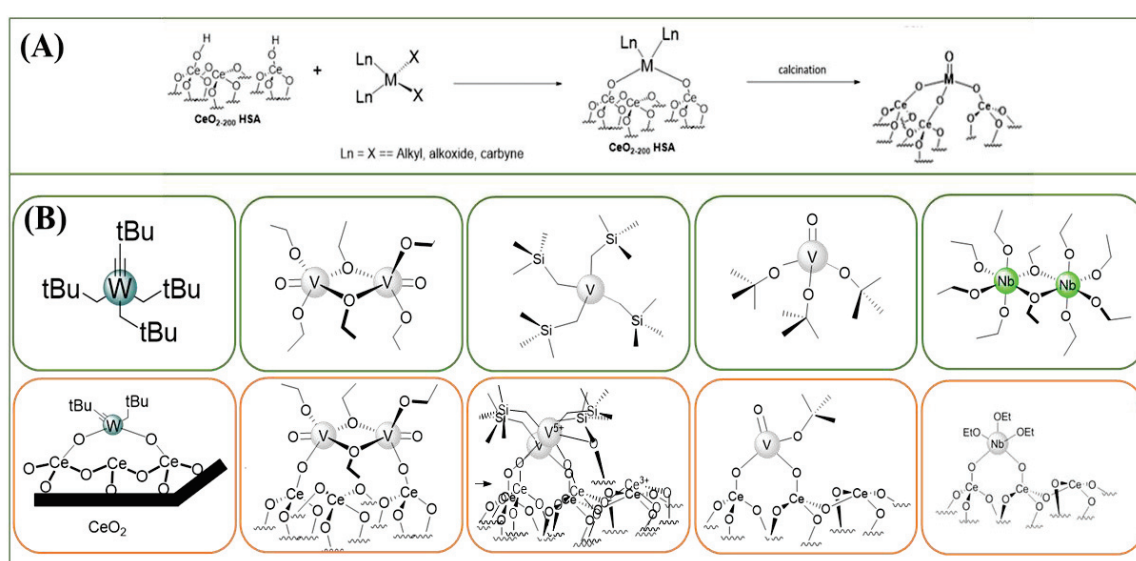


Fig. 14 (A) Schematic illustration of the general approach used in this thesis to prepare the catalytic materials; (B) structure of metallic molecular complexes and corresponding materials obtained after the grafting reaction

The target of this thesis is to develop single site NH_3 -SCR catalysts based on group V and VI transition metal oxo supported on ceria. The development of such beyond state of the art catalysts requires research efforts in the synthetic methodology, characterization and fundamental comprehension of the ceria support. The chosen synthetic approach, namely surface organometallic chemistry, is based on judicious choice of the organometallic precursor and controlled treatment of the support. Selected organometallic precursors of group V and VI transition metal ($\text{M}=\text{W}, \text{V}, \text{Nb}$) have been grafted onto ceria dehydroxylated at $200\text{ }^\circ\text{C}$ followed by calcination under air at high temperature, giving catalytic materials for NH_3 -SCR investigation. A schematic illustration of the synthesis process is depicted in Fig. 14A. The resulting materials are characterized by Elemental analysis, FT-IR, XPS, EPR, SSNMR, Raman, and XAS. Concerning the grafting step, the following organometallic

complexes have been applied: $[W(\equiv C*t*Bu)(CH_2*t*Bu)_3]$, $[V(=O)(OEt)_3]_2$, $[V(=O)(O*t*Bu)_3]$, $[V(CH_2SiMe_3)_4]$, and $[Nb(OEt)_5]$. Fig. 14B summarizes the main surface species obtained after the grafting of the corresponding precursors in toluene at room temperature. In most cases, the grafting reaction yields bipodal monomeric metal species (for $[W(\equiv C*t*Bu)(CH_2*t*Bu)_3]$, $[V(=O)(O*t*Bu)_3]$, and $[Nb(OEt)_5]$). Exceptions are found for $[V(=O)(OEt)_3]_2$, which gives monopodal dimeric species after the grafting reaction, and $[V(CH_2SiMe_3)_4]$, which after a unique reactivity involving Ce-O-Ce bridge opening through electron transfer and oxidation of vanadium (IV), presumably gives tripodal vanadium species. These results suggest the complexity of the surface of ceria support and that the structure of the resulting surface species is strongly related to the nature of the organometallic ligand and the polarity of ceria support.

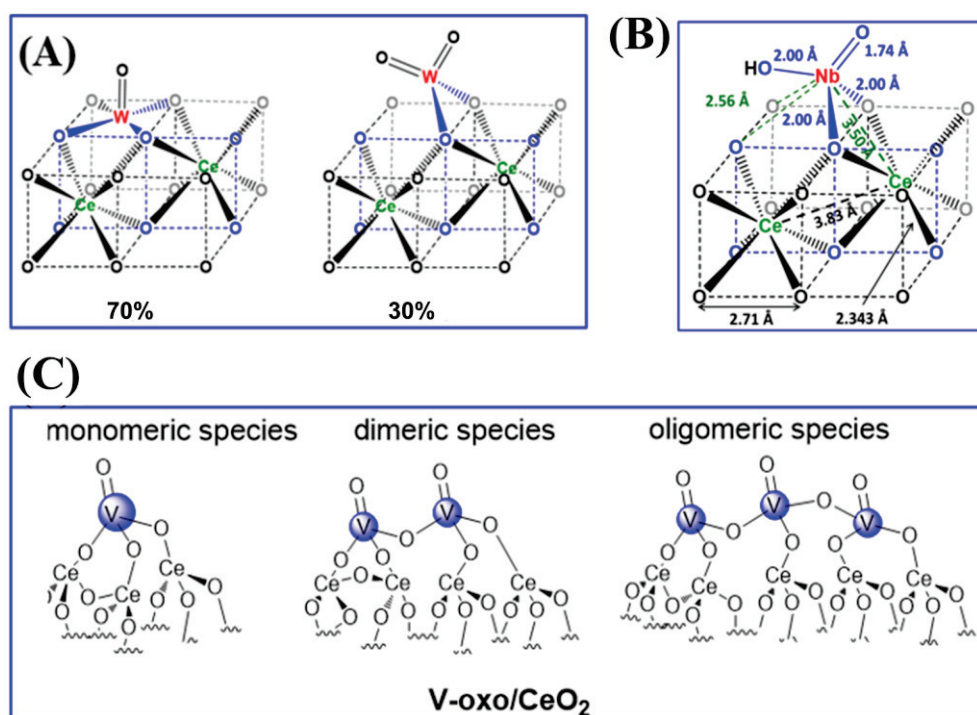


Fig. 15 Illustration of the structure of (A) tungsten-oxo, (B) niobium-oxo, and (C) vanadium-oxo supported on ceria

In the second step, the grafting materials were calcined under air at high temperatures. In the case of tungsten-oxo (Fig. 15A), calcination of grafted species provides a mixture of isolated tungsten mono-oxo (70%) and tungsten bis-oxo species (30%), which is confirmed by Raman, FT-IR, and EXAFS. Moreover, the calcination of $[Nb(OEt)_5]/CeO_{2-200}$ gives an isolated Nb-oxo site described as $[(\equiv CeO)_2Nb(=O)(OH)]$ with a proposed structure shown in Fig. 15B. As for the case of vanadium, even though the goal was to get isolated vanadium species, a

mixture of monomeric (major species), dimeric and oligomeric vanadium-oxo species supported on ceria were always observed after calcination, independently of the precursor used, (Fig. 15C). These results suggest that vanadium surface species are extremely mobile on a ceria surface under the calcination conditions. The mobility of an element on an oxide surface may be related to the dissociation energy of M-O as well as the formation energy of M-O-M self-assembly. As no database gathering the dissociation energy of M-O bond (M = V, Nb, W) in M-O-Ce fragment exists, the general dissociation bond energy may give an indication. The bond dissociation energy of V-O is 644 kJ/mol, while that of W-O is 653 kJ/mol and Nb-O needs 753 kJ/mol. This may explain the enhanced mobility of vanadium with respect to niobium and tungsten.

5.2 Comparison of the NH₃-SCR performance over Metal-oxo/CeO₂ (Metal=W, Mo, Nb, V) catalysts

Metal oxides and ion-exchanged zeolites are the most widely investigated catalyst for the NH₃-SCR reaction. Ceria has attracted great attention to the NH₃-SCR reaction due to its oxygen storage ability. The oxides of groups V and VI (VO_x, NbO_x, WO_x, and MoO_x) are widely used as promoters for ceria-based catalysts and exhibit high SCR activity. However, metals from group VIII are usually regarded to be the active site in ion-exchanged zeolites. Even though both metal oxides and ion-exchanged zeolite catalysts require acidity and redox ability, they could take part in the different NH₃-SCR mechanisms due to their difference in catalyst composition and structure.

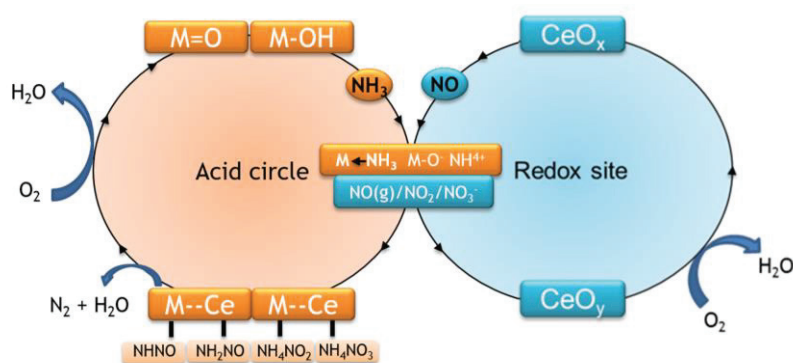


Fig. 16 Schematic illustration of the NH₃-SCR mechanisms

Based on the proposed mechanisms in literature, there are two dominating pathways, known as the E-R and L-H mechanisms[32]. Common features of both proposals involve surface acidity and redox properties (as shown in Fig. 16). Concerning the acidity, there is an ongoing

debate about the importance of Lewis and Bronsted acidity. Several reports claim that the Lewis acidity is the most essential for the reaction, while other works show that it is rather the Bronsted sites that are involved in the reaction. Moreover, it has also been proposed that both acidities may act differently at low and high temperatures during the NH₃-SCR of NO. Since ceria has less Lewis acid sites, the adsorption and activation of NH₃ are usually reported to take place on Lewis acidic sites (M=O) and Brønsted acidic sites (M-OH) to form various NH_x (x=1, 2, 3, 4). Due to the unique oxygen storage ability of ceria support, NO is more likely to be adsorbed and activated on the ceria support to form active NO_x (gaseous NO, bridge nitrite, bidentate nitrate, monodentate nitrite)[6,33–36]. Then, the adsorbed or active species NH_x and NO_x react to form intermediates comprising N-N bond (NHNO[37], NH₂NO[15,38,39], NH₄NO₂[34,37], NH₄NO₃[39,40]), which decompose to N₂ and H₂O. At the end, the reduced catalytic sites are regenerated by oxidation with O₂ present in the feed. Therefore, the controversies in NH₃-SCR reaction over ceria-based catalysts are on i) the active sites (M=O or M-OH) and surface species (NH_x and NO_x) after activation by NH₃/NO; ii) restructuring of the adsorbed/gas phase species to create the N-N bond, followed by decomposition pathways of the intermediates and N₂ release. The pursued debate is associated to the structure-reactivity relationship which is difficult to establish from conventional catalysts comprising a mixture of different surface species. However, the SOMC prepared catalysts offer this opportunity as the final catalysts are well-defined and generally contain isolated metal sites. In the series of the prepared materials, vanadium-based catalysts showed a tendency to agglomerate upon calcination and resulted in a mixture of different surface species, though the monomeric species remain the major ones. Conversely, niobium and tungsten give monomeric species, even after calcination.

The series of prepared M-oxo/CeO₂ (M=W, Mo, Nb, V) comprising the same metal loading (0.2 mmol metal per 1g ceria) has been tested for NH₃-SCR on NO and compared to bulk ceria catalysts prepared by classical method with the same metal loading. The NO conversion and N₂ selectivity are shown as functions of temperature in Fig. 17. All M-oxo/CeO₂ catalysts exhibit better catalytic performance than bulk ceria and the corresponding catalysts prepared by classical method, and the order of their activity follows: W-oxo/CeO₂ > Nb-oxo/CeO₂ > Mo-oxo/CeO₂ > V-oxo/CeO₂. There is an agreement in literature that acidity and redox properties are essential to complete the catalytic cycle of NH₃-SCR.

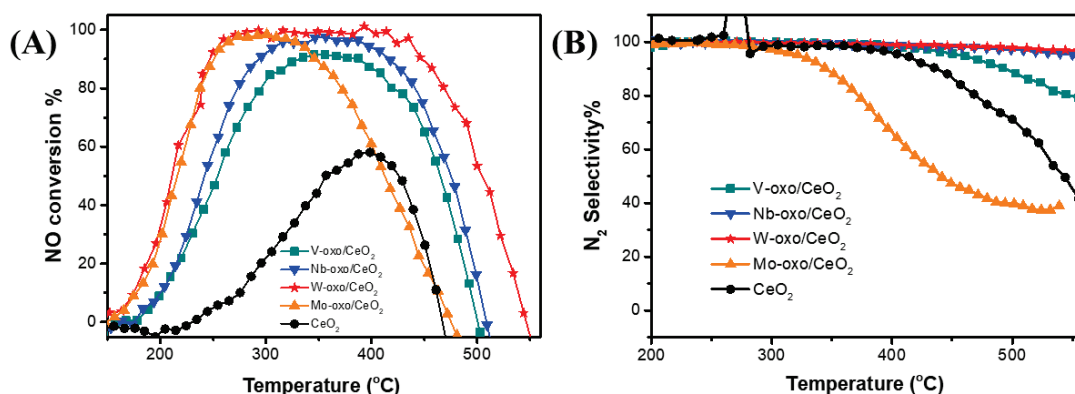


Fig. 17 (A) NO conversion and (B) N₂ selectivity of bulk ceria, tungsten-oxo, molybdenum-oxo/CeO₂, vanadium-oxo, and niobium-oxo supported on ceria

A general observation of all SOMC catalysts is the isolated (at least the major species) nature of the sites and the presence of Ce³⁺, forming the crucial acid/redox pair which is proposed to be the active site for the reaction. The W-oxo/CeO₂ is found to be the most active catalyst, owing to an exceptionally high thermal stability with a single site nature. Nb-oxo/CeO₂ shows slightly lower performances than the tungsten system. Noteworthy, there is a remarkable difference on the NO conversion, particularly for the high temperature region between the W/Nb and Mo/V systems. Both Mo-oxo/CeO₂ and V-oxo/CeO₂ exhibit a dramatic drop in the NO conversion around 350 °C. Moreover, these catalysts show a decrease in the N₂ selectivity at higher temperatures. The latter phenomenon can be explained by the oxidation of ammonia, which causes an inhibition of the NH₃-SCR reaction and lower N₂ selectivity. In fact, both vanadium and molybdenum can undergo thermal reduction at this temperature, resulting in a reduced oxide specie active in oxidation reactions. For example, vanadium(IV) is reported to catalyze ammonia oxidation to nitric oxide.[41] The enhanced activity of transition metal functionalized ceria is attributed to the enhanced acidity. For instance, NH₃-TPD has been conducted for W-oxo/CeO₂ and V-oxo/CeO₂ in Chapter II and III respectively. No Bronsted acidity was found and no significant difference between the total amounts of acid sites was observed between these catalysts. Hence, the introduction of isolated V, Nb, Mo or W oxo species on ceria causes additional Lewis acidity, in agreement with the proposed structures, boosting the NH₃-SCR activity over the Lewis acid/redox pair. The fact that W-oxo/CeO₂ is the most active is probably related to the exceptionally stable tungsten single site in reaction conditions with a high Lewis acidity. The fact that Nb-oxo/CeO₂ also shows promising overall

performances may indicate that a stable d^0 system is also preferred. Ongoing DFT studies may explain the observed tendency as well as the mechanism.

6 Conclusion

A ceria-based catalyst comprising isolated niobium-oxo is reported using surface organometallic chemistry. This methodology involves two steps: the grafting of $[\text{Nb}(\text{OEt})_5]$ on ceria by a protonolysis reaction with OH groups, offering a firmly bonded surface organometallic fragment with high dispersion; calcination of the latter material leads to isolated niobium-oxo-hydroxy as major species. The products in each step were characterized by FT-IR, SSNMR, EXAFS, and Tof-SIMS to disclose the major surface species, monomer, accompanied with a minor quantity of dimeric species. The catalytic investigations show promising activity and selectivity. Finally, the catalytic performances of the series of SOMC catalysts based on W, Mo, V and Nb with the same metal loading (molar) have been compared. It appears that the W-oxo/ CeO_2 is the most active catalyst among the synthesized materials in the low temperature region, as well as in the high temperature region. Recalling all the characterization data, the exceptionally high activity of W-oxo/ CeO_2 is attributed to the highly dispersed Lewis acid/redox pair formed during the preparation and the high stability of tungsten during the operating conditions.

Table 2 Summary and comparison of the catalyst preparation and catalytic performance in this chapter

Catalysts	Loading	Synthesis method	Precursor	Calcination temperature	NO conversion
$\text{CeO}_2\text{-}200$	N.D.	N.D.	N.D.	N.D.	58% at 400 °C
[0.2Nb-b]	0.2 wt%	SOMC	$[\text{Nb}(\text{OEt})_5]$	500 °C	60% at 350 °C
[0.5Nb-b]	0.5 wt%	SOMC	$[\text{Nb}(\text{OEt})_5]$	500 °C	72% at 350 °C
[1.0Nb-b]	1.0 wt%	SOMC	$[\text{Nb}(\text{OEt})_5]$	500 °C	$T_{80}(301\text{-}374\text{ °C})$
[1.8Nb-b]	1.8 wt%	SOMC	$[\text{Nb}(\text{OEt})_5]$	500 °C	$T_{80}(279\text{-}451\text{ °C})$

Reference

- [1] Y.S.H. Najjar, Gaseous Pollutants Formation and Their Harmful Effects on Health and Environment, Innovative Energy Policies. 1 (2011) 1–9. <https://doi.org/10.4303/iep/e101203>.
- [2] J.H. Kim, J.H. Kim, H.S. Kim, H.J. Kim, S.H. Kang, J.H. Ryu, S.S. Shim, Reduction of NO_x Emission from the Cement Industry in South Korea: A Review, Atmosphere. 13 (2022) 121. <https://doi.org/10.3390/atmos13010121>.
- [3] İbrahim Aslan Reşitoğlu, NO_x Pollutants from Diesel Vehicles and Trends in the Control Technologies, 161-177, ISBN 978-1-78985-248-6.

- [4] Y. Shan, J. Du, Y. Yu, W. Shan, X. Shi, H. He, Precise control of post-treatment significantly increases hydrothermal stability of in-situ synthesized Cu-zeolites for NH₃-SCR reaction, *Applied Catalysis B: Environmental*. 266 (2020) 118655. <https://doi.org/10.1016/j.apcatb.2020.118655>.
- [5] L. Han, S. Cai, M. Gao, J.Y. Hasegawa, P. Wang, J. Zhang, L. Shi, D. Zhang, Selective Catalytic Reduction of NO_x with NH₃ by Using Novel Catalysts: State of the Art and Future Prospects, *Chemical Reviews*. 119 (2019) 10916–10976. <https://doi.org/10.1021/acs.chemrev.9b00202>.
- [6] L. Chen, D. Weng, Z. Si, X. Wu, Synergistic effect between ceria and tungsten oxide on WO₃-CeO₂-TiO₂ catalysts for NH₃-SCR reaction, *Progress in Natural Science: Materials International*. 22 (2012) 265–272. <https://doi.org/10.1016/j.pnsc.2012.07.004>.
- [7] B. Liu, J. Liu, L. Xin, T. Zhang, Y. Xu, F. Jiang, X. Liu, Unraveling Reactivity Descriptors and Structure Sensitivity in Low-Temperature NH₃-SCR Reaction over CeTiO_x Catalysts: A Combined Computational and Experimental Study, *ACS Catalysis*. 11 (2021) 7613–7636. <https://doi.org/10.1021/acscatal.1c00311>.
- [8] S. Liu, R. Zhang, P. Li, H. Chen, Y. Wei, X. Liang, Morphology effect of diverse ceria with active tungsten species on NH₃-SCR behaviors, *Catalysis Today*. 339 (2020) 241–253. <https://doi.org/10.1016/j.cattod.2019.02.004>.
- [9] C. Sun, H. Li, L. Chen, Nanostructured ceria-based materials: Synthesis, properties, and applications, *Energy and Environmental Science*. 5 (2012) 8475–8505. <https://doi.org/10.1039/c2ee22310d>.
- [10] L. Li, P. Li, W. Tan, K. Ma, W. Zou, C. Tang, L. Dong, Enhanced low-temperature NH₃-SCR performance of CeTiO_x catalyst via surface Mo modification, *Chinese Journal of Catalysis*. 41 (2020) 364–373. [https://doi.org/10.1016/S1872-2067\(19\)63437-6](https://doi.org/10.1016/S1872-2067(19)63437-6).
- [11] A.A.S. Gonçalves, F. Ciesielczyk, B. Samojeden, M. Jaroniec, Toward development of single-atom ceramic catalysts for selective catalytic reduction of NO with NH₃, *Journal of Hazardous Materials*. 401 (2021) 123413. <https://doi.org/10.1016/j.jhazmat.2020.123413>.
- [12] W. Tan, C. Wang, S. Yu, Y. Li, S. Xie, F. Gao, L. Dong, F. Liu, Revealing the effect of paired redox-acid sites on metal oxide catalysts for efficient NO_x removal by NH₃-SCR, *Journal of Hazardous Materials*. 416 (2021) 125826. <https://doi.org/10.1016/j.jhazmat.2021.125826>.
- [13] Z. Zhang, Y. Li, P. Yang, Y. Li, C. Zhao, R. Li, Y. Zhu, Improved NH₃-SCR deNO_x activity and tolerance to H₂O & SO₂ at low temperature over the Nb_mCu_{0.1-m}Ce_{0.9}O_x catalysts: Role of acidity by niobium doping, *Fuel*. 303 (2021) 121239. <https://doi.org/10.1016/j.fuel.2021.121239>.
- [14] R. Qu, X. Gao, K. Cen, J. Li, Relationship between structure and performance of a novel cerium-niobium binary oxide catalyst for selective catalytic reduction of NO with NH₃, *Applied Catalysis B: Environmental*. 142–143 (2013) 290–297. <https://doi.org/10.1016/j.apcatb.2013.05.035>.
- [15] S. Liu, H. Wang, R. Zhang, Y. Wei, Synergistic effect of niobium and ceria on anatase for low-temperature NH₃-SCR of NO process, *Molecular Catalysis*. 478 (2019) 110563.

<https://doi.org/10.1016/j.mcat.2019.110563>.

- [16] J. Guo, X. Zhang, P. Guan, C. Liu, H. Huang, F. Xue, X. Dong, S.J. Pennycook, M.F. Chisholm, Single Atom Niobium in Graphitic Layers for Enhanced Oxygen Reduction Reaction, *Microscopy and Microanalysis*. 19 (2013) 1680–1681. <https://doi.org/10.1017/s1431927613010398>.
- [17] J.F. Wu, A. Ramanathan, R. Kersting, A. Jystad, H. Zhu, Y. Hu, C.P. Marshall, M. Caricato, B. Subramaniam, Enhanced Olefin Metathesis Performance of Tungsten and Niobium Incorporated Bimetallic Silicates: Evidence of Synergistic Effects, *ChemCatChem*. 12 (2020) 2004–2013. <https://doi.org/10.1002/cctc.201902131>.
- [18] M.K. Samantaray, E. Pump, A. Bendjeriou-Sedjerari, V. D'Elia, J.D.A. Pelletier, M. Guidotti, R. Psaro, J.M. Basset, Surface organometallic chemistry in heterogeneous catalysis, *Chemical Society Reviews*. 47 (2018) 8403–8437. <https://doi.org/10.1039/c8cs00356d>.
- [19] A. Hamieh, R. Dey, B. Nekoueishahraki, M.K. Samantaray, Y. Chen, E. Abou-Hamad, J.M. Basset, Single site silica supported tetramethyl niobium by the SOMC strategy: Synthesis, characterization and structure-activity relationship in the ethylene oligomerization reaction, *Chemical Communications*. 53 (2017) 7068–7071. <https://doi.org/10.1039/c7cc02585h>.
- [20] P.A. Zhizhko, N.S. Bushkov, A. V. Pichugov, D.N. Zarubin, Oxo/imido heterometathesis: From molecular stoichiometric studies to well-defined heterogeneous catalysts, *Coordination Chemistry Reviews*. 448 (2021) 214112. <https://doi.org/10.1016/j.ccr.2021.214112>.
- [21] K.C. Szeto, Z.R. Jones, N. Merle, C. Rios, A. Gallo, F. Le Quemener, L. Delevoye, R.M. Gauvin, S.L. Scott, M. Taoufik, A Strong Support Effect in Selective Propane Dehydrogenation Catalyzed by Ga(*i*-Bu)₃ Grafted onto γ -Alumina and Silica, *ACS Catalysis*. 8 (2018) 7566–7577. <https://doi.org/10.1021/acscatal.8b00936>.
- [22] R.M. Rakhmatullin, V. V. Pavlov, V. V. Semashko, EPR study of nanocrystalline CeO₂ exhibiting ferromagnetism at room temperature, *Physica Status Solidi (B) Basic Research*. 253 (2016) 499–503. <https://doi.org/10.1002/pssb.201552542>.
- [23] L.J. Burcham, J. Datka, I.E. Wachs, In Situ Vibrational Spectroscopy Studies of Supported Niobium Oxide Catalysts, *Journal of Physical Chemistry B*. 103 (1999) 6015–6024. <https://doi.org/10.1021/jp990289a>.
- [24] Z. Wu, A.J. Rondinone, I.N. Ivanov, S.H. Overbury, Structure of vanadium oxide supported on ceria by multiwavelength Raman spectroscopy, *Journal of Physical Chemistry C*. 115 (2011) 25368–25378. <https://doi.org/10.1021/jp2084605>.
- [25] A. Benninghoven, *Chemical Analysis of Inorganic and Organic Surfaces and Thin Films by Static Time-of-Flight Secondary Ion Mass Spectrometry (TOF-SIMS)*, *Angewandte Chemie International Edition in English*. 33 (1994) 1023–1043. <https://doi.org/10.1002/anie.199410231>.
- [26] S.B. Bukallah, M. Houalla, D.M. Hercules, Characterization of supported Nb catalysts by ToF-SIMS, *Surface and Interface Analysis*. 29 (2000) 818–822. [https://doi.org/10.1002/1096-9918\(200012\)29:12<818::AID-SIA931>3.0.CO;2-4](https://doi.org/10.1002/1096-9918(200012)29:12<818::AID-SIA931>3.0.CO;2-4).

- [27] J. Abou Nakad, R. Rajapaksha, K.C. Szeto, A. De Mallmann, M. Taoufik, Preparation of Tripodal Vanadium Oxo-Organometallic Species Supported on Silica, $[(\equiv\text{SiO})_3\text{V}(=\text{O})]$, for Selective Nonoxidative Dehydrogenation of Propane, *Organometallics*. 41 (2022) 2784–2797. <https://doi.org/10.1021/acs.organomet.2c00377>.
- [28] V. V. Zhivonitko, I. V. Skovpin, K.C. Szeto, M. Taoufik, I. V. Koptug, Parahydrogen-Induced Polarization Study of the Silica-Supported Vanadium Oxo Organometallic Catalyst, *Journal of Physical Chemistry C*. 122 (2018) 4891–4900. <https://doi.org/10.1021/acs.jpcc.7b12069>.
- [29] F. Zhang, K.C. Szeto, M. Taoufik, L. Delevoye, R.M. Gauvin, S.L. Scott, Enhanced Metathesis Activity and Stability of Methyltrioxorhenium on a Mostly Amorphous Alumina: Role of the Local Grafting Environment, *Journal of the American Chemical Society*. 140 (2018) 13854–13868. <https://doi.org/10.1021/jacs.8b08630>.
- [30] N. Popoff, E. Mazoyer, J. Pelletier, R.M. Gauvin, M. Taoufik, Expanding the scope of metathesis: A survey of polyfunctional, single-site supported tungsten systems for hydrocarbon valorization, *Chemical Society Reviews*. 42 (2013) 9035–9054. <https://doi.org/10.1039/c3cs60115c>.
- [31] N. Merle, T. Tabassum, S. L. Scott, A. Motta, K. Szeto, M. Taoufik, R. M. Gauvin, and L. Delevoye, High-field NMR, reactivity, and DFT modeling reveal the $\gamma\text{-Al}_2\text{O}_3$ surface hydroxyl network. 61 (2022) e202207316. <https://doi.org/10.1002/anie.202207316>
- [32] C. Tang, H. Zhang, L. Dong, Ceria-based catalysts for low-temperature selective catalytic reduction of NO with NH_3 , *Catalysis Science and Technology*. 6 (2016) 1248–1264. <https://doi.org/10.1039/c5cy01487e>.
- [33] Z. Chen, S. Ren, Y. Zhou, X. Li, M. Wang, L. Chen, Comparison of Mn doped CeO_2 with different exposed facets for NH_3 -SCR at low temperature, *Journal of the Energy Institute*. 105 (2022) 114–120. <https://doi.org/10.1016/j.joei.2022.08.007>.
- [34] S. Zhan, H. Zhang, Y. Zhang, Q. Shi, Y. Li, X.J. Li, Efficient NH_3 -SCR removal of NO_x with highly ordered mesoporous $\text{WO}_3(\chi)\text{-CeO}_2$ at low temperatures, *Applied Catalysis B: Environmental*. 203 (2017) 199–209. <https://doi.org/10.1016/j.apcatb.2016.10.010>.
- [35] W. Tan, J. Wang, Y. Cai, L. Li, S. Xie, F. Gao, F. Liu, L. Dong, Molybdenum oxide as an efficient promoter to enhance the NH_3 -SCR performance of $\text{CeO}_2\text{-SiO}_2$ catalyst for NO_x removal, *Catalysis Today*. 397–399 (2022) 475–483. <https://doi.org/10.1016/j.cattod.2021.07.007>.
- [36] Y. Peng, K. Li, J. Li, Identification of the active sites on $\text{CeO}_2\text{-WO}_3$ catalysts for SCR of NO_x with NH_3 : An in situ IR and Raman spectroscopy study, *Applied Catalysis B: Environmental*. 140–141 (2013) 483–492. <https://doi.org/10.1016/j.apcatb.2013.04.043>.
- [37] J. Liu, H. Cheng, J. Tan, B. Liu, Z. Zhang, H. Xu, M. Zhao, W. Zhu, J. Liu, Z. Zhao, Solvent-free rapid synthesis of porous CeWO_x by a mechanochemical self-assembly strategy for the abatement of NO_x , *Journal of Materials Chemistry A*. 8 (2020) 6717–6731. <https://doi.org/10.1039/d0ta01541e>.
- [38] C. Croisé, R. Pointecouteau, J. Akil, A. Demourgues, N. Bion, X. Courtois, F. Can, Insight into the praseodymium effect on the NH_3 -SCR reaction pathways over W or Nb

- supported ceria-zirconia based catalysts, *Applied Catalysis B: Environmental*. 298 (2021) 120563. <https://doi.org/10.1016/j.apcatb.2021.120563>.
- [39] Z. Ma, X. Wu, H. Härelind, D. Weng, B. Wang, Z. Si, NH₃-SCR reaction mechanisms of NbO_x/Ce_{0.75}Zr_{0.25}O₂ catalyst: DRIFTS and kinetics studies, *Journal of Molecular Catalysis A: Chemical*. 423 (2016) 172–180. <https://doi.org/10.1016/j.molcata.2016.06.023>.
- [40] X. Wang, K. Zhang, W. Zhao, Y. Zhang, Z. Lan, T. Zhang, Y. Xiao, Y. Zhang, H. Chang, L. Jiang, Effect of ceria Precursor on the Physicochemical and Catalytic Properties of Mn-W/CeO₂ Nanocatalysts for NH₃ SCR at Low Temperature, *Industrial and Engineering Chemistry Research*. 56 (2017) 14980–14994. <https://doi.org/10.1021/acs.iecr.7b03466>.
- [41] G. Yang, M. Ryo, J. Roy, D.R. Lammel, M.B. Ballhausen, X. Jing, X. Zhu, M.C. Rillig, Multiple anthropogenic pressures eliminate the effects of soil microbial diversity on ecosystem functions in experimental microcosms, *Nature Communications*. 13 (2022) 4260. <https://doi.org/10.1038/s41467-022-31936-7>.

CHAPTER V

Conclusion and perspectives

General conclusion

NO_x emission is a fact that needs to be addressed. The most efficient way is a post treatment, and NH₃-SCR appears to be the most promising. Although such a system has already been integrated in industrial plants and recent mobile vehicles, the commercial catalysts still need improvements, notably in the stability, efficiency and a broader operating temperature window. Moreover, the current commercial catalyst, being a mixed vanadium tungsten oxide supported on titania suffers from V₂O₅ emission (toxic) at high temperature. Therefore, the choice and design of novel efficient NH₃-SCR catalysts are imminent. Apart from TiO₂, CeO₂ has been demonstrated to be a promising support material for NH₃-SCR, due to its superior oxygen storage, thermal stability, and acidity. The most common strategy to increase the activity of ceria is to introduce another element in order to increase the acidity and to create the necessary acid/redox pair, proposed as active site for this reaction. However, the classical methods used for the preparation of catalysts based on ceria usually provide an uncontrolled mixture of surface species. Obviously, such materials are unsuitable for mechanistic studies, determination of the active site and eventually distinguishing the catalytic role of each element. Recently, single-site catalysis attracts a lot of attention due to a higher atom efficiency and since it is more suitable for active site probing and mechanistic studies. As all sites are supposedly accessible, the activity per metal is expected to increase.

The aim of this thesis is to develop novel ceria-based single-site catalysts using new synthetic approaches for the reduction of nitrogen oxides by ammonia. Surface organometallic chemistry on ceria has been investigated for the first time and exemplified by using organometallic complexes based on metal from groups V and VI as precursors. Stable metal-oxo supported on ceria are obtained by grafting of selected organometallic precursors on ceria dehydroxylated at 200 °C followed by controlled calcination. The resulting materials are well-characterized and evaluated in a continuous flow reactor for NH₃-SCR reaction. Based on the well-understanding of surface species, the structure-activity and mechanisms are discussed.

Prior to the grafting reaction, CeO₂, with different pretreatments has been thoroughly characterized by DRIFT, XPS, XRD, BET, and solid state NMR (¹H, ¹⁷O). Furthermore, chemical titration with Al(*i*Bu)₃ has been conducted in order to quantify the concentration of surface OH-groups of the support calcined at 500 °C and dehydroxylated at 200 °C (this appears to be the optimal pretreatment conditions). W-oxo supported on ceria is obtained in

two steps by grafting of $W(\equiv C tBu)(CH_2 tBu)_3$ through protonolysis reaction followed by a calcination under air at 600 °C. The grafting process offered a firmly bonded surface organometallic fragment with high dispersion on support ceria, **[W-a]**. The grafted species is characterized by Elemental analysis, FT-IR, XPS, EPR, SSNMR, and XAFS, offering a precise structure expressed as $[(\equiv CeO)_2 W(\equiv C tBu)(CH_2 tBu)]$. The grafted species **[W-a]** appears to be an isolated, bipodal tungsten complex bearing a neopentyl and neopentylidyne ligand. Moreover, paramagnetism, probably due to substantial amount of Ce^{3+} is present according to the results of EPR and XPS, and has notably perturbed the solid-state NMR signals.

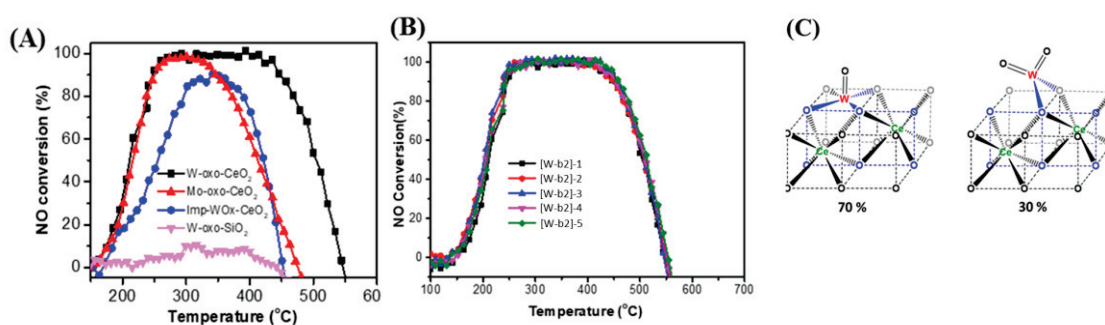
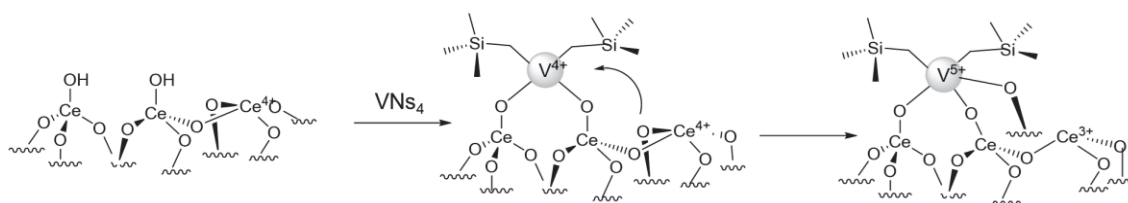


Fig. 1 (A) NO conversion of tungsten and molybdenum catalysts prepared by SOMC and impregnation method on ceria and silica for comparison; (B) Recycling studies of **[W-b]** in NH_3 -SCR; (C) Proposed structure of **[W-b]**

In the second step, **[W-a]** is calcined to form the supported tungsten-oxo species, **[W-b]**. The nature of **[W-b]** is discovered to be composed of a mixture of isolated tungsten mono-oxo and tungsten bis-oxo species using the aforementioned spectroscopic methods. Additionally, XPS demonstrates the presence of Ce^{3+} in **[W-b]**, confirming the presence of the required acid redox pair, which is likely to be the active site for NH_3 -SCR. **[W-b]** exhibited high catalytic activity with full conversion between 250 and 450 °C and exceptionally high thermal stability during several experimental cycles under typical deNO_x conditions (with 12% O₂). Surprisingly, the determined acidic properties by NH_3 -TPD were lower than for the catalyst prepared by conventional impregnation. However, **[W-b]** shows higher NO_x conversion than WO_x/CeO₂ prepared by classical impregnation. This result suggests that the catalytic performance is not directly associated with the amount and strength of acid sites present on the surface. The extraordinarily high activity of **[W-b]** can be related to a systematic formation of Lewis acid/redox pair being highly dispersed throughout the surface. For comparison, $Mo(\equiv C tBu)(CH_2 tBu)_3$ has been grafted onto ceria in the same manner and tested in NH_3 -SCR. The conversion profile is basically the same as **[W-b]** at low temperature until

about 300 °C before the curve drops rapidly. Simultaneously, the N₂ selectivity decreases. This is due to a thermal reduction to Mo^V which is active in ammonia oxidation, as reported in literature. The essential findings are summarized in Fig. 1.

The previously described method is extended to vanadium. Different vanadium precursors ([V(=O)(OEt)₃]₂, [V(CH₂(SiMe₃)₃)₄] and [V(=O)(OtBu)₃]) have been employed to be grafted onto a ceria previously dehydroxylated at 200 °C. Interestingly, the resulting structures of the grafted species are different, as revealed by Elemental analysis, DRIFT, NMR and EPR. For the first time, a unique Ce-O-Ce bridge opening mechanism has been proposed, involving an electron transfer from oxygen to vanadium, accompanied by oxidation of vanadium (IV), yielding a tripodal bis-neosilyl vanadium(V) species. This structure is confirmed by XANES (Scheme 1).



Scheme 1 Proposed mechanism for the transformation of V⁴⁺ to V⁵⁺ upon grafting

Calcination of all these grafted species yield the corresponding vanadium oxo species on ceria ([V1-b], [V2-b] and [V3-b]) and were characterized by DRIFT, Raman, ⁵¹V NMR, EPR and XANES. Compared to tungsten, where a monomeric tungsten oxo species is obtained, the resulting vanadium oxo species always contain a mixture of different vanadium species on the surface (Fig. 2A), extending from monomeric to oligomeric, as determined by DRIFT and ⁵¹V NMR. Although monomeric vanadium oxo species constitute the main fraction of the mixture, these results show that vanadium is extremely mobile on a ceria surface under the calcination conditions (500 °C under air). The catalytic performance in NH₃-SCR is investigated for this series of catalysts and compared to a vanadium-based catalyst prepared by classical impregnation. Catalysts prepared by SOMC exhibit higher NO conversion than the catalyst synthesized by impregnation. Otherwise, the catalytic performances among the SOMC prepared catalysts are similar, with a fairly high conversion in the range of 300-400 °C and high selectivity in N₂ (Fig. 2B). Above 400 °C, the conversion and selectivity drop, probably due to a partial reduction to vanadium (IV) known to be active in the oxidation of NH₃. [V1-b] (prepared from [V(=o)(O)t₃]₂) seems to show slightly better performances. For the vanadium system, a series of catalysts with different loadings (0.2, 1.2, 2.1 and 4.0 wt%) has

been prepared in the same manner using $[V(=O)(O)t_3]_2$ as precursor. A structural tendency is the increase of the number of oligomeric species with the loading. The catalytic results show a gradual increase in the NO conversion in the low temperature region as the loading increases. On the other hand, the catalytic performances of the highest loaded catalyst are lower in the high temperature region (Fig. 2C). This result indicates that there may be two different mechanisms involved in the NH_3 -SCR reactions. In the low temperature region, NO conversion is favored by the presence of oligomeric vanadium species, while in the high temperature region it is favored by the presence of isolated vanadium species.

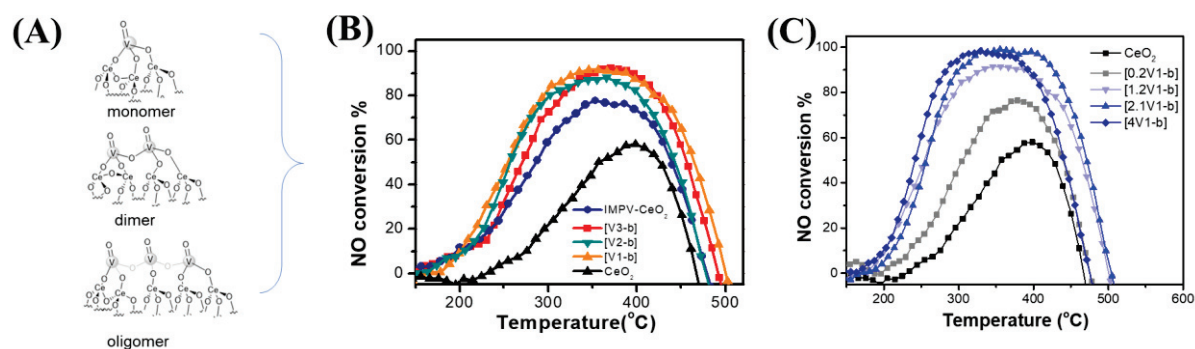


Fig. 2 (A) NO conversion of Vanadium catalysts prepared by SOMC and impregnation method on ceria a for comparison; (B) NO conversion of **[V1-b]** with different loading; (C) Proposed structure of vanadium-based catalysts supported on ceria prepared by SOMC

To further extend the surface organometallic chemistry approach for the preparation of highly active NH_3 -SCR catalyst, the corresponding niobium system has been investigated, using $[Nb(OEt)_5]_2$ as a precursor. The same grafting procedure is adapted and the resulting material is characterized by Elemental analysis, DRIFT and solid state NMR, revealing a bipodal structure bearing four ethoxide ligands as the major surface species. Calcination of the latter species gives an isolated niobium **[Nb-b]** bearing an oxo and a hydroxyl ligand (Fig. 3B) as the major surface species, as suggested by DRIFT, TOF-SIMS and EXAFS. The catalytic performances of **[Nb-b]** are rather promising with high conversion and selectivity in a broad temperature window (Fig. 3A). Similar to the series of vanadium, a series of **[Nb-b]** with different loadings (0.2, 0.5, 1.0 and 1.8 wt%) has been prepared and tested in NH_3 -SCR.

Obviously, the catalytic conversion of NO increases when the niobium loading increases under the same GHSV. These results confirm the positive effect provided by the addition of isolated niobium centers on ceria. Increasing the Nb loading, mostly as an isolated form, also expands the operating temperature window for the NH_3 -SCR reaction.

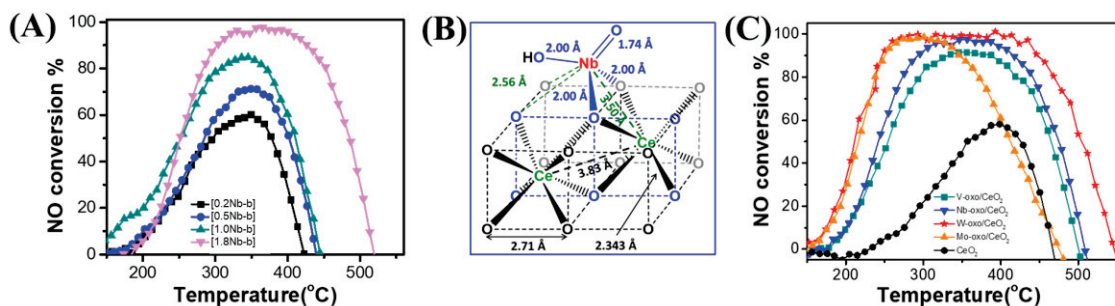


Fig. 3 (A) NO conversion of [Nb-b] with different Nb loadings; (B) Proposed structure of the niobium catalyst supported on ceria prepared by SOMC; (C) NO conversion obtained with different metal-oxo catalysts prepared by SOMC and with ceria for a comparison

Finally, the catalytic performances of the series of prepared M-oxo/CeO₂ (M=W, Mo, Nb, V) comprising the same metal loading (0.2 mmol metal per 1g ceria) is compared (Fig. 3C). All M-oxo/CeO₂ catalysts exhibit better catalytic performances than bulk ceria and corresponding catalysts prepared by classical methods. The order of their activity follows: W-oxo/CeO₂ > Nb-oxo/CeO₂ > Mo-oxo/CeO₂ > V-oxo/CeO₂. A general observation of all SOMC catalysts is the isolated (at least for major species) nature of the presumed catalytic sites and the presence of Ce³⁺, forming the crucial acid/redox pair which is proposed to be the active site for the reaction. The W-oxo/CeO₂ is found to be the most active catalyst, owing to the exceptionally high thermal stability, high dispersion and the single-site nature. Noteworthy, there is a remarkable difference in the NO conversion, particularly in the high temperature region, between W/Nb and Mo/V systems. Both Mo-oxo/CeO₂ and V-oxo/CeO₂ exhibit a dramatic drop in conversion around 350 °C. Moreover, these catalysts show a decrease in the N₂ selectivity at higher temperature. The latter phenomena can be explained by the oxidation of ammonia, which causes an inhibition of the NH₃-SCR reaction and a lower N₂ selectivity. In fact, both vanadium and molybdenum can undergo thermal reduction at this temperature, resulting in reduced pieces active for the oxidation reaction of ammonia to nitric oxide. The fact that W-oxo/CeO₂ is the most active is probably related to the exceptionally stable tungsten single site possessing a Lewis acid/redox pair.

This thesis has assembled important elements for a novel generation of NH₃-SCR catalysts. For the first time, single site catalyst has been addressed to this reaction, and the results are encouraging. Particularly, the tungsten system, comprising only single-site species, shows to be the most active, selective and stable catalyst among the series of synthesized materials. The exceptionally high activity of this catalyst is attributed to the high thermal stability, high

dispersion and the single site nature of tungsten supported on CeO₂. These properties are prerequisites to obtain highly active NH₃-SCR catalyst for early transition state metal (group V and VI) supported on ceria. As ceria supported single-site catalysts of groups V and VI are disclosed, next investigations may be directed to a systematic study of the mechanism over such catalysts. Ongoing DFT studies may explain the observed tendency as well as the mechanism. Moreover, specific *in-operando* experiments can be envisaged. For instance, *in-operando* XAS experiment may provide the oxidation state and structural changes upon the catalytic reaction. In-operando DRIFT may probe different intermediates formed during the reaction. In-operando EPR may shed light on oxidation state under the reaction conditions. Moreover, reactivity studies using isotopic labelled reactants may further reveal intermediates by using solid state NMR.

Experimental section

1 General Procedure

All syntheses were performed under pure and dry argon, using the standard Schlenk techniques and a glove box. Solvents were purified and dried according to standard procedures.

2 Preparation of materials

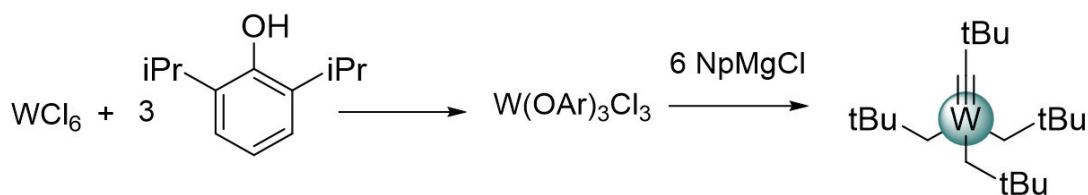
2.1 Chapter II: Surface Organometallic Chemistry of $[W(\equiv C tBu)(CH_2 tBu)_3]$ on CeO_2 for the development of highly active NH_3 -SCR catalysts

2.1.1 Treatment of support CeO_2

Ceria (CeO_2) HAS-5 ACTALYS 922 from Solvay (Rare Earth La Rochelle) was used as the original support. In the investigation of effect of calcination temperature on the support, ceria was respectively calcined at 300 °C, 400 °C, 500 °C, 600 °C for 16 h. After evacuated under a vacuum at a high temperature, it was kept in the glovebox.

The typical support used in this study for grafting various molecular complexes is synthesized as follow: ceria (CeO_2) HAS-5 ACTALYS 922 from Solvay (Rare Earth La Rochelle) was calcined for 16 h at 500 °C under a dry airflow and then evacuated under a vacuum at a high temperature. After rehydration under reduced pressure at 100 °C, ceria was partially dehydroxylated at 200 °C under a high vacuum (10^{-5} mbar) for 16 h to give a yellow solid, noted as CeO_{2-200} .

2.1.2 Preparation of $[W(\equiv C tBu)(CH_2 tBu)_3]$



Scheme 1 Preparation of the molecular complex $[W(\equiv C tBu)(CH_2 tBu)_3]$

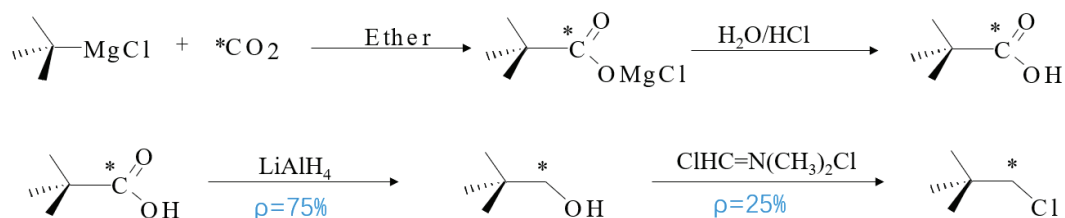
Tungsten complexes $W(\equiv C tBu)(CH_2 tBu)_3$ ^[1] were prepared according to [scheme 1](#). Solution of 2,6-diisopropylphenol (7.5 mL) in toluene (25 mL) was transferred by cannula into WCl_6 (5 g, 12.6 mmol) pre-dissolved in toluene (60 mL) to form a dark red solution which is kept on stirring for 12 h. The solution was filtered, and the filtrate was distilled under a vacuum. The residue $W(OAr)_3Cl_3$ was properly dried on the high vacuum line to obtain dark blue

powders. Yield = 89%.

Neopentyl magnesium chloride was synthesized by mixing and excess of Mg and neopentyl chloride in diethyl ether. The reaction was initiated by 1,2 dibromoethane Br-(CH₂)₂-Br and left for reflux at 45-50 °C for 12 h. Then, the solution was allowed to settle down and filtered by cannula. Then the concentration of Neopentylmagnesium chloride in the resulting solution was determined by 0.5M 2,6-diisopropylphenol (THF solution).

6.42 g (7.2 mmol) of W(OAr)₃Cl₃ was dissolved in diethyl ether (50 mL). Neopentylmagnesium chloride (6 eq.) was gradually injected into the solution at -5 °C. Then, the mixture was kept stirred for 12 h at room temperature. The resulting solution was light yellow with an abundant white precipitate. The solvent in the resulting solution was distilled, and pentane was added to extract the product. Then the solution was filtered over Celite® and distilled under a vacuum. The resulting products were sublimated at 100 °C to obtain yellow powders, which were stored in the freezer in the glovebox.

The 30% labeled W(≡C*t*Bu)(CH₂*t*Bu)₃ was synthesized by substituting 30% Neopentylmagnesium chloride for labeled Neopentylmagnesium chloride in the above procedure, which is prepared according to the literature [3], as shown in Scheme 2.



Scheme 2 Schematic illustration of forming ¹³C labeled complex NpMgCl

2.1.3 Preparation of [W(≡C*t*Bu)(CH₂*t*Bu)₃]/CeO₂₋₂₀₀ [W-a]

A mixture of [W(≡C*t*Bu)(CH₂*t*Bu)₃] (300 mg) and CeO₂₋₂₀₀ (2 g) was stirred in pentane (MBraun SPS, Carlo Erba, 99%) for 4 h at room temperature. The [W(≡C*t*Bu)(CH₂*t*Bu)₃]/CeO₂₋₂₀₀ material was washed three times with pentane via filtration–condensation cycles. Then, all the volatiles were condensed into a 6 L vessel to quantify neopentane evolved during the grafting reaction. After evaporation of the solvent, the resulting grey powder was dried under high vacuum (10⁻⁵ mbar).

2.1.4 Preparation of W-oxo/CeO₂ [W-b]

[W(\equiv C*t*Bu)(CH₂*t*Bu)₃]/CeO₂₋₂₀₀ [W-a] was calcined under dry air with a gas flow rate of 45 mL min⁻¹ at 600 °C for 16 h. High vacuum was applied directly after the calcination process at 600 °C to avoid the adsorption of water. Then the sample was transferred and kept in the glove box.

2.1.5 Preparation of WO_x/CeO₂ by impregnation method

The impregnated catalyst based on tungsten (W) supported on ceria was prepared by conventional wet impregnation using ammonium metatungstate hydrate (Aldrich, 99.99%) as precursor. According to the analysis by TGA (4.20% loss until 82 °C, 7.54% loss until 214.93 °C, 8.17% loss until 608 °C), there are 2.37% H₂O contains inside ammonium metatungstate hydrate (Ca. (NH₄)₆H₂W₁₂O₄₀*4H₂O). In a typical reaction, at room temperature, a water-based solution of ammonium metatungstate hydrate (95 mg in 5 mL of water) was added to 2 g of ceria. The suspension was stirred overnight at room temperature, and then water was evacuated in a rotary evaporator at 50 °C. The material obtained was then calcined under dry air at 500 °C for 16 h.

2.1.6 Preparation of Mo-oxo/CeO₂

[Mo(\equiv C*t*Bu)(CH₂*t*Bu)₃] was synthesized according to literature[2]. A mixture of [Mo(\equiv C*t*Bu)(CH₂*t*Bu)₃] (180 mg) and CeO₂₋₂₀₀ (2 g) was stirred in pentane (MBraun SPS, Carlo Erba, 99%) for 4 h at room temperature. The [Mo(\equiv C*t*Bu)(CH₂*t*Bu)₃]/CeO₂₋₂₀₀ material was washed three times with pentane via filtration–condensation cycles. After evaporation of the solvent, the resulting grey powder was dried under high vacuum (10⁻⁵ mbar). To obtain Mo-oxo/CeO₂, [Mo(\equiv C*t*Bu)(CH₂*t*Bu)₃]/CeO₂₋₂₀₀ was calcined under dry air with a gas flow rate of 45 mL min⁻¹ at 600 °C for 16 h. High vacuum was applied directly after the calcination process at 600 °C to avoid the adsorption of water. Then the resulting yellow sample was transferred and kept in the glove box.

2.2 Chapter III: Novel vanadium supported on CeO₂ catalysts prepared by SOMC: Effect of precursors and amounts of vanadium on the activity of NH₃-SCR reaction

2.2.1 Preparation of [V(CH₂SiMe₃)₄]

Vanadium Complex V(CH₂SiMe₃)₄ was prepared according to the described procedures [4]. VCl₄ (10 mmol) in 50 ml of diethyl ether was added dropwise to a hexane solution of

$\text{Me}_3\text{SiCH}_2\text{Li}$ (40.00 mmol) at 20 °C over one hour. The resulting green reaction solution was filtered out from LiCl, and the solvents were removed under a vacuum. The residue was solved in 30 ml of pentane, and recrystallized at -78°C, giving dark green crystals of $\text{V}(\text{CH}_2\text{SiMe}_3)_4$ (m.p. 42 °C).

2.2.2 Preparation of $[\text{V}(=\text{O})(\text{OtBu})_3]$

$[\text{V}(=\text{O})(\text{OtBu})_3]$ was prepared according to the literature [5]. Typically, $[\text{V}(=\text{O})(\text{OtBu})_3]$ was synthesized by combining the 20 g of V_2O_5 (Aldrich) and 165 ml *t*BuOH in benzene (300 ml) in two steps. Schlenk line was used throughout the entire preparation process, completed in an inert environment. The water from the reaction and the reflux condenser was collected using a Dean-Stark trap. The temperature was raised to approximately 100 °C for 48 hours. Following the reaction, the solution changed its color from red to orange. Unreacted V_2O_5 was removed by filtration from the solution. After the solvent was distilled, white crystals were seen. The crystals were purified by sublimation after being dried in a high vacuum line. Following purification, the compound was identified by the presence of two signals in the $^{13}\text{C}\{\text{H}\}$ NMR spectrum, one at 31.4 ppm for the protons of CH_3 , and the other at 86 ppm for the quaternary C of the tert-butoxide ligand.

2.2.3 Preparation of $[\text{V}(=\text{O})(\text{OEt})_3]/\text{CeO}_2$ [*xV1-a*] (*x*= 0.2%, 1.2%, 2.1%, 4%)

A given amount of $[\text{V}(=\text{O})(\text{OEt})_3]_2$ and CeO_{2-200} (2 g) in toluene (20 mL) was mixed at 25 °C for 4 h. After filtration, the solid $[\text{V}(=\text{O})(\text{OEt})_3]_2/\text{CeO}_{2-200}$ was washed three times with 10 ml of toluene and 10 mL of pentane. The resulting powder was dried under vacuum (10^{-5} Torr) and was kept in the glovebox. The saturated materials present 2.1 wt% V and 2.36 wt%. Different amounts of $[\text{V}(=\text{O})(\text{OEt})_3]_2$ were loaded on the support CeO_{2-200} without washing. The resulted materials named [*xV1-a*] (*x*=0.2 wt%, 1.2 wt%, 2.1 wt%, 4 wt%) according to the vanadium weight.

2.2.4 Preparation of $[\text{V}(\text{CH}_2\text{SiMe}_3)_4]/\text{CeO}_2$, [*V2-a*]

A slight excess of $[\text{V}(\text{CH}_2\text{SiMe}_3)_4]$ (250 mg) and CeO_{2-200} (2 g) in pentane (20 mL) was mixed at 25 °C for 4 h. After filtration, the solid $[\text{V}(\text{CH}_2\text{SiMe}_3)_4]/\text{CeO}_{2-200}$ was washed three times with pentane. The resulting powder was dried under vacuum (10^{-5} Torr). This material presents a saturation of the vanadium precursor with 1.29 wt% V and 2.14 wt% C on the surface of ceria.

2.2.5 Preparation of $[V(=O)(OtBu)_3]/CeO_2$ [V3-a]

CeO_{2-200} (2 g) and $[V(=O)(OtBu)_3]$ (250 mg) were combined in pentane (10 mL) and stirred at 25 °C for four hours. After filtration and washed 3 times, the resultant powder was vacuum-dried (10^{-5} mbar). Elemental analysis: V 1.0 wt% and C 1.75 wt%.

2.2.6 Preparation of V -oxo/ CeO_2 , [xV1-b] (x= 0.2%, 1.2%, 2.1%, 4%)

The grafting material $[V(=O)(OEt)_3]_2/CeO_{2-200}$ was calcined under dry air with the gas flow rate of 45 mL min⁻¹ at 500 °C for 16 h. Vacuum was applied after the calcination process to avoid water adsorption. Then the sample was transferred and kept in the glove box. The [xV1-b](x=0.2 wt%, 1.2 wt%, 2.1 wt%, 4 wt%) were obtained by calcining the corresponding $[V(=O)(OEt)_3]_2/CeO_{2-200}$.

2.2.7 Preparation of V -oxo/ CeO_2 , [V2-b], [V3-b]

The material $[V(CH_2SiMe_3)_4]/CeO_{2-200}$ [V2-a] and $[V(=O)(OtBu)_3]/CeO_{2-200}$ [V3-a] were respectively calcined under dry air with a gas flow rate of 45 mL/min at 500 °C for 16 h. Vacuum was applied after the calcination at 500 °C to avoid water adsorption. Then the obtained materials were called [V2-b] and [V3-b] and kept in the glove box.

2.2.8 Preparation of VO_x/CeO_2 by impregnation method, IMPV- CeO_2

Typically, a water-based solution of ammonium metavanadate (Aldrich, 99.99%) NH_4VO_3 (29.6 mg in 10 mL of water) was added to 1 g of CeO_2 . Oxalic acid was added to accelerate the dissolution according to the molar ratio NH_4VO_3 : Oxalic acid =1:3. The suspension was stirred overnight at room temperature, and then water was evacuated in a rotary evaporator at 50 °C. VO_x/CeO_2 was obtained after calcination under dry air at 500 °C for 16 h, which is named IMPV- CeO_2

2.3 Chapter IV: Selective Catalytic Reduction of NO_x with NH_3 over niobium supported on CeO_2 prepared by Surface Organometallic Chemistry

2.3.1 Preparation of $[Nb(OEt)_5]_2/CeO_{2-200}$ [Nb-a]

A slight excess of $[Nb(OEt)_5]$ (350 mg) and CeO_{2-200} (4 g) in toluene (20 mL) was mixed at 25 °C for 4 h. After filtration, the solid $[Nb(OEt)_5]_2/CeO_{2-200}$ was washed three times with 10 ml of toluene and 10 mL of pentane. The resulting powder was dried under vacuum (10^{-5} Torr). This material presents a saturation of the vanadium precursor with the accessible

hydroxyl groups of the ceria surface (1.8 wt% Nb).

2.3.2 Chapter IV Preparation of Nb-oxo/CeO₂ [Nb-b]

The material [Nb(OEt)₅]/CeO₂₋₂₀₀ was calcined under dry air with the gas flow rate of 45 mL min⁻¹ at 500 °C for 16 h. Vacuum was applied right after calcination process at 500 °C to avoid water adsorption. Then the sample was transferred and kept in the glove box.

3 Characterization methods

3.1 Mass balance

Elemental analyses were performed at Mikroanalytisches Labor Pascher (Remagen, Germany). Gas-phase analyses were performed on a Hewlett Packard 5890 series II gas chromatograph equipped with a flame ionization detector and KCl/Al₂O₃ column (30 m², 0.32 mm).

3.2 Diffuse reflectance infrared spectra

Diffuse reflectance infrared spectra were collected in a Nicolet 6700 FT-IR spectrophotometer at a resolution of 4 cm⁻¹. An airtight IR cell with CaF₂ windows was employed and the final spectra comprise 64 scans. The in-operando DRIFTS-GC/MS experiments were carried out in an integrated system comprising mass flow controllers (Brooks), FT-IR adapted high temperature reaction chamber (Harrick Scientific) and online GC/MS (Agilent GC 6850 MS 5975C). The reaction chamber was equipped with ZnSe windows and fitted into the Praying Mantis optical unit also provided by Harrick. In the glove box, the sample was placed onto a porous stainless-steel frit in the reaction chamber. A selected gas (argon, nitrogen oxide or synthetic air) was continuously flowing through the sample. FT-IR spectra were recorded in a Nicolet 6700 spectrophotometer with a MCT detector and 4 cm⁻¹ resolution. The final spectra were obtained after subtraction with KBr spectra taken at the same temperature (and same heating rate) as the background.

3.3 Raman

Raman spectra were acquired using the 532 nm line of an Ar-ion laser (Melles Griot). The excitation beam was focused on the sample by a 50X working distance microscope and the scattered light was analyzed by an air-cooled CCD (Labram HR, Horiba Jobin Yvon). The fluorescence was subtracted from the spectra for clarity. Spectra were performed in the ex situ

mode at room temperature in ambient air. A 500 s acquisition time was used for each spectrum and spectra were accumulated from 550 to 1250 cm^{-1}

3.4 NMR

Solution NMR spectra were recorded on an Avance 300 Bruker spectrometer. All chemical shifts were measured relative to residual ^1H or ^{13}C resonances in a deuterated solvent: C_6D_6 (7.15 ppm for ^1H , 128 ppm for ^{13}C). ^1H and ^{13}C solid state NMR spectra were recorded on a Bruker Avance 500 spectrometer with a conventional double-resonance 4 mm CP-MAS probe. The samples were introduced under argon in a zirconia rotor (4 mm), which was then tightly closed. In all the experiments, the rotation frequency was set to 10 kHz. Chemical shifts were given concerning tetramethylsilane (TMS) as an external reference for ^1H and ^{13}C NMR. The ^{51}V MAS NMR spectrum was acquired in a Bruker DSX 300 spectrometer (^{51}V : 78.9 MHz) using a single pulse excitation. The signal was optimized with crystalline V_2O_5 ($\delta = -609$ ppm) as external standard with a pulse angle of $\pi/2$. Two spinning rates were used in order to determine the isotropic chemical shift (7 kHz and 10 kHz).

3.5 X-ray diffraction

X-ray diffraction was performed on a Siemens D8 diffractometer at Bragg–Brentano geometry (ISA, Villeurbanne). The instrument is equipped with a Cu tube ($\lambda = 1.5406 \text{ \AA}$). Diffractograms were collected in $10\text{-}70^\circ$ 2θ range by ethanol dispersion over Silicon support and treated using DIFFRAC.EVA Bruker software.

3.6 X-ray absorption spectra

For the tungsten containing materials, the extended X-ray absorption fine-structure (EXAFS) spectra were acquired at ELETTRA, using the XAFS beamline (experiment code: 20145422)55 at room temperature at the tungsten L_{III} -edge. A pair of Si(111) crystals were used as the monochromator and the harmonics were rejected by the detuning of the second crystal. The spectra were recorded in the transmission mode between 9.9 and 11.43 keV. Three scans were collected for each sample. Each dataset was simultaneously collected with a W metal foil reference (11206.7 eV), and it was later aligned according to that reference (maximum in the first derivative of the first peak of the W foil). The W-supported samples were packaged within a nitrogen-filled glovebox in a double airtight sample holder equipped with Kapton windows. The data analyses were carried out using the "Athena" program and the EXAFS fitting "RoundMidnight" program, from the "MAX" package, using spherical

waves. The FEFF8 program was used to calculate the theoretical files for phases and amplitudes based on model clusters of atoms. The scale factor, $S_0^2 = 0.94$, was evaluated from $[W(\equiv C t Bu)Np_3]$ molecular complex diluted in BN and conditioned as a pellet (one carbon at 1.76(1) Å, with three carbon atoms at 2.10(1) Å in the first coordination sphere, and one carbon atom at 3.25(3) Å and three carbon atoms at 3.34(3) Å in the second coordination sphere). The refinements of the fits were carried out by fitting the structural parameters N_i , R_i , σ_i for each path and the energy shift, ΔE_0 (the same for all shells), using "RoundMidnight".

X-ray absorption near edge structure (XANES) spectra were acquired at ESRF on BM23 beam-line, at room temperature. At the vanadium K edge a double Si(111) crystal was used as monochromator and a system based on a total reflection through a double X-ray mirror with an incidence angle variable from 2 to 5 mrad allowed harmonic rejection to a level better than 10^{-5} . The spectra were recorded in the transmission mode between 5.3 to 6.44 KeV at room temperature (295 K). Each data set was collected simultaneously with a V metal foil reference and was later aligned according to that reference (first maximum of the derivative of the V foil spectrum set at 5465.1 eV). The molecular complexes and vanadyl sulfate were homogeneously mixed with dry BN and the supported V samples were packaged as pellets within an argon filled glovebox in a double air-tight sample holder equipped with kapton windows. The data analyses were performed by standard procedures using in particular the program "Athena".

3.7 X-ray Photoelectron Spectroscopy (XPS)

The XPS analyses were performed using a Kratos Ultra DLD spectrometer. The monochromatized Al K α radiation (1486.6 eV) was used as the excitation source, run at 12 kV and 15 mA and CAE analyzer mode. The sample powders were analyzed, mounted on double-sided adhesive tape (conductive carbon). The pressure in the analysis chamber was in the range of $5 \cdot 10^{-9}$ Torr during data collection. The binding energies (BE) of the different core levels were referred to the Ce u''' component associated to the Ce 3d_{3/2} component set at 916.7 eV. Ce 3d region has been recorded in the first place to reduce the effects of X-ray irradiation on the sample (12 scans/1490 s). Analyses of the peaks were performed using the software CasaXPS LTD. Curve-fitted using a Shirley background with a fixed Lorentzian-to-Gaussian ratio of 30%. Atomic concentrations were calculated from the peak area using Relative Sensitivity Factors (R.S.F) provided in the software.

3.8 Electron Microscopy: TEM, STEM and EDX

Scanning Transmission Electron Microscopy-High Angle Annular Dark Field (STEMHAADF) images were obtained in a probe-corrected Titan ETEM G2 (FEI) with a working voltage of 300 kV, coupled with a HAADF detector at CLYM (IRCE Lyon).

X-ray Energy Dispersive Spectra (EDS) were obtained with an EDAX detector. The samples were dispersed in toluene and a small amount of solution was deposited on a Cu-carbon grid.

4 Catalytic tests

The NH₃-SCR catalytic evaluations were performed in a quartz fixed-bed reactor. A total gas flow rate of 300 mL min⁻¹ (Hourly space velocity: 318 000 h⁻¹) at atmospheric pressure, typically composed of 300 ppm NO (air-liquid, crystal grade), 350 ppm NH₃ (air-liquid, crystal grade), 10 vol% O₂ (air-liquid, crystal grade), and 5% H₂O (when used), was sent through 30 mg of the presented catalyst diluted with 500 mg of silicon carbide to ensure a volume of 1 cm³. The reactor equipped with an internal thermometer was heated from room temperature to 600 °C at a heating rate of 10 °C min⁻¹. The system was maintained at 600 °C for 10 min before cooling down. Analyses of the gas concentrations of NO, NO₂, N₂O, and NH₃ were conducted using Antaris IGS FTIR (Thermo Fisher) equipped with a gas cell of 200 mL. N₂ selectivity was evaluated assuming that the outlet gas contains no N compounds other than NO, NO₂, N₂O, and NH₃. The catalytic activity and N₂ selectivity were calculated according to reference [6].

$$\text{NO}_x \text{ conversion (\%)} = \frac{[\text{NO}_x]_{\text{in}} - [\text{NO}_x]_{\text{out}}}{[\text{NO}_x]_{\text{in}}} \times 100\%$$
$$\text{N}_2 \text{ selectivity (\%)} = \frac{[\text{NO}_x]_{\text{in}} + [\text{NH}_3]_{\text{in}} - [\text{NO}_x]_{\text{out}} - [\text{NH}_3]_{\text{out}} - 2[\text{N}_2\text{O}]}{[\text{NO}_x]_{\text{in}} + [\text{NH}_3]_{\text{in}} - [\text{NO}_x]_{\text{out}} - [\text{NH}_3]_{\text{out}}} \times 100\%$$

5 Temperature programmed analysis

5.1 NH₃-TPD

Ammonia temperature-programmed-desorption (NH₃-TPD) was carried out in quartz reactor connect to an Antaris IGS FTIR (Thermo Fisher) for ammonia quantification. The catalyst (50 mg) was charged into the quartz reactor, and NH₃ was flushed through the reactor for 2 h at room temperature. Then, the reactor was extensively purged under argon before the temperature was increased from room temperature to 600 °C at a rate of 10 °C min⁻¹ under a flow of Ar (20 ml/min), and then the reactor cooled down.

5.2 NH₃ Adsorption detected by microcalorimetry

The adsorption experiments were performed at 110 °C in a heat flow microcalorimeter (Tian-Calvet type, C80 from Setaram) linked to a conventional volumetric apparatus and equipped with a Barocel capacitance manometer (Datametrix) for pressure measurements. Prior to the SO₂ or NH₃ adsorption, the samples were treated overnight at 400 °C (1 °C/min) under air and outgassed 1 h also at 400 °C.

The differential heats of adsorption were measured as a function of coverage by repeatedly sending small doses of probe molecule over the powders until an equilibrium pressure of about 67 Pa was reached [7]. The samples were then outgassed for 30 min at the same temperature and a second adsorption was performed (still at 110 °C) until an equilibrium pressure of about 27 Pa was attained in order to calculate the amount of irreversible adsorption at this pressure. The difference between the amounts of gas adsorbed at 27 Pa during the two adsorption runs corresponded to the number of strong adsorption sites.

5.3 H₂-TGA

Hydrogen temperature-programmed-reduction was carried out in the TGA, using a PerkinElmer instrument (Pyris Diamond TG/DTA analyzer). The catalyst (around 50 mg) was charged into TGA, and H₂ was pulsed into the reactor to purge until the sample mass was stable. Then, the temperature was increased from room temperature to 1000 °C at a rate of 10 °C min⁻¹ under a flow of H₂ (5 ml/min), and then the reactor was cooled down. The mass difference was calculated assuming loss of oxygen.

References

- [1] D. Clark and R. Schrock, Multiple metal-carbon bonds.12. ¹Tungsten and molybdenum neopentylidyne and some tungsten neopentylidene complexes, *Journal of the American Chemical Society*, 100 (1978) 6774–6776. <https://doi.org/10.1021/ja00489a049>
- [2] R. P. Saint-Arroman, M. Chabanas, A. Baudouin, C. Copéret, J. M. Basset, A. Lesage, and L. Emsley. Characterization of Surface Organometallic Complexes Using High Resolution 2D Solid-State NMR Spectroscopy. Application to the Full Characterization of a Silica Supported Metal Carbyne: $\equiv\text{SiO-Mo}(\equiv\text{C}t\text{Bu})(\text{CH}_2t\text{Bu})_2$, *Journal of the American Chemical Society*, 123 (2001) 3820-3821. <https://doi-org/10.1021/ja002259n>
- [3] M. Taoufik, E. Le Roux, J. Thivolle-Cazat, C. Coperet, J.-M. Basset, B. Maunders and G.

J. Sunley, Alumina supported tungsten hydrides, new efficient catalysts for alkane metathesis, *Topics in Catalysis*, 40 (2006) 65–70. <https://doi-org/10.1007/s11244-006-0108-4>

[4] G.A. Razuvaev, V.N. Latyaeva, L.I. Vyshinskaya, V.V. Drobotenko; Synthesis and properties of covalent tri- and tetravalent vanadium; *Journal of Organometallic Chemistry*, 208 (1981) 169-192. [https://doi.org/10.1016/S0022-328X\(00\)82672-8](https://doi.org/10.1016/S0022-328X(00)82672-8)

[5] J. Abou Nakad, R. Rajapaksha, K.C. Szeto, A. De Mallmann, M. Taoufik, Preparation of Tripodal Vanadium Oxo-Organometallic Species Supported on Silica, $[(\equiv\text{SiO})_3\text{V}(=\text{O})]$, for Selective Nonoxidative Dehydrogenation of Propane, *Organometallics*, 41 (2022) 2784-2797. <https://doi-org/10.1021/acs.organomet.2c00377>

[6] Y. Peng, K. Li and J. Li, Identification of the active sites on $\text{CeO}_2\text{-WO}_3$ catalysts for SCR of NO_x with NH_3 : an in-situ IR and Raman spectroscopy study, *Applied Catalysis B: Environmental*, 140 (2013) 483–492. <https://doi.org/10.1016/j.apcatb.2013.04.043>

[7] A. Auroux, Microcalorimetry Methods to Study the Acidity and Reactivity of Zeolites, Pillared Clays and Mesoporous Materials, *Topics in Catalysis*. 19 (2002) 205-213. <https://doi-org/10.1023/A:1015367708955>

RESUME en français

L'objectif de cette thèse est de préparer de nouveaux catalyseurs à base de métaux des groupes V et VI supportés sur oxyde de cérium pour la réduction sélective des oxydes d'azote (NOx) par l'ammoniac (NH₃-SCR). La chimie organométallique de surface a été utilisée pour obtenir des sites isolés de type métal oxo, hautement actifs, en utilisant des précurseurs moléculaires de V, Nb et W à ligands alkyls ou alcoolates. Un catalyseur à base de tungstène oxo a été obtenu en deux étapes. La première consiste en une réaction de protonolyse entre le complexe [W(=CtBu)(CH₂tBu)₃] et les groupes hydroxyles d'une cérine traitée à 200 °C pour former une espèce supportée bipodale unique, [(=CeO)₂W(=CtBu)(CH₂tBu)], caractérisée par DRIFT, analyse élémentaire, XPS, RMN du solide, BET et EXAFS. La seconde, une calcination contrôlée du matériau sous air, permet d'accéder à un mélange d'espèces oxo-tungstène caractérisées par DRIFT, analyse élémentaire, XPS, Raman, RPE, RMN, BET, NH₃-TPD, H₂-TPR, TEM et EXAFS. Les spectroscopies Raman et EXAFS montrent la formation de deux espèces : mono-oxo, [(=CeO)₄W(=O)] et bis-oxo, [(=CeO)₂W(=O)₂], dans un rapport 70/30. Avec [Nb(OEt)₅]₂ comme précurseur, cette nouvelle approche a été étendue à la préparation d'un site isolé de structure [(=CeO)₂Nb(=O)(OH)], révélée par DRIFT et EXAFS. Contrairement aux cas du tungstène et du niobium, pour le vanadium cette approche a conduit à un mélange d'espèces surfaciques monomères, dimères, oligomères et à un dépôt de V₂O₅, ceci du fait de la mobilité du vanadium à la surface de la cérine et cela quel que soit le précurseur moléculaire utilisé, ([V(=O)(OEt)₃]₂, [V(CH₂SiMe₃)₄] ou [V(=O)(OtBu)₃]). La concentration des espèces obtenues à la surface de la cérine a été déterminée par analyse quantitative des spectres infrarouge et RMN ⁵¹V. Les résultats montrent que la proportion en site isolé diminue lorsque la teneur en vanadium augmente. Les performances catalytiques en NH₃-SCR de ces nouveaux matériaux ont été évaluées entre 50 et 600 °C dans un réacteur sous flux continu (300 ppm NO, 360 ppm NH₃, 12% O₂, He). Comparé aux catalyseurs à base de métaux-oxo du groupe V (V, Nb) supportés sur cérine, le catalyseur à base de tungstène oxo présente une haute activité dans une large gamme de température et montre une stabilité remarquable après plusieurs cycles catalytiques. Pour justifier cette plus forte activité du tungstène oxo supporté sur cérine, comparée à celles du niobium ou vanadium oxo, des explications fondées sur les propriétés intrinsèques du tungstène sont avancées.

Keywords: DeNOx, Ammoniac, catalyseurs supportés, tungstène-oxo, vanadium-oxo, niobium-oxo, cérine, XAS

RESUME en anglais

The aim of this thesis is to prepare new catalysts based on metal oxo of groups V and VI supported on cerium oxide for the selective reduction of NOx by NH₃. Surface organometallic chemistry has been employed in this work to obtain highly active isolated metal oxo sites by using organometallic precursors of V, Nb, and W bearing alkyls or alkoxide ligands. For instance, tungsten oxo-based catalyst has been achieved in two steps. The first step consists of protonolysis reaction of the complex [W(=CtBu)(CH₂tBu)₃] with ceria dehydroxylated at 200 °C, giving a well-defined bipodal species expressed as [(=CeO)₂W(=CtBu)(CH₂tBu)], characterized by DRIFT, Elemental analysis, XPS, SS NMR, BET and EXAFS. Controlled calcination of this surface species under air results in a mixture of tungsten oxo species characterized by DRIFT, Elemental analysis, XPS, Raman, EPR, SS NMR, BET, NH₃-TPD, H₂-TPR, TEM and EXAFS. Notably, Raman and EXAFS spectroscopies revealed the formation of a mixture of tungsten mono-oxo [(=CeO)₄W(=O)] and tungsten bis-oxo [(=CeO)₂W(=O)₂] surface species in a ratio of 70/30. Using [Nb(OEt)₅]₂ as precursor, this new approach has been extended to the preparation of isolated Nb oxo site expressed as [(=CeO)₂Nb(=O)(OH)], revealed by DRIFT and EXAFS. Contrary to the tungsten and niobium systems, this novel synthetic approach gives a mixture of surface species composed of monomeric, dimeric, oligomeric and even V₂O₅, independent on the nature of the applied organometallic precursors ([V(=O)(OEt)₃]₂, [V(CH₂SiMe₃)₄] et [V(=O)(OtBu)₃]), due to the mobility of vanadium on ceria surface. The concentration of these species on the ceria surface has been determined by quantitative analysis of IR and ⁵¹V MAS NMR data, showing that the percentage of isolated sites decreases upon increasing the vanadium loading. The catalytic performance in NH₃-SCR of these new catalysts has been evaluated between 50 – 650 °C in a continuous flow reactor containing 300 ppm NO, 360 ppm NH₃ and 12% O₂ in He. Compared to metal oxo of group V transition state metal supported on ceria, the tungsten oxo-based catalyst presents high activity within a broad temperature window and exhibits exceptional stability after multiple catalytic test cycles. Tentative to explain the high activity of tungsten oxo supported on ceria, compared to niobium oxo and vanadium oxo, associated with the intrinsic properties of tungsten have proceeded.

Keywords: DeNOx, Ammonia, single site, Ceria, XAS spectroscopy, tungsten-oxo, vanadium-oxo, niobium-oxo

Intitulé et adresse de l'unité ou du laboratoire

Catalyse, Polymérisation, Procédés et Matériaux (CP2M) ; UMR 5128, 43 Blvd du 11 Novembre 1918, PO BOX 2077, 69616 Villeurbanne Cedex, France